EXPERIMENTAL INVESTIGATIONS INTO 4-D PRINTING OF BARIUM TITANATE AND GRAPHENE REINFORCED PVDF MATRIX COMPOSITES

A dissertation submitted
in the fulfillment of the requirements
for the degree of

DOCTOR OF PHILOSOPHY

Submitted by

Ravinder Sharma

Regd, No: 901708005

<u>Under the guidance of</u>

Dr. Ajay Batish
Professor Mech. Engg.
TIET, Patiala

Dr. Rupinder Singh
Professor Mech. Engg.
NITTTR, Chandigarh

Mechanical Engineering Department
Thapar Institute of engineering and technology
(Deemed to be University), Patiala
October, 2021

CERTIFICATE

Certified that the work presented in the thesis entitled "**Experimental investigations into 4-D printing of barium titanate and graphene reinforced PVDF matrix composites**" being submitted by Mr Ravinder Sharma (Regd. No. 901708005) in fulfilment of the requirement for the award of the degree of 'Doctor of Philosophy' in the Department of Mechanical Engineering, Thapar Institute of Engineering and Technology, Patiala, is an authentic record of the candidate's own work carried out during the period from July 2017 to October 2021 at this institute under our supervision. The matter presented in this dissertation has not been submitted for the award of any other degree in any university.

Dr. Ajay Batish
Professor, MED,
TIET, Patiala

Dr. Rupinder Singh
Professor, MED
NITTTR, Chandigarh

DECLARATION

I hereby certify that the work which is being presented in this thesis, entitled **"Experimental investigations into 4-D printing of barium titanate and graphene reinforced PVDF matrix composites"**, in the fulfilment of the requirement for the award of degree of 'Doctor of Philosophy' in Mechanical Engineering submitted to the Department of Mechanical Engineering of Thapar Institute of Engineering and Technology (Deemed to be University), Patiala is an authentic record of my own work carried out under the supervision of Dr. Ajay Batish Professor, Mechanical Engineering Department, Thapar Institute of Engineering and Technology, Patiala and Dr. Rupinder Singh, Professor, Mechanical Engineering Department, National Institute of Technical Teachers Training & Research, Chandigarh.

The matter presented in this dissertation has not been submitted in part or full to any other university or institute for the award of any degree in India or abroad.

Ravinder Sharma

ACKNOWLEDGEMENT

First of all, I would like to express my gratitude to my supervisor Dr. Ajay Batish, Professor, Mechanical Engineering Department, Thapar Institute of Engineering and Technology, Patiala and Dr. Rupinder Singh, Professor, Mechanical Engineering Department, National Institute of Technical Teachers Training & Research, Chandigarh for their invaluable guidance, moral support and encouragement during the entire period of this research which cannot adequately be expressed in words in this acknowledgement.

I would like to extend my acknowledgment to my Doctoral committee member Dr. O. P. Pandey, Dr. Vivek Jain, and Dr. Vineet Srivastava for their valuable observations, suggestions, and feedback. I am very much grateful to my friends Dr. Sandeep Sharma, Dr. Ranvijay Kumar, and Rahul Gupta, for their help and support.

I would like to thank Dr Nishant Ranjan, who provided a great support during my dissertation writing. A special thanks to S. Bhagwan Singh and Smt Amarjeet kaur of Patiala, who always gave me love and Support me like a son,

I would like to thanks my parents, Dr. Ashok Sharma and Smt. Kiran Sharma, whose consistent love and support motivate me throughout the period of research. I would also like to thank my sister Mrs Mamta Bhardwaj and brother in law Mr Tejeshwar Bhardwaj, for their valuable support which helped me in achieving the goal.

Special thanks to my wife Insp. Deepti Sharma for her understanding, patience, and support during the research period.

Above all, I thank almighty whose blessings have enabled me to accomplish this research work.

Ravinder Sharma

LIST OF PUBLICATIONS

Total publications = 11 (SCI-5, Scopus-5,Book Chapter-1)
Manuscripts under review= SCI-1

a. SCI Publications

S. No.	Title of Paper	Journal Name and details (Year/Vol./ Issue/ DoI)	Status	Impact factor
1	On synergistic effect of $BaTiO_3$ and graphene reinforcement in PVDF matrix for 4D applications	Proceedings of the Institution of Mechanical Engineers, Part C, 2021 DoI:10.1177/09544062211015763 (Sage publication)	Published	1.762
2	On effect of chemical-assisted mechanical blending of barium titanate and graphene in PVDF for 3D printing applications	Journal of thermoplastic composites, 2020 DoI:10.1177/0892705720945377 (Sage publication)	Published	3.330
3	On mechanical and surface properties of electro-active polymer matrix-based 3D printed functionally graded prototypes	Journal of thermoplastic composites,2020 DoI:10.1177/0892705720907677 (Sage publication)	Published	3.330
4	Study on barium titanate and graphene reinforced PVDF matrix for 4D applications	Journal of thermoplastic composites,2019 DoI:10.1177/0892705719865004 (Sage publication)	Published	3.330
5	On flexural and pull out properties of smart polymer based 3D printed functional prototypes	Sadhana-academy proceedings in engineering sciences, 2021 DoI:10.1007/s12046-021-01709-x (Springer Publication)	Published	1.188
6	Effect of mechanical blending and chemical assisted mechanical blending on PVDF nano-composites: mechanical, thermal, morphological and 4D properties	journal of materials engineering and performance (Springer Publication)	Under Review	1.819

b. Scopus publications

S. No.	Title of paper	Journal/ Vol. /Issue/Year/ DOI	Status/ pp
1	On multi response optimization and process capability analysis for surface properties of 3D printed functional prototypes of PVC reinforced with PP and HAp	Materials Today Proceedings Vol 28, 2020 DoI:10.1016/j.matpr.2020.01.092	1115-1122
2	Mechanical characterization of FDM filaments with PVDF matrix reinforced with Graphene and Barium Titanate	IOP Conf. Series: Materials Science and Engineering, 999, 2020 IOP Publishing DoI:10.1088/1757-899X/999/1/012010	012010
3	Investigations for Barium Titanate and Graphene Reinforced PVDF Matrix for 4D Applications	Encyclopedia of Renewable and Sustainable Materials Vol.1, 2020 DoI:10.1016/B978-0-12-803581-8.11306-2 (Elsevier Publication)	366-375
4	Investigations on chemical assisted mechanically blended 3D printed functional prototypes of PVDF-BaTiO$_3$-Gr composite	Encyclopedia of Materials: Plastics and Polymers Section: Fundamentals of thermoset and thermoplastic polymers & their recycling and sustainability, 2021 DoI:10.1016/B978-0-12-820352-1.00144-9 (Elsevier Publication)	Published
5	On Dynamic Mechanical Analysis of Mechanically Blended 3D Printed Functional Prototypes of PVDF-BaTiO3-Gr Composite	Encyclopedia of Materials: Plastics and Polymers Section: Fundamentals of thermoset and thermoplastic polymers & their recycling and sustainability, 2021 DoI: 10.1016/B978-0-12-820352-1.00145-0 (Elsevier Publication)	Published

c. Book chapters

S. No.	Title of paper	Book Detail **(DoI No.)**	Status
1	PVDF-graphene-BaTiO$_3$ composite for 4D applications	4D Printing, 2021 (Elsevier Publication)	In-Press

ABSTRACT

3D printing of smart materials is one of the disruptive innovations in the field of advanced manufacturing. From the past one decade significant advancements have been reported in this sector with respect to printers, materials, and processes. Fused deposition modelling (FDM) (one of the low cost 3D printing technologies) has entered into the field of smart manufacturing, in which active materials are being used particularly for dynamic 4D applications. FDM has been widely explored for different range of thermoplastics and thermosetting composites. Researchers have worked on the in-house development of thermoplastic composite based feedstock filaments by using various polymers such as polyvinyl chloride (PVC), poly lactic acid (PLA), polypropylene (PP), acrylonitrile butadiene styrene (ABS) etc. for numerous applications. But, hitherto little has been reported on the preparation of smart polymer based feedstock filament for 3D printing of functional prototypes having 4D properties. In this research work an electro-active polymer, polyvinylidene fluoride (PVDF) was reinforced with graphene (Gr), and barium titanate (BTO) for the preparation of composite.

Two different methods of blending have been explored for the development of smart polymer based composite (i) mechanical blending (MB) of materials and (ii) chemical assisted mechanical blending (CAMB). In the first stage, based upon the melt flow index (MFI), different proportions/compositions of PVDF-Gr-BTO were selected for extrusion with twin screw extruder (TSE). Further to optimize the process parameters of TSE three input parameters (a) extruder temperature, (b) rotational speed (rpm) and (c) composition were selected. The prepared feed stock filaments of MB based composites were subjected to mechanical, thermal dimensional and morphological analysis. The analysis of variance (ANOVA), suggested the optimised settings of TSE for fabrication of MB based composite feedstock filament as: extruder temperature 200°C, rotation speed 40 rpm with composition PVDF (78%) + Gr (2%) + BTO (20%) (by weight %). The prepared feedstock filament was used to run on low cost open source FDM setup for 3D printing of standard prototypes by selecting the infill speed (IS), infill angle (IA) and infill density (ID) as input parameters. Prepared samples were subjected to tensile, flexural, pull-out and morphological testing. The fabricated specimens were also subjected to dimensional variation, shore-D testing and dynamic mechanical analysis (DMA). Further 3D printing of scaffolds was performed at optimised settings for process capability analysis to ascertain the industrial usability for batch production.

In the second stage, process parameters of TSE were optimised for the preparation of CAMB composite based feedstock filament. Further the prepared filament at optimised settings of TSE was used for 3D printing of standard scaffolds. The process parameters of FDM were also optimised for 3D printing of parts using prepared composite by CAMB. The 3D printed standard tensile and flexural samples were tested for process capability analysis.

In final stage optimised settings of FDM obtained for 3D printing of parts using MB and CAMB composites were used for fabrication of thin cylindrical discs (diameter 10 mm and thickness 0.4 mm), followed by electric poling (for possible piezoelectric characterization). The results of X-ray diffraction (XRD) and Fourier transmission infrared spectroscopy (FTIR), analysis shows more β-phase formation in the electrically poled sample as compared to non-poled specimen. Finally, a comparative study of mechanical, thermal, morphological, and 4D properties of PVDF-BTO-Gr nano-composites prepared by MB and CAMB was performed. The differential scanning calorimetry (DSC) analysis suggested that composite prepared by MB is thermally more stable as it absorbs more heat -31.09J/g during heating cycle. Further, the results of the study suggested that 3D printed functional prototypes prepared by CAMB are having better mechanical, morphological, and dielectric properties. The piezoelectric coefficient (d_{33}) 20 pC/N and 30.2 pC/N was observed on 3D printed specimen (prepared from filament processed with MB and CAMB respectively), suitable for pressure sensors, touch sensitive buttons or other user interface control, actuators for bio-mimetic based 4D applications.

TABLE OF CONTENTS

LIST OF TABLES

LIST OF FIGURES

ABBREVIATIONS

ABS	Acrylonitrile Butadiene Styrene
AM	Additive Manufacturing
ANOVA	Analysis of Variance
BTO	Barium Titanate
CAMBD	Chemical assisted mechanical blended
CAMB	Chemical assisted mechanical blending
CAD	Computer Aided Design
DSC	Differential scanning calorimetry
DPE	Direct Piezoelectric Effect
EAP	Electroactive polymer
EBM	Electron Beam Melting
F	Fisher’s Value
FDM	Fused deposition modelling
Gr	Graphene
LOM	Laminated object manufacturing
MS	Mean of Squares
MBD	Mechanical blended
MB	Mechanical blending
D_{33}	Piezoelectric coefficient
PLA	Poly Lactic Acid
PMC	Polymer Matrix Composite
PVC	Polyvinyl chloride
PVDF	Polyvinylidene Fluoride
P	Probability
RP	Rapid Prototyping
SEM	Scanning electron microscope
SLS	Selective Laser Sintering
SMA	Shape memory alloys
SMP	Shape memory polymers
SN	Signal to Noise
SSE	Single Screw Extruder

SCS	Solid Creation System
SGC	Solid Ground Curing
STL	Standard Triangulation Language
SLA	Stereolithography
SS	Sum of Squares
3D	Three Dimensional
3DP	Three-Dimensional Printing
TSE	Twin Screw Extruder
2D	Two Dimensional

CHAPTER 1

INTRODUCTION

1.1 Overview of AM

The AM, also known as 3D printing or RP has been commercially introduced since the late 1980s. The first time, Charles W. Hull, used the AM system for 3D printing of a tea cup on 9th March 1983 [1]. After that in a chronological manner, Carl R. Deckard in 1986 invented a new setup, selective sintering for fabrication of parts. It was considered as first development in the field of AM. In 1988 a team of Helisys, Inc. developed a laminated manufacturing system, in which layers were produced and bonded together for the fabrication of the final product [2]. The dimensions of layers were marked by an electronic file. Further, in 1989, a scientist of Stratasys Inc. invented a new method for creating the 3D object, named 'FDM'. After that many more methods have been further developed by scientists/researchers across the globe. Based on the type of raw material, AM processes are mainly classified in three types: (i) liquid-based, (ii) solid-based, and (iii) powder-based technologies (see Figure 1.1). The processes included in this are considered as most relevant in the present and promising for the future of the industry [3]. As compared to conventional manufacturing systems, AM is considered as a relatively new manufacturing approach for the automatic fabrication of prototypes. Unlike the conventional manufacturing processes, in which a subtractive manner of machining is used, AM joins the material to build a product. Designs that may be difficult to process by another method can be easily processed with AM systems [4]. In 2012, ASTM sets the standards for AM and defines that AM is capable of producing the parts by joining the material in layer by layer fashion [5].

Although a considerable amount of progress has been made in this field, however, still a lot of research work needs to be done to overcome the various challenges that have troubled the manufacturers till now [6]. Among the major advances that this process presents to product development are time and cost reduction, human interaction, and consequently the product development cycle [7]. Also, the possibility to create almost any shape that could be very difficult to machine, in a very small time frame is a major advantage of AM technologies. In simple AM gives ability to the user to directly print the final object from digital data.

However, AM has not been adopted to date for mass production in any of the manufacturing sectors, but scientists, medical professionals, market researchers, and artists are using it extensively [8, 9]. With AM, scientists can rapidly build and analyze models for theoretical comprehension and studies. Doctors can build a model of a damaged body to analyze it and plan better the procedure, market researchers can see what people think about a particular new product, and AM makes it easier for artists to explore their creativity [10].

Earlier, the lack of material availability restricted the application domain of AM techniques. However, in the last decade researchers have developed new materials based upon their utilities in various areas like medical, engineering, energy harvesting, etc., and till now they are doing efforts to make the AM feasible for the production of end-use products [12]. For part fabrication, 2D layers are deposited in the x-y plane, whereas, in the z-direction, layers are deposited along with the height. All the AM processes follow the same principle of layer-by-layer manufacturing system. Thus, AM is also known as the layer manufacturing process [13].

The procedure followed by all AM processes is as follows [6,11]:

Step 1: Create a 3D model of the part in CAD software including all the dimensions of the product

Step 2: Convert this CAD file into STL file format

Step 3: Processing and slicing the file with any slicer software into 2D layers and describe the printing conditions like part orientation, printing speed, Infill density, etc.

Step 4: 3D printing of part

Step 5: Post-processing (if required) like removal of support material.

Thus AM quickly converts the 3D geometrical model into a real-time object without using any physical tools, dies, or fixtures. Thus 3D printing is a very flexible and cheap technique for the production of any type of testing sample before original production.

1.1.1 Classification of the AM Processes

AM processes are mainly classified into three categories: (1) Liquid-based (2) Solid based and (3) Powder-based processes [14]. The classification of AM processes is shown in Figure 1.1.

(i) **Liquid-based AM processes:-** In this types of AM process, raw material is used in the liquid form and solidifies by curing process. For example: SLA, SCS, SGC etc.

(ii) **Solid-based AM processes**: - In this types of AM processes solid form of raw material is used at initial stage. Apart from powders, all types of solid raw materials like pallets, rolls, laminates, wires include in this category of AM processes. For example: LOM, FDM etc.

(iii) **Powder-based: -** In this type of AM processes powder is used as a raw material, and solidifies by the sintering process. For examples: SLS, 3DP, EBM etc.

In this research study, the FDM process has been used.

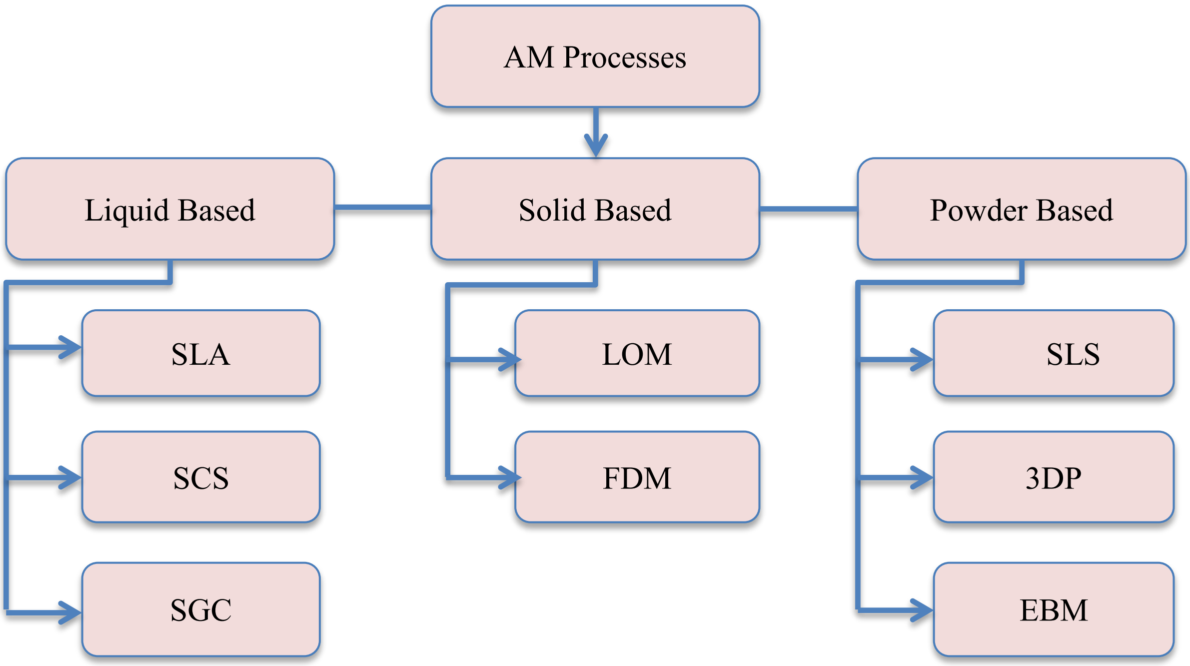

Figure 1.1 Classification of AM processes

1.2 An overview of FDM

FDM is a low-cost RP technique, which works on the principle of AM, in which material is deposited in a layered manner. FDM was invented by S.S. Crump a U.S. citizen in 1988 and patented as a RP Technology by Stratasys Ltd in 1992 [15]. Nowadays, FDM is one of the most popular AM process for the fabrication of models as well as final products. FDM is mostly used for making patterns, experimental models, and in production applications [16].

For the fabrication of any part, a 3D design of the part is initially created by a designer in CAD software. Then this digitally created 3D model is converted into STL format. Further, this file is processed and sliced with any slicer software into 2D layers and this software is also used to describe the printing conditions like part orientation, printing speed, Infill density, etc. [17].

In FDM, the thermoplastic filament is extruded in semi-liquid form through the heated nozzle. All FDM machines are having two sets of nozzles. The first nozzle is used to deposit the printing material, whereas; the second nozzle is used for printing of support material.

Nozzle temperature is set according to the melting point of the raw material. Electromechanical drives have been used to feed the filament wire [18]. The vertical and horizontal movement of the extrusion head is controlled by computer software. The nozzle first deposits the molten material in x-y directions. Once a layer is completed, the nozzle head moves upward in the Z direction and then re-apply the same layer over the previous one. This cycle repeats until the whole part is fabricated [19]. Figure 1.2 shows the constructional and working diagram of the FDM setup [9].

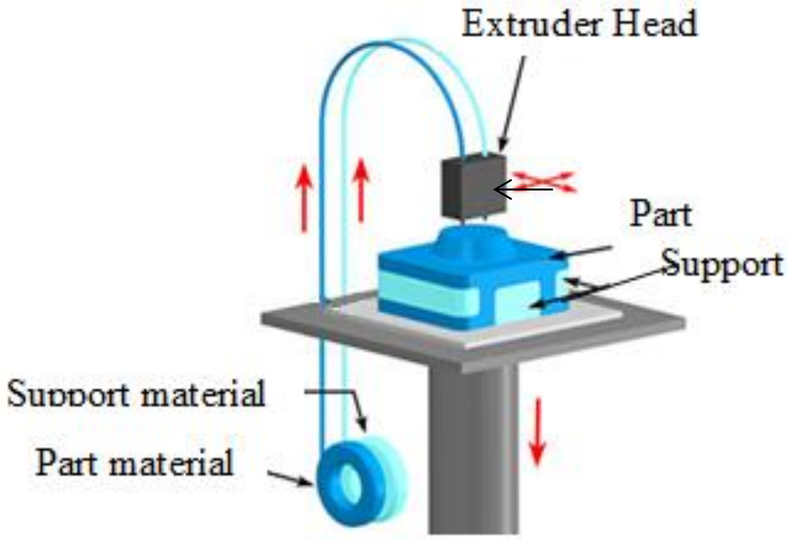

Figure 1.2 FDM Schematic

During the fabrication stage, sometimes there is a need to print the extra supportive material for providing support to overhang edges of the structure. Thus the second nozzle is used to deposit that material on the required space [20]. Mostly, the supportive material is soluble in water or in some other solvent. Once the part is completely built up, extra material is split away from the main product in the post-processing stage. Hence the fabricated product is ready to use. Figure 1.3 shows the steps followed in the 3D printing process.

Generally, FDM machines are taking thermoplastic or polymer matrix composite (PMC) based feedstock filament as a printing material. The open-source FDM printer provide simple operating conditions and good control over the input variables, such as infill speed, infill angle, infill density, raster width, printing temperature, type of fill etc. [21]. By varying these printing parameters, it is possible to produce customized parts on-demand and allows optimizing the product design.

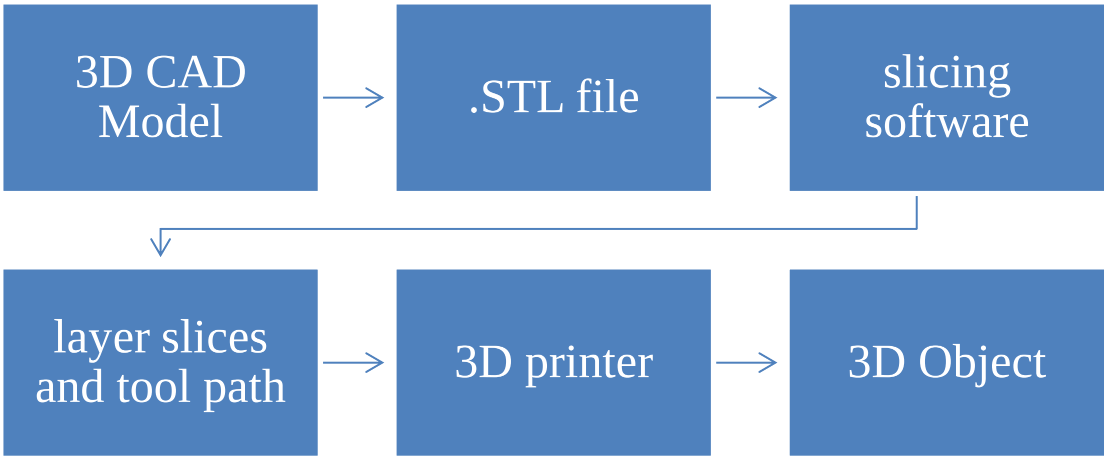

Figure 1.3 Steps follow in the 3D printing process

Research studies highlighted that the properties of fabricated parts are a function of process variables and can be efficiently improved with appropriate adjustment [6]. For functional prototypes the mechanical properties are very important, also it is essential to study the effect of process variables on the mechanical properties of the parts which can be efficiently improved by process optimization [22].

Mostly, FDM machines allow altering their basic processing parameters. The thermoplastic polymers used in FDM, exhibiting different physical, thermal, rheological, and mechanical properties. Some polymers having high melting temperature, like ABS polymer (210-250℃), whereas; some lies in low melting temperature zone like PLA polymer (185-220℃). Thus to adjust the processing condition as per the material used is necessary. Mostly, FDM systems follow the base-up approach. According to requirement FDM machines are available in different bed sizes. The most commonly used desktop 3D printer fabricates 200 × 200 × 200 mm^3. However, at industrial level, a size of 1000 × 1000 × 1000 mm^3 may also be used. Another, alternative way to produce big products on small 3D printers is to divide the product into small sizes of the different number of parts. Each small part is fabricated separately followed by assembly of parts [22-23].

In the last decade, FDM (3D printing) technology has been adopted for part fabrication in various fields, such as dental and orthopaedics, telecom, aeronautics, sporting, architectural, and automotive industries [24-25]. Moreover, due to high accuracy and precision, FDM technology has entered in the field of energy harvesting. An easy to use, less maintenance expenditures, and capability to produce any intricate part make the FDM process most demandable in modern industries [26].

1.2.1 Advantages of FDM process

- Easy to design and fabricate any type of model/prototype
- Flexibility in manufacturing
- Minimal wastage of raw material
- More sustainable
- Rapid production process
- Very low tolerance
- Ease in a material change
- Support removal is easy (Usually the support is of water soluble material)

1.2.2 Disadvantages of FDM process

- A skilled operator is required to run the FDM machine
- Less availability of raw material
- Small bed size leads limited product size
- Chocking of a nozzle head
- Unpredictable distortion and shrinkage
- Need post-processing
- Material swelling at elevated temperature
- A gap in between layers may reduce the strength of the product
- Surface roughness

Even after three decades of the invention of AM, most of its prominent processes like FDM are still facing the problem of material availability. On the flip side, the cost of commercially available and patented materials is very high. To overcome this problem, researchers are constantly working on methods to develop FDM-based feedstock filament by incorporating numerous polymers, powders, ceramics, metals, and so on. So far various PMC based feedstock filaments have been prepared by reinforcement of different metal powders or ceramics to improve the inherent properties of the polymer matrices [27-28]. Some of the majorly used polymers as printing material of FDM are ABS, PLA, PA6, PVC etc. or the composites based upon these polymers [29-31].

Along with this some of the 3D printing materials are more useful for structures that can be transformed in a pre-programmed way in response to a stimulus. Recently given the popular name of “4D printing” perhaps a better way to think about it, i.e. the object transforms over time [32].

1.3 4D Printing

4D printing was first introduced by an American designer, ‘Skylar Tibbits’ at MIT, California, in 2013. A complete demonstration with a full experiment on 4D printing was shown to the public. According to Tibbits’s statement, 4D printing is a process in which materials to be printing having the capability of transform over a certain period, or it is a system of customized materials that can alter/change their shape or any other physical property with the passage of time i.e. fourth dimension. It means the 3D printed object is doing dynamic activities over time [33].

4D printing uses the same techniques of 3D printing, through computer programmed deposition of material in successive layers to create a 3D object. However, 4D printing adds the dimension of transformation over time. In another definition 4D printing is a product building process, which incorporates the AM technology for depositing the layers of programmable multi-material or composite material. After fabrication, the product reacts with the stimuli from the environment (humidity, temperature, etc.) or itself and changes its properties accordingly. The ability to do so arises from the near-infinite configurations at a micrometer resolution, creating solids with highly engineered molecular spatial distributions [34] and thus allowing unprecedented multifunctional performance. 4D printing is the relatively latest in bio fabrication technology and rapidly emerging as a new paradigm in disciplines such as bioengineering, materials science, chemistry, and computer sciences [32].

1.3.1 Types of 4D Printing

4D printing can be defined as the ability of a material to change its shape or physical properties over the period of time. Many common terms such as autonomic 4D printing and autonomic self-changing are used to define such property in materials. The changes in physical properties of man-made materials are not found commonly without any external triggering. Thus, 4D printing can be of the following two types:

- Autonomic (without any intervention): In this type of 4D printing materials, there is no need for any type of external intervention/external triggering.
- Non-autonomic (needs human intervention/external triggering).

Recently, one of the actively researched areas lies in the AM of smart materials and structures. 4D printing may be defined as an AM process that integrates smart materials into the starting form of the printing material for 3D printed structures/components. After fabrication, the 3D object would respond in an intended manner to external stimuli from the environment or through human interference, resulting in a change in shape or physical properties over time [35].

1.4 Smart materials

The most essential part of 4D printing technology is its printing material, because it is the programmable material that adds the dimension of transformation over time to 4D printing.

Smart materials are those materials that can change their shape or properties under the influence of external stimuli. With the introduction of smart materials, the AM fabricated components that alter their shape or properties over time (the 4th dimension) as a response to the applied external stimuli. Hence, this gives rise to a new term called '3D printing of smart materials' [36].

Smart materials like shape memory material and EAPs have become an interest at the global level for their use in the field of textiles, nanotechnology, biomedical and electronic sensors. SMA, SMP, and EAPs are from the family of smart materials. Figure 1.4 shows the various types of smart materials.

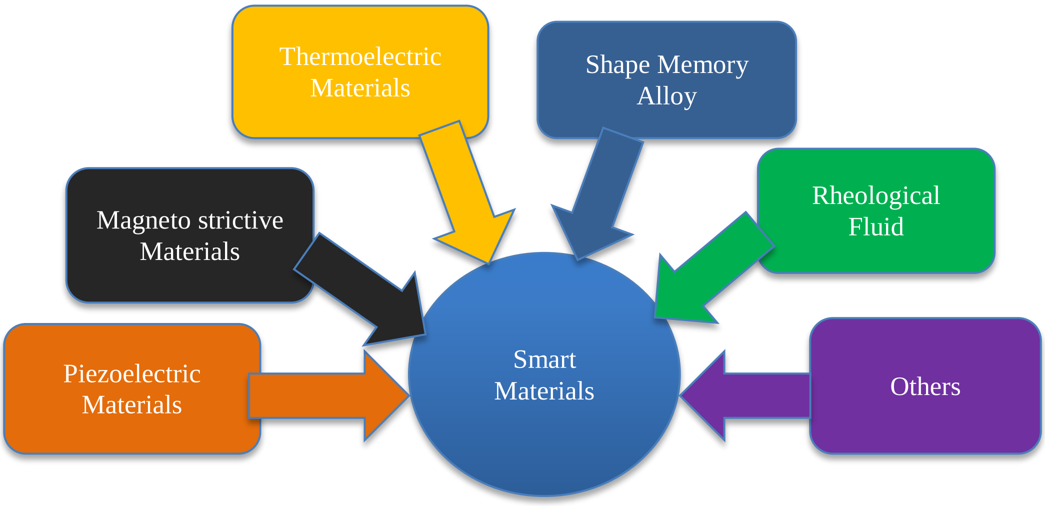

Figure 1.4 Types of smart materials

The shape memory effect of SMAs and SMPs shows the unique capability of smart materials to remain in the desired shape and retains their original shape when triggered by external stimuli from the environment. This functional property of SMAs and SMPs enhances their role in the field of AM, such as automatic assembly and disassembly, for example; the fasteners made up of such materials can perform auto disassembly under the effect of external stimuli. These cross-functional smart material-based devices show significant variations in a controllable manner when triggered artificially or environmentally [37].

From the last few years, 3D printing of active materials has been considered as a disruptive innovation in the field of advanced manufacturing. When these printed objects are subjected to some externally applied stimulus, then they are capable of transforming their one or more properties with passage of time. These types of post-processing activities are performed by some special types of active materials such as smart materials, shape-memory polymers, and shape-memory alloys. Smart polymer-based matrix composites (SPMC) can be easily tailored due to their lightweight, high flexibility, easy deformation properties, and low processing cost. For all such advantages, SPMC attained great interest among the researchers' community for offering a wide range of innovative solutions for the fabrication of smart devices in the field of electronics, microelectronics, sensing, photonics, adhesion, and biotechnology [38].

1.5 Piezoelectricity

The name "piezo" comes from the Greek, signifying "to press"; in present-day terminology. Piezoelectricity quickly developed as another field of exploration in the last two decades of the nineteenth century. Pierre and Jacques Curie tracked down the piezoelectricity in specific materials, for example, quartz; topaz, and, zinc blende. After one year, another scientist predicted the opposite impact of piezoelectricity, i.e. the applied voltage produces the mechanical distortion in material or we can say strains in the material. First time the piezoelectricity quartz was utilized in the mid-1920s for the control of oscillators, after that piezoelectric phenomenon is started to use in frequency control [39].

Thus in simple terminology, piezoelectric material accumulates electrical charges when mechanical stress is applied. This is called the piezoelectric effect, while, the conversion of electric field into mechanical strain is called the reverse piezoelectric effect.

Figure 1.5 (a) shows a molecular structure with no charge in it. As it shows there is no charge in a material before any subjective force and the center points of both positive and negative charges are coincide and show its electrically neutral condition [40]. Figure 1.5 (b) shows the charge is generated under the impact of external force. In the presence of external force over the molecular surface internal reticular may be distorted and separate the negative and positive centers and generates the dipoles. Thus, both opposing faced poles cancel each other and resulting in an electric charge on the surface (Figure 1.5 (c)). This is known as polarization of material and the effect is pronounced as direct piezoelectric effect (DPE). The electric field generated by polarization is used for the transformation of mechanical energy to deform the material into electric energy [40].

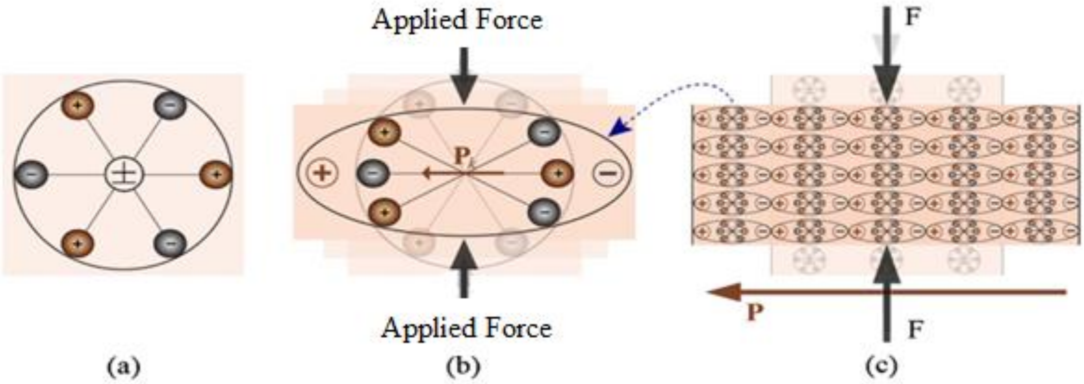

Figure 1.5 (a) A molecule having no piezoelectric polarization (neutral state); (b) Polarization (P_k) in a molecule under applied force (c) The polarized surface of piezoelectric material under the effect of external force

Two metal electrodes are deposited on both opposite surfaces of a piezoelectric material. These metal electrodes were connected externally with a galvanometer using short-circuiting wire. Mechanical force was applied on the outer surfaces of piezo crystal and a fixed charge appears on the crystal's surface connected to the electrodes (Figure 1.6(a)). The electric field was generated by this polarization and causes the free charge flow in the conductor. The charge will flow, until the produced charge neutralizes the effect of polarization. Thus it means there is net zero charge flow in the steady-state of a piezoelectric crystal. Polarization is also gone after the removal of external force and flow of charge reversed and the crystal gone into its original still condition (Figure 1.6 (b)). The whole process was displayed on a galvanometer by making peaks of current [40].

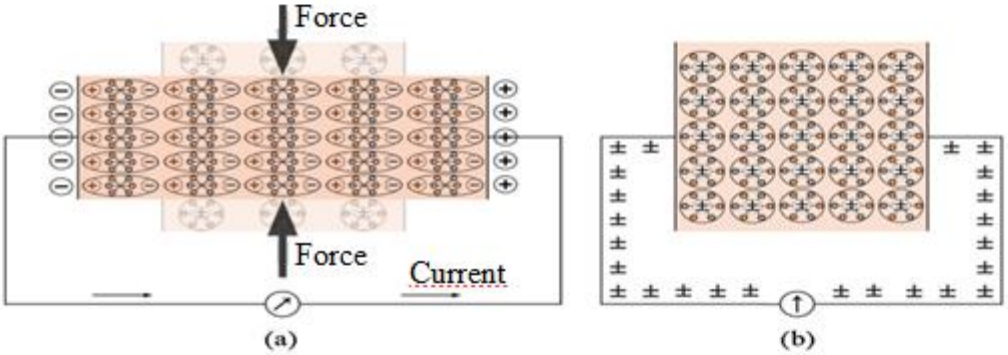

Figure 1.6 (a) Current flows under the external load when both terminals are short-circuited; (b) No current under neutral state

However, some piezoelectric materials shown the converse of the piezoelectric effect (CPE) that is a mechanical strain are produced in the crystal under the application of electric voltage. In this case, an electric current was supplied through the electrodes and resulted in mechanical deformation into the material. This type of transformation is generally applied in nano- positioning systems. The DPE plays a vital role in pressure sensors, vibrational energy scavenging, structural health monitoring, and energy harvesting. On the flip side, CPE is used in shape control, actuation, and ultrasonic motors.

Before understanding various coefficients of piezoelectricity for solid piezoelectric material, the direction of material due to the anisotropic nature of piezoelectric material must first be defined. Typical piezoelectric coefficients are denoted as Aij where 'i' denoted as the direction of the electrical measurement, and 'j' denotes the direction of the mechanical movement [41-42]. Figure 1.7 shows the typical dimensions of piezoelectric material for defining the piezoelectric constants [41].

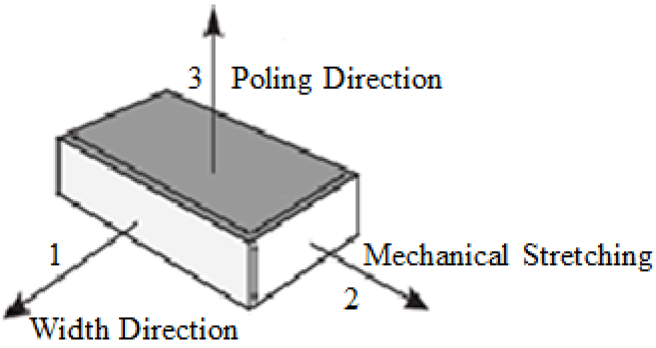

Figure 1.7 Schematic representations of dimensions in piezoelectric material

Some of the important piezoelectric constants regarding this study are:

Piezo strain constant: d3j ($C/m^2/N/m^2$) represents the piezoelectric effect in the film. This constant indicates how many charges can be accumulated in 1 m^2 when 1 Pa of pressure is applied along the "j" axis. Typical values of d_{33} for PVDF and its copolymer are between 5 and 30 pC/N.

Piezo stress constant: g_3j (Vm/N) represents the electric field induced in the "3" direction by stress of 1 Pa is applied along the "j" axis. It is often called piezo voltage constant and the typical g_{33} values for PVDF polymer are around 200-300 Vm/N [42-44].

The piezoelectric device-based energy harvesting techniques open the doors to develop autonomous and self-actuated electronic devices. Piezoelectric ceramics and quartz have been extensively used in electronic applications for a long time. The zinc oxide (ZnO) and lead zirconate titanate (PZT) are majorly used piezoelectric materials in electromechanical systems and transducers. Among the above said piezoelectric materials, PZT attained much attention due to its high value of the piezoelectric coefficient. Nevertheless, the brittleness and toxicity become a constraint in the application domain of PZT. Thus, to minimize their impact on the environment and health, researchers made intensive efforts to develop lead-free piezoelectric materials. Some researchers have developed nanowires of ZnO to generate a sufficient amount of power to lighten a light-emitting diode. However, the length of these nanowires was up to few micro-meters only which restrict their energy generation capacity [45]. From the last two decades, researchers are trying to employ piezoelectric polymers as sensors, actuators, and many more applications in the field of electronics and biomedical engineering. The major advantages of using piezoelectric polymers are their thermal, mechanical, electrical, chemical, and surface properties that can be easily tailored by applying different processing conditions [46, 47]. Moreover, polymer-based piezoelectric materials offer nontoxic, non-brittle, lower stiffness, and high tensile strength, which could be another possible approach for fabrication of flexible energy harvesting [48]. The piezoelectric property of PVDF was found in 1969, which opened the possibility of creation of relatively a new class of elastic polymers with a low dielectric constant [49]. The piezoelectric properties of the EAPs receive an acute interest from industrial research to produce low-cost energy harvesting devices. But low actuation and low power generation capacity of EAPs restrict their applications.

A multifunctional piezoelectric material receives immense interest from both academic and industrial research scholars as a low-cost energy-harvesting material [50]. It has been reported that piezoelectric or mechanical energy harvesting is a path toward the development of autonomous and self-powered electronic devices [51]. In the past decade, numerous studies have reported that low-power electronic devices and light-emitting diodes have increased energy efficiency to a significant level [52]. Earlier piezoelectric quartz and ceramics have been used in a majority of electronics applications. However, in recent years piezoelectric polymers gain such high popularity among researchers due to their versatile applications in the field of actuators, sensors, electronics, and biomedical engineering.

The mechanical, electrical, thermal, surface, and chemical properties of piezoelectric polymers can be easily tailored by different processing techniques [53-55]. The major attractive properties of the polymers such as light in weight, electrically and mechanically tough, and their compatibility with the organic and inorganic materials result in the development of multi-functional smart materials for a wide range of applications [45, 46, 56, 57]. Magnetostrictive materials, shape-memory polymers, piezoelectric materials, self-healing materials, pH-sensitive materials, thermoelectric materials, and so on are some of the types of smart materials [45-49, 58, 59]. These piezoelectric materials are used to produce a voltage under the application of mechanical stress or vice versa and are known as electro-active materials.

1.6 An overview of EAPs

The EAPs, are polymers that exhibit a change in size or shape when stimulated by an electric field. A typical characteristic property of an EAP is that it will undergo a large amount of deformation while sustaining large forces [60]. EAPs can be easily deformed or manufactured into various shapes.

Ferroelectric polymers (dielectric polymers) are a group of crystalline polar polymers. These polymers maintain a permanent electric polarization, which can be reversed, or switched, in an external electric field [61]. Ferroelectric polymers, such as PVDF, are used in acoustic transducers and electromechanical actuators because of their inherent piezoelectric response, and as heat sensors because of their inherent pyroelectric response [62].

1.7 Extrusion process

Extrusion is the process in which, a block/billet of any metallic or polymeric material is reduced in cross-section by forcing it to flow through a die orifice under high pressure [63]. The schematic of a simple extrusion process in Figure 1.8 shows that the ram is applying a force on a material in a fully closed area with only one way to exit (via die) as per the required shape [64].

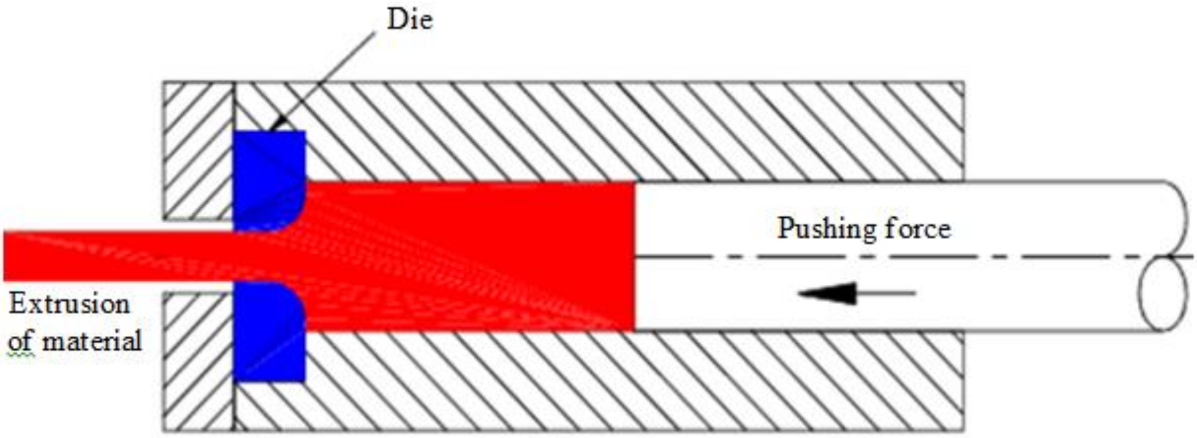

Figure 1.8 Schematic of extrusion process

The extrusion process is a forming technology in which a metal or thermoplastic polymer is forced to extrude/flow through a small cross-section with a predefined shape. The extrusion process is most widely used in the production of hollow tubes, wires, pipes and cylindrical bars. [64]. This process is similar to the drawing process except that the drawing process uses strong pressure to pull the polymer and metal piece. The compression force allows for greater distortion compared to drawing. The most common materials to be extruded are thermoplastic polymers and metals [65].

1.7.1 Types of an extrusion process

There are three types of extrusion processes, as shown in Figure 1.9: (a) based upon the direction of flow materials, (b) based on extrusion temperature, and (c) types of equipment [66].

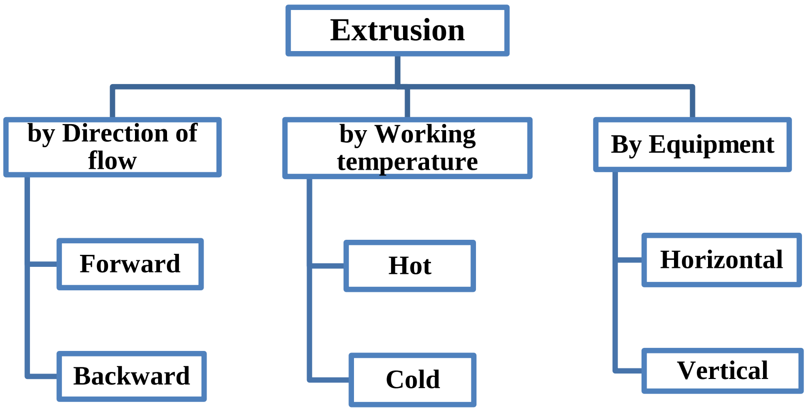

Figure 1.9 Different type of extrusion process

According to Figure 1.10, there are mainly two types of screw extruders [67]: (a) SSE and (b) TSE, and further subdivided according to the rotation of screws and position of screws. In this research study, a counter-rotating parallel type TSE has been used.

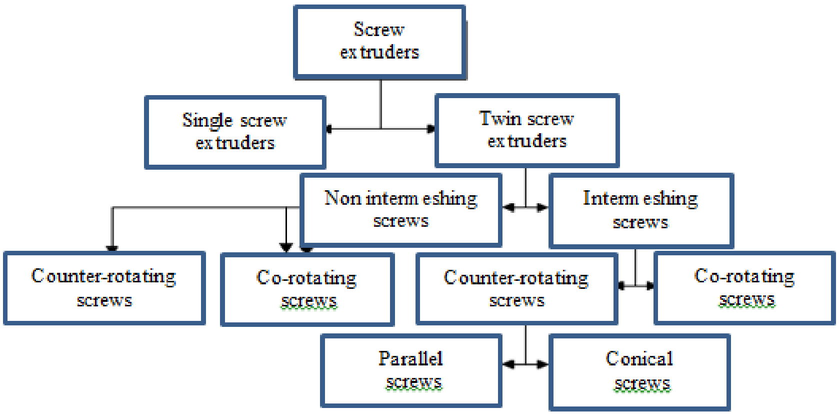

Figure 1.10 Type of extruders according to screw and their direction of rotation

In a SSE, a hopper is mainly used to hold and store the input materials (thermoplastic polymer and its composites). The gearbox is primarily used to control the rotation speed of the screw in the barrel zone. Thermocouples are installed at some distance on the extruder's barrel for measuring the temperature at different zones of the barrel. Finally, the semi-molten material is extruded through the die opening.

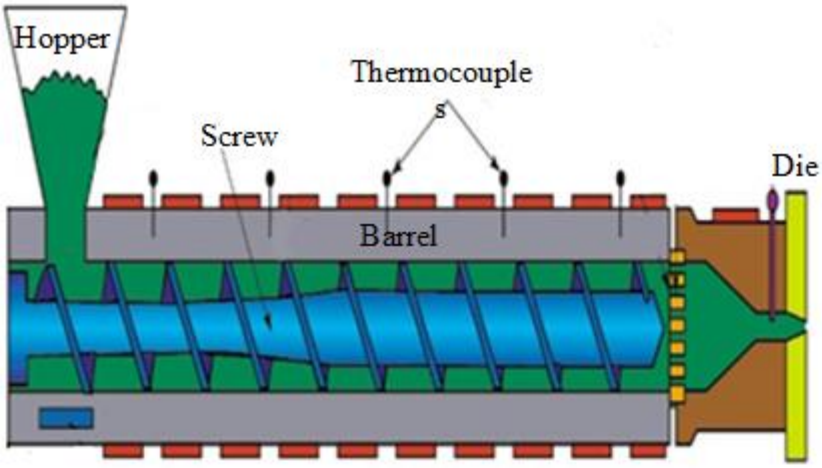

Figure 1.11 Detailed schematic of SSE

In this research study, a counter-rotating parallel-type screw extruder has been used. Figure 1.11 and Figure 1.12 show a detailed schematic of a SSE and TSE respectively [68-69].

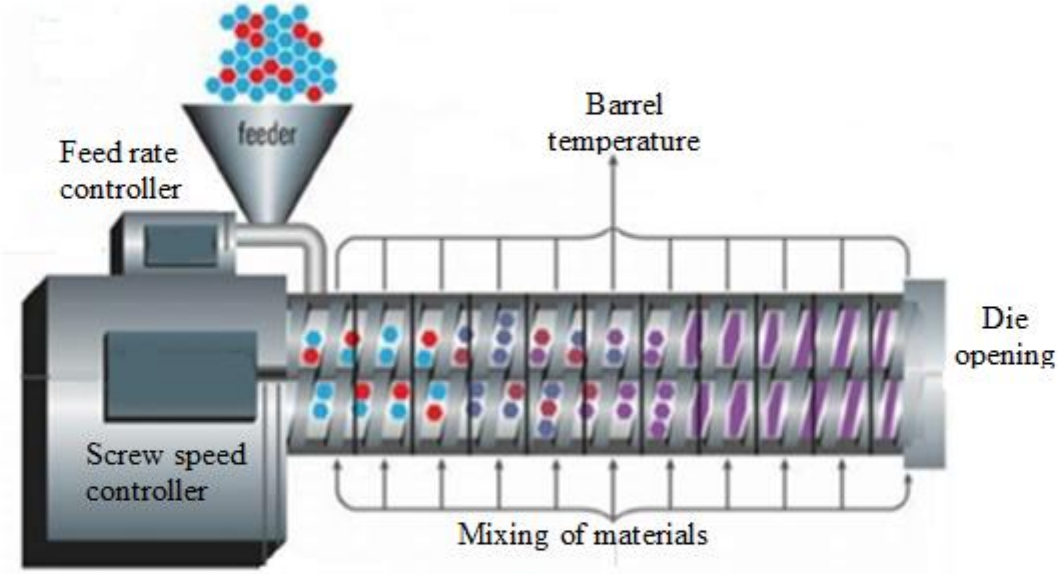

Figure 1.12 Detailed schematic of TSE

Since the advent of thermoplastic polymers extrusion process becomes a highly demandable technology and also used in automobile, biomedical, petrochemical, packaging, agriculture machinery, building materials, electronics, and in many defense applications [70].

People are mostly using thermoplastic polymer in their daily life as compared to other non-polymer or metallic things. A thermoplastic polymer is used as raw materials in most of the regularly used applications. The extrusion process is the most important step in thermoplastic polymer processing [71]. Moreover, extruders have been also used for the processing of ceramics, food, pulp, packaging, electrode, feed, building materials, explosives, etc. Further, in the development of thermoplastic polymer-based products the extrusion parameters have great significance [72-73].

In extruders, screw is rotating in the barrel at high temperatures to push sturdy material in a forward direction at a predefined flow rate [74]. Screw material must have very high mechanical strength, to resist the deformation under high temperature and pressure conditions. During the rotation of the screw rod of an extruder, the thermoplastic polymers are sheared and plasticized mainly by the screw edges, and therefore the thermoplastic polymers are pushed in a forward direction [75]. As a result, the screw edges are subject to cutting stress and frictional force. In some situations, plastic backflow occurs, which may lead to reduce the plasticizing effect and decline productivity [76-77].

1.8 Organization of the Thesis

This study has been divided into 6 different chapters as briefly outlined in Figure 1.13.

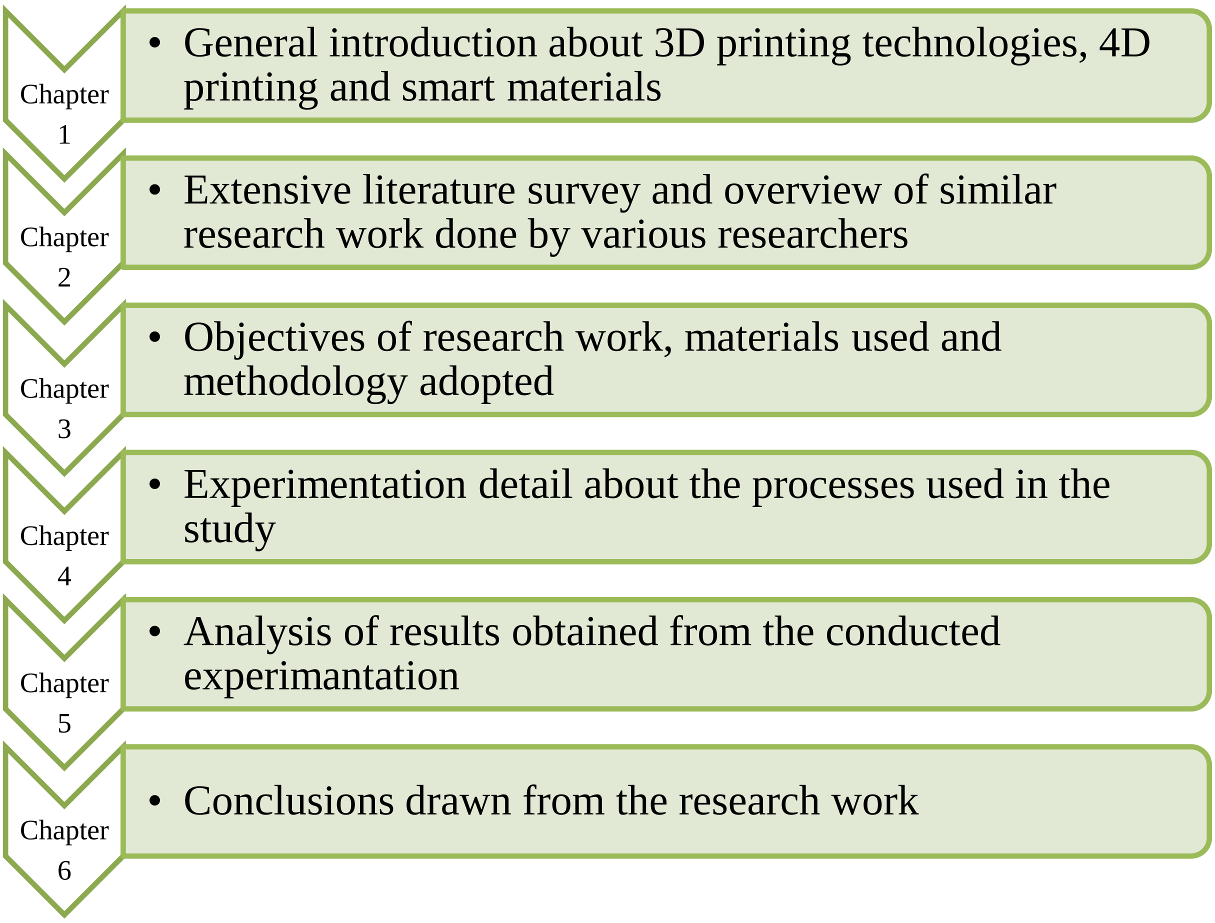

Chapter 1
- General introduction about 3D printing technologies, 4D printing and smart materials

Chapter 2
- Extensive literature survey and overview of similar research work done by various researchers

Chapter 3
- Objectives of research work, materials used and methodology adopted

Chapter 4
- Experimentation detail about the processes used in the study

Chapter 5
- Analysis of results obtained from the conducted experimantation

Chapter 6
- Conclusions drawn from the research work

Figure 1.13 Organization of thesis

CHAPTER 2

LITERATURE REVIEW

This chapter details the different outcomes and results of previous studies conducted for TSE, FDM, and the application of functional prototypes. For conducting this literature survey approximately, 500 studies have been collected from different libraries, publications, and web sources. Previous studies reported for mechanical, thermal, morphological, and piezoelectric properties of feedstock filaments and functional prototypes as a result of varying different process parameters associated with manufacturing processes. The outcomes and discussions of the most relevant studies are as follows:

2.1 Literature review on smart materials

Roy et al., studied and concluded that smart materials are capable of reproducible and significant variations among their one or more properties, under the effect of external stimuli [78]. Classification of smart material depends upon its output response such as shape-memory materials that recover their original shape at high temperature or with the variation of stress, piezoelectric materials which produces voltage under the application of mechanical stress, pyroelectric polymers, magnetostrictive materials, self-healing materials, pH-sensitive materials, and many other materials. Smart materials are also known as active materials.

Hadimani et al., used the granules of PVDF for the fabrication of piezoelectric fiber-shaped sensors [79]. The fibers of PVDF were extruded through a customized melt extruder. For poling fibers were stretched at a high temperature of 80 °C with an extension ratio of 4:1 and simultaneously high voltage of 13000 V was applied to the 0.5 mm diameter wire during the extrusion. Further non-poled and poled fibers were subjected to FTIR analysis for the confirmation of β phase in poled fibers of PVDF. SEM analysis was performed to examine the microstructures, tensile strength, and young's modulus of unpled and poled fibers.

Patel et al., developed the energy harvesting generators of PVDF, PP, and PZT for the production of power as a function of temperature [80]. It has been reported that the PZT produces more voltage than polymer-based generators at room temperature. However with the increase in temperature the power generation capacity of PZT decreases whereas, for PVDF, voltage output increased linearly with the increase of temperature. In the case of PP, the voltage output initially increases up to 70 °C, after that it started to decline.

Grinberg et al., fabricated a sensor for medical applications, using polyamide 11 (PA11) polymer reinforced with BTO ceramic [81]. As BTO is an inorganic and biocompatible, lead-free material, thus it was selected as a piezoelectric material for biomedical sensors. A solvent casting method was used for the preparation of ferroelectric composite. Further, an extruder was used for the fabrication of feedstock filament and FDM was used for 3D printing of a sensor.

Ramadan et al., described the piezoelectric polymers into three different categories: bulk polymers, composite polymers, and voided charged polymers [82]. Bulk polymers are solid films of polymers having a piezoelectric effect due to their molecular structure and orientation of molecules. Composite polymers are a combination of flexibility of polymers with a high piezoelectric effect of ceramics. In piezo composites, the inorganic materials are reinforced in the polymers to develop a flexible sensor with a high electromechanical effect. The third type of piezoelectric polymers is voided charged polymers. This type of polymers is completely different from the first two categories. Gas voids are formed in the polymers films and further internal dipoles are created by charging the film surfaces. For voided charged polymers the polarization is dependent on the applied stress.

Ribeiro et al., highlighted the application of piezoelectric polymers in tissue engineering [83]. As active scaffolds are the main needs in tissue engineering, for the proper reformation of particular tissues. For proper functionality of tissues, electromechanical materials, especially piezoelectric materials may show strong potential. Moreover, electroactive material may also use during the regeneration of tissue.

Guo et al., highlighted the electrospinning method for the preparation of polyurethane (PU)/PVDF scaffolds [84]. The piezoelectric and mechanical properties of the fabricated scaffolds were examined. XRD, FTIR, and DSC analyses were performed for the phase characterization of developed scaffolds. It was found that the electrospinning method helped in conversion of the non-piezoelectric phase of PVDF into the piezoelectric β-phase. Moreover, the results of the study reported that the piezoelectricity of developed scaffolds increased the fibroblast movements in vitro and in vivo. Thus the fabricated scaffolds of PU/PVDF showed their potential for wound healing applications.

Zeng et al., stated that piezoelectric composites are the best material for the development of ultrasonic devices [85]. Earlier, piezoelectric composite parts were fabricated by mixing, mold forming, and dicing-filing techniques. However, in this study researchers used the Mask-Image-Projection-based (MIP) SLA process was used for the fabrication of BTO based piezoelectric composites having honeycomb structure design. A high-density sintered part was fabricated with this 3D printing technique. This piezoelectric constant of the fabricated complex structure was 60 pC/N. Further, this developed structure was installed in an ultrasonic device and its material provides a promising response. The power output for ultrasound sensing through this structure was also found significant. The effect of 3D printing technology on the fabrication of complex piezoelectric composites was also demonstrated that could not be easily fabricated with other methods like dicing-filling.

Malik and Ray used the micromechanical analysis to determine the piezoelectric constant of composites reinforced with piezoelectric fibers [86]. To predict these coefficients, two different approaches strength of materials (SoM) and method of cells (MoC) were used. An electric field is assumed to be in the transverse direction of fibers. It was found that with the increase of fiber volume fraction (FVF) more than the critical FVF, the piezoelectric coefficient of the developed composite was significantly increased than the normal piezoelectric constant of fibers.

Takagi et al., highlighted the powder processing method for the fabrication of PZT/Pt composites [87]. Further, for the development of piezoelectric actuators, the mechanical, elastic, piezoelectric, and dielectric properties of composites were examined. It was found that with the increase of Pt content, the dielectric constant and piezoelectric constant of the composites decreased. However, Pt contents increased the mechanical strength of the composites especially fracture toughness. Strain gages were used to measure the deflections induced in the structures by an electric field. The data measured was found in line with the analytical data obtained from classical lamination theory (CLT).

Safari et al., described the two different methods of solid freeform fabrication (SFF) for the fabrication of piezo composites [88]. Sanders Prototyping (SP) and fused deposition of ceramics (FDC) methods were used for piezo composite fabrication by incorporating different patterns of connectivity such as (1-3), (2-2), (3-1), (3-2), and (3-3). Further FDC method was employed to prototype a variety of actuators like oval, spiral, tube arrays, and telescoping actuators. It was highlighted that for the fabrication of sensors and actuators with complex internal structure and intricate geometry, the SFF method was used.

Qiu et al., prepared the metal cored piezoelectric ceramic fibers of the PNN-PZT mixer [89]. The fibers of PNN-PZT powder were extruded and further, an organic solvent was used to put the 50 mm Pt rod in the center of 250 mm fibers of PNN-PZT. SEM analysis was performed to investigate the joint at the boundary of the cut piece along the cross-section and in the longitudinal direction. A proper joining between the PNN-PZT fibers and Pt core was found. Further, a relationship between polarization and the electric field was examined by using a Radiant RT-6000. The outcome of this relationship showed the ferroelectricity in the developed composite material.

Darestani et al., highlighted the effect of electric poling on the pre-fabricated thin membranes of PVDF [90]. PVDF membranes were poled in the high voltage electric field for the fabrication of piezoelectric membranes. The results of SEM analysis showed the change in crystallinity and microstructure of PVDF membrane after poling process. Further DSC and FTIR analysis confirmed the formation of the β-phase crystals in the PVDF membranes. To obtain the piezoelectric effect from the PVDF membrane, DMA and surface displacement measurement methods were used. It was found that poled membranes produced electric signals under the applied dynamic load. Moreover, the laser vibrometer also detected some vibrations in PVDF membranes when they were energized by AC signals.

Xu et al., fabricated and characterized the piezoelectric nanofibers of PMN-Pt mixture by using the electrospinning method followed by high-temperature processing [91]. Nanofibers having a diameter in the range of 148-216 nm were prepared. To obtain the properly aligned arrays of nanofiber, an electric field-assisted technique was used. Based on the theoretical model piezo response force microscopy (PFM) was used to measure the piezoelectric coefficient (d_{33}) fabricated nanofibers. The output value of d_{33} of individual nanofiber of (PMN-Pt) was found 50±2 pm/V. Thus these observed properties promote the developed nanofibers for use in energy harvesting applications.

Yildirim et al., designed, developed, and investigated the performance of PVDF-TrFE based biocompatible piezoelectric membrane actuator (PMA) [92]. A spin coating method was used for the fabrication of a thin membrane (1-μm) of PVDF-TrFE with actuator layers of 1.5 μm thickness. An atomic force microscope (AFM) was used to measure the surface roughness of thin film and a value of 7.9 nm was observed. A polarization of 5.38 $\mu C/cm^2$ was measured at 200V. A tip less probe of AFM with AI coating was used to measure the deflection in the thin film. At 9 V, a displacement of 432 nm was obtained from PMA under non-resonant conditions with a diameter of 2250 μm. It was stated that the proposed membrane of PMA may be used as micro pumps in biomedical applications.

Sharma et al., reported the fabrication of a thin-film pressure sensor of PVDF–TrFE copolymers by using a cost-effective standard lithography process [93]. For the β-phase formation, a thin layer having a thickness of 1 μm of PVDF–TrFE was spin-coated. Based upon the thickness of the developed film, it was observed that a film of 1 μm has shown better performance without any electrical or mechanical poling as compared to the 6 μm thick film. Results of Raman spectroscopy showed that the film having less thickness having more content of β phase as compared to films having more thickness.

Xu et al., proposed a design of a sensor comprising of micron-sized PVDF pillars, which produce a charge under the effect of stress-induced acoustic waves [94]. Researchers focused on the fabrication of highly sensitive acoustic pressure sensors with a small footprint. The mechanical coupling produced in micro pillars is ensured by an acoustic medium. To increase the sensitivity and decrease the capacitance of the sensor, electrodes were patterned properly. An optimization algorithm was used to determine the sensor parameters such as height and diameter of pillars, the total number of micro pillars, the gap between the micro pillars, etc., and the effect of electrical and mechanical properties of the sensor. The piezoelectric response of developed micro pillars of PVDF under the applied strain was measured by using the Nano-indentation test.

Haddadi et al., studied the effect of hydrophobic and hydrophilic nano-silica (SiO_2) on the mechanical, morphological, and piezoelectric properties of PVDF nanofibers [95]. An electrospinning method was used for the fabrication of nanofibers of a solution containing PVDF and 1.5 wt% of both hydrophobic and hydrophilic $SiO_{2.}$ FE-SEM analysis was used to study the diameter distribution and morphology of developed nanofibers. To examine the effect of nano-silica on the mechanical properties of nanofibers, a tensile test was performed. Further for the piezoelectric coefficient of nanofibers was evaluated by output voltages as a function of loading force. It was observed from the output voltage that the addition of SiO_2 enhanced the piezoelectric properties of PVDF-based nanofibers. Moreover, the doping of hydrophilic SiO2 also increased the mechanical properties and diameter of fibers.

Chen et al., highlighted the properties of PVDF as ferroelectric polymers integrated with electronic devices (ED) to make them flexible [96]. The multifunctional properties such as ease of processing, flexibility to stretch and bend, biocompatibility, and chemical stability make them capable of applications in energy harvesting, biomedical sensors, and electronic skins. Further, it was stated that PVDF-based flexible ED is capable to use as portable sensors, nonvolatile memories, and energy transducer.

Wang et al., stated that PVDF has been widely accepted as a sensing material due to its ferroelectric and electroactive properties [97]. Post-fabrication processing is required to activate these properties in the piezoelectric polymer. Mechanical stretching and electric poling are mainly used for β phase activation in PVDF. In this study, a human-related forced sensor of PVDF fabrics was reported with high breathability and flexibility. An electrospinning setup was used for the fabrication of PVDF-based nano-fibrous fabrics and further for characterization of developed fabrics SEM, FTIR, and XRD analysis was performed. The fabricated forced sensor has been tested for sensitivity and found an excellent response to mechanical forces. Thus it was stated that this type of sensor can be used to sense the garment pressure, heartbeat, blood pressure, and respiration rate, etc.

Gaytan et al., highlighted the binder jet AM setup for the fabrication of BTO specimens [98]. The process parameters such as layer thickness, binder saturation, and sintering profiles were optimized to achieve the density and crystal structure of 3D printed specimens. SEM analysis was performed to characterize the morphology of surface and cross-sectional grains, XRD analysis revealed that formation of hexagonal phase in the BTO when the sintered temperature was increased to 1400 °C. Vector network analyzer and K_u-band wave-guide setup were used to obtain the dielectric constant of BTO samples. The measured relative permittivity was in the range of 8.6 to 6.23 at the frequency range of 12.4-18 GHz. A density equivalent to 0.65 times of theoretical density was observed at a sintered temperature of 1400 °C. The d_{33} value showed by the sample sintered at 1400 °C was 74.1.

Karaki et al., highlighted the two-stage sintering method for the fabrication of fine-grain piezo ceramic of BTO [99]. SEM analysis showed the irregular and small-sized domain structure inside the specimens. The results showed that the specimen fabricated at optimized conditions having a high piezoelectric coefficient and large dielectric constants with a grain size of 1.6 µm. The d_{33} meter showed the maximum value of 460 pC/N in the sample. The Curie temperature of 126°C was found in the sample. The obtained results highlighted that these lead-free ceramics fabricated by a low-cost manufacturing process can be easily used in actuators, ultrasonic generators, and piezoelectric vibrators.

Eswaraiah et al., fabricated the composites of PVDF reinforced with functionalized graphene (FG) [100]. The effect of different proportions of FG on the electromagnetic interference (EMI) shielding efficiency and electrical conductivity of the developed composite was investigated. It was observed that with the increase of FG concentration in composite the conductivity of PVDF also increased.0.5 wt.% of FG change in electric conductivity of PVDF from 10^{-16} S.m^{-1} to 10^{-4} S.m^{-1}. Thus a conductive network was observed in the polymer matrix. Moreover, composite containing 5wt % FG, showed 20 dB and 18 dB EMI shielding effectiveness in (8–12 GHz) X-band region and (1–8 GHz) broadband region, respectively.

Uchino highlighted one important type of smart material that has been used widely as piezoelectric material that produces electric charge or voltage when experiencing an externally applied stress and vice versa [101]. Different categories of piezoelectric materials offer different capabilities.

Kim et al., stated that piezoelectric polymeric materials have some unique characteristics as compared to other piezoelectric materials [102]. These materials are suitable for systems that require mechanical flexibility, small active elements, biocompatibility, and solution-based process ability. However, it is still a difficult task to fabricate piezoelectric polymeric materials into complex 3D structures or small active elements. Thus, further improvement in the manufacturability of piezoelectric polymers will have a huge contribution to the development of various applications which require micro-scale and nano-scale piezoelectric polymers, such as bio diagnostic devices, micro-scale, and nano-scale electromechanical systems, imaging systems, compact sensor designs, and electronics.

Literature review conducted on the smart materials reveals that under the effect of external stimuli like heat, temperature, moisture, force etc. smart materials become active and alter one of its properties. Shape memory polymers, electroactive polymers (EAPs), pyroelectric polymers, magnetostrictive materials and self-healing materials are some examples of smart materials. Among these EAPs produce electricity when external force is applied on it. Thus literature survey described about various processing techniques such as solvent casting, spin coating, SLA SFF for the development of thin sensors, energy harvesting devices from piezoelectric polymers. It has been also revealed from the literature survey that the reinforcement of piezoelectric ceramics helps to enhance their piezoelectric properties of EAPs

2.2 Literature survey on extrusion of feedstock filament

Frederick et al., tried to develop a new energetic material of functionally graded polymer-based composites using the TSE process [103]. TSE process was used for both non-energetic and energetic composite materials. The effect of TSE parameters on the mixing and mechanical properties of developed composite was studied. It was found that the melting or heating temperature of the extruder acted as important process parameters and TSE provides better mixing capability and produced high-density parts with higher mechanical strength.

Nath et al., experimented and concluded that hydroxyapatite (HAp) is a biocompatible and bioactive ceramic and reinforced with high-density polyethylene (HDPE) for fabrication of composites used in biomedical applications/field [104]. For reinforcement of HAp in HDPE polymer, TSE was used for blending of materials and found the homogeneous distribution of filler particles in the polymer matrix. It was concluded that final fabricated parts are dimensionally more accurate than other manufacturing processes.

Singh et al., have conducted single screw extrusion of cryogenically ground nylon 6 based thermoplastic materials with aluminum (Al) and aluminum oxide (Al_2O_3) reinforcement [105]. The composition of nylon 6-Al- Al_2O_3 has been selected as per the MFI test (as per 3D printing compatibility). The feedstock filaments were prepared by varying die temperature (190-215°C), die temperature (175-185°C), and screw speed (20-35rpm).ANOVA table was used to optimize the process parameters. Results of ANOVA suggested that only two process parameters (die temperature and material composition) were found significant at a 95% confidence level. However, screw speed and barrel temperature were found insignificant. The results of the study suggested that feedstock filament comprising of 60%nylon 6-30%Al-10%Al_2O_3 (by weight %) shown maximum mechanical strength. The developed feedstock filament was used to run on existing FDM setup for 3D printing of parts [106].

Singh et al., performed some experiments on the extrusion process for mixing of materials and fabrication of feedstock filament for 3D printing [107]. The effect of process parameters on the various properties like rheological, mechanical, and thermal properties was evaluated, and found the best settings of process parameters for processing of different polymers. TSE process has been widely used in the field of food processing, polymer technology, pharmaceuticals, biomedical, and orthopaedics applications. Thermoplastic polyurethane (TPU) and PVDF are the most commonly used smart polymers, with a wide range of applications.

Bedi et al., worked on TSE for reinforcement of silicon carbide (SiC) and Al_2O_3 in HDPE and LDPE thermoplastic polymers for the fabrication of rapid tool using 3D printing (FDM) process [108]. For this experimental work, 4 different process variables such as screw speed (35-45 rpm), applied load (5-15 kg), compositions (TPS, DPS, SPS with varying SiC and Al_2O_3), and barrel temperature (185-195°C) were selected as input process parameters for fabrication of feedstock filament. Finally, it was concluded that thermoplastic composition is the most affected process parameters (74.94 %) followed by screw speed (6.35 %) and then barrel temperature (4.74 %). However, the applied load was found least effective process parameters for the fabrication of HDPE based feedstock filament

Daniel and Cross conducted an experiment for blending of polymers with other thermoplastics or some filler [109]. TSE process provides a high dispersion rate, accurate size of extrusion, high mechanical strength, and self-wiping actions. It was also observed that the TSE process is a better process than the single screw extrusion process due to its high melting capacity and high solids intake rate. In the TSE process, the geometry of screws and other process parameters also affect the properties of final products.

Kumar et al., conducted some experiments on the reinforcement of banana fiber with HDPE, LDPE, ABS, and PA6 thermoplastic polymers for enhancing the mechanical properties of the final manufactured product [110]. TSE process was used for blending filler particles with polymer matrices. Finally, it was concluded that in the case of PA6 and ABS best composition was 5% banana fibers whereas 1% of banana fiber reinforced with LDPE and HDPE provides maximum tensile as well as flexural strength. It was also found that barrel temperature acted as the most effective process parameters towards the mechanical strength of the fabricated parts.

Maridass and Gupta highlighted the response surface methodology for the optimization of process parameters of TSE [111]. Screw speed and barrel temperature were selected for the processing of rubber powder. For both, the parameters of five levels were chosen to experiment. A second-order mathematical equation was used to fit the responses of both variables and analyzed the obtained charts. It was found that barrel temperature of 219 °C and screw speed of 20 rpm is the optimum condition for the processing of rubber powder. Further for the confirmation experiments were conducted practically.

Ranjan et al., conducted an experiment on the TSE process for manufacturing of biocompatible grade of feedstock filament by reinforcement of hydroxyapatite (HAp) and chitosan (CS) fillers in PVC [112]. The extrusion process performed on TSE by varying process parameters such as the size of HAp particles (53-150 µm), barrel temperature (180-200°C), screw speed (30-50 rpm), and applied load (10-12 kg). It was concluded that 96% of PVC with 4% of HAp-CS extruded at 50rpm screw speed and 200°C barrel temperature were the best process parameters.

Regibeau et al., conducted an experiment to optimize the reactive extrusion polymerization process for continuous synthesis of poly lactic glycolic acid (PLGA) and PDLLA, for biomedical and pharmaceutical applications [113]. To optimize the process parameters, PLGA and PDLLA were taken in the proportion of 50:50. A medical-grade extruder’s parameters were optimized for the synthesis of aliphatic polyesters. The feedstock filaments of composites developed via TSE were further used to run on the 3D printer for the fabrication of scaffolds. It was also stated that PLLA, PLGA, and PDLLA polymers are best suitable thermoplastic biopolymers for extrusion processes and biomedical applications

Sharma et al., optimized the process parameters of TSE for the fabrication of EAP-based composite comprising of PVDF/Gr/BTO [114]. Two variables of TSE, screw speed, and screw temperature were selected at three different levels along with material composition as the third parameter. A Taguchi L9 orthogonal array was used for high accuracy of results. The results of ANOVA suggested that a filament contains 20% BTO when processed at 200 °C extruder temperature and 40 rpm screw speed shown a high degree of dispersion in the polymer matrix. Further, the developed composite-based feedstock filament was used to run on FDM for the fabrication of a piezoelectric sensor.

Literature survey conducted on the extrusion process revealed that TSE provides better dispersion of filler particles in the base polymer matrix. Researchers have also used SSE for the development of feedstock filament from Single polymer matrix. However, TSE has been used for the development of polymer matrix composite based feedstock filaments. It has been also revealed from the literature survey that process parameters of TSE played dominate role on the geometrical, mechanical and other properties of developed feedstock filament.

2.3 Literature review on 3D printing

Li et al., worked on the fabrication of ABS-based FDM prototypes with locally-controlled properties filling density and filling orientation and make a comparison between the theoretical and experimental analysis [115]. They observed that the parts fabricated at raster angle 45/-45 having minimum young's modulus as compare to parts fabricated at 90° raster angle having maximum young's modulus and also there is a difference between the theoretical and experimental outcome values.

Upcraft et al., compared various RP technologies including SLA, SLS, FDM, LOM, 3D printing, and multi-jet modeling [116]. It also covers surface roughness considerations and mechanical properties including dimensional accuracy and compares costs of various systems. They concluded that in the case of FDM when the caster angle was increased from 10°-90°, the surface roughness of the fabricated model was decreased. The dimensional accuracy of FDM parts was 97% when compared to CAD data. The FDM is a cost-effective way to produce 3D structures as compared to other RP techniques.

Modeen et al., stated that the file generated in CAD software could be easily converted into a machine-compatible file. [117]. Marcinova et al., shared the data about progress and normally accessible materials that are utilized for item fabricating by FDM i.e., an RP innovation [118]. While utilizing diverse innovation of fast model the primary condition of item material might be accessible in many shapes. There can be fluid, powder shape, or solid form. It can be also accessible in different types of solids like wire, laminates, or beds. The material utilized as a part of this exploration paper incorporates nylon, paper, resin wax, ceramics. In

FDM be materials that are utilized are ABS, polypropylene, polyamide, and polyethylene. Some extraordinary materials are utilized in the FDM system are nitrile, HAp, silicon, stainless steel, PZT, and Al_2O_3.

Romero et al., compared the 3D printed product with the conventional master cast and also studied the material consumption and cost that occurred in both processes [119]. It was concluded that rapid manufacturing produced the best-fit parts with negligible material wastage when compared to the conventional manufacturing class. The results also show the saving of cost in the RP process.

Torres et al., optimized the process parameters of FDM (infill percentage, layer thickness, and post-heat treatment on the mechanical strength of the prototypes ANOVA was used for the optimization process [120]. They concluded that the layer thickness and infill percentage have more effects on the mechanical strength of 3D printed parts. However, the post-processing heat treatment (at three different time intervals 0 to 20 mins) affects the mechanical strength of less dense part only.

Singh et al., studied that the reinforcement of graphene in ABS polymer matrix can be directly printed with an open-source 3-D printer and graphene is responsible for enhancing the electrical and thermal conductivity of the ABS polymer [121].

Dul et al., fabricated 3D parts of ABS reinforced with graphene nano-platelets (xGnP) [122]. It was observed that both stress and strain at break were decreased with the addition of xGnP in ABS. Moreover, higher thermal stability was induced on 3D printed parts by xGnP, as indicated by a reduction in both coefficients of linear thermal expansion and creep compliance.

Berretta et al., investigated the effect of carbon nano-tubes proportions on 3D printing of polyether ether ketone (PEEK) thermoplastic material polymer [123]. Carbon nanotubes were reinforced in PEEK and feedstock filaments were fabricated by varying the proportion of carbon nano-tubes from 1% to 25% by weight. The results of the study highlighted that the specimen 3D printed with 5% carbon nanotubes according to weight percentage shown better thermal properties. It was also suggested that 3D printed carbon nanotubes reinforced PEEK might be used in high-temperature applications.

Feng et al., developed the feedstock filament of ABS-based composites by reinforcing cellulose nano-crystal and methacrylate resin in it [124]. Further 3D printing of standard specimens was performed by varying the infill density. The effect of infill density on the mechanical properties of the fabricated parts was evaluated. Results of the study were highlighted that the tensile strength of parts prepared from methacrylate resin-cellulose nano-crystal doped composites was higher than the virgin ABS-based 3D printed parts fabricated at 80% infill density.

Jamroz et al., compared the tensile modulus of 3D printed polyvinyl alcohol (PVA) reinforced with aripiprazole particles [125]. It was found that the mechanical breaking force of the 3D printed product was comparable with the casted one as 47.25 ± 3.72 MPa and 52.15 ± 9.27 MP respectively. It was suggested that the sustainability of drug delivery is a serious issue. The 3DP technique has a wide perspective to produces sustainable products.

Kariz et al., developed a feedstock filament of PLA reinforced with wood particles for the 3D printing of prototypes [126]. The proportion of wood particles was varied in between 0% to 50% by wright. The results of this study highlighted that tensile modulus was improved with 10% wood content but decreased with 50% wood content in the PLA matrix. It was suggested that the reinforcement of wood fiber in recycled polymers may provide good options in the field of waste management.

Kaur et al., performed the 3D printing of virgin PLA, nylon 6, and carbon fibers reinforced PLA [127]. The results of the study suggested that carbon fibers reinforced PLA sustained more as compared to the other two and shown the highest Young’s modulus (0.6GPa) and yield strength (17MPa). The developed composite might be helpful in civil engineering applications, especially micro-architectures structure with a lightweight.

Leon-Cabezas et al., performed 3D printing of PLA with reinforcement of thermos chromic and photochromic agent (5%) for investigations of color degradation per unit time [128]. 3D printed parts were heated, such as blue color (30-35°C) and red color (37-31°C) and sunlight treatment in yellow and violet color. The results of the study highlighted that parts heating in presence of a thermo-chromic agent, taken higher heating in red color to get colorless, and also proved the better aesthetic sustainability in red color. Thus it may be used in the maintenance of aesthetic and toy components.

Mohamed et al., studied the effect of layer thickness, air gap, raster angle, build orientation, road width, and several contours on tribological properties of additively manufactured polycarbonate-ABS blend [129]. The wear rate of FDM's manufactured parts decreased with the decrease in layer thickness. However, with the increase in raster angle and air gap wear rate increased. It was found that the lowest and highest values for both road width and number of contours produced high wear rates as compared to the wear rate of the parts prepared at the center level of those parameters. It was observed that parts 3D printed with 0^{o} and 90^{o} printing angle (raster angle) shown more strength as compared to parts prepared at other raster angles. It was also found that orienting the raster angle along with the printing direction provides maximum tensile strength

Hao et al., compared the thermoplastic and thermosetting polymers based on 3D printed parts based on mechanical properties [130]. Epoxy resin was 3D printed by reinforcing carbon fiber. Results of the study highlighted that the mechanical strength of thermosetting composites was higher than the 3D printed parts of the thermoplastic composite under the same experimental conditions. The FDM system follows the base-up approach. According to requirement, FDM printers are available in different bed sizes. the most commonly used desktop 3D printer fabricates 200 × 200 × 200 mm^3. However, at an industrial level, a size of 1000 × 1000 × 1000 mm^3 may be used. Another, alternative way to produce big products on small 3D printers is to divide the product into small sizes of a different number of parts. Each small part is fabricated separately and further assembled.

Silva et al., highlighted that PLA polymer is widely used as biomedical implants or scaffolds and drug delivery systems [131]. PLA's best properties are biodegradability, which makes it more suitable for biomedical field or tissue engineering applications. Due to its superior quality of easily printable on a 3D printer, PLA as a scaffold may a very good wise decision.

Singh and Ranjan investigated the biocompatible polymers and bioactive fillers, for improving the growth of bone tissues. Biocompatible feedstock filament was prepared for FDM by reinforcement of biocompatible grade of polymers with fillers (HAp) with the help of TSE [132]. This investigation highlights that best settings of TSE for the preparation of in-house feedstock filament-based upon mechanical and thermal analysis. The material composition was 96% polymer matrix (comprising of 70% of PVC and 30% of PP) and filler (HAp) as 4%, extruder temperature 200°C and rotational speed 50 rpm with load applied of 20kg were the optimized observed conditions. The results were also supported by microstructure analysis. The final feedstock filament prepared as per the suggested parametric settings was run on commercial FDM setup without any change in the system's hardware/ software for the preparation of biocompatible scaffolds.

Wei et al., highlighted the flexibility in the 3D printing process and its capability to further improve the piezoelectric properties of the fabricated parts [133]. BTO derived from milled precursors was fabricated by extrusion free-forming process. A required tetragonal phase of BTO was formed at a very low temperature of 950°C. A green part obtained from the extrusion was further sintered to form the dense structures. The sintered ceramic with a density of 5.66 g/cm^3 showed the piezoelectric constant of 420 pC/N and dielectric constant

4380 at a frequency of 1 kHz. Conclusively it was stated that this method can be used as the low-cost manufacturing process of piezoelectric sensors.

Literature survey shows that researchers have developed the feedstock filaments of polymer matrix composites as raw material for FDM a 3D printing setup. It has been revealed that the process parameters of FDM have significant role on the various properties of fabricated specimens. Thus researchers have optimized the process parameters of FDM for in house developed feedstock filaments of various polymer matrix (PLA, ABS, PVC, PP etc.) based composites. However very few have reported about the optimized process parameters of FDM for PVDF based composites.

2.4 Literature review on 4D printing

Roach et al., stated that poly-jet printing and syringe printing are the most popular forms of 4D printing, but other 3D printing technologies such as FDM, SLS, and SLA are processes that could be incorporated in 4D printing technology [134]. However, some 4D printing technologies may require multi-materials and multiple nozzles, which limits what 3D printing methods can be used. Exploring different printing methods may allow for different smart materials to be 3D printed that are stronger, lighter, induce different property changes, and react to different stimuli.

According to Pei, 4D printing is ‘the process of building a physical object using appropriate AM technology, laying down successive layers of stimuli-responsive composite or multi-material with varying properties [135]. After being built, the object reacts to stimuli from the natural environment or through human intervention, resulting in a physical or chemical change of state through time.

Tibbits et al., stated 4D printing as a new process that ‘entails multi-material prints with the capability to transform over time, or a customized material system that can change from one shape to another, directly off the print bed’ with ‘the fourth dimension described here as the transformation over time, emphasizing that printed structures are no longer static, dead objects; rather, they are programmable active and can transform independently [136].

Zhou et al., outlined that rigid materials can be 3D printed along with smart materials to create specific areas of a part that act as joints and hinges for bending [137]. This process of 3D printing parts that change shape over time when exposed to external energy has been termed 4D printing by Skylar Tibbits from the Massachusetts Institute of Technology (MIT).

Leist and Zhou highlighted the onset of multi-material 3D printing and the combination of smart materials into the printable material has led to the development of an exciting new technology called 4D printing [138]. This paper will introduce the background and development into 4D printing; discuss water-reactive 4D printing methods and temperature reactive 4D printing, modeling and simulation software, and future applications of this new technology. Smart materials that react to different external stimuli are described, along with the benefits of these smart materials and their potential use in 4D printing applications; specifically, existing light-reactive smart materials. 4D printing has the prospective to simplify the design and manufacturing of different products and the potential of automating actuation devices that naturally react to their environment without the need for human interaction, batteries, processors, sensors, and motors.

Tibbits et al., highlighted that construction must be made smarter and solve the problem of wasting large amount of energy, materials, money, and time for building [139]. These issues can be solved using design programs and software to embed information into the materials that make the material and construction more accurate. In the beginning, Tibbits proposed a process called self-assembly, which uses small units that form larger structures when exposed to external energy.

Tibbits et al., outlined that self-assembly may be applied to 1D strand forming organized 2D and 3D shapes, along with 2D planar shapes forming 3D objects [140]. Self-assembly may not be efficient for every purpose, which means different sectors and applications must be identified that benefits most from self-assembly.

A market research report predicts that the 4D printing industry could be worth $63.00 million in 2019 and $555.60 million in 2025 (Markets and Markets 2015). The market report predicts that 4D printing may find applications in the automotive, textiles, construction, healthcare, utility, aerospace, and military industries. It is predicted that the defense and military sector would have the largest share, followed by the aerospace industry. These are just a minor number of application ideas for 4D printing that reflect several 3D printing methodologies and activation energies.

2.4.1 Developments in 4D printing

In this section, some developments of 4D printing that exhibit physical changes of the printed components/ structures are illustrated. They are classified according to whether they are printed with a combination of multiple materials or with a single material.

2.4.1.1 4D printing with a single material

In this section, 4D printing of either a single smart material or a mixture of smart material and conventional material as the starting form for printing has been detailed.

Torres et al., proposed an integrated 3D printing process with corona poling to fabricate piezoelectric PVDF sensors without the post poling process [141]. This proposed process, named ‘Integrated 3D Printing and Corona poling process’ (IPC), uses the 3D printer’s nozzle and heating bed as anode and cathode, respectively, to create poling electric fields in a controlled heating environment. The nozzle travels along the programmed path with a fixed distance between the nozzle tip and the sample’s top surface. Simultaneously, the electric field between the nozzle and bottom heating pad promotes the alignment of the dipole moment of PVDF molecular chains. The crystalline phase transformation and output current generated by printed samples under different electric fields in this process was characterized by a FTIR and through fatigue load frame. It is demonstrated that piezoelectric PVDF films with enhanced β-phase percentages can be fabricated using the IPC process.

Gladman et al., got success in 3D printing of a single smart material using a syringe nozzle and photo polymerization of their smart material for their 4D printing research at Harvard’s School of Engineering and Applied Sciences (SEAS) [142].

Kamila outlined that 3D printing of components consisting of a single smart material or a mixture of smart and conventional materials [143]. The smartness of the materials plays a more important role in achieving the intended response than in the case of a multi-material component. The smartness of the smart materials or mixtures describes the self-adaptability, self-sensing, shape memory, decision making, and multiple functionalities of the materials or mixtures.

Kim et al., stated those characteristics that determined how the printed components change their properties in response to the external stimulus and also described various promising applications of these materials [144]. Further, the recent developments of 4D printing that consist of either a single smart material or a mixture of materials as the starting form was highlighted, including enhanced smart nanocomposites and 3D printing of SMPs.

Dadbakhsh et al., studied the effect of selective laser melting (SLM) process parameters on the transformation temperature of fabricated parts of nickel titanium and found that SLM restores the 0.5% SME in the fabricated structure [145].

Rossiter et al., fabricated a thin membrane with a thick circular collar (thickness of the central membrane was approximately 90μm) of acrylic-based photopolymer by PolyJet and found that thin membrane produces large strain upon activation by electricity [146]. Thus it demonstrated that 3D printing has the potential to produce electroactive actuators.

Bodkhe et al., demonstrated the production of 4 V from a 3D printed sensor of PVDF reinforced with BTO [147]. The 3D scaffolds were fabricated with a Solvent evaporation-assisted 3D printing process and were able to stabilize the β-phase at room temperature.

2.4.1.2 4-D printing of multiple materials

Raviv et al., found an important factor to consider when designing a component with multiple materials is the availability of the 3D printing technology [148]. Moreover, in the developments of 4D printing of multiple materials, the design of the components plays a critical role as the conventional materials do not react to the external stimulus. Hence, the degree of the change in the printed components upon activation is usually determined by the design of the components. To illustrate this point, some examples of the developments in 4D printing of multiple materials are discussed. These examples include printed actuators for soft robotics, self-evolving structures, anti-counterfeiting system.

Srivastava et al., stated another class of smart materials that are gaining popularity are SMPs [149]. SMPs possess the ability to remember a permanent shape and transform to a temporary shape when exposed to some external stimuli such as temperature,

Hager et al., studied that SMP could create products that react to their environment automatically without the need for complex, heavy, and expensive electronic actuation systems [150]. Some other smart materials, called self-healing materials, that possess the ability to react to external stimulus and repair themselves, which may prove useful for devices exposed to extreme environments.

Lendlein stated that smart materials are essential to the development of 4D printing research [151]. There are many smart materials in development; however, not every smart material can be 3D printed. Also, smart materials do not need to possess shape change to be important to 3D printing research. Materials that possess the ability to change color, hardness, or transparency may become important in camouflage technology, signaling for users, detecting foreign substances, and biomedical applications.

Ge et al., created a 4D printing technique that uses a combination of heat and stress to activate a shape memory composite to bend at different rates and directions depending on the design of the hinges [152]. Glassy polymers in the form of fibers exhibit SMEs when heated above their glass transition temperature (Tg) and are 3D printed within an elastomeric matrix combination of elastomer and glassy polymer fibers create a soft composite, which the team has named printed active composites (PACs).

Mao et al., were successful in implementing their 4D printing techniques for the creation of self-assembling origami structures: a box, pyramid, a three-hinged airplane, and a five-hinge airplane [153]. A box with six rigid sides connected by PAC hinges is 3D printed in a flat shape. The PAC hinges are pre-programmed with definitive bending angles using the relation of PAC hinge length and applied strain to determine the bending angle. The walls of the box should bend at 90°, so the hinges required a strain of 20% to be applied while the material is heated above its glass transition temperature (Tg), cooled, then releasing the pre-strain. The component managed to form the box shape with minor irregularities due to inconsistencies when straining the material (see Figure 2.1a and 2.1b).

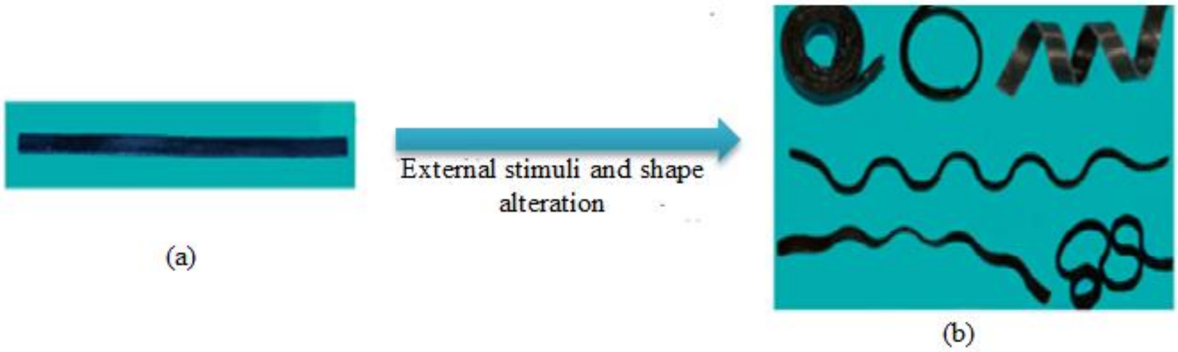

Figure 2.1(a) Initial flat shape of PAC without heat activation. **2.1(b)** Flat PAC material displays bending, twisting, and way shape changes when heat and stress are applied depending on the orientation of the PAC fiber.

Ge et al., found that the inclusion of smart materials in their 3D printing components could save time and material. 3D printing a 20 mm × 20 mm × 20 mm hollow cube with a wall thickness of 1 mm could took 10 minutes when printed in a flat 2D shape then activated to become a 3D cube [154]. However, direct 3D printing a cube with the same dimensions took 3 hours to print, and post-processing for removal of support material took numerous hours.

Kravchenko et al., found that light is an effective activation technique because it is an abundant source of energy, wireless, and controllable [155]. However, it can be difficult to transform light energy into mechanical energy for use in SMPs. Light-activated SMPs have been used in areas of self-assembly structures, complex folding methods, transformative surface deformations.

For this research work, a bibliographic analysis has been performed by using the web of science database by putting keywords; PVDF polymer, Piezoelectric property, and 3D printing. A total of 119 research papers/articles/chapters have been found and downloaded in the “.ris” format, by using “VOS viewer software (version 1.6.16”). 33810 terms have been found for this bibliographic analysis. By selecting minimum occurrences of 6, a total of 88 have met the threshold level. Further from 88 items, the best suitable 53 terms have been suggested by VOS viewer software and lastly, 30 terms have been selected for mapping and relations among those have been developed.

Figure 2.2 shows the bibliographic relevance analysis of the 3D printing of PVDF for piezoelectric applications by VOS viewer. All 30 terms are divided into four clusters with different colors (red, green, blue, and yellow). Two major clusters have been formed for previously conducted research works (shown in red and green color). As observed from Figure. 4, several studies have been reported on the PVDF matrix for sensor applications processed with SLA. Moreover, 3D printing of polymer matrix for the preparation of the composite using graphene, carbon nanotubes, and investigations related to piezoelectric coefficient, piezoelectric properties, etc. has been also reported.

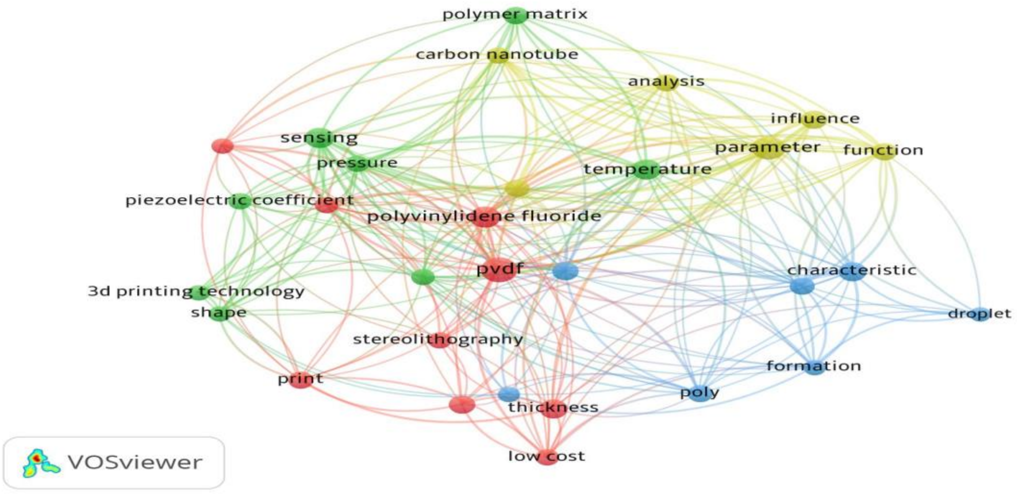

Figure 2.2 Bibliographic analysis (map) for keywords; PVDF polymer, Piezoelectric property, and 3D printing by using www.scopus.com database.

Figure 2.3 shows the bibliographic map analysis or relationship between all selected 30 terms. By clicking upon the node of 3D printing it has been predicted that there is a gap of study in 3D printing of PVDF and PVDF-based composites by reinforcement of carbon nanotubes, BTO, etc. for the fabrication of actuators and sensors. Moreover, a gap has been also found in the study of mechanical properties of PVDF matrix-based 3D printed parts. Further, the studies may be performed for the fabrication of piezoelectric devices by 3D printing of BTO and Gr in the PVDF matrix.

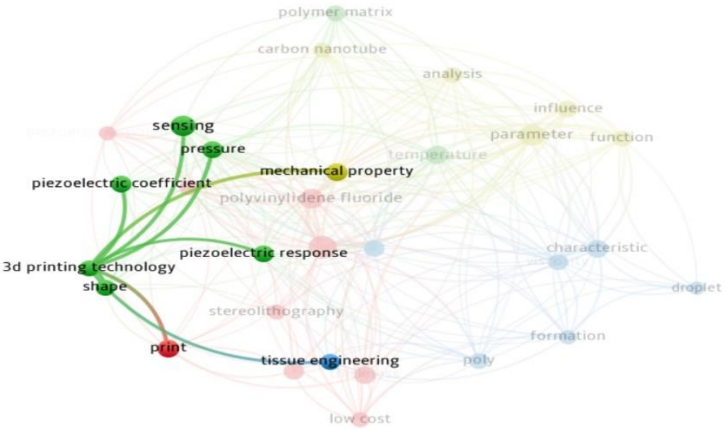

Figure 2.3 Bibliographic analysis for 3D printing process with different areas using www.scopus.com database.

2.5 Research gaps

The literature review was conducted on smart materials-based EAPs and their application in the field of energy harvesting, biomedical sensors, actuators, transducers, and many more. Some literature reported on the processing conditions of these EAPs such as type of process, pre-processing treatment, post-processing treatment, and their applicability capacity. Some researchers worked on the fabrication of sensors using PVDF polymers to utilize their extraordinary properties such as high flexibility, high piezoelectric properties, nontoxic, non-reactivity to chemicals, etc. Literature survey also revealed the development of piezoelectric polymers based composites doped with piezo ceramics such as BTO, ZnO, PZT, etc. to enhance the mechanical properties and piezoelectric properties of the EAPs by using various methods such as solvent casting, electrospinning method, etc. Some researchers also reported the optimization of the best process setting of TSE for the fabrication of feedstock filament using polymers or composites based on the polymers and 3D printing of prototypes by using these developed filaments. However, to date still, some research gap is noticed in reported literature on the processing and fabrication of PVDF composites based on piezoelectric sensors reinforcement by lead-free piezo- ceramics. Based on the literature review, the following gaps have been identified:

- It has been observed that many researchers have worked in the field of 3D printing of commercially available materials, but very few have reported the 3D printing of EAP matrix for 4D applications. Since 4D printing is an emerging field in AM, not much data has been reported regarding 4-D printing with FDM which is one of the low-cost AM processes.
- Smart materials nowadays, are being used in actuators, sensor applications and can be fabricated by conventional manufacturing processes as well as by 3D printing. Some of the commonly available smart materials are PVDF and BTO. To date, very little work has been reported for the preparation of 4D printed parts by using PVDF, graphene, and BTO as processing material on FDM.

  The proposed study is expected to fill these gaps for biomedical sensor applications.

2.6 Problem formulation

Literature survey revealed that in the past two decades many researchers have worked on the development of piezoelectric based sensors from ceramics, EAPs, and composites of EAPs reinforced with piezoelectric ceramics using various processing conditions such as solvent casting, electrospinning, powder sintering etc. On the flip side, many researchers have worked on the development of FDM based feedstock filament using polymer matrices or composites based upon these polymers, like PLA, PVC, PVDF, PEEK, reinforced with fillers to enhance the properties as per the required applications. However few have reported on the development of FDM-based feedstock filament using PVDF matrix reinforced with BTO and Graphene nano-powder using twin-screw compounder for possible 4D printing applications.

This research work is conducted to develop a spool of smart materials-based composites comprising PVDF/Gr/BTO by using a twin-screw compounder/extruder (TSE). The different proportions /compositions of the fillers in PVDF have been processed at different parametric settings of TSE). After that developed feedstock filament has deployed on an open-source commercial FDM machine for the 3D printing of scaffold/ functional prototypes. Composites of different proportions were prepared by two different methods of mixing: (1) Mechanical blending (MB), (2) Chemical assisted mechanical blending (CAMB). Process parameters of TSE and FDM have been optimized for the mechanical thermal and dimensional properties of the developed filament and fabricated prototypes, respectively. Fabricated parts at optimized settings of FDM have further subjected dynamic mechanical analysis (DMA) to determine viscoelastic properties of the developed composites.

It has been also observed that researchers have worked on fabrication of sensors using these types of EAPs and piezoelectric ceramics. Thus, the optimized settings of FDM have been used for the fabrication of thin cylindrical discs for measuring the piezoelectric properties, dielectric constant. To obtain the piezoelectric properties, 3D printed samples were subjected to post-processing treatment by using electrical poling. Thus, this study may help to explore FDM’s capability of 3D printing of smart material-based composites having 4D properties.

CHAPTER 3

MATERIALS AND METHODS

This chapter details the research objectives selected based on research gaps found from previously reported literature. The selected materials and various processing methods used for the preparation of feedstock filaments and functional prototypes have been discussed. The methodology adopted for the completion of this research work is also mentioned in this chapter.

3.1 Objectives

Following were the objectives of the present study:

1. To prepare the different proportions of BTO, and Gr as reinforcement in PVDF matrix for 4D printing applications (based upon MFI analysis).

2. To prepare FDM feedstock filament (for commercial open-source 3D printer) of BTO and Gr reinforced PVDF by:
    a) Mechanical mixing with twin-screw extrusion
    b) Chemical mixing

3. To perform rheological, thermal analysis (based upon differential scanning calorimetry) and tensile testing of feedstock filaments prepared by using mechanically/chemically blended samples and parametric optimization based upon the suitable design of experiments.

4. To print functional prototypes on FDM with feedstock filaments prepared and perform its parametric optimization from a mechanical/piezoelectric properties viewpoint.

5. To establish storage/loss modulus properties (by dynamic mechanical analysis), thermal stability, material properties (based on XRD and FTIR), and piezoelectric coefficient of functional prototypes.

6. To perform process capability analysis of finally prepared 4D material for batch production.

3.2 Methodology

The methodology adopted for the completion of this research work is shown in Figure 3.1.

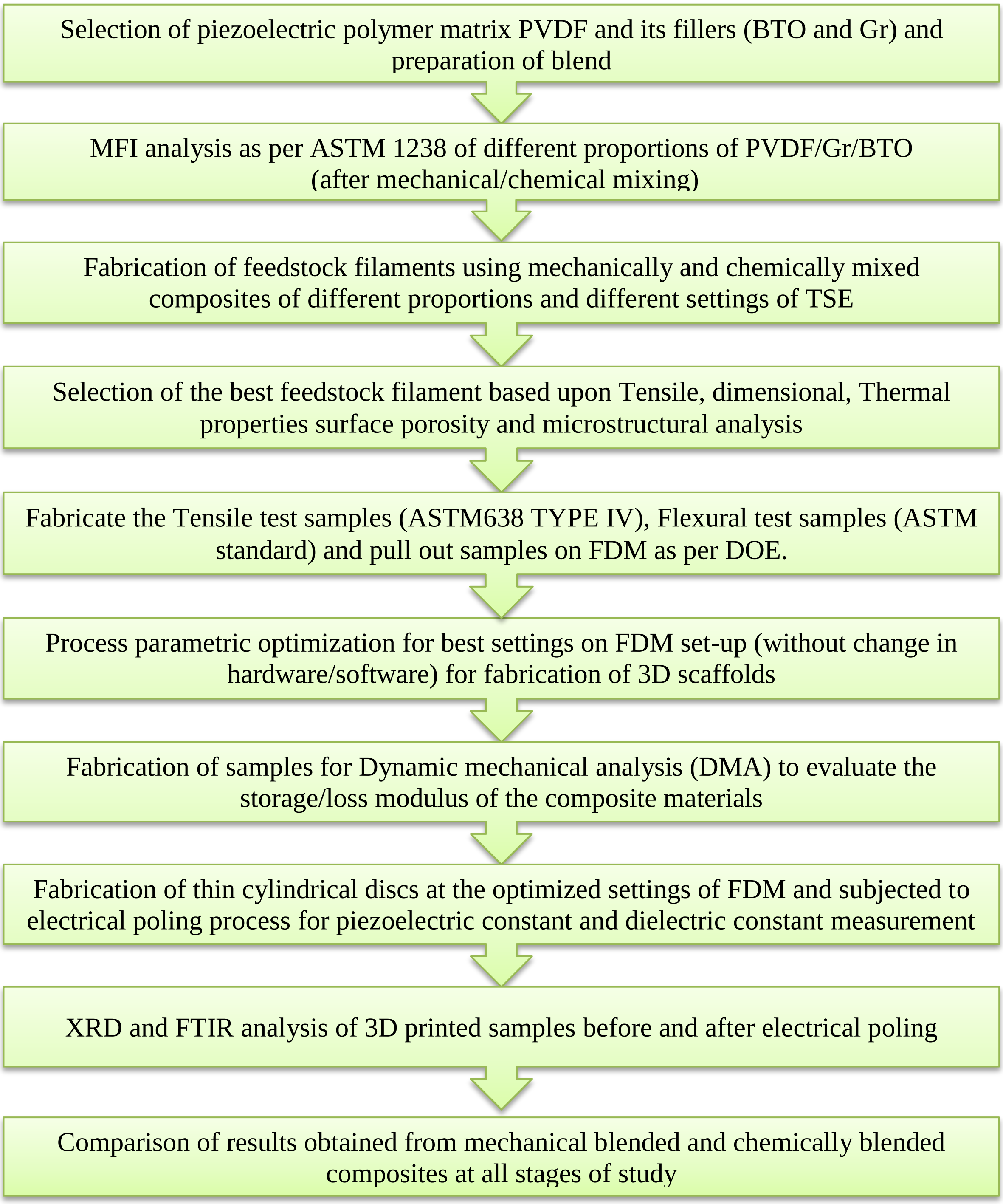

Figure 3.1 Methodology adopted for the completion of this research work

3.2.1 Different stages of work

This research work deals with the development of functional prototypes of 4D feedstock filaments using PVDF reinforced with Gr and BTO nanoparticles. The study is divided into five stages:

Stage 1

Optimization of process parameters of TSE for fabrication of feedstock filament using MBD composites of PVDF/BTO/Gr based on dimensional, mechanical, thermal, and morphological properties.

Stage 2

3D printing of standard tensile and flexural prototypes as per ASTM D-638 Type IV and ASTM D-790, respectively, **by using the feedstock filament prepared from MBD composites (as per stage 1)**. Optimize the Process parameters of FDM based upon mechanical and morphological properties of 3D printed parts. The optimized process parameters of FDM were further used for 3D printing of standard specimens for process capability analysis.

Stage 3

Optimization of process parameters of TSE for fabrication of feedstock filament using CAMBD composites of PVDF/BTO/Gr based on dimensional, mechanical, thermal, and morphological properties.

Stage 4

3D printing of standard tensile and flexural prototypes as per ASTM D-638 Type IV and ASTM D-790, respectively, **by using the feedstock filament prepared from CAMBD composites (as per stage 3)**. Optimize the Process parameters of FDM based upon mechanical and morphological properties of 3D printed parts. The optimized process parameters of FDM were further used for 3D printing of standard specimens for process capability analysis

Stage 5

The optimized process parameters of FDM on **stage 2 and stage 4** were further used for 3D printing of thin cylindrical disc for material and piezoelectric characterization. A comparative study has been performed to compare the results obtained from MB and CAMB process at various stages.

3.3 Selection of materials

3.3.1 PVDF

PVDF is lightweight, flexible, low acoustic impedance, high piezoelectric constant, and a good candidate for acoustic or biomedical sensors. The crystallinity of the PVDF polymer is a major factor in the piezoelectric constant [156]. Typical piezoelectric polymers have a crystalline region that has an internal dipole moment. These dipole moments are randomly oriented without any mechanical or electrical poling process [157], and the net dipole moment is zero in this condition. This type of structure is called α-phase PVDF that has no piezoelectric response. In α-phase PVDF crystalline regions will align such that all dipole moments cancel each other as shown in Figure 3.2 [130]. The α-phase PVDF film is commonly used as an insulating material because of its low thermal conductivity, low density, and high chemical and heat resistance. With post-processing such as mechanical stretching and electrical poling under a high electric field, crystalline regions inside the bulk PVDF film will align in the electric field direction [158]. The PVDF structure with this morphology is called β-phase film.

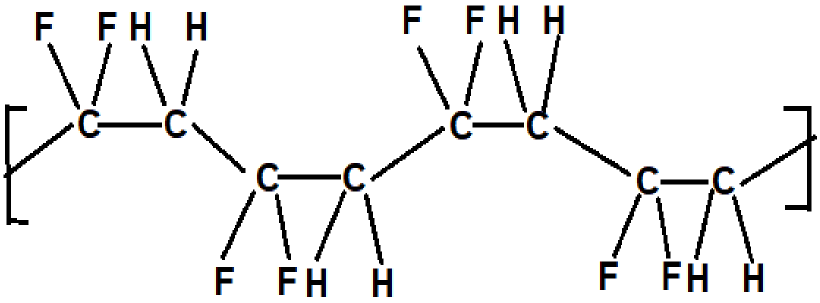

Figure 3.2 Chemical structure of α phase PVDF structure

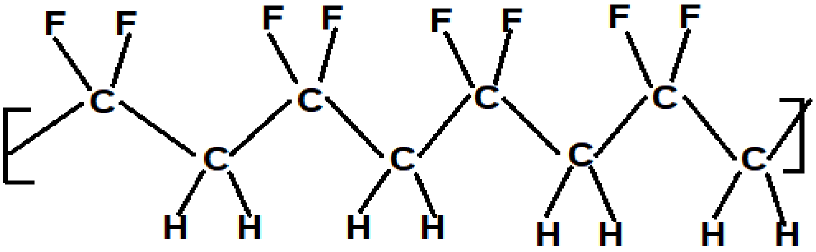

Figure 3.3 Chemical structure of β phase PVDF structure

The β-phase structure of PVDF has fluorine on the one side and hydrogen on the other side, as shown in Figure 3.3 This will form a net dipole moment in a stacked direction inside the β-phase PVDF crystalline regions. When stress is applied to this stacked polymer chain region, it will change the local dipole distributions and induce an electric field in the stack. The induced electric field accumulates the charges at both the top and bottom surface of the film, demonstrating the principle of the piezoelectric effect. Various studies show ways to increase the β-phase portion in the film by mechanical or electrical poling [159]. It has been shown that the higher β-phase portion of PVDF film shows a higher piezoelectric constant as a sensor material. Typically, around 90~95% of the β-phase portion shows a strong piezoelectric response for PVDF polymer [160]. Copolymers of PVDF such as PVDF tetra-fluoro ethylene (PVDF-TrFE) show higher crystallinity due to its chemical structure, resulting in a better piezoelectric response. Upon application of post-processes to the PVDF film, the β-phase PVDF film retains its morphology unless there are severe changes in temperature to the film. The maximum operating temperature for the β-phase PVDF film is 80ºC and 110ºC for the β-phase PVDF-TrFE film. PVDF-TrFE is a good candidate material for piezoelectric polymer sensors because it can achieve a high portion of β-phase morphology without poling process. The physical, mechanical, and thermal properties of PVDF are shown in Table 3.1.

Table 3.1 Physical, mechanical, and thermal properties of PVDF

Name of property	**Unit**	**Value**	**Test method**
Physical properties			
Density at 23 ^{o}C	g/cm^3	1.75-1.80	ASTM D792
MFI at 2.16 kg	g/(10min)	5.5-11	ASTM D1238
Water absorption (24 hours at 23^{o}C)	%	<0.04	ASTM D 570
Mechanical properties (Tensile strength (ISO 527-2, 50 mm/min))			
Stress at yield	MPa	50-60	ASTM D638
Stress at break	MPa	30-50	ASTM D638
Elongation at yield	%	5-10	ASTM D638
Elongation at break	%	20-300	ASTM D638
Shore-D hardness		73-80	ASTM D 2240
Thermal properties (DSC analysis)			
Melting point	°C	170-175	ASTM D3418
Heat of fusion (80 °C to end of melting)	J/g	58 – 67	ASTM D3418
Crystallization point	°C	134 – 144	ASTM D3418
Glass transition (Tg)	°C	-40	ASTM D4065

Solef PVDF used in this research work is a fluorinated semi-crystalline polymer produced by the polymerizing of vinylidene fluoride. This type of fluorinated thermoplastic has been widely consumed for the last three decades. PVDF has high stability without any addition of foreign material even in harsh environments. The unique properties of PVDF lead the equipment to longer life. Some other important properties of PVDF are as follows:

- Resistance towards highly reactive chemicals and solvents
- Good wear resistance
- Toughness and High mechanical strength
- High thermal stability (can withstand up to 300 °F)
- Reluctance to accept nuclear and UV radiations
- High resistance to fire
- Easily processed and molded by melting techniques like extrusion

Applications of PVDF

- PVDF is mainly used in chemical industries
- Semiconductor industries
- Cables and wire industries
- Automotive industries
- Fuel cells and Lithium-ion batteries
- Pharmaceutical and food industries
- Building materials and chimney linings

PVDF solef (6008/0001) was selected as a base polymer matrix. Even though PVDF has less piezoelectric coefficient than piezo ceramics, but it has more useful due to its remarkable properties such as high flexibility, biocompatibility, high fatigue life, ease of deformation, and many more. The PVDF granules used in this present study were procured from the local vendor (Deval Enterprises, Vadodara, India).

3.3.2 BTO

BTO is the inorganic compound with the chemical formula $BaTiO_3$. BTO is a white powder and transparent as larger crystals [161]. The BTO is a piezoelectric ceramic and is mainly known for its lead-free and inorganic nature. It is a ferroelectric ceramic material, with a photorefractive effect. It is used in capacitors, electromechanical transducers, and nonlinear optics [162]. Due to the large dipole moment, BTO is commonly used as reinforcement in the EAPs to increase their piezoelectric properties. For this research work, BTO was procured from Ultra Nanotech Pvt. Ltd. Bengaluru, India. Table 3.2 shows the specifications of the BTO used in current research work (supplier data). Figure 3.4 (a) and (b) shows transmission electron microscopy image of BTO and X-ray diffraction (XRD) analysis (according to the supplier data), respectively.

Table 3.2 Specifications of the BTO

Name	Unit	Value /type
Particle size	nm	100
Purity	%	99.9
Specific surface area	m^2/g	10.42
Density	g/cm^3	5.85
Colour	--------	white
Morphology	--------	spherical

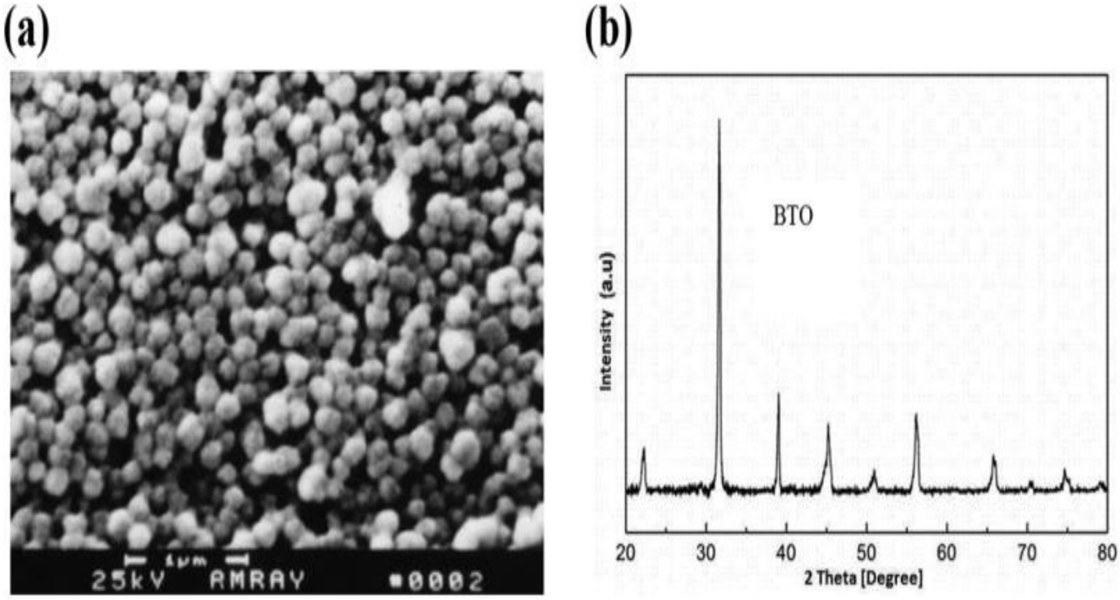

Figure 3.4 (a) Transmission electron microscopy image of BTO (b) X-ray diffraction (XRD) analysis of BTO (according to the supplier data)

3.3.3 Gr

The Gr is an allotrope of carbon having single layer sp2 hybridization arranged in a two-dimensional hexagonal lattice. It is the basic structural element of many other allotropes of carbon, such as graphite, diamond, charcoal, carbon nanotubes, and fullerenes [163]. It is the strongest material ever tested. This material has received an intense interest because of its mechanical, thermal, and electrical properties [164]. Gr has selected as the filler in the polymer matrix. A study conducted by a group of researchers highlighted that Gr improves the thermal, electrical, and mechanical properties of the polymer matrix.

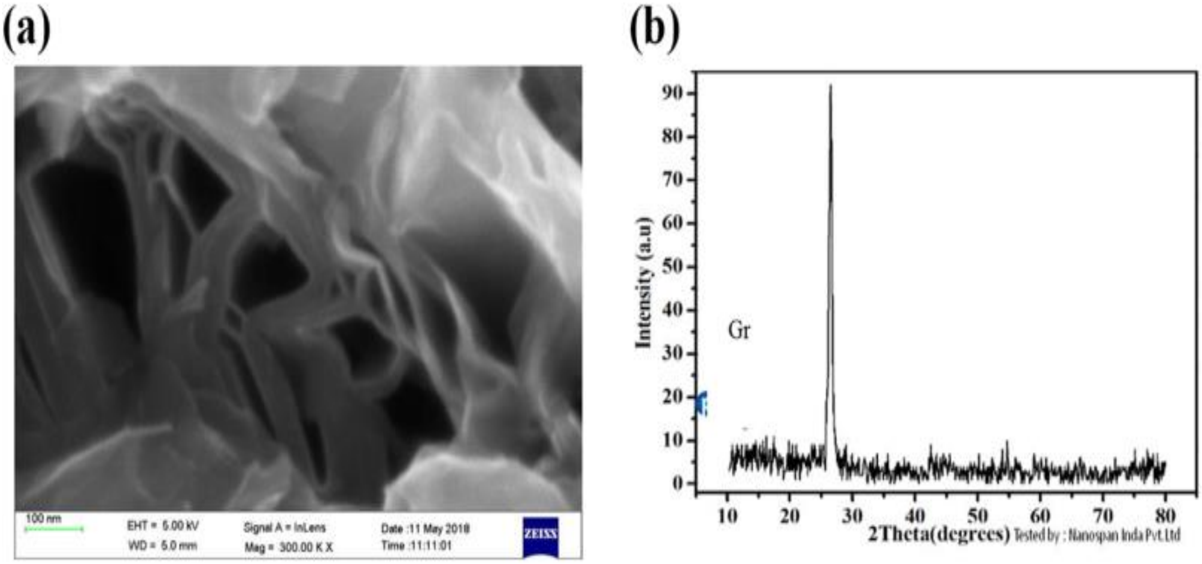

Figure 3.5 (a) SEM image of Gr and **(b)** XRD of Gr (according to the supplier data)

Gr was also used as filler in the base polymer matrix. In this study, Gr was procured from a local vendor (Platonic nanotech Pvt. Ltd., Jharkhand, India). The specifications of the Gr are shown in Table 3.3 (supplier data).

Table 3.3 Specifications of the Gr

Name	Unit	Value/type
Physical form	------	Fluffy
Colour	------	Grey-black
Thermal conductivity	Watts/m-K	3000
Electrical conductivity	Siemens/m	10^7
Tensile modulus	GPa	1000
Thickness	nm	5-10
Length	um	5-10
Density	g/cm^3	3.1
Number of layers	------	4-8
Surface area	m^2/g	200-210

3.4 Methods

3.4.1 MFI

MFI is used to identify the flow ability of PVDF and composites based upon it.

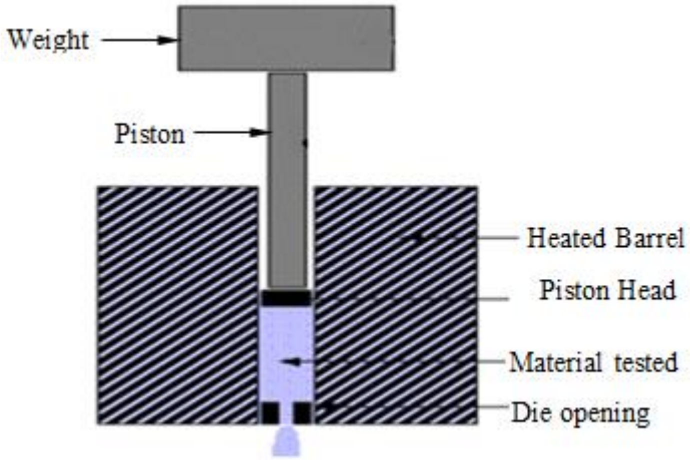

Figure 3.6 Basic construction of MFI tester

The successful running of extruded filament in the existing FDM setup depends upon the stiffness and consistent diameter of the feedstock filament, and it can be achieved only by appropriate selection of proportion of ceramics or other reinforcements in the polymer matrix. Therefore, the behavior of the composite under processing conditions can be specified by rheological properties. MFI is generally used to measure the flow capacity of the pure material or the composite prepared from this material. Certain standard conditions have been utilized during the testing as per American society for testing and materials (ASTM) standards for most of the materials. Temperature, weight, time are key factors in finding the MFI of any material. In this process, the material is flowing at a high temperature under the effect of constant weight through a small opening for 10 minutes. Thus, to calculate the MFI of any material the discharged material is collected and measured its weight. The schematic diagram of the MFI setup in which material is flowing through the heated barrel is shown in Figure 3.6 [165].

Generally, the polymers having an MFI value near 2.4 g/ 10 min run properly in the FDM setup. MFI tester used in this research work is made of Shanta Engineering, (Model: 2013), Pune, India. This setup of the MFI tester can withstand a temperature of 400℃.

The barrel of the MFI tester is completely covered/ wrapped by a heater coil. To minimize the leakage and dissipation of heat, the outer surface of the heater coil is completely insulated the temperature controller automatically cuts the heating once it reached the required level. A step-by-step complete procedure of MFI adopted in this study is as follows:

- Initially switch on the MFI tester and set its temperature level.
- The polymer granules or composites based upon it are poured into the cylinder.
- Allow the machine to reach at pre-set temperature (230 ^{o}C) and maintain the same temperature of the whole cylinder.
- Then pressure is applied on the poured material through the piston usin g predefined standard weight (as per ASTM D1238 standard) to push the material and start the timer from the control panel option.
- Under the effect of applied load (2.16 kg) semi-molten material starts to flow through the small opening of the die.
- Allows the material to come through die for 10 minutes. After that remove the load from the piston.
- Collect the material and measured its weight using a high-accuracy digital weighing scale.
- Thus, the measured weight of material per 10 minutes is known as MFI of the material. See formula writes below:

$$\text{MFI} = \text{Weight of sample in g/ 10 min.}$$

3.4.2 Trial runs for fabrication of feedstock filament

The rheological behavior of the material can be altered as per requirement by various means such as by adding metal powders, ceramics into the base polymer matrix to improve the inherent properties of the material. The addition of fillers like BTO, Gr increases the application domain of the base polymer matrix such as biomedical sensors, energy harvesting applications, transducers, etc.

In this research work, PVDF, an electroactive smart polymer having biocompatible nature is used as a base material due to its extraordinary piezoelectric properties for sensor applications. Piezoelectric ceramic BTO and Gr powder has been added to the base matrix at different proportions to study the effect of reinforcement on the PVDF properties.

For the fabrication of feedstock filament, a continuous flow of material must be required through the extruder.

Extrusion is a manufacturing technique in which material in granular form is poured from a hopper in a hot cylindrical barrel. The material starts melting in the heated barrel and is forced to push through a small opening in continuous form. In a SSE a long screw of a fixed profile is rotating inside the barrel and pushed the molten material to extrude through the die.

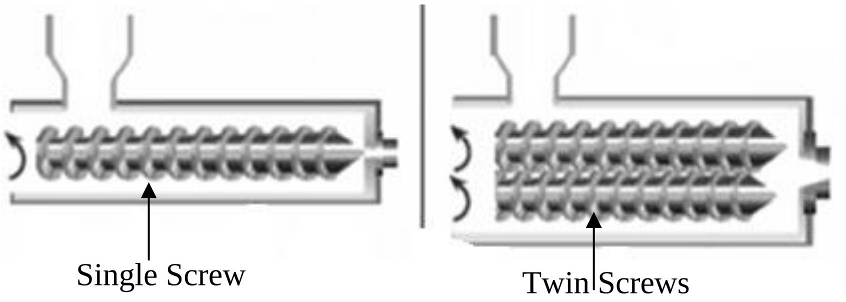

Figure 3.7 Cross-section view of SSE and TSE

A TSE is used to produce proper dispersion of the fillers in the base polymer matrix. These two screws are rotating inside the extruder barrel. In some TSE's the direction of rotation may same or in a counter direction. Figure 3.7 shows a cross-section view of SSE and TSE [166]. TSE is mainly used for compounding purposes. Various factors are considering while the extrusion of filament on TSE such as screw speed, extruder temperature, torque, load. die opening size etc. A filament in continuous form with good mechanical strength is the basic requirement for the proper running of it on FDM. Initially, PVDF/Gr/BTO based mixture in different proportions is prepared and checked the flow ability of the material, and based on MFI a total of 3 different proportions were selected for further fabrication of feedstock filament. Working and photographic views of TSE setup are shown in Figure 3.8.

Figure 3.8 Working and photographic view of TSE setup

In this study, a counter-rotating variant of TSE (Mini CTW HAAKE model, manufactured by: Thermo Scientific) was used [167]. The operating parameters of TSE were temperature in the range of 30℃ to 300℃ and screws speed 0-300 rpm. Three different proportions of PVDF/Gr/BTO were selected for the fabrication of feedstock filament. Two parameters of

TSE were also selected (each at three levels) along with the composition for optimization of TSE process parameters. As per the literature review for this in-house developed composite TSE setting must be optimized. Thus, to obtain the optimum process parametric settings of TSE for PBGC, a total of 9 wires were extruded according to Taguchi L9 orthogonal array. Out of these 9 different experimental settings one best was selected for fabrication of feedstock filament for 3D printing of parts.

3.4.3 PVDF/Gr/BTO based developed feedstock filament for 3D printing of scaffolds on FDM setup

The developed feedstock filament comprising of PVDF/Gr/BTO was used to optimize the FDM process parameters for the fabrication of functional prototypes. The FDM setup offers various process parameters to be controlled while the fabrication of 3D scaffolds. The process parameters of FDM are shown in Table 3.4. Out of these process parameters, three important factors were selected in this research work. The FDM process variables were optimized based on these three variables by using L9 orthogonal array. The remaining process parameters were kept constant in this research study. An open-source FDM setup (Model: Accucraft i250D; Company: Divide by Zero, India) having bed size 250×200×200 mm^3 was used in this present study is shown in Figure 3.9.

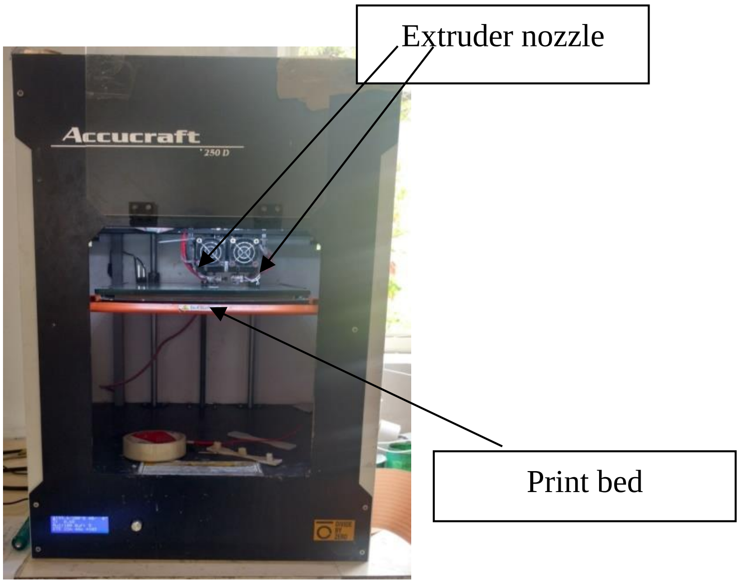

Figure 3.9 Open source Accucraft i250D 3D printer

Table 3.4 Basic configuration of the open-source 3D printer (Accucraft i250D)

Properties	**Value**
Nozzle diameter of the extruder	0.3 mm
Input feedstock filament diameter	1.75 mm
Fill pattern	Rectilinear, Triangular, Square, Zigzag, Linear, Honeycomb
Speed of perimeter	0-200 mm/s
Printing speed	0-300 mm/s
Traveling speed of Nozzle	0-300 mm/s
Extruder temperature (Maximum working temperature)	275 ℃
Maximum bed Temperature	100 ℃
Best printable materials recommended	PLA, ABS, PP, PA6, PETG, PC, PMMA, HIPS
Printing accuracy	80-150 µm
Extruder	2

3.4.4 Optimization of process variables of TSE/ FDM

To optimize the selected input process variables based on required output responses Signal-to-Noise (SN) was calculated. For a successful process, the strength of the signal should be always more than the noise level. As per the required properties, the SN ratio of the material is calculated on the "Larger the better" or "Smaller the better" basis. For mechanical strength (tensile or flexural), surface hardness, it is calculated using the following formula:

$$\eta = -10 \, log \left[\frac{1}{n} \sum_{k=1}^{n} \frac{1}{y^2} \right]$$

whereas for some properties such as surface roughness, dimensional accuracy, SN ratios can be calculated as;

$$\eta = -10 \, log \left[\frac{1}{n} \sum_{k=1}^{n} y^2 \right]$$

where, SN ratio is represented by η,

n = no. of experiments,

y; represents the properties of the material for experiment 'k'

To observe the best settings above mentioned SN ratio relations are used. As in the case of TSE, the best settings/process parameters are those, where the maximum value of SN ratio is found

To obtain the optimum condition/ values at best-observed settings for any property the following equation has been used:

$$\eta_{opt} = dn+(dn_{A1}- dn) +(dn_{B2}- dn) +(dn_{C3}- dn)$$

where ‘dn’ is the overall mean of SN ratios, dn $_{A1}$ is the mean of SN ratio for the first parameter at level 1, dn $_{B2}$ is the mean of SN ratio for the second parameter at level 2, and dn $_{C3}$ is the mean of SN data for the third parameter at level 3. The term ‘dn’ is not any standard term. Researchers may use any term to represent these equations.

Now, two different equations are used to calculate the value of y_{opt}^2 for smaller the better and larger the better case

In case of smaller the better

$$y_{opt}^2 = (1/10)^{\eta opt/10}$$

In the case of Larger is better

$$y_{opt}^2 = (10)^{\eta opt / 10}$$

The values calculated by using a mathematical approach are defined as predicted values of properties at optimum parametric settings. Thus, there is a need to perform confirmatory experiments to validate the results of the mathematical approach.

3.4.5 Fabrication of cylindrical discs for piezoelectric characterization of a developed composite of PVDF/Gr/BTO

After parametric optimization of process parameters of FDM for mechanical, dimensional, morphological properties of 3D printed parts of PVDF/Gr/BTO, the best-observed settings were used for 3D printing of cylindrical discs for piezoelectric characterization of the material. The best process variables of TSE were initially selected for the fabrication of feedstock filament-based composite developed from smart materials. Two types of feedstock filaments were extruded: (1) mechanically blended based, (2) chemically blended based composites. These extruded feedstock filaments were further used on the FDM machine for the 3D printing process. The best process settings of FDM obtained from optimization of mechanical properties were further used for 3D printing of thin cylindrical discs for piezoelectric characterization of developed materials. The nozzle head of the FDM (Divide by Zero) machine along with 3D printing of cylindrical disc is shown in figure 3.10.

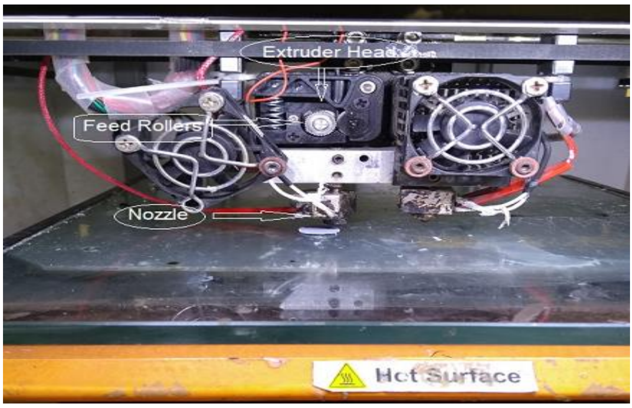

Figure 3.10 3D printing of a thin cylindrical disc

3.4.6 Electrical poling of 3D printed parts for piezoelectric characterization

After successfully fabrication of cylindrical discs, one of the specimens was prepared for the electrical poling process, where the transformation of PVDF β-phase occurs, as indicated by extensive research. For the electric poling process, the specimen should be conductive in nature. Thus, to make the 3D printed part electrically conductive, silver paint was coated on both sides of the disc. The silver paint is of two types, one is for room temperature use, and another is high temperature resistive silver paint to withstand the high-temperature conditions.

Figure 3.11 Setup used for electrical poling of specimen

In this research work, specimens were subjected to electrical poling at high temperature; therefore, a high temperature resistive silver paint was used for coating the surfaces of 3D printed disc. In this process, the specimen is subjected to a high voltage electric field. This applied electric field aligns the orientation of atoms/ molecules and arranges their dipoles. Thus, there is a change in the phase in the crystal structure of a material. PVDF is an EAP. It changes its phase structure when subjected to any electrical poling or mechanical stretching. Thus, there is a change in α to β phase. The complete setup of the DC polling unit used in this research work is shown in Figure 3.11.

3.4.7 Piezoelectric constant Measurement

The piezoelectric property of BTO/Gr/PVDF-based 3D printed films can be characterized by measuring the piezoelectric constant (d_{33}) by using a two-probe method. A d_{33} meter (Model YE2730A D_{33} make: Marine India) has been used with a high degree of resolution i.e., 0.1 pC/N. This meter is capable of direct measurement of the piezoelectric constant of piezoelectric crystals, ceramics, and polymeric. Although, any type of sample can be easily used to measure piezoelectric constant, but the disk-type sample is more preferable.

3.4.8 Thermal analysis, Mechanical analysis, morphological analysis, material characterization of developed composites, and 3D printed prototypes

The developed composites of PVDF/Gr/BTO were subjected to various types of properties analysis at various stages of fabrication. For thermal analysis, a fabricated feedstock filament was used. Feedstock filaments fabricated by both mechanical and chemical blended methods were subjected to thermal analysis by using DSC3 setup, company: METTLER TOLEDO, and operated with computerized software *STAR*^{e} (SW 14.00). The whole testing is performed under the flow of N_2 gas. The thermal behavior of the specimen is compared with the standard specimen. Both the samples were placed inside the small-sized aluminum/platinum-based crucibles. One of these two crucibles is known as a reference and the other is known as a sample as shown in Figure 3.12 Thus the thermal behavior of the developed composite was analyzed by DSC at two consecutive heating and cooling cycles.

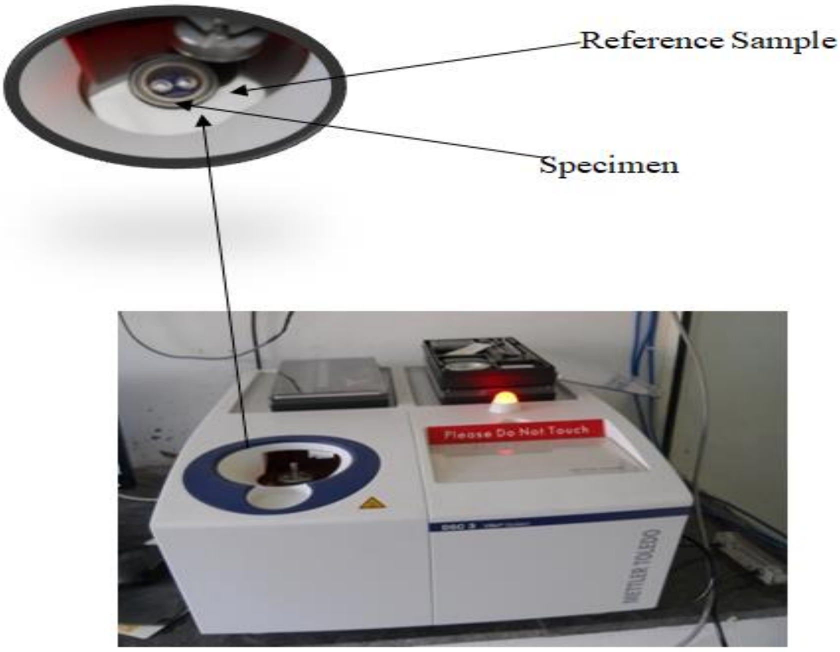

Figure 3.12 DSC setup

Further, the mechanical properties of the fabricated feedstock filaments and 3D printed parts were analyzed by using a universal testing machine (model: UTM, SE-500 kgf, Make Shanta Engineering, India). For morphological analysis such as surface porosity of the filaments, a metallurgical microscope model: XJL-17, was used as per ASTM standards. It works on the computerized metallurgical image analysis software (MIAS). The 3D printed samples of tensile as per ASTM D-638, flexural (ASTM D-790) and pull-out specimens were mechanically tested on the same UTM machine. Standard testing conditions such as 50 mm/min loading rate, room temperature, etc. are followed during the mechanical testing of the parts. The results of mechanical testing were obtained in the form of PL, BL, PS, BS, peak elongation, and break elongation.

For the surface hardness of 3D printed parts of PVDF/Gr/BTO, shore-D hardness testing was used. Shore-D hardness was tested as per the ASTM-D2240 standard. A shore-D durometer (digital meter) having a knob, is placed over the specimen and applied some pressure to determine the hardness of the surface. This meter gives the digital value of the surface hardness in shore-D.

The fractured surfaced of mechanically tested 3D printed parts were morphologically analyzed by using SEM (Model no. JEOL JSM-6510LV SEM, Japan), images captured at different magnification levels. The sample for SEM analysis was initially prepared by doing gold coating over its surface (in case of non-conductive sample only). After that samples are fixed on the sample holder and put in the vacuum chamber. SEM is also providing detailed high magnification images of the sample by raster a focused electron beam across the surface in a vacuum chamber and identifying auxiliary or backscattered electron signals. An Energy Dispersive X-Ray analyzer (EDA/EDX) is likewise used to give identification of element ID and quantitative compositional data. An energy-dispersive spectroscopy (EDS) detector is used to differentiate the characteristics/properties of different elements into an energy spectrum, and EDS system software is used to analyze the energy spectrum to determine the abundance of specific elements. Area mapping is used to determine whether the reinforced materials are dispersed properly throughout the base material or not.

3.4.9 XRD Analysis

XRD is a fast-analytical technique that is mainly used for compound and phase identification of a crystalline material (solid/powder form). It also provides detailed information on unit cell dimensions. For this research study, compound and phase testing have been performed on

XRD machine (Model No.: - ECO D8 ADVANCE, manufactured by: - BRUKER Company) and output results have been saved in. raw and .txt format. For XRD data analysis (phase identification, cluster analysis, and crystallographic analysis) Bruker AXS Measurement Centre and X'Pert HighScore Plus software were to be used in this study. Figure 3.13 shows the experimental setup of the XRD machine.

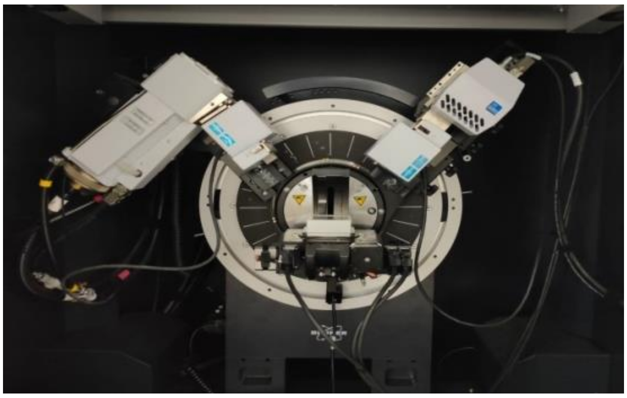

Figure 3.13 Experimental setup of XRD machine

3.4.10 FTIR Analysis

FTIR spectroscopy is normally using for fast and accurate identification of compounds such as adhesives, fillers, thermoplastic polymers, paints, resins, coatings, blends, compounded plastics, rubbers, and reinforced thermoplastic polymers. FTIR spectroscopy is the most effective tool for determining the surface composition in chemical form. The absorbance of a sample to an incident infrared spectrum with the range of 600 to 4500 cm^{-1} constitutes the analysis. FTIR's are also explaining the incomplete polymerization when it is compared with a standard specimen. FTIR is also be used for imaging and microscopy of particle and rubber interfacial modification. For this research work FTIR machine (Model No.: - INFRA 3000B FTIR; manufacture by - Analytical) has been used that as shown in Figure 3.14.

Figure 3.14 Orthogonal view of FTIR spectroscopy machine

3.4.11 DMA

Polymers react to an external force by two different methods: (1) Elasticity, in which the original shape is recovered after stretching, and (2) Viscous response, which absorbs energy to prevent breakage. Viscoelasticity of polymers depends upon the temperature and time. DMA is used for the characterization of material properties such as viscoelastic properties, mechanical properties with respect to temperature, frequency, and time. DMA is incorporated with controlled heating and cooling system. The time scale is used to determine the frequency effect on the material's resistance towards permanent deformation. The sample of various materials like elastomers, thermoplastics, metals, and ceramics is subjected to repeatedly apply small cyclic load. The output responses of DMA are in the form of storage and loss modulus. The phase shift that occurs in the force and displacement amplitude is known as tan delta. In DMA material is subjected to different modes of deformation. As the test is performed as a function of temperature, thus it may also be known as dynamic mechanical thermal analysis (DMTA). In the case of thermomechanical analysis (TMA) the sample is subjected to a static load and analyses the changes that occur with respect to time and temperature. The results of TMA give the change in dimensions and coefficient of thermal expansion. However, In DMA an oscillatory force is applied at a particular frequency and reports the stiffness and damping capacity of the sample. Undoubtedly, both the tests detect transitions; however, DMA is more sensitive than TMA. Thus to predict the real-time performance of polymer, three parameters force, time and temperature are strategically used in DMA. Some other properties that may be easily studied with DMA are as follows:

1. Viscoelastic spectrum
2. To evaluate the Tg of the materials
3. To see the changes that occurs in the elastic modulus of the polymer with respect to time, temperature, and frequency
4. Damping behaviour known as tan delta/loss modulus
5. Comparison among various polymers based on failure analysis, quality, etc.

3.4.12 Working of DMA

In DMA testing, a sample of a predefined geometry is subjected to a sinusoidal deformation. A clamp system is used to hold a solid polymeric sample for DMA. A sample is first fabricated of required dimensions as per clamp sizes. The type of clamp depends upon the mechanical motion required for a specific study such as; tensile for the stretch, compression for push, flexure for bending, and shear for the motion of layers parallel to the surface. There are mainly two clamps: one is moveable and the other one is fixed to hold the sample. A moveable clamp is used to apply the cyclic force and displace the sample repeatedly. Figure 3.15 shows the different modes of deformation in DMA . A clamp system is programmed to displace the sample within a constant specified distance. Controlled stress is applied to the material and the sample will deform up to a certain amount under the controlled stress. The amount of deformation is directly related to the stiffness of the material. The sinusoidal force is generated through a motor and further transmitted with the drive shaft. A stabilizing bearing is used to keep the driveshaft in position during the force transmission. During the displacement amplitude of the response is measured. Based upon the sample's dimension and geometry, for each cycle, the stress and strain response of the sample is calculated. These observed or calculated values are a function of time, temperature, and frequency of applied force. Thus in dynamic testing sinusoidal displacement results in sinusoidal elastic response of the sample. The main aim of DMA is not to break the sample; however, it is used to evaluate the elastic and viscous response of the sample in the linear viscoelastic region (LVR), which means low force conditions are applied that do not break the structure.

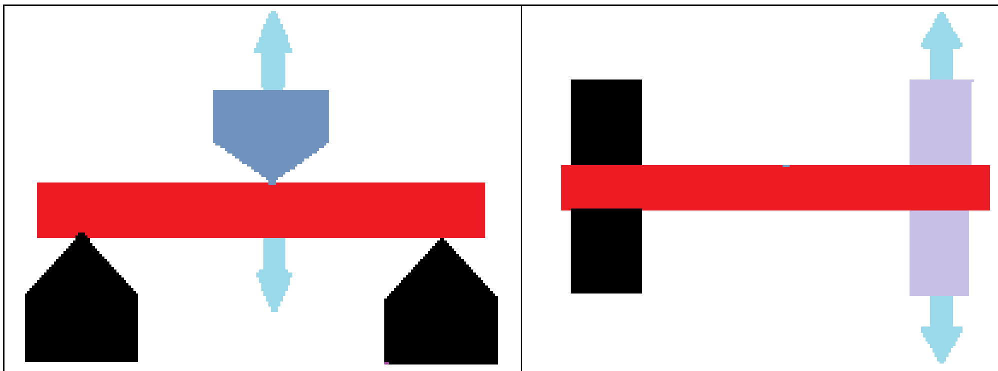

(a) 3-point bending (b) Cantilever bending

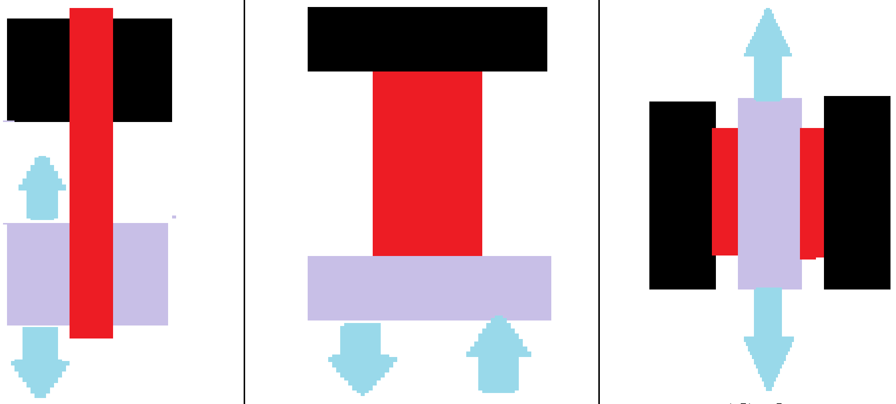

(c) Tension (d) Compression (d)Shear

Figure 3.15 Different modes of deformation used in DMA (source: Mettler Toledo)

DMA is generally used to evaluate the conditions that may alter the original viscoelastic behaviour of the material and may lead to long-lasting small deformations in original form. If the thermoplastic polymer is heated during DMA testing, it will lose its original elasticity after some particular temperature and deforms permanently. This all occurs at glass transition (Tg) temperature. In DMA the material deforms only in micrometers so a small applied force ensures the measurable of Tg in the viscoelastic spectrum. Due to very small deformation, the sample does not squeeze or pulled apart from the clamps during the testing. The phase angle (δ) is determined by the degree to which the curve of stress goes out of phase with respect to the strain input curve. This phase angle represents the relationship between strain input and stress output. Further trigonometric equations are derived from this relationship to describe three quantifiable properties as follows.

E’ =Storage Modulus
E” =Loss Modulus
E”/E’ = Tan δ

E’ represents the material’s capacity to absorb the applied mechanical energy during the loading conditions. Consequently, it is associated with the shape recovery and stiffness of material under the loading cycle. However, E” corresponds to the damping capacity of the material. It indicates the ability of the polymer to disburse mechanical energy by internal molecular motions. The ratio of E”/ E’ is represented by the tan delta (δ).

In this research work, a single cantilever method is used. The force of 1 N is applied cyclically with a frequency of 10 Hz. The sample was displaced by 10 µm. The increase in temperature during DMA testing depends upon the thermal properties of the material, like melting point, etc. The temperature in this research work is increased from 30°C to 130°C. The temperature of the machine was increased at the rate of 3 K/min.

The research objectives along with the methodology adopted for the completion of them has been discussed in this chapter Therefore, the experimentation performed to complete these objectives has been discussed in the next chapter of ‘Experimentation’.

CHAPTER 4
EXPERIMENTATION

In this chapter, the experimental work conducted on TSE and FDM for the preparation of feedstock filament and functional prototypes has been described. Various process parameters of the TSE and FDM have been varied in this research work. The design of experiment (DOE) was prepared as per Taguchi L9 orthogonal array (OA). Experimental work conducted at various stages is as follows:

4.1 Experimentation at stage 1

4.1.1 Pilot Experimentation

This research work started with the selection of smart materials-based EAP. PVDF was selected as a base polymer matrix due to its outstanding piezoelectric properties. Moreover, it has certain advantages over piezo ceramics such as light in weight, flexibility, high sensitivity towards applied mechanical loads, etc. In this research work, solef PVDF 6008/0001 grade was used. The material was procured from the local market (Deval Enterprises, Vadodara, India). The BTO is a ceramic material, having excellent piezoelectric properties. Its large dipole moment can be used to reinforce in the polymer matrix to enhance its piezoelectric properties. BTO is inorganic and lead-free filler among the other piezoelectric ceramics. The BTO having particle size 100 nm was also procured from the local market (Ultra Nanotech Pvt. Ltd. Bengaluru, India). Along with BTO, Gr was selected as filler in the polymer matrix. The Gr is a highly conductive material. A study conducted by a group of researchers highlighted that Gr is helpful to improve the thermal, electrical, and mechanical properties of the polymer matrix [107]. For this study, Gr (physical form: fluffy, colour: gray-black, thermal conductivity: 3000 W/mK, tensile modulus: 1000 GPa, electrical conductivity: 107 Siemens/m, purity: 99%, thickness: 5–10 nm, length: 5–10 μm, density: 3.1 g/cm3, number of layers: 4–8, surface area: 200–210 m2/g) was also procured from the local market (Platonic Nanotech Pvt. Ltd, Mahagama, Godda, Jharkhand, India). BTO and Gr were mixed into the PVDF matrix by using two different methods of blending. The final composition of mechanically and chemically blended composites was used on TSE for the fabrication of feedstock filament. The fabricated filaments were used for the 3D printing of standard prototypes.

In the pilot experimentation, BTO and Gr powder were reinforced in PVDF matrix in different proportions, for the development of smart polymer-based composite for possible 4D printing applications. The BTO was added to the PVDF matrix in five different proportions. The effect of BTO on the flowability of the PVDF polymer was studied. Similar to BTO, Gr was also added in the PVDF matrix in five different proportions and its effect on the flowability was observed. MFI testing was performed to evaluate the rheological properties of the mixed materials.

4.1.2 Flow ability characterization for selection of proportion fillers in polymer matrix

A successful running of extruded filament in the existing FDM setup depends upon the stiffness and consistent diameter of feedstock filament and it can be achieved only by appropriate selection of proportion of ceramics or other reinforcements in a polymer matrix. Therefore, the behaviour of the composite under processing conditions can be specified by rheological properties. Flowability of the material plays a prominent role in uniformity and other mechanical properties of the extruded filament. Thus, to characterize the rheological properties of the blended material, a MFI test was performed. Initially, the prepared composite of PVDF+Gr+BTO was preheated at high temperature for 3-5 min and after that constant pressure was applied through the piston to flow the material through a standard die having diameter2.0955 ± 0.0051 mm and length 8.000 ± 0.025mm (in some cases different orifice is used). MFI tester used in this research work is made of Shanta Engineering, Pune, India (see Figure 4.1).

Figure 4.1 Melt flow tester used for flowability check

The line chart (Figure 4.2) shows the effect of BTO and Gr on the MFI of PVDF composite matrix with a single type of reinforcement. The results of MFI testing show that, in both types of fillers, with the addition of filler contents in PVDF matrix, the flowability of the polymer decreases. The MFI of the pure PVDF was found 8 gm/ (10min). It has been observed experimentally that with the addition of 20% and 30% of BTO, the MFI value of composite is reduced to 3.57 g/10min and 2.4g/10min respectively and in the case of Gr, only 1-2% of reinforcement is sufficient enough to reduce the MFI value of PVDF by 1-1.25 g/10 min.

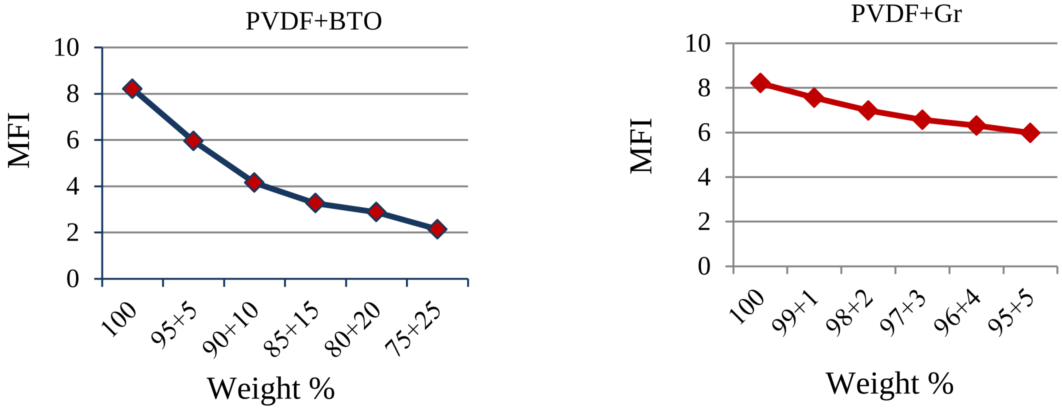

Figure 4.2 Effect of addition of BTO and Gr on MFI of PVDF respectively

Based upon the results of MFI (Figure 4.2), Gr was added 2% by weight in the PVDF matrix whereas BTO was reinforced up to 20% by weight in PVDF+Gr+BTO composite matrix. It has been observed that as BTO proportion is increased from 0 to 20 the MFI value of the PVDF composite matrix is decreased. Based on MFI testing three different proportions of PVDF/Gr/BTO were selected for the fabrication of feedstock filament using TSE. Table 4.1 shows the proportion of composition by weight.

Table 4.1 MFI at different proportion of materials

Composition/Proportion (wt%)	X [PVDF (98%) +Gr (2%)]	Y [BTO]
A	90	10
B	85	15
C	80	20

The results of MFI testing ascertain the feasibility of the extrusion of feedstock filament with a uniform diameter. Further in pilot experimentation viscosity of the composition was measure by using resulted values of MFI. To calculate the density of composition a ratio proportion method was used.

The measured values of MFI of all three compositions were further used for measuring the shear rate of the composition. Further, the viscosity (μ), has been calculated from shear stress (τ) divided by the shear rate (γ). To calculate the shear stress and shear rate following equations have been used.

$$\tau = \frac{\mathrm{r\ x\ F}}{2\ \mathrm{x}\ \pi\ \mathrm{x}\ \mathrm{R}^2\ \mathrm{x\ l}} \qquad --------(4.1)$$

$$\gamma = \frac{4\ \mathrm{x\ Q}}{\pi\ \mathrm{x\ r}^3} \qquad --------(4.2)$$

where r is nozzle radius 0.105 cm

R is the radius of piston 0.4737 cm

l is nozzle length 0.8 cm

F is test load L in kg x 9.807 x 10^5 dynes

(Here L is 2.16 kg)

Since the geometry of melt flow indexer is fixed, thus after putting the values of radius of the nozzle (r), test load (F), nozzle length (l), and radius of the piston (R) in equation 4.1, then shear stress (τ) is :

$$\tau = 9.13\ \mathrm{x}\ 10^4\ \mathrm{L\ dynes}\ --------(4.3)$$

where, shear rate γ depends on the volumetric flow rate Q (in cc.s^{-1}) and. The volume flow rate Q can be determined by dividing the volume V extruded during the time t and Q is calculated as:

$$\mathrm{Q} = \frac{\mathrm{MFI}}{\rho\ \mathrm{x}\ 600} \qquad ---------(4.4)$$

From equation 4.2 and 4.4 shear rate can be calculated as

$$\gamma = \frac{\mathrm{MFI}}{\pi\ \mathrm{x\ r}^3\ \mathrm{x}\ \rho\ \mathrm{x150}} \qquad --------(4.5)$$

After putting the values of MFI, a radius of nozzle (r), density (ρ) in equation 4.5,

$$\gamma = \frac{1.83\mathrm{x\ MFI}}{\rho}\ \ 1/\mathrm{s} --------(4.6)$$

To calculate viscosity equation 4.3 is divided by equation 4.6

$$\mu = \frac{9.13\ \mathrm{x}\ 10\text{^}4\ \mathrm{L\ x}\ \rho}{1.83\ \mathrm{x\ MFI}}\ \ \mathrm{dynes} - \mathrm{s}\ \ --------(4.7)$$

or

$$\mu = \frac{9.13\ \mathrm{x}\ 10\text{^}4\ \mathrm{L\ x}\ \rho}{1.83\ \mathrm{x\ MFI\ x}\ 10}\ \ \mathrm{Pa} - \mathrm{s}\ \ --------(4.8)$$

Thus equations 4.7 and 4.8 were used to calculating the values of viscosity for all selected compositions of the material.

4.1.3 Mechanical blending of PVDF/Gr/BTO for fabrication of feedstock filament

For the fabrication of feedstock filament, three different compositions of PVDF/Gr/BTO were selected on the basis of MFI. The proportion of Gr was kept fixed as 2% of the PVDF by weight percentage. The addition of BTO in PVDF+ Gr was in three different proportions such as: 10%, 15%, and 20% by weight of PVDF/Gr/BTO. For all these three compositions viscosity is calculated by using the above-mentioned equations.

4.1.4 Extrusion of feedstock filament

A Thermo scientific (Make: HAAKE, Germany) TSE was used to fabricate the feedstock filament. The TSE has two corotating screws. It is operated by computer software. Commercial TSE is well known for providing a high degree of dispersion, so it has been used for compounding two or more materials. The temperature of the extruder depends upon the melting point of the material. It has a small opening and the diameter of the opening can be changed by changing the diameter of the die. The uniformity in diameter of feedstock filament played a very dominating role in its successful use in FDM setup.

To select the level of processing parameters a pilot study was performed by taking the levels on basis of literature and melting point of polymer matrix The composition of PVDF/Gr/BTO was extruded at different combinations of extruder temperature and screw speed. After 10- 15 pilot experiments at different set of combinations of screw speed and extruder’s temperature, three levels of each were selected. It has been experimentally observed that the mixture was not extruded in the continuous form below 175°C temperature and 30 rpm respectively. However, As the temperature was raised above 210°C with rpm 70 the molten material is getting extruded at a very fast rate with compromise on dimensional stability (visual observations). Therefore, to achieve good mechanical and thermal properties with a consistent diameter of the wire, the barrel temperature may be put in a range of 180°C to 200°C and the rpm of twin screws within the range of 40 to 60. To obtain a high degree of dispersion the die opening was chocked for 10 min while the screws were continuously rotating at a predefined speed. The process parameters of the extruder (temperature and rpm) affect the dimensional accuracy as well as the mechanical and thermal properties of the filament.

4.1.5 DOE and control log of experimentation for TSE

To obtain the optimum conditions of TSE for fabrication of PVDF/Gr/BTO based feedstock filament for 3D printing of prototypes, DOE was prepared. A complete control log of experimentation was set according to Taguchi L9 orthogonal array. A total of 9 experiments were set to perform at different combinations of compositions along with TSE parameters (extruder temperature and screw speed). To reduce environmental or human error, each experiment was conducted three times. Thus, a total of 27 (9x3) experiments were conducted to obtain the optimized settings of TSE. A complete log of experimentation is shown in Table 4.3. Based on MFI three different proportions of BTO in PVDF/Gr were selected and two parameters of TSE i.e. screw speed and extruder temperature was selected for experimentation. The three levels of extruder temperature were 180, 190, and 200°C. The three levels of screw speed were 40, 50, 60 rpm.

Table 4.2 Input process parameters of TSE at all three levels

Input Parameters	**Level**
Composition/proportion (wt%)	A, B, C
Temperature (in ^{o}C)	180, 190, 200
Revolution (in rpm)	40, 50, 60

As selecting the two most important variable parameters of TSE along with composition as third parameters were used to perform the experiments. There are 3 different levels of each that have been selected as shown in Table 4.2.

Table 4.3 Control log of experimentation as per Taguchi L9 orthogonal array

S.NO.	Temperature	Rpm	Composition
1	180	40	A
2	180	50	B
3	180	60	C
4	190	40	B
5	190	50	C
6	190	60	A
7	200	40	C
8	200	50	A
9	200	60	B

For the extrusion of feedstock filaments, experiments were performed as per a combination of variables shown in Table 4.3. To prepare the blend of Gr, BTO, and PVDF, 2-3 drops of coconut oil were put into mixed materials so that the filler particles may stick to the polymer granular, the prepared mixer of materials was then fed into the barrel of TSE through the hopper. The 7 ml volume of material is fed at a time in TSE at the preselected temperature. The die opening of TSE was chocked and allowed to get mixed for 10 min. Initially during mixing the rpm of the extruder was set at 100 rpm and the temperature of the extruder was set at 250 °C. After 10 min of mixing the screw speed and temperature was set as per the control log (see Table 4.5). After that, the die was opened and collects the filament over the spool. While extrusion process diameter of filament should be kept uniform for proper running on the 3D printer. The feedstock filament of 1.75 ± 0.05 mm size is prepared on TSE setup. A total of 9 filaments were extruded as per the suggested experimental settings.

4.1.6 Tensile testing of feedstock filaments

The extruded feedstock filaments of PVDF/Gr/BTO were subjected to mechanical testing on UTM to obtain the tensile properties of the filaments. Tensile testing provides the force required to break the material in an elongation direction. It also provides information about the stretch capacity of the material or how much material could be elongated before reaches permanent deformation. Thus the strength of the material at peak level and breakpoint is observed in tensile testing of the material. In this research work to obtain the PL, BL, PS, and BS of the filaments tensile testing was performed on the UTM (see Figure 4.3).

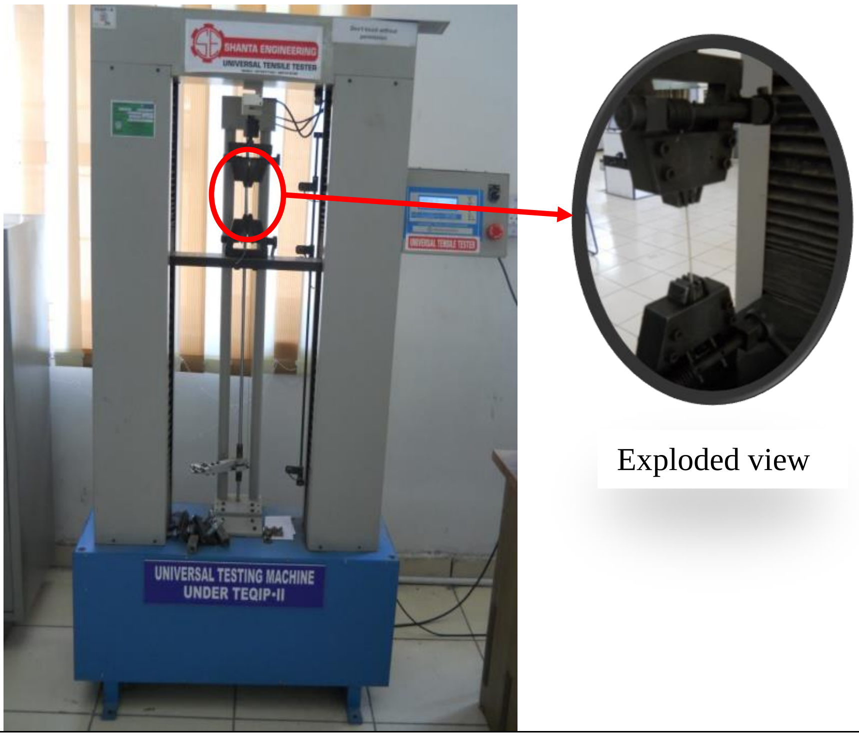

Figure 4.3 Tensile testing of feedstock filament on UTM

The UTM having capacity up to 5 KN and load cell of 0.5 N, capable for testing of polymers/plastic materials only was used in this research work. Any shape of polymeric material can be used in this machine for testing the tensile properties. The extruded feed stock filaments were fixed in the jaws of the UTM and loading conditions were set on the computer. After measuring the initial gap in between the jaws, tensile testing was performed.

4.1.7 Dimensional accuracy of the feedstock filaments

Since the main purpose of this study is to develop a smart polymer-based feedstock filament comprising of PVDF/BTO/Gr composite (PBGC), for FDM process. The existing FDM setup supports only the filament having a diameter within the range of 1.75±0.05mm. Thus, it was necessary to perform the dimensional analysis of the extruded filaments. Therefore, after the extrusion of feedstock filaments as per the different processing parameters, they were subjected to dimensional measurement. To measure the diameter of the filaments a Mitutoyo micrometer (as per ISO-3611-1978) accurate up to three decimal places was used. To minimize the experimental error, a total of three readings were taken at three different places over the total span length of the filaments. The average of three measured readings was taken as the diameter of the filament. Table 4.4 shows the measured diameter of the filaments along with required diameter and error.

Table 4.4 Measured dimensions of the extruded filaments

Exp No.	Parameter (A) *Temp (℃)*	Parameter (B) *RPM*	Parameter(C) *Composition wt%*	Ø1 (mm)	Ø2 (mm)	Ø3 (mm)	Ø avg	Ø req	δ Ø
1	180	40	A	1.67	1.68	1.69	1.68	1.75	0.07
2	180	50	B	1.68	1.62	1.65	1.65	1.75	0.10
3	180	60	C	1.60	1.63	1.63	1.62	1.75	0.13
4	190	40	B	1.74	1.70	1.72	1.72	1.75	0.03
5	190	50	C	1.75	1.78	1.78	1.77	1.75	0.02
6	190	60	A	1.76	1.82	1.79	1.79	1.75	0.04
7	200	40	C	1.74	1.76	1.72	1.74	1.75	0.01
8	200	50	A	1.78	1.79	1.71	1.76	1.75	0.01
9	200	60	B	1.82	1.78	1.74	1.78	1.75	0.03

4.1.8 Surface porosity analysis

The surface properties of the feedstock filament also affect its use in the 3D printing process. After the mechanical and dimensional testing of all fabricated filaments were subjected to surface properties analysis. To ascertain the effect of processing conditions on the surface properties (such as porosity/voids and surface roughness) of the extruded filaments, morphological analysis was performed. A metallurgical microscope was used to capture the photomicrographs of the samples at ×100 magnification. The surface porosity (Φ) of the samples was measured as per ASTM B-276 by commercially available metallurgical image analysis software (MIAS).

4.1.9 DSC

Thermal behaviour also plays a dominant role in the selection of material for particular applications. As PVDF is well known for its high thermal resistance properties, therefore, some investigations are also needed to find the effect of reinforcement on the thermal properties of the PVDF. To establish the thermal properties of the pure PVDF and feedstock filament comprised of PVDF, BTO and Gr were subjected to DSC analysis. The feedstock filaments having the best and worst mechanical properties were subjected to DSC testing. Each specimen was undergone two heating and two cooling cycles during the thermal testing. Thermal analyses were performed at two successive heating-cooling cycles, having a temperature range of 30℃ to 250℃, and the heating rate was set at 10K/min. The whole experimentation was performed under a controlled N_2 gas environment. In this research work, a total of three samples were prepared, the first sample was taken from the virgin PVDF and second and third sample was taken from the filament possessing the best and worst mechanical strength respectively. To measure the thermal transition, DSC (Make: METTLER TOLEDO, Swiss) operated with A STAR^e (SW 14.00) the software has been used, Initially, the samples were kept in a hot air oven at 90℃ for 30 mins to eliminate any unrequired particles and any existing thermal history During the first thermal cycle sample was heated from 30℃ to 250℃ at the heating rate of 10K/min. The first heating cycle gives the complete detail of the melting of the material such as; the starting of melting, end of melting, and a peak of melting point. Moreover, the energy absorbs during the heating is also determined with the help of DSC analysis. In the cooling cycle, the solidification range of the material is observed in thermal testing. DSC analysis also gives information regarding the release of energy during the solidification of the material. To determine the reusability of the material, the sample was subjected to more than one heating and cooling cycle. If similar results are found in 2nd heating and cooling cycle then the material is said to be thermally stable for reusability. As shown in Figure 4.4, DSC sensor uses two crucibles for heating and cooling, one for the reference and another one use with the sample. For thermal testing, a controlled environment of N_2 gas was maintained at the flow rate of 50 ml/min.

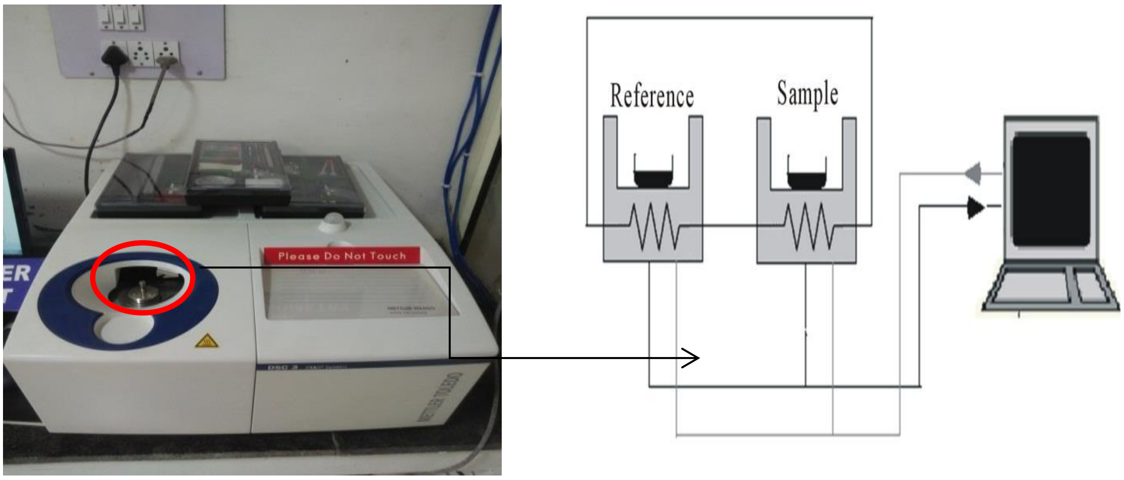

(a) (b)

Figure 4.4 (a) DSC setup and (b) DSC testing chamber for sample

4.1.10 Morphological analysis of feedstock filaments of PBGC prepared by mechanical mixing of materials

After successful investigations of mechanical and thermal properties, the specimen of the in-house developed feedstock filament comprised of PVDF, BTO, and Gr, having best and worst mechanical strength were subject to microscopic analysis using SEM, EDA/EDX and Area mapping.. The microphotographs of the samples were taken on the JEOL JSM-6510LV SEM (Japan) at different magnification levels. As the samples were made up of non-conductive polymer, therefore a coating of gold layer has been made over its surface.

4.2 Experimentation at stage 2

4.2.1 Selection of process parameters of FDM and DOE, for 3D printing of standard specimens of mechanically blended feedstock filament of PBGC

The feedstock filament of mechanically blended composites (MBC) of PBG extruded at optimized settings of TSE was further used to run on an open-source FDM printer for 3D printing of standard specimens as well as piezoelectric sensors. The printed parts for piezoelectric applications must have good mechanical strength. Therefore, mechanical properties need to be optimized before the fabrication of the final part for any particular application. Initially, three types of specimens were fabricated on 3D printer as per ASTM standards to investigate the required mechanical properties of the developed smart materials-based composite. Tensile specimens, flexural specimens, and pull-out specimens were 3D printed on an FDM machine. Further, these fabricated specimens were subjected to destructive testing on the UTM machine, and results of mechanical testing were optimized using Minitab 17.00 software.

The optimized experimental settings of TSE on the basis of tensile strength and dimensional accuracy were used to produce the feedstock filament for further use on FDM. For 3D printing of any part, various process variables of the 3D printer should be adjusted properly. An open-source 3D printer has various input parameters which affect the properties of 3D printed parts are shown in the form of a fish bone diagram (see Figure 4.5). All these process variables can be easily manipulated as per the requirement during the fabrication of the part. Some of them are very effective however, some have less effect on the properties of 3D printed parts. Out of these controllable process parameters, three process parameters [Infill speed (IS), Infill angle (IA), and Infill density (ID)] have been provisionally selected based on the literature review. These three parameters play a more significant role than other parameters, whereas the remaining process parameters are kept constant for this research work (Table 4.5).

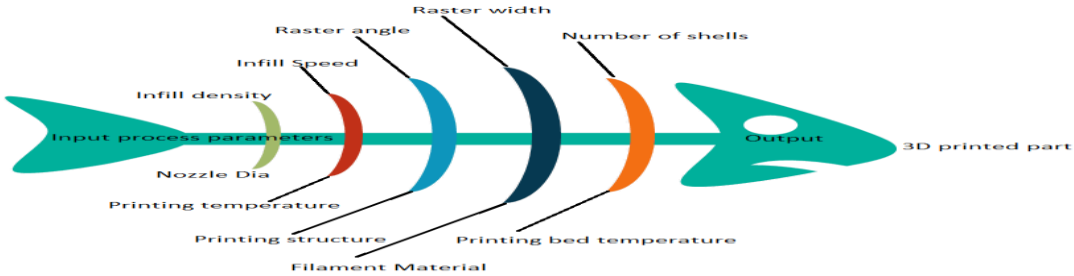

Figure 4.5: Various controllable process parameters of FDM

On the basis of pilot experimentation and literature review, three levels of each input parameter were selected (see Table 4.5), The remaining process parameters such as nozzle diameter, part orientation, nozzle temperature, bed temperature, infill pattern, number of parameters, etc were kept fixed. (Table 4.6).

Table 4.5 Selected input parameters of FDM

Input process variables of FDM (each at 3 levels)			
Input Parameters	Level 1	Level 2	Level 3
IS (mm/s)	50	70	90
IA (°)	0	45	90
ID (%)	60	80	100

Table 4.6 Process parameters of FDM kept constant in this study

Process variable	**Operating condition**
Fill pattern	Rectilinear
Filament diameter	1.75 mm
First layer thickness	0.40 mm
Layer thickness	0.28 mm
Extruder temperature	260^{o}C
Bed Temperature	85^{o}C
Infill speed	60 mm/s
Nozzle diameter	0.5 mm
Number of parameters	3
Fan output	50%

The complete design of the experiment to produce the parts is used to evaluate the correlation between input process variables and proposed output characteristics for optimization of process parameters of FDM, DOE was prepared as per Taguchi L9 (3^3) orthogonal array. Both types of specimens (tensile and flexural) were fabricated as per the same DOE. To minimize the experimental error a total of 3 sets of experiments/repetitions have been carried out at all 9 settings. of selected controllable parameters, A complete log of experimentation for fabrication of both types of specimen is shown in table 4.7.

Table 4.7 A control log of experimentation for 3D of parts

Experiment No. → Parameters ↓	1	2	3	4	5	6	7	8	9
IS (mm/s)	50	50	50	70	70	70	90	90	90
IA (^{o})	0	45	90	0	45	90	0	45	90
ID (%)	60	80	100	80	100	60	100	60	80

Mechanical testing on the fabricated parts is performed as per the ASTM D638 and ASTM D790 (American standard for tensile testing of plastics) at natural ambient conditions. An open-source 3D printer used for the fabrication of specimens is shown in Figure 4.6.

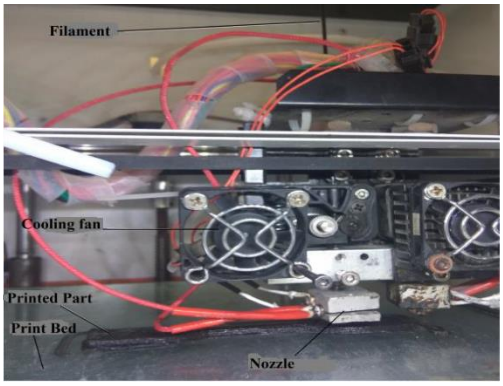

Figure 4.6: Extruder head of the 3D printer

4.2.2 3D printing of standard tensile specimens

To determine the tensile properties of MBC of PBG, standard bone-shaped tensile specimens were 3D printed. An ASTM D638 TYPE IV (international standard of plastic testing) was used for 3D printing of tensile specimens. A total of 9 specimens were fabricated as per the DOE shown in (Table 4.7). Figure 4.7 and Table 4.8 shows the standard dimensions of a bone-shaped tensile specimen to be 3D printed

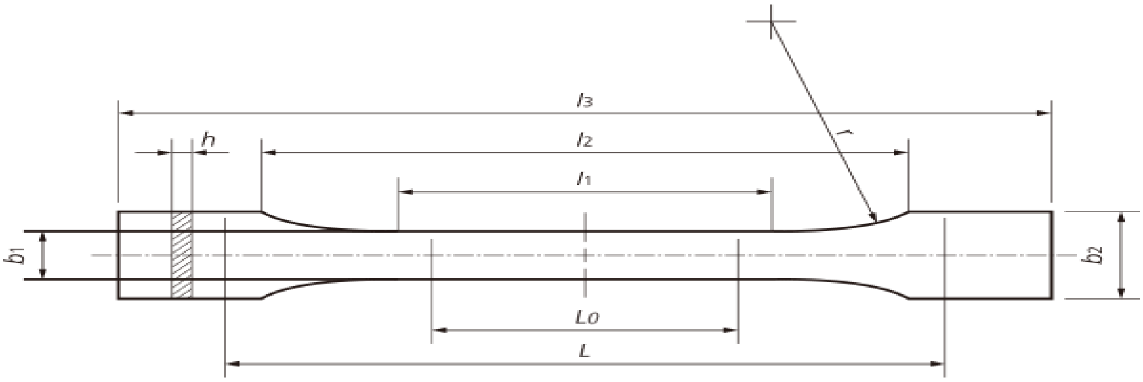

Figure 4.7 Schematic of standard tensile specimen according to ASTM D638 type IV

Table 4.8 Standard dimensions of tensile specimen according to ASTM D 638 type IV

Size	Type IV Dimension
Distance between grip	65 mm
Gauge length, l_1	25 mm
Thickness, h	3.2 mm
Grip section width, strong$_2$	20 mm
Parallel section width, strong$_1$	605 mm
Parallel length, l_2	33 mm
Full length, l_3	125 mm

As per the dimensions given above, 3D printing of parts is performed. Figure 4.8 shows the fabricated tensile specimens and infill angle at which they are 3D printed.

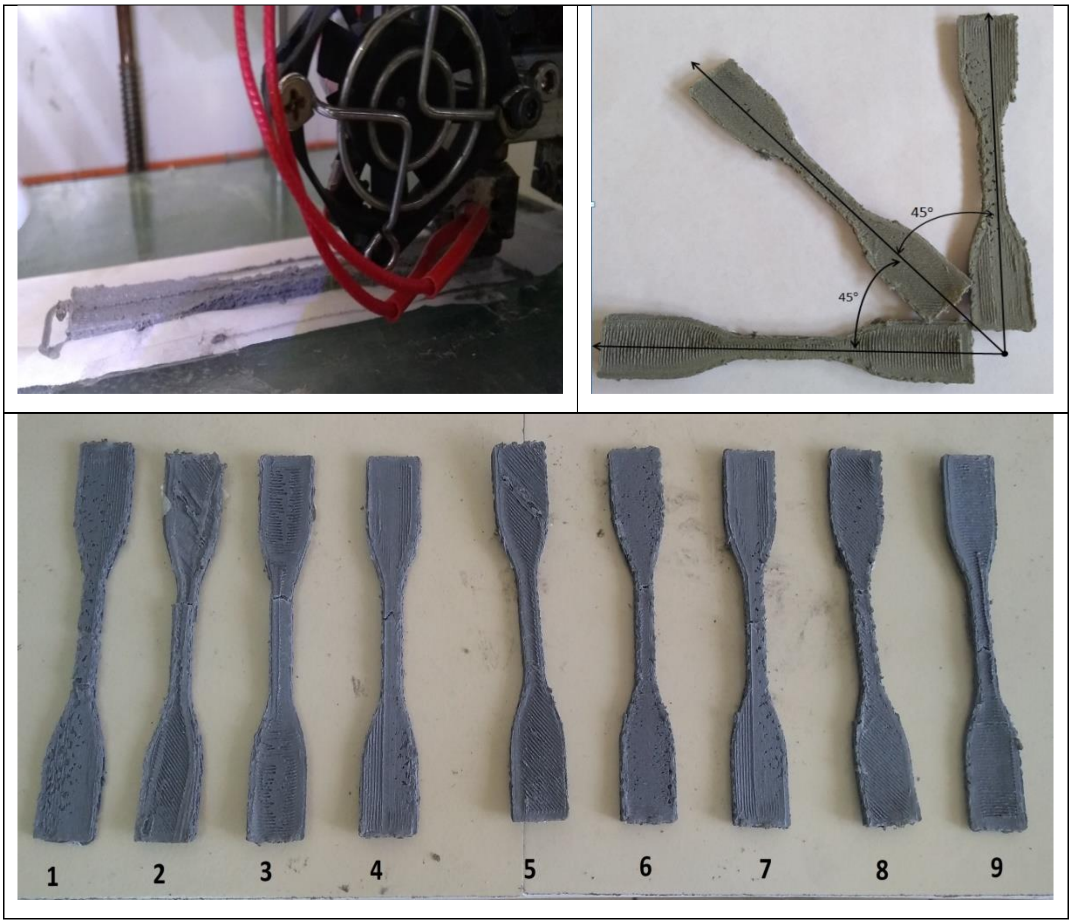

Figure 4.8 (a) 3D printing of specimens, (b) 3D printed tensile samples to depict the effect of IA. and (c) finally printed tensile samples

4.2.3 3D printing of standard flexural specimens

Similar to the tensile specimens, flexural specimens were also 3D printed as per the ASTM D790. The same DOE was used for the fabrication of flexural specimens. the standard dimensions of flexural specimens (in Table 4.9) along with the sketch are shown in Figure 4.9.

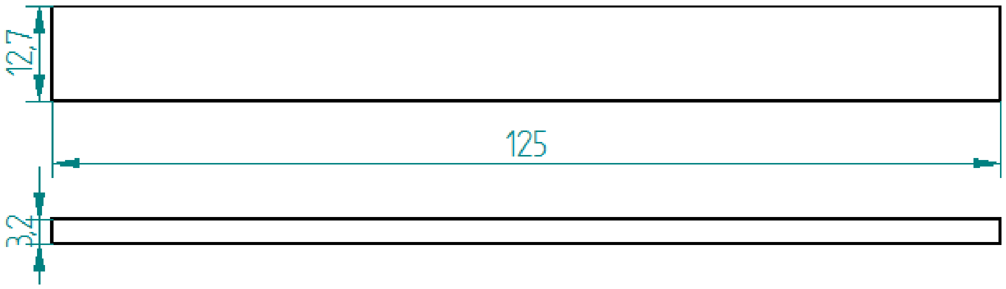

Figure 4.9 Schematic of standard flexural specimen according to ASTM D790-17

Table 4.9 Standard dimensions of flexural specimen according to ASTM D790-17

Size	Dimension
Full length	125 mm
Parallel length	12.7 mm
Thickness	3.2 mm

As per the dimensions shown in Figure 4.9, 3D printing of parts is performed, whereas Figure 4.10 (a) & 4.10 (b) shows the fabricated parts and their orientation of printing respectively. The UTM and flexural testing of specimen used in this research work is shown in Figure 4.12(a)

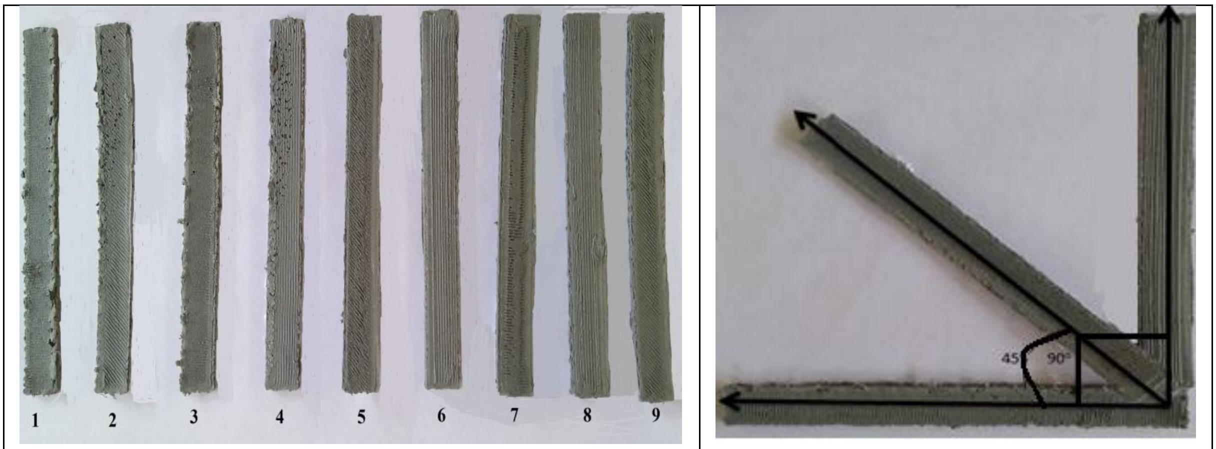

(a) (b)

Figure 4.10 (a) 3D printed parts, (b) orientation of 3D printing of prototypes.

4.2.4 Pull out testing

Similar to flexural testing, experiments were also performed for pull-out testing that is a relative comparison to check out the pull-out strength of the printed parts. For the establishment of pull-out properties of 3D printed samples, an eyebolt screw was used. It was screwed inside the 3D printed specimen with 3 cycles of thread. The schematic of the screwed eyebolt with the specimen is shown in Figure 4.11. To draw the profile of an eyebolt screw, a profile projector was used, and the major dimensions of the screw were pen downed i.e., an outer and inner diameter of the screw, thread angle and pitch, etc. The image drawn with the help of the profile projector is shown in Figure 4.13 at ×25 magnification.

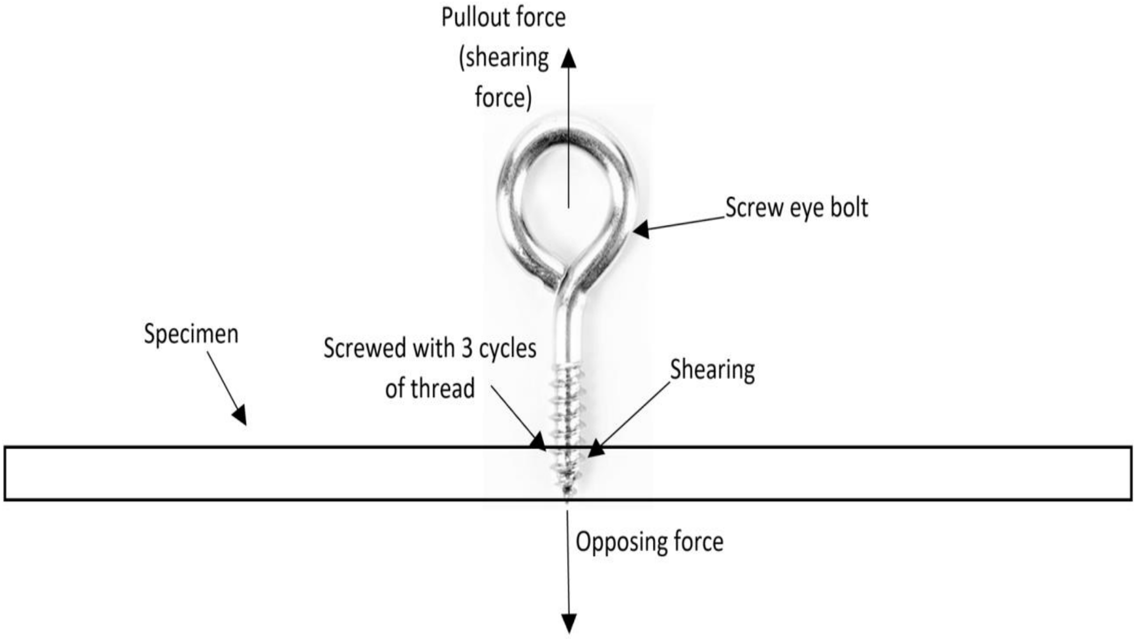

Figure 4.11 Schematic of pull-out test

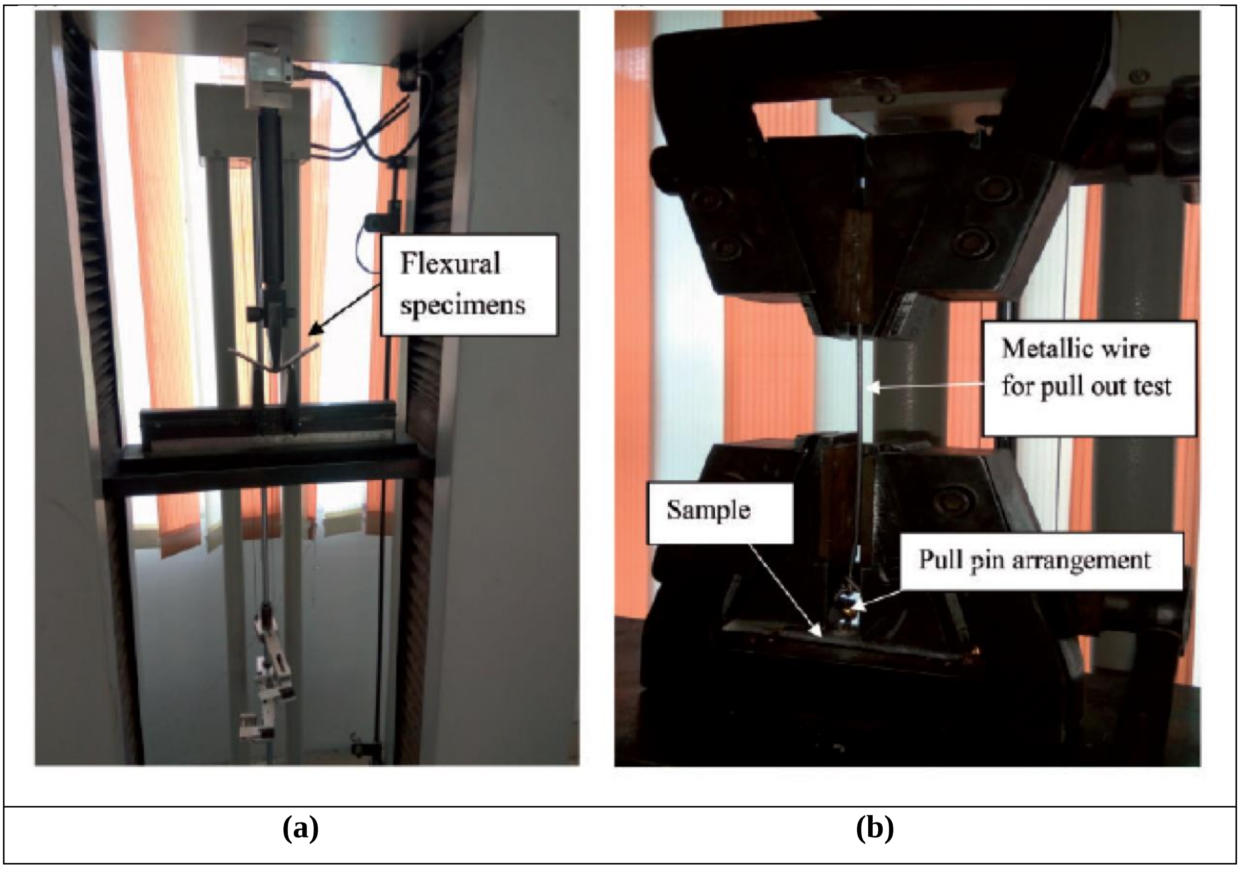

(a) **(b)**

Figure 4.12 (a) Flexural testing and (b) Pull-out testing performed on UTM

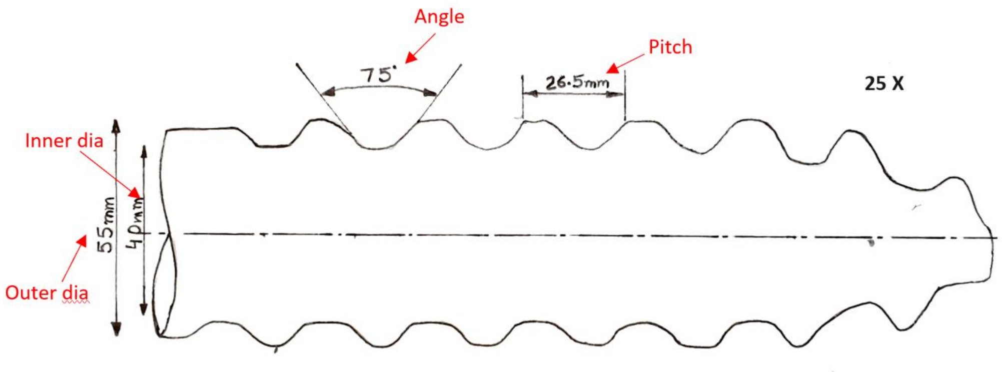

Figure 4.13 Thread profile of a screw drawn with profile projector

The pull-out test was performed on the universal testing machine (UTM) (Make: Shanta Engineering, Pune, India) of 5000N capacity. For the pull-out test, a screw was tightened in the specimen, and pulling (shear) force was applied to the specimen on UTM. Some properties of pull-out test like PL, BL, peak elongations, break elongation were obtained directly from the UTM, whereas some properties like shear strength at peak, shear strength at break, shear modulus, modulus of toughness were calculated using the following mathematical relations.

Where, Outer diameter (D) = 55/25=2.2 mm (since at ×25 magnification was used for measurement)

Inner diameter (d) = 40/25 = 1.6 mm

Pitch (P) =26.5/25 = 1.06 mm

Angle = 75^{o}

As observed from Figure 8, only the first 3 cycles were used for screwing the eyebolt with the specimen.

So, the Area under shear = $3\times(\pi\times D\times P)$

$= 3\times(\pi\times 2.2\times 1.06)$

$= 21.97\ \text{mm}^2$

The shear strength at the peak is calculated with the formula: -

Shear strength at peak = load at peak/area under shear

The shear strength at Break is calculated with the formula: -

Shear strength at Break = load at break/area under shear

The shear modulus is calculated with the formula: -

Shear modulus = shear strength at peak/strain at peak

The modulus of toughness is calculated with the formula: -

Modulus of toughness =1/2 × shear strength at break × strain at break

4.2.5 Shore D hardness of 3D printed parts

To measure the hardness values of the 3D printed parts a shore D hardness tester was used (see Figure 4.14). It gives resulted values up to three decimal places. The measured surface hardness values (shore-D) of the 3D printed parts lying within 63 to 74. The maximum hardness value has been found in experiment no 3. The shore-D hardness value of the confirmatory experiment was 75.2 Shore D i.e., highest values than others.

Figure 4.14 Shore D Durometer used for hardness testing

4.2.6 Surface porosity of 3D printed parts

To ascertain the effect of process parameters of FDM on the surface properties (such as porosity/voids and surface roughness) of 3D printed parts, morphological analysis was performed. For 3D printing of all types of standard specimen's similar process parameters of FDM was used, thus only the surfaces of tensile specimens were subjected to microscopic analysis to determine the surface porosity of parts. A metallurgical microscope was used to capture the photomicrographs of the samples at ×100 magnification. The surface porosity (Φ) of the samples was measured as per ASTM B-276 by commercially available metallurgical image analysis software (MIAS).

4.2.7 Scanning Electron Microscopy (SEM), Energy Dispersive Spectroscopy (EDS) and Area Mapping Analysis

After the mechanical testing of 3D printed specimens (tensile and flexural parts), the samples that showed best and worst tensile and flexural properties were subjected to microscopic analysis on SEM followed by EDS and Area mapping. The JEOL JSM-6510LV SEM (Japan) was used to take the microphotographs of the fractured samples at three different levels of magnification. For SEM analysis the sample should be conductive in nature. Thus, to make the polymeric samples conductive, a gold layer has been coated over its surface. Further, the samples were put into vacuum chambers to capture the microphotographs.

4.2.8 Dynamic Mechanical analysis (DMA)

The dynamic mechanical analysis was used to characterize the material's property with respect to temperature, frequency, stress, or combination of all these parameters. In DMA the viscoelastic behaviour of the material is determined by the stress-strain relations. On the application of strain in the sinusoidal form as an input, as compared with the output response of stress measured by DMA in the form of a sinusoidal curve. For viscoelastic materials, the curve of stress will go out of phase with respect to input strain. The degree to which the curve went out is known as phase angle (delta). Thus, phase angle works as a function of how much the stress response lags the input strain. The results of DMA are generally observed in the form of storage modulus (E'), loss modulus (E''), and tan delta (E''/E'). E' describes the energy storage capacity of material under cyclic loading or we can say stiffness and shape recovery of the polymer during cyclic loading. However tan delta **(δ)** defines the damping of material or dissipation of energy by material under loading conditions. The more the value of tan **δ**, the more mechanical energy will be dissipated by material in the form of an internal molecular motion under the applied load. Thus, it represents that the material having lower tan **δ** and high storage modulus will be stiffer and more load-bearing capacity under the low force cyclic conditions. The materials having high tan δ will dissipate more mechanical energy lead to more damping under cyclic loading. In this research work dynamic mechanical analyzer (Make: Mettler Toledo) a swiss model operated with STARe (S.W 16.30) software was used. Rectangular bar type samples (15 mm length, 6 mm wide, and 2.5 mm in thickness) of MBC of PBG were 3D printed. A single cantilever method of bending was used to evaluate the viscoelastic properties of the developed materials. A controlled force of 1N is dynamically applied at the frequency of 10 Hz. Under this cyclic loading, the sample oscillated at a constant displacement of 10 µm. The force was applied to the samples by using a single cantilever bending method. During the testing, the temperature was increasing from 30°C to 130°C at a rate of 3K/min.

4.3 Experimentation at stage 3

4.3.1 Development of PVDF/Gr/BTO based composite by chemical assisted mechanical blending (CAMB) method

In this stage of research work, the smart polymer-based composites have been prepared by chemical mixing of the materials. Thin films of composites in different proportions have been prepared by mixing the BTO and Gr in the PVDF matrix in the presence of N-N-dimethylformamide (DMF) and dimethyl sulfoxide (DMSO) solvent. DMF is considered the least hazardous among the solvents used for PVDF and has a boiling point of about 153 °C. Dimethyl sulfoxide (DMSO) was added as a β-phase initiating agent [147].The developed composite has been processed and extruded in the form of filament on TSE. Further, to study and optimize the process parameters of TSE for mechanical, dimensional, thermal, and morphological properties of the filament, the Taguchi approach has been used. The developed filament was used to run on open-source FDM to print the standard tensile specimens. Further process parameters of FDM for mechanical properties of 3D printed parts have been optimized.

- **Chemical blending of materials**

This is the second stage of this research work, in this initially, materials have been blended chemically, followed by mechanical blending and extrusion of filament on TSE, therefore, similar three proportions of filler to base materials were taken to ascertain the effect of the blending method on the various properties of extruded filaments and 3D printed parts. The weight percentage of Gr was kept fixed as 2% of the weight of PVDF, whereas; BTO was taken in the range of 10 to 20% of the total weight. Thus, the selected three proportions are shown in Table 4.10.

Table 4.10 Selected different proportion of materials

Composition/Proportion (wt%)	X PVDF (98%) +Gr (2%)	Y BTO
A	90	10
B	85	15
C	80	20

(a) Ultra-sonication process

(b) Stirring of solution

(c) Slurry poured over glass substrate for heating

(d) Thin composite film after evaporation of DMF

Figure 4.15 Setup used in the chemical mixing process

For 20g of the mixture, 2g of BTO was sonicated in DMF for 2 hours for complete dispersion. The quantity of DMF was taken as 1 ml for 0.2 g of BTO. Simultaneously in another vessel, a mixture of 360 mg Gr and 17.64 g of PVDF granules were dispersed in 100 ml of DMF on a hot plate magnetic stirrer for 2 hours. During the magnetic stirring, the temperature of the base plate was kept constant at 50^oC. Both solutions were mixed and 2ml of DMSO was added to it. This nano-composite solution of PBGC was again stirred at the same parameters for the next 30 min. Some amount of Gr and BTO was settled down at the bottom of the liquid slurry. Hence solution was again put on ultra-sonication for 20 mins. For complete evaporation of DMF solvent, the slurry of the mixture was poured over the glass substrate and heated at 100^oC for the next 12 hours inside the oven. A thin film PVDF/Gr/BTO nanocomposite was formed over the glass substrate and can be easily removed from the glass surface. The same procedure has been repeated by maintaining the same solute-solvent ratio for all three compositions/proportions (Table 4.10). The setup used for chemical mixing is shown in Figure 4.15 (a-d).

The complete methodology adopted for chemical mixing is shown in Figure 4.16, in the form of a flow chart.

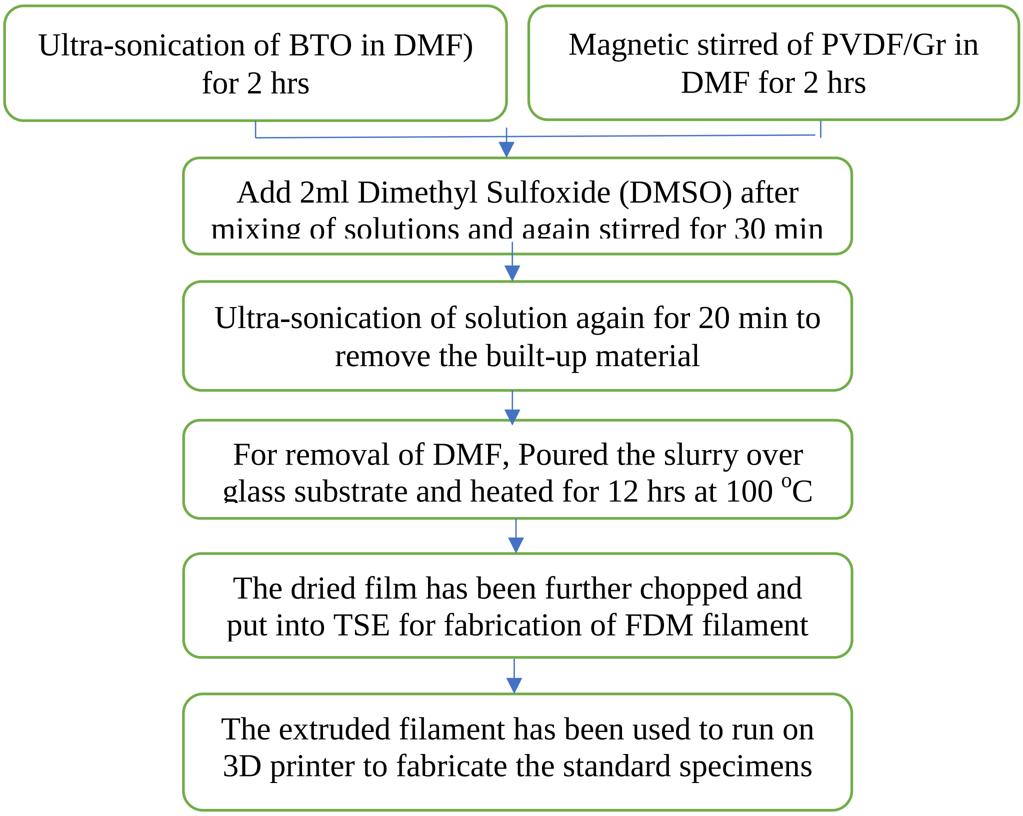

Figure 4.16 Methodology adopted for the synthesis of composites via chemical mixing.

After the successful development of a smart polymer-based composite of PBG via the chemical mixing method, the flow ability of all three compositions was identified. To characterize the rheological properties of the chemically blended material, a MFI test was performed as per the ASTM D-1238. The same procedure as used in mechanical mixing was used to measure the MFI value. The output values of MFI for all three proportions were further used to calculate the viscosity of the developed composites (in Table 4.11). The density of composite shown in Table 4.11 was calculated by the ratio proportion method by taking the values of density of materials mentioned.

Table 4.11 Density, MFI values and viscosity for different compositions/proportions

Composition/ Proportion (wt%)	Density (ρ) g/cm^3	MFI g/(10min) CAMB sample	Viscosity (μ) in (Pa-S) of CAMB sample
A	2.187	3.98	5924.31
B	2.392	3.20	8059.03
C	2.597	2.90	9654.85

Note: Three repeated observations were taken and average value has been quoted.

4.3.2 Fabrication of feedstock filaments of CAMB composites of PBG

After successfully synthesis of nanocomposite films of all three proportions of PVDF/Gr/BTO sheets were cleaved into small sizes. These cleaved parts of the sheets were put into the TSE for the development of feedstock filament. The temperature of the co-rotating screws and extruder's barrel was set according to the melting point of the material. The diameter of the small opening of TSE can be adjusted by changing its die.

For extrusion of feedstock filament of CAMB composites, the same experimental conditions were selected as used for mechanically blended composites. The range of barrel temperature was taken from 180°C to 200°C and the rotation speed of screws was taken in the range of 40-60 rpm. To optimize the process parameters of TSE, a 09 set of experiments (with three repetitions) were performed at different settings of TSE as per Taguchi L9 orthogonal array (OA) (Table 4.12).

Table 4.12: Control log of experiment

Exp No.	Temp (°C)	RPM	Composition
1	180	40	A
2	180	50	B
3	180	60	C
4	190	40	B
5	190	50	C
6	190	60	A
7	200	40	C
8	200	50	A
9	200	60	B

The PBGC prepared with chemical blending has been fed to the TSE setup (as per Table 4.12). The feedstock filaments extruded from TSE were collected for further testing.

4.3.3 Tensile Testing of feedstock filaments

The 9 sets of filaments of chemically blended composites of PBG were subjected to tensile testing to determine the mechanical strength of the feedstock filaments. The same UTT used for testing mechanically blended feedstock filaments was used for the destructive testing process.

4.3.4 Dimensional Analysis

After the extrusion process, filaments were also tested for dimensional properties of the developed feedstock filament. Each filament was measured at three places throughout its length to predict the more accurate average diameter with the least variation. The filament shown best mechanical strength and having a diameter in the range of 1.75±0.05 mm was used to run on the existing open-source 3D printing machine.

4.3.5 Surface analysis

After mechanical and dimensional analysis, the surface porosity of fabricated feedstock filaments was investigated. Feedstock filaments having smooth surfaces may also run continuously in FDM machines. To check the surface porosity a metallurgical microscope was used to capture the photomicrographs of the samples at ×100 magnification.

4.3.6 Thermal analysis

The feedstock filaments of CAMB composites of PBG shown best and worst mechanical properties were further subjected to DSC testing for their thermal behaviour. For thermal testing, samples weighing the range of 3 mg to 8 mg were prepared from the extruded filaments. To determine the reusability of the material, the sample was subjected to more than one heating and cooling cycle. If similar results are found in the 2nd heating and cooling cycle then the material is said to be thermally stable for reusability.

4.3.7 Morphological analysis of feedstock filaments of PBG composites prepared by CAMB method

After successful investigations of mechanical, dimensional, and thermal properties, feedstock filaments of PBGC prepared by chemical assisted mechanical blending method were further subjected to microscopic analysis on SEM, EDAX and Area mapping. For SEM analysis, microphotographs of fractured surfaces of filaments having the best and worst mechanical properties were taken on the JEOL JSM-6510LV SEM (Japan) at different magnification levels.

4.4 Experimentation at stage 4

4.4.1 3D printing of standard prototypes

The filament comprising PBGC after CAMB with maximum mechanical strength was used run on an open-source FDM printer (Make: Divide by zero, Mumbai, Maharashtra, India). To study the effect of process parameters of FDM, standard tensile specimens were fabricated, as per ISO 527–2 (an international standard for tensile testing of reinforced plastics). Three process parameters IS, IA, and ID were chosen based on pilot experimentation and literature review (as similar were used in 3D printing of parts from feedstock filament prepared by mechanical mixing of materials. The other fixed parameters were nozzle diameter: 0.5 mm, the temperature of the bed: 85 °C, fan output: 50%, and fill pattern: rectilinear, and so on. For the optimization process, each selected process variable was further divided into three levels. To optimize the process parameters by performing a minimum number of experiments, again, Taguchi L9 OA was used. For all selected nine settings, 3D printing of standard tensile specimens as per ASTM D638 IV was performed with three repetitions. Further similar settings of FDM were used for 3D printing standard flexural specimens (as per ASTM D 790). Flexural specimens were fabricated at all 9 alternative settings. Pull–out specimens were also 3D printed as per Taguchi L9 orthogonal array.

4.4.2 Destructive testing of 3D printed parts

The 3D printed dumbbell-shaped specimens, of PBGC, were subjected to destructive tensile testing as per the ASTM D 638 (International standard for tensile testing of reinforced plastics) at room temperature. Destructive testing of the specimens was performed on UTM. The output of tensile testing in the form of PL, BL. PS and BS were noted. The stress-strain curves were plotted to understand the mechanism of deformation of the material. To optimize the tensile strength of the 3D printed parts, (ANOVA), a statistical tool, has been used.

Similar to the tensile parts, the flexural and pull-out specimens were also subjected to destructive testing. For flexural testing same UTM machine was used with different types of fixtures. The results of flexural testing were noted in the form of PL, BL, PS, BS, flexural modulus (FM), and modulus of toughness (MoT). Further the results of flexural testing were optimized by using a statistical tool ANOVA.

Similar to flexural testing, experiments were also performed for pull-out testing that is a relative comparison to check out the pull-out strength of the printed parts. For the establishment of pull-out properties of 3D printed samples, an eyebolt screw was used. It was screwed inside the 3D printed specimen with 3 cycles of thread. The dimensions of the screw threads are shown in Table 4.13.

For the pull-out test, the screw was tightened in the specimen, and pulling (shear) force was applied to the specimen on UTM. The results obtained from the pull-out test in the form of PL, BL, shear strength at peak, shear strength at break, shear modulus, and MoT. The process parameters of FDM were further optimized for pull-out properties by using an ANOVA tool.

Table 4.13 Thread profile of a screw

S. No.	Terminology	value
1.	Outer Diameter	2.2 mm
2.	Inner Diameter	1.6 mm
3.	Pitch	1.06 mm
4.	Thread angle	75^o

.

4.4.3 Surface properties analysis

The surface porosity of 3D printed parts was ascertained with a metallurgical microscope. Photomicrographs of the surfaces of the 3D printed specimen were taken at x100 magnification. The surface porosity (Φ) of the samples was measured as per ASTM B-276 by commercially available metallurgical image analysis software (MIAS).

4.4.4 SEM, EDS and Area Mapping Analysis of fractured surfaces of 3D printed parts

After the destructive testing of 3D printed specimens (tensile and flexural parts), the samples have shown the best and worst tensile and flexural properties were subjected to microscopic analysis on SEM. The JEOL JSM-6510LV SEM (Japan) was used to take the microphotographs of the fractured samples at three different levels of magnification. For

4.4.5 DMA

FDM process parameters are shown best and worst flexural properties were used for the fabrication of specimens for DMA testing. The rectangular bar type samples (15 mm in length, 6 mm wide, and 2.5 mm in thickness) of chemically blended composites of PVDF/Gr/BTO were 3D printed. The dynamic mechanical analyzer (Make: Mettler Toledo) a swiss model operated with STARe (S.W 16.30) software was used. DMA tesing was performed under similar condition used for samples prepared MB composites.

4.5 Experimentation at stage 5

4.5.1 3D printing of cylindrical disc

The optimized process parameters of FDM on stage 2 and stage 4 were further used for 3D printing of cylindrical discs. The PVDF/BTO/Gr nano-composite filament prepared by MB and CAMB method, having the best mechanical and thermal properties were used to run at optimized settings of FDM (Make: Divide by zero) for fabrication of cylindrical discs having a diameter of 10 mm and thickness of 0.4 mm. The temperature of the extruder head and the bed were kept at 260°C and 80°C respectively. Initially, a CAD model of the disc has been created in the Solid work's software. Then this file was saved in STL format. K-slicer software has been used to slice the .STL files into layers and generate the G-Codes for machine processing. Further, this sliced file has been sent to FDM setup to fabricate a cylindrical disc. Figure 4.17 3D printed cylindrical disc for piezoelectric characterization of the composite.

Figure 4.17 3D printed disc

4.5.2 Electrical poling process

These cylindrical discs were further prepared for the electrical poling process. Silver paint is coated on both sides of the disc to make it conductive. The type of silver paint used depends upon the temperature of the working environment. A high voltage electric supply was passed through the disc for poling the sample. To avoid any type of electric breakdown, the disc was dipped in silicone oil at a high temperature. This will also accelerate the transformation of the PVDF β-phase, as indicated by extensive research. High temperature resistive silver paint was coated on both sides of the disc. This coated disc was then placed in between the copper electrodes of poling unit. This poling unit supplies a very high electric field of 35kV/mm. As BTO powder requires only 3.5 kV/mm, thus to avoid any electric breakdown the sample was dipped in the silicon oil at 120 °C, which also helps to quick initialize the polarization process. The entire poling process was run for 3 hours on the 3D printed disc.

4.5.3 Material characterization

4.5.3.1 XRD Analysis

XRD is a fast-analytical technique that is mainly used for compound and phase identification of a crystalline material (solid/powder form). It also provides detailed information on unit cell dimensions. As PVDF is a semi-crystalline material with no more than 50-60 % crystal content. PVDF mainly exists in three crystalline phases such as α, β, and ɣ-phases. In this research work, for crystal structure characterization of 3D printed specimens of BTO/Gr/PVDF, X-ray diffraction analysis was performed. The specimen for XRD testing was 3D printed at the optimized settings of FDM. Further for poling, the sample was subjected to a high voltage supply at elevated temperatures. The 3D printed specimen before poling and after poling was analyzed through XRD (Figure 16). The observed spectrums have been matched with standard directory cards (for PVDF and BTO the ICDD/JCPDS:00-038-1638 and ICDD/JCPDS: 01-079-2264 were used respectively).

4.5.3.2 FTIR Analysis

FTIR spectroscopy is normally using for fast and accurate identification of compounds such as adhesives, fillers, thermoplastic polymers, paints, resins, coatings, blends, compounded plastics, rubbers, and reinforced thermoplastic polymers. FTIR spectroscopy is the most effective tool for determining the surface composition in chemical form. The absorbance of a sample to an incident infrared spectrum with the range of 600 to 4500 cm^{-1} constitutes the analysis. FTIR's are also most effectively observed and explain regarding incomplete polymerization when it has compared with a standard specimen. FTIR is also be used for imaging and microscopy of particle and rubber interfacial modification. For this research work FTIR machine (Model: INFRA 3000B FTIR manufactured by: - Analytical) has been used.

4.5.4 Piezoelectric characterization

The piezoelectric property of BTO/Gr/PVDF-based 3D printed films can be characterized by measuring the d_{33} by using a two-probe method. A d_{33} meter (Model YE2730A D33 make: Marine India) has been used with a high degree of resolution i.e. 0.1 pC/N. This meter is capable of direct measurement of the piezoelectric constant of piezoelectric crystals, ceramics, and polymeric. Although, any type of sample can be easily used to measure piezoelectric constant, but the disk type sample is more preferable. In this study, 3D printed cylindrical disc having a diameter of 10 mm and thickness is 0.4 mm was used for testing. To make the 3D printed specimen a good conductor of electricity, a layer of conductive silver paint has been coated on both sides of the cylindrical disc. The prepared disc has been placed under the probes, and then the knob has been rotated until it tightens the disc properly. After that switch on the meter, that displays the digital value of d_{33} in pC/N.

The experimentation performed for the completion of this research work has been completely described in this chapter. Further, the results obtained from the whole experimentation work have been discussed in chapter 5.

CHAPTER 5

RESULTS AND DISCUSSION

In this chapter, the results obtained from experiments conducted at different stages have been discussed. An ANOVA has been used to optimize the process parameters of TSE and FDM for the fabrication of feedstock filaments and functional prototypes at 95% confidence level. The process variables have been optimized on the basis of mechanical, thermal, morphological, and piezoelectric properties of MB and CAMB composites of PVDF/Gr/BTO. The results of this study are as follows:

- **Selection of best proportion of Gr-BTO as reinforcement in EAP PVDF**

In the pilot experimentation, efforts were made to select the best proportion of filler particles in the base polymer matrix based on the flowability of the developed composite. Smart materials based on BTO and Gr nano powder were reinforced in the smart polymer-based PVDF matrix for possible sensor applications. Initially, BTO and Gr powders were added separately in PVDF to determine their effect on the flow-ability of the PVDF. From the pilot experimentation, three different proportions were selected based on MFI, so that the developed composite can easily flow through the TSE with uniform diameter formation.

5.1 Results and discussion (Stage 1)

5.1.1 MFI of mechanically blended compositions of PVDF/Gr/BTO

Based upon the MFI testing conducted in the pilot experimentation, Gr was added 2% by weight in PVDF matrix, whereas BTO was reinforced up to 20% by weight in PVDF + Gr + BTO composite matrix. It has been observed that as BTO proportion is increased from 0 to 20 the MFI value of PVDF composite matrix is decreased. Based on MFI testing, three different proportions of PVDF/Gr/BTO were selected for the fabrication of feedstock filament using TSE. Table 5.1 shows the proportion of composition by weight and their respective MFI values.

The results of MFI testing ascertain the feasibility of the extrusion of feedstock filament with a uniform diameter. Further the results of MFI were used to determine the viscosity of the composition prepared by mechanical mixing of materials. To calculate the density of composition a ratio proportion method was used. Table 5.2 shows the composition along with the density of the composition in g/cm^3.

Table 5.1 MFI at different proportion of materials

Composition/Proportion (wt%)	X [PVDF (98%) +Gr (2%)]	Y [BTO]	MFI (X+Y) (g/10min)
A	90	10	3.11
B	85	15	2.68
C	80	20	2.32

Table 5.2 Density of different compositions/proportions

Composition/ Proportion (wt%)	Density (ρ) g/cm^3
A	2.187
B	2.392
C	2.597

Note: Three repeated observations were taken and the average value has been quoted.

To calculate the viscosity of all three compositions, density and MFI values were used. as per the following equations

$$\mu = \frac{9.13 \text{ x } 10\text{^}4 \text{ L x } \rho}{1.83 \text{ x MFI}} \quad \text{dynes} - \text{s}$$

or

$$\mu = \frac{9.13 \text{ x } 10\text{^}4 \text{ L x } \rho}{1.83 \text{ x MFI x } 10} \quad \text{Pa} - \text{s}$$

As per the above equations viscosity of the compositions was calculated (shown in Table 5.3).

Table 5.3 Calculated viscosity of all three compositions

Composition/ Proportion (wt%)	Density (ρ) g/cm^3	MFI g/(10min) MBD sample	Viscosity (μ) in (Pa-s) MBD sample
A	2.187	3.11	7581.59
B	2.392	2.68	9622.73
C	2.597	2.32	12068.57

5.1.2 Tensile testing of feedstock filaments prepared by a mechanically blended method

Feedstock filaments of MBC of PVDF/Gr/BTO prepared as per design of experiments were subjected to tensile testing. The tensile testing was performed on UTM (Make Shanta Engineering, India) by using a load cell of 10 kN with an accuracy of 0.5N. The results of tensile testing in the form of peak load (PL), break load (BL), peak strength (PS), and break strength (BS) are shown in Table 5.4).

Table 5.4 Results of tensile testing of feedstock filaments

EXP. NO.	PL (N)	BL (N)	PS (MPa)	BS (MPa)
1	46.95±2	41.32±1.9	19.57 ±1.09	17.21±1.05
2	54.64±3.2	49.87±3.1	22.34±1.09	20.40±1.05
3	63.61±3.8	59.52±3.7	26.50±0.62	24.80±0.87
4	56.50±2.8	51.10±2.7	23.59±0.90	21.24±0.83
5	67.56±3.3	61.66±3.4	28.15±0.92	25.69±0.45
6	52.56±2.1	43.86±2	21.90±1.78	18.28±2.12
7	70..97±2.5	63.60±2.4	29.57±0.93	26.50±1.19
8	55.02±1.4	47.70±1.5	22.92±0.62	19.85±1.18
9	58.97±2.2	53.69±2.0	24.57±0.87	22.37±0.80

The stress-strain curves obtained from tensile testing of feedstock filaments are shown in Figure 5.1.

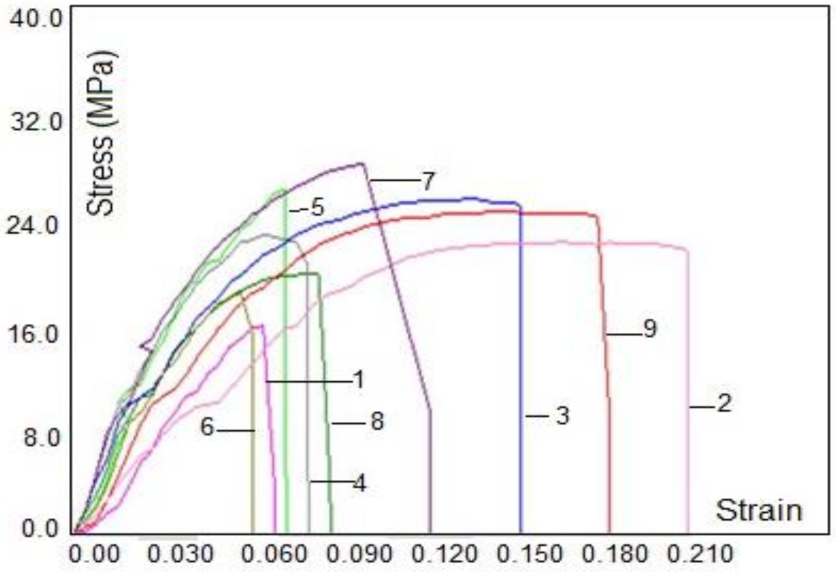

Figure 5.1 Stress-strain curves for the prepared feedstock filament.

Further the results of tensile testing were used to obtain the fracture toughness of the material i.e., area under the curve or energy absorbed. It has been calculated from the BS of the material and strain of the developed composites observed in tensile testing. MoT of extruded filaments is shown in Table 5.5.

Table 5.5 MoT of extruded filaments

EXP. NO.	Strain	BS (MPa)	MoT (MPa) (1/2×strain×BS)
1	0.049	17.21	0.43
2	0.197	20.40	2.01
3	0.148	24.80	1.84
4	0.696	21.24	0.74
5	0.064	25.69	0.82
6	0.049	18.28	0.45
7	0.109	26.50	1.45
8	0.082	19.85	0.81
9	0.179	22.37	2.01

Further to optimize the process parameters Minitab 17.00 software has been used. For these mechanical properties, the signal-to-noise (SN) ratios at larger the better type case is shown in Table 5.6. To calculate the optimum values of mechanical properties ANOVA a statistical tool was used.

Table 5.6 SN values for PL, BL, PS and BS

PL (SN)	BL(SN)	PS(SN)	BS(SN)
33.43	32.32	25.81	24.71
34.75	33.96	27.15	26.35
36.07	35.49	28.47	27.88
35.04	34.17	27.44	26.56
36.59	35.80	28.99	28.19
34.41	32.84	26.81	25.23
37.02	36.07	29.41	28.46
34.81	33.57	27.20	25.96
35.41	34.60	27.80	26.99

5.1.3 Optimization for PS

Figure 5.2 shows the SN response for PS. The SN graph represents that the proportion of materials shows a remarkable effect when changed from level 1 to level 3. Two parameters of TSE were selected and from the SN graph, it has been found that only one out of two parameters put a significant effect on the PS of the specimen. As the weight percentage of BTO in the PVDF and Gr was increased from 10 to 20, the PS also increases. In the case of temperature when it was raised from 180 to 200°C, the PS increases, it may be due to uniform mixing of the fillers in the polymer matrix at high temperature. The rpm of the screws remains near to the mean value and shows not a major effect on the strength at peak of the specimen.

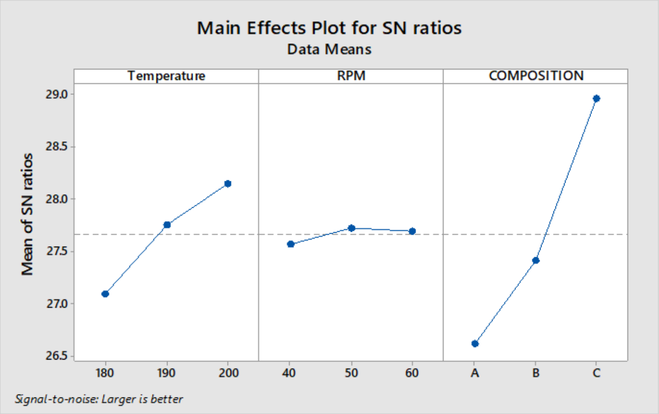

Figure 5.2 SN responses for PS

The analysis for SN values was carried out at a 95% confidence level. The value of 'P' is 0.05 at 95% confidence level in standard table. It means the parameters having an 'P' value of less than 0.05 are significant otherwise insignificant. ANOVA of SN ratios for PS (Table 5.7) shows that two parameters, composition, and temperature are significant at a 95% confidence level. The composition has a major contribution towards the PS i.e. more than 82%, whereas temperature has a 16% contribution. The rpm is found insignificant and the total percentage error was only 0.63%, which represents the higher level of accuracy in this model.

Table 5.7 ANOVA for SN ratios (PS)

Factor	DoF	Seq. SS	Adj SS	Adj MS	F	P	%C
Temperature	2	1.6902	1.69022	0.84511	25.98	0.037	16.40
RPM	2	0.0417	0.04166	0.02083	0.64	0.610	0.41
Composition	2	8.5044	8.5044	4.25220	130.72	0.008	82.56
Residual Error	2	0.0651	0.0651	0.03253			0.63
Total	8	10.3013					

DoF: degree of freedom; Seq SS: sum of squares; Adj SS: adjusted sum of squares; F: Fisher value; P: probability, %C: percentage contribution

Response table shown in Table 5.8 displays the ranks of input process parameters on the basis of the SN ratio for PS. Observed results show that composition majorly affects the PS of the filament.

Table 5.8: Response table for SN ratios at larger the best

Levels	Temperature	RPM	Composition
1	27.09	27.57	26.61
2	27.75	27.73	27.41
2	28.14	27.69	28.96
Delta	1.05	0.16	2.34
Rank	2	3	1

5.1.3.1 Prediction of PS

To calculate the optimized value following equation has been used:

$$\eta_{opt} = m + (m_{A3}–m) +(m_{B2}–m) +(m_{C3}–m)$$

where overall mean value of SN ratios is ‘m’, MINITAB has been used to obtain the value of ‘m’. m_{A3} is mean of SN values for temperature at level 3 and m_{B2} and mc_3 are mean of SN values for RPM and composition at level 2 and level 3 respectively.

$yopt^2 = (1/10)^{\eta opt/10}$ for properties where, lesser is better

$yopt^2 = (10)\eta_{opt}/ 10$ for properties where, largest is better

So, m= 27.66.

Now from the Table 5.8

$m_{A3} = 28.14$, $m_{B2} = 27.73$ and $m_{C3} = 28.96$.

η_{opt} =27.66+(28.14-27.66)+(27.73-27.66)+(28.96-27.66).

Now η_{opt}= 29.51 dB

$y_{opt}^2 = (10)^{\eta opt / 10}$

$y_{opt2} = (10)^{29.51 / 10}$

$y_{opt} = 29.88$

The calculated value for strength at the peak is 29.88 MPa. The confirmatory experiment was conducted at best-suggested settings (Figure 5.2) i.e. 200 °C processing temperature, 50 rpm, and composition/ proportion ‘C’ (as per Table 5.4) and the observed value is 29.92 MPa which is very close to the observed value).

5.1.4 BS

The SN response graph for BS is shown in Figure 5.3. The results are similar to the previous case of PS.

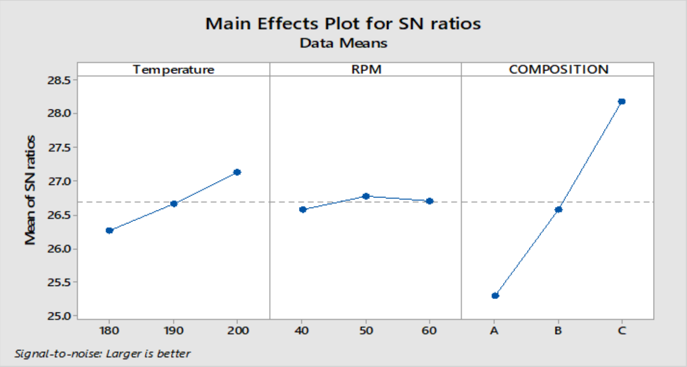

Figure 5.3 SN responses for BS

The ANOVA at 95% confidence level for SN response is shown in Table 5.9 (a).

Table 5.9 (a) ANOVA for SN ratios (BS)

Factor	DoF	Seq. SS	Adj SS	Adj MS	F	P	%C
Temperature	2	1.1444	1.1444	0.57218	21.74	0.044	8.32
RPM	2	0.0657	0.0657	0.03285	1.25	0.445	0.47
Composition	2	12.4941	12.4941	6.24705	237.31	0.004	90.82
Residual Error	2	0.0526	0.0526	0.02632			0.38
Total	8	13.7569					

Table 5.9(b) is the response table to shows the rank of process parameters as per SN ratios of BS. Table values suggest that composition puts a major effect on the BS with rank 1, whereas temperature stood 2nd followed by rpm with least effect.

Table 5.9 (b) Response table for SN ratios at larger the best

Levels	Temperature	RPM	Composition
1	26.27	26.57	25.30
2	26.66	26.78	26.58
3	27.14	26.71	28.18
Delta	0.87	0.21	2.88
Rank	2	3	1

5.1.4.1 Prediction of BS

To calculate the optimized value following equation has been used.

$\eta_{opt} = m + (m_{A3}–m) +(m_{B2}–m) +(m_{C3}–m)$

where the overall mean value of SN ratios is 'm', MINITAB has been used to obtain the value of 'm'. m_{A3} is the mean of SN values for the temperature at level 3 and m_{B2} and m_{C3} are the mean of SN values for RPM and composition at level 2 and level 3 respectively.

$yopt^2 = (1/10)^{\eta opt/10}$ for properties where, lesser is better

$yopt^2 = (10)^{\eta opt/10}$ for properties where, largest is better

So. m= 26.68

Now from the Table 5.9 (b)

$m_{A3} = 27.14$, $m_{B2} = 26.78$ and $m_{C3} = 28.18$

$\eta_{opt} =26.68+(27.14-26.68)+(26.78-26.68)+(28.18-26.68)$

Now $\eta_{opt}= 28.74$ dB

$y_{opt}^2 = (10)^{\eta opt / 10}$

$y_{opt2} = (10)^{28.74 / 10}$

$y_{opt} = 27.35$

The calculated value for BS is 27.35 MPa and the observed value is 27.42 MPa which is very close to the observed value.

5.1.5 Surface porosity

To ascertain the effect of processing conditions on the surface properties (such as porosity/voids and surface roughness) of the extruded filaments, morphological analysis was performed. A metallurgical microscope was used to capture the photomicrographs of the samples at ×100 magnification. The surface porosity (Φ) of the samples was measured as per ASTM B-276 by commercially available metallurgical image analysis software (MIAS). Figure 5.4 shows the photomicrographs of the surfaces of the filaments with the percentage of Φ on the surface. The red zone shows the porosity in the captured area for the analysis of percentage porosity. It has been observed from the photomicrograph's filament shown maximum tensile strength has less porosity (Φ=4.93%) on its surface as compared to the other filaments. Whereas the filament having poor mechanical properties is having more percentage of porosity (Φ=8.98%). Thus the results of porosity are in line with the results of mechanical testing.

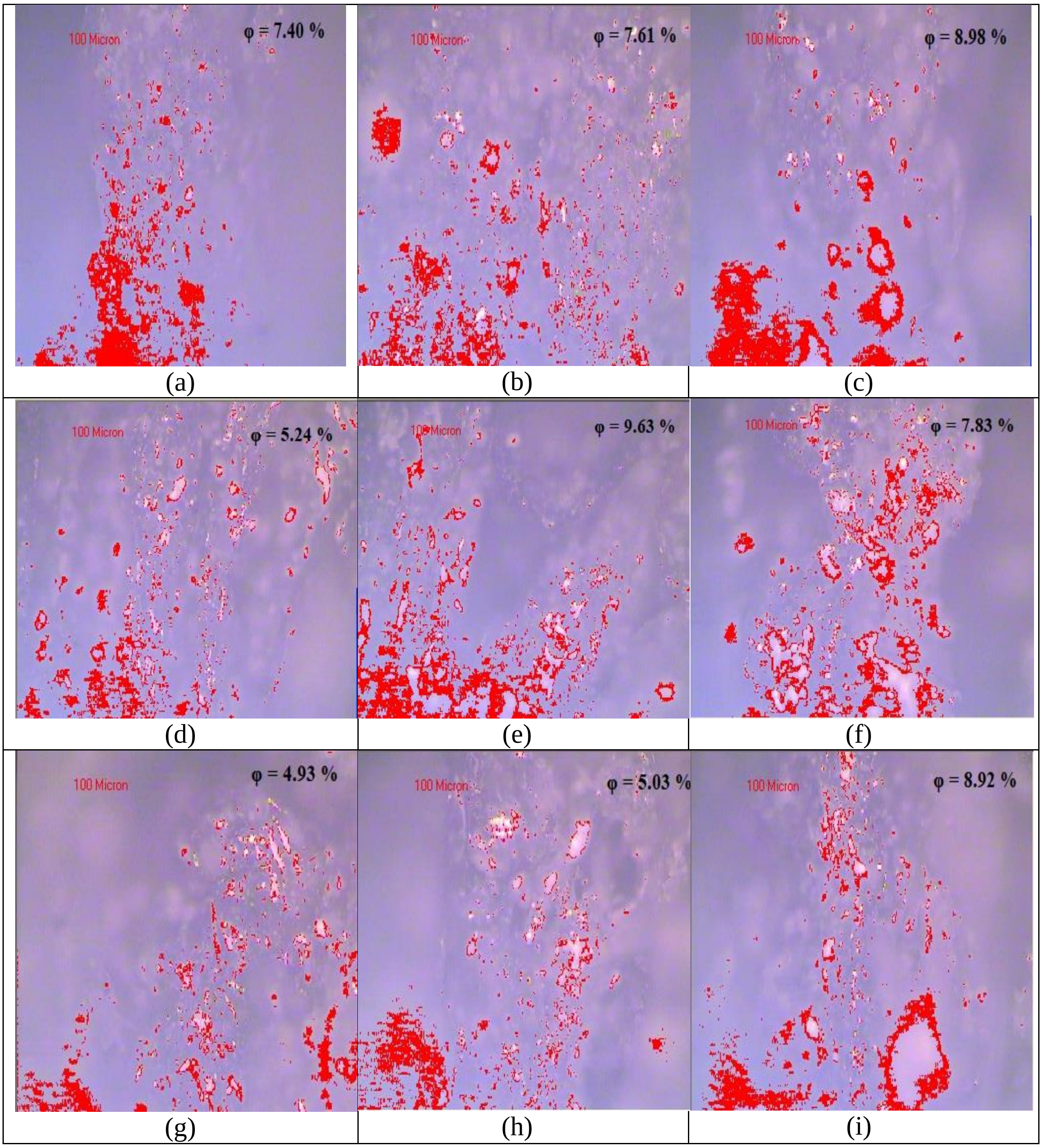

(a) (b) (c)

(d) (e) (f)

(g) (h) (i)

Figure 5.4 Surface porosity of all the extruded filaments

5.1.6 Dimensional analysis

As existing FDM setup supports only the filament having a diameter within the range of 1.75±0.05mm. Thus, it was necessary to perform the dimensional analysis of the extruded filaments. Therefore, after the extrusion of feedstock filaments as per the different processing parameters, they were subjected to dimensional measurement. To minimize the experimental error, a total of three readings were taken at three different places over the total span length of the filaments. The average diameters (Ø) of the three measured dimensions were compared with the required standard diameter of the filament. Measured dimensions of the filament and their comparison with the standard dimensions are shown in Table 5.10. It has been observed that the filament extruded as per experiment No. 7 and 8 has minimum deviation, whereas the filament extruded as per experiment no. 3 has maximum deviation. These observations are in line with the results of mechanical testing.

Table 5.10 Measured dimensions of the extruded filaments

Exp. No.	Parameter(A) *Temperature (℃)*	Parameter(B) *RPM*	Parameter(C) *Composition wt%*	Ø Avg (mm)	Ø (required) (mm)	ΔØ
1	180	40	A	1.68	1.75	0.07
2	180	50	B	1.65	1.75	0.10
3	180	60	C	1.62	1.75	0.13
4	190	40	B	1.72	1.75	0.03
5	190	50	C	1.77	1.75	0.02
6	190	60	A	1.79	1.75	0.04
7	200	40	C	1.74	1.75	0.01
8	200	50	A	1.76	1.75	0.01
9	200	60	B	1.78	1.75	0.03

5.1.7 Thermal Analysis

Thermal behaviour also plays a dominant role in the selection of material for particular applications. After optimization of mechanical strength of the extruded filament wire, it has been observed that the filament extruded as per the settings suggested i.e. 200°C processing temperature, 50 rpm and composition/ proportion ‘C’ has the best mechanical strength. As PVDF is well known for its high thermal resistance properties, therefore, some investigations are also needed to find the effect of reinforcement on the thermal properties of the PVDF.

To establish the thermal properties of the pure PVDF and feedstock filament comprised of PVDF, BTO and Gr were subjected to DSC analysis. In this research work, a total of three samples were prepared, the first sample was taken from the virgin PVDF and second and third sample was taken from the filament possessing the best and worst mechanical strength respectively. To measure the thermal transition, DSC (Make: METTLER TOLEDO, Swiss) operated with A STAR^{e} (SW 14.00) the software has been used,

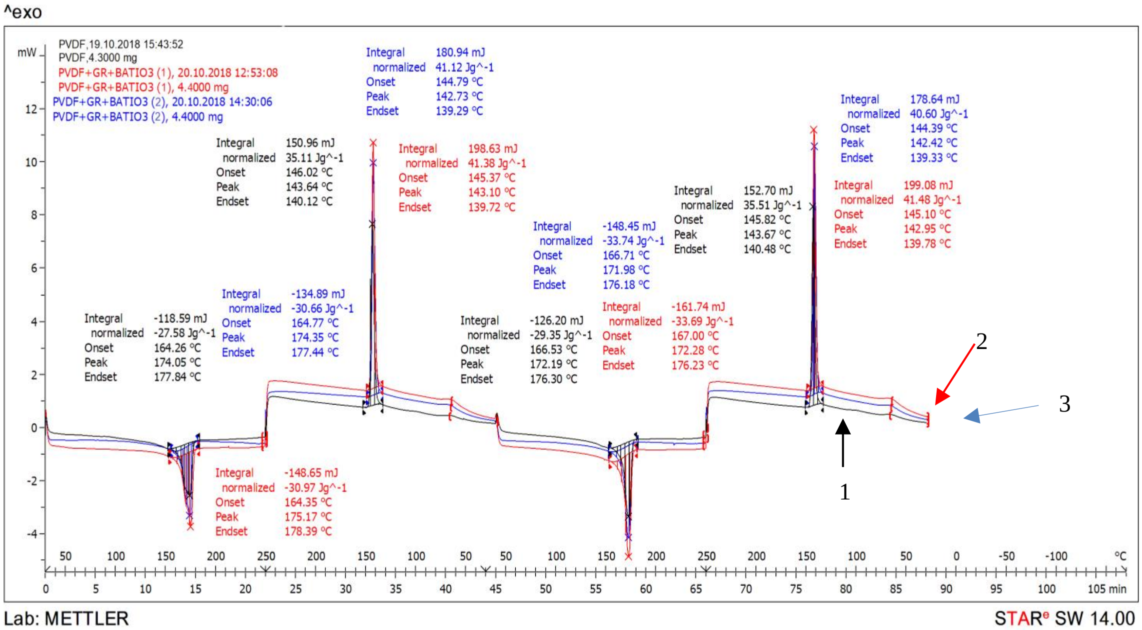

Figure 5.5: DSC graphs of virgin PVDF and composites developed by reinforcement of BTO and Gr in PVDF at different proportions

Figure 5.5 compares the thermal graphs of all three different samples; curve 1 is of pure PVDF and whereas curve 2 and curve 3 are for filament having best mechanical properties (prepared at 200°C processing temperature, 50 rpm and composition/ proportion 'C) and worst mechanical properties respectively. Thermal analyses were performed at two successive heating-cooling cycles, having a temperature range of 30℃ to 250℃, and the heating rate was set at 10K/min. The whole experimentation was performed under a controlled N_2 gas environment. In the first thermal cycle of curve 1 (virgin PVDF), it has been observed that there is a valley that starts at 164℃ and ends at 177℃, the melting point of the PVDF is at 174℃. During cooling, the solidification starts at 146℃ and ends at 140℃. The same trend has been seen in the 2nd cycle of the treatment and a negligible change in melting of the material has been observed. Therefore, the DSC results for virgin PVDF supports that it is thermally stable. The DSC curves of sample 2 (prepared at 200°C processing temperature, 50rpm and composition/ proportion 'C') best sample from mechanical properties viewpoint and sample 3 (poor sample from mechanical properties viewpoint) clearly represent that the melting and solidification temperature of the prepared composite is almost similar to the corresponding temperatures of virgin PVDF. This means that the addition of BTO and Gr does not affect the liquefying and freezing temperature of the PVDF. Thus, it has been indicated that even after 2 repeated cycle's behaviour of material has shown remarkable consistency.

In the case of energy absorption rate, in the first thermal cycle, virgin PVDF absorbed only 27.59 Jg-^{1} energy, whereas the sample having more proportion of BTO, absorbed maximum energy 30.97 Jg^{-1}. Moreover, the energy absorption rate in all three samples has been increased in 2nd thermal cycle. Thus, it highlights that the developed composites not only support the reusability, in fact it acts as a thermodynamic sink.

5.1.8 Microscopic analysis

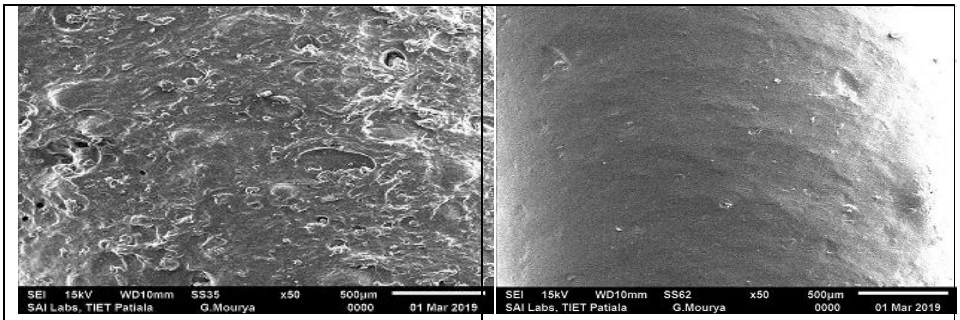

(a) At ×50 | (b) At ×50

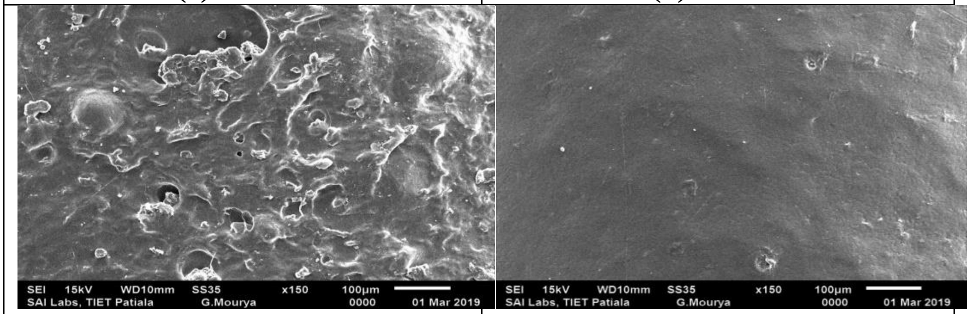

(a) At ×150 | (b) At ×150

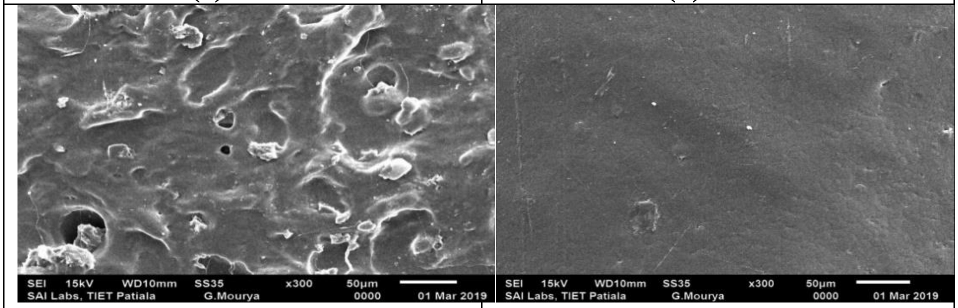

(a) At ×300 | (b) At ×300

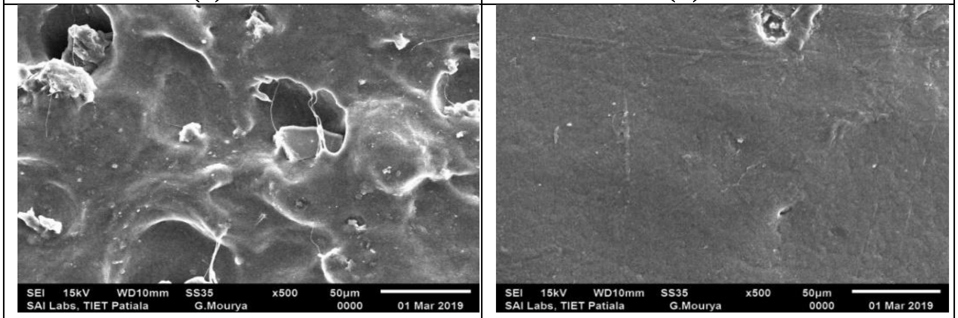

(a) At ×500 | (b) At ×500

Figure 5.6 SEM images of sample having poor and best mechanical properties at four different magnification levels

After successful investigations of mechanical and thermal properties, the specimen of the in-house developed feedstock filament comprised of PVDF, BTO, and Gr, having best and worst mechanical strength were subject to microscopic analysis. The microphotographs of the samples were taken on the JEOL JSM-6510LV SEM (Japan) at different magnification levels. As the samples were made up of non-conductive polymer, therefore a coating of gold layer has been made over its surface. SEM images were taken at magnification levels 50x, 150x, 300x, and 500x are shown in Figure 5.6 for a sample having poor mechanical properties and best mechanical properties (prepared at 200°C processing temperature, 50rpm and composition/ proportion ‘C). Micrographs clearly represent that the filament extruded as per the settings suggested i.e. 200°C processing temperature, 50 rpm, and composition/ proportion ‘C has a fine surface finish as compared to the specimen extruded as per experiment no. 1. It has been observed that the sample extruded at 200°C, 50rpm, and having 20% BTO shows better dispersion (at different magnification).

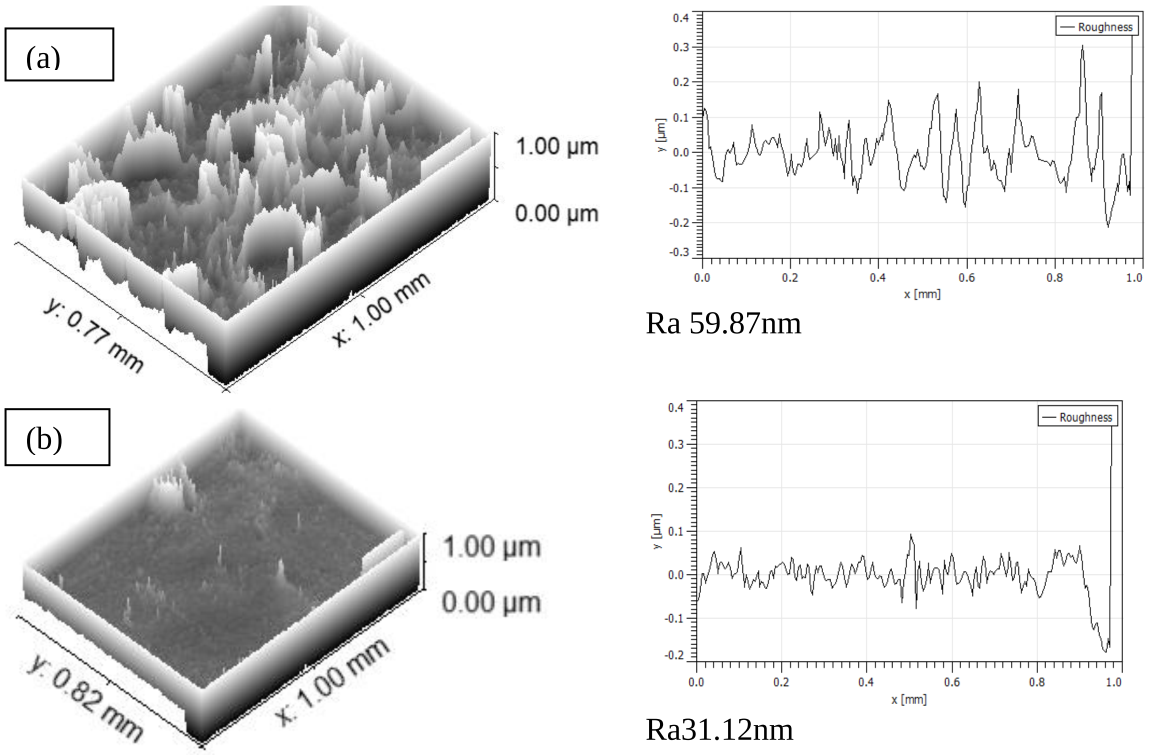

Ra 59.87nm

Ra31.12nm

Figure 5.7 (a) and (b): Rendered SEM images of the extruded samples at worst and best parametric settings.

The rendered images of the SEM at X-500 magnification have been used to measure the surface roughness (Ra) of the extruded samples (as shown in Figure 5.7). It has been found that the Ra value of sample extruded at settings having poor mechanical properties is more than the Ra value of sample extruded settings having the best mechanical properties.

Figure 5.8 (a) and (b) shows the EDX analysis of composite filaments at different proportions of PVDF, BTO, and Gr. The element analysis for the filament having poor mechanical strength shown in Figure 5.8 (a) represents that it contains the majority of carbon and fluoride whereas, it contains very less amount of barium, oxygen, and titanium. On the flip side, the element analysis of the filament having the best-required properties (Figure 5.8 (b) shows that it has more amount carbon, barium, titanium, and oxygen as compared to the previous one. Thus, it has been indicated by the EDX analysis that the addition of BTO and Gr are directly responsible for the enhancement of mechanical and thermal properties of the developed composite.

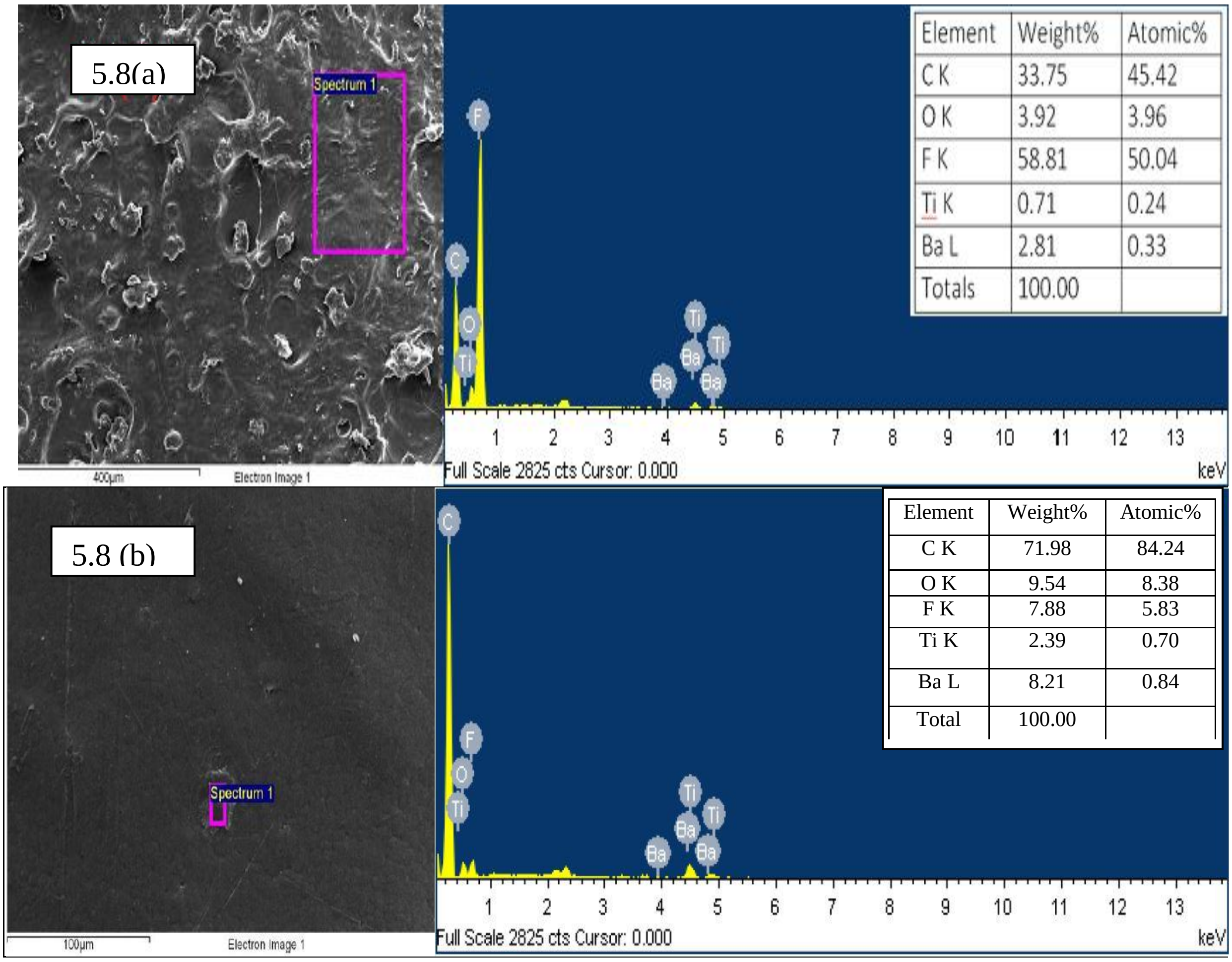

Element	Weight%	Atomic%
C K	33.75	45.42
O K	3.92	3.96
F K	58.81	50.04
Ti K	0.71	0.24
Ba L	2.81	0.33
Totals	100.00	

Element	Weight%	Atomic%
C K	71.98	84.24
O K	9.54	8.38
F K	7.88	5.83
Ti K	2.39	0.70
Ba L	8.21	0.84
Total	100.00	

Figure 5.8 (a) EDX analysis of sample having worst mechanical and thermal properties, **(b)** Sample having best mechanical and thermal properties

Further, the fractured surfaces of feedstock filaments having the best and worst mechanical properties were also subjected to SEM analysis. Morphological analysis of fractured surfaces of feedstock filament was performed by taking microphotographs at various magnification levels of X50, X150, X300, and X500 (see Figure 5.9). It has been observed from the microphotographs that dimple formation occurs at both the surfaces, In case of filament shown best mechanical strength also shows proper joining of fibres over its surface, whereas in case of filament shown poor mechanical strength shows rough and improper fractured surface like not a proper joining in between the fibres/ filler particles with PVDF matric.

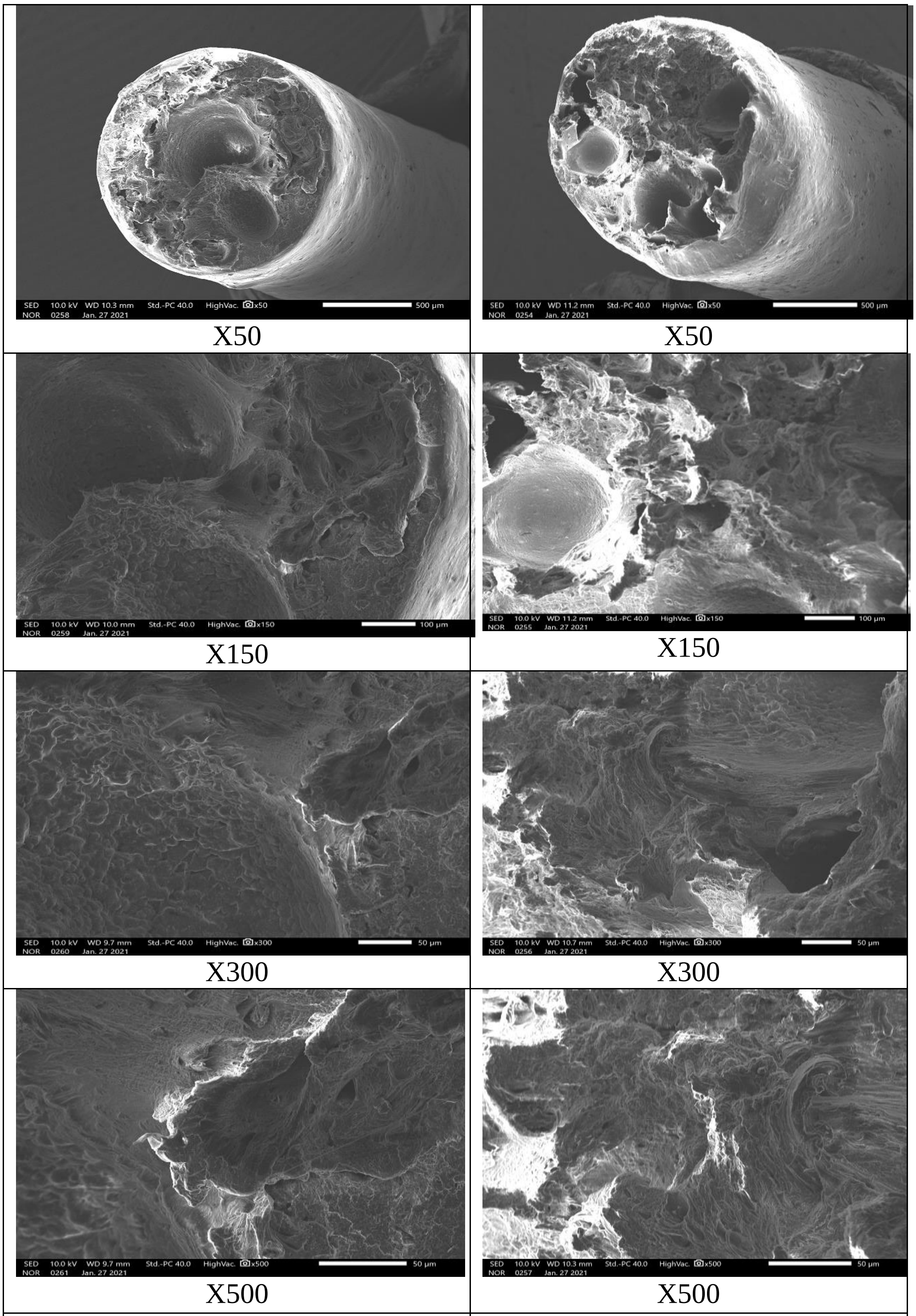

(a) SEM images of MB feedstock filament (best mechanical properties)

(b) SEM images of MB feedstock filament (worst mechanical properties)

Figure 5.9 SEM images of fractured surfaces of feedstock filaments

5.2 Results and discussion (Stage 2)

- **Destructive testing of 3D printed parts for optimization of FDM process parameters**

After the successfully completion of extrusion of feed stock filament by taking a fixed proportion of materials at optimized settings of TSE, by keeping the diameter of the wire at 1.75±0.05 mm, 3D printing of the part has been performed. To optimize the FDM process parameters, standard tensile, flexural and pull-out specimens were 3D printed as per the design of experiments and Further, a mechanical testing was performed on the fabricated structures.

5.2.1 Tensile Testing of 3D printed specimens

3D printed tensile specimens prepared as per control log of experimentation were subjected to destructive testing as per ASTM D-638 standard. The tensile testing of dumbbell shaped specimens was performed on UTM (Make Shanta Engineering, India) by using a load cell of 10KN and accuracy of load cell is 0.5 N. The results of tensile testing in the form of PL, BL, PS and BS are shown in Table 5.11).

Table 5.11 Tensile properties of printed 3D parts

Experiment No.	PL (N)	BL (N)	PS (MPa)	BS (MPa)
1	659±3	632±3	34.32±0.14	32.92±0.13
2	731±7	695±6	38.07±0.38	36.20±0.29
3	770±11	731±10	40.10±0.59	38.07±0.50
4	694±8	663±8	36.15±0.40	34.53±0.41
5	764±8	726±3	39.79±0.39	37.81±0.14
6	630±11	605±10	32.81±0.59	31.51±0.53
7	727±12	694±13	37.86±0.63	36.15±0.65
8	612±7	589±6	31.88±0.36	30.68±0.31
9	638±8	616±8	33.23±0.42	32.08±0.40

The output values obtained from the tensile results shown that the maximum value of PL (770 N) and BL (731N) has been found in experiment no. 3, Whereas the output values of PS and BS for the same experiment are 40.10 MPa and 38.07 MPa respectively. The minimum values of tensile properties were obtained in experiment no 8. In which the observed values of PL is 612 N and BL 589 N. The levels of parameters at which the best values have found are infill speed (IS) 50 mm/s, infill angle (IA) 90° and infill density (ID) is 100%. It may be due to very fine printing happened at very low speed whereas there might be proper bonding in between the layers at no void condition that is 100% ID. However for experiment no. 8

that was conducted at highest IS i.e. 90 mm/s and ID is minimum (60%) among the selected level of values. Thus, it might lead to poor printing at high speed and less strength at low density level.

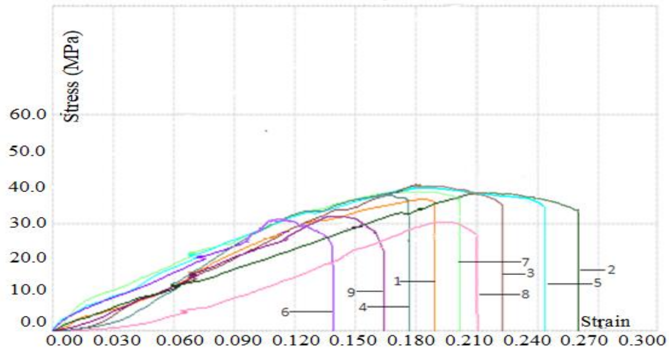

Figure 5.10 Stress-strain curve of 3D printed parts

The stress strain curve obtained from the tensile testing is shown in Figure 5.10. The area under the curve represents the MoT. The calculated values of MoT are shown in Table 5.12. It has been observed that the maximum value of MoT is 4.706 MPa for experiment no. 2.

Table 5.12 MoT of printed parts

Experiment no.	BS (MPa)	Strain	MoT (MPa) (1/2*BS*strain)
1	32.92	0.189	3.111
2	36.20	0.260	4.706
3	38.07	0.223	4.245
4	34.53	0.176	3.038
5	37.81	0.244	4.613
6	31.51	0.143	2.253
7	36.15	0.202	3.651
8	30.68	0.210	3.221
9	32.08	0.168	2.694

To optimize the process parameters of FDM for mechanical properties (PS, BS, PL, and BL) ANOVA method has been used on Minitab statistical software. The ANOVA table for PS is shown in Table 5.13. It represents that there are only two significant parameters that are IS and ID by having P value less than 0.05 whereas in case of IA the P value is not less than 0.05 so it is not found significant at 95 % confidence level. The value of residual error is found to be 0.022 that is only 0.49% of the total value which supports that model used for optimization model is significant.

Table 5.14 shows the rank of input parameters at larger the better condition for SN values of PS. It shows that the most prominent factor that affects mechanical properties of the fabricated parts is ID, followed by the IS at positon 2. Whereas the IA does not shown much effect on the tensile properties of the parts as it is lying around the mean value.

Table 5.13 ANOVA Table for PS

Factor	DoF	Seq.SS	Adj SS	Adj MS	F	P	%C
IS	2	0.912	0.912	0.456	42.42	0.023	20.37
IA	2	0.132	0.132	0.66	6.16	0.140	2.95
ID	2	3.411	3.411	1.706	158.67	0.006	76.19
Residual Error	2	0.022	0.022	0.010			0.49
Total	8	4.477					

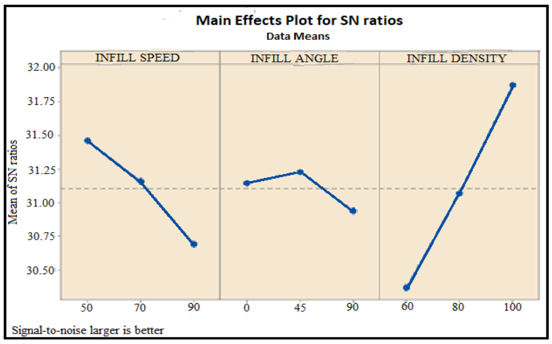

Figure 5.11 Main effects plot for SN ratios

The main graph of SN responses (see Figure 5.11) for PS shows that the first level of IS (50 mm/s), second level of IA (45°) and third level of ID (100%) are best settings of FDM setup for 3D printing of parts of this material.

Table 5.14 Rank table of input parameters (larger the better)

Levels	IS	IA	ID
1	31.46	31.15	30.37
2	31.16	31.23	31.07
2	30.69	30.94	31.87
Delta	0.77	0.29	1.51
Rank	2	3	1

The SN responses obtained from Minitab software has been further used to calculate the optimized values of PS at larger the better status by using the following equations.

$\eta_{opt} = P+(P_A–P) +(P_B–P) +(P_C–P)$ (5.1)

$Y_{opt}^{2} = (1/10)^{\eta opt/10}$ (for lesser the better properties) (5.2)

$y_{opt}2 = (10)^{\eta opt/\ 10}$ (for larger the better properties) (5.3)

Similarly, to calculate the optimized values for BS, PL and BL above mentioned equations have been used.

So, To calculate the optimized value PS following equation has been used:

$\eta_{(opt)} = P + (P_A–P) +(P_B–P) +(P_C–P)$

$Y_{opt}^2 = (10)^{\eta opt/10}$ for properties where, largest is better

P= Mean of SN for PS =31.10

P_A =Max IS from rank table = 31.46

P_B = Max IA from rank table = 31.23

P_C = Max ID from rank table = 31.87

$\eta_{(opt)}$ = 31.10 + (31.46–31.10) +(31.23–31.10) +(31.87–31.10)

$\eta_{(opt)}$ =32.36

$Y_{opt}^2 = (10)^{32.36/10}$

Y_{opt}=42.65 MPa

The calculated value of PS is 42.65 MPa. A confirmatory experiment was performed at the best parametric settings suggested (see Figure 5.10) i.e., IS 50 mm/s, IA 45° and ID is 100% and the observed output value of PS is 42.98 MPa, which is found to be very close to the calculated value.

The contour graphs of PS, BS, PL, and BL are shown in Figure 5.12. Contour plats represent the effect of change in two significant input parameters on the output responses. Contour graphs have drawn by taking the IA constant i.e., 45°. IS is taken in the Y direction and ID was taken in X direction, whereas in z axis it shows the change in values of output response with respect to input parameters.

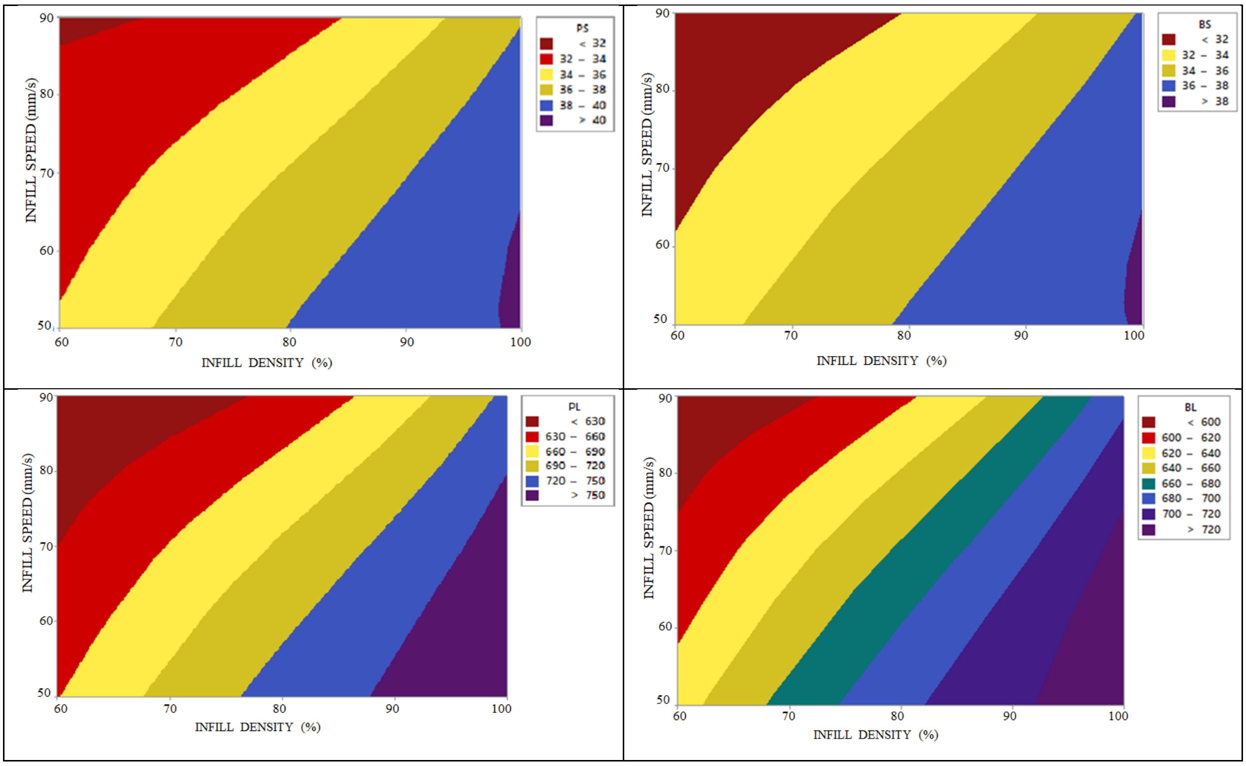

Figure 5.12 Contour graphs of tensile properties

5.2.2 Regression equations and surface plot analysis

The resulted output values of mechanical testing of each property were further used to fit in regression model at three level of interaction, the regression equations of PS, BS, PL and BL are shown in the Table 5.15.

These regression equations have been used to draw the surface plots by keeping the IA constant at 45° (as it was least significant factor). Output responses were taken in Y-axis whereas input parameters IS and ID were taken in X and Z axis respectively. Figure 5.13 shows the surface plots of mechanical properties with respect to input parameters. It has been clearly identified from the surface plots that at lower IS (50 mm/s) and higher ID (100%) helps to improve the mechanical properties of the printed parts.

Table 5.15 Regression equations of tensile properties

PS= 29.44- 0.0794 IS- 0.00809 IA+ 0.1563 ID	(5.4)
BS=28.31- 0.0690 IS- 0.00714 IA+ 0.1411 ID	(5.5)
PL = 565.3 - 1.525 IS - 0.155 IA+ 3.000 ID	(5.6)
BL = 543.5 - 1.325 IS - 0.1370 IA+ 2.708 ID	(5.7)

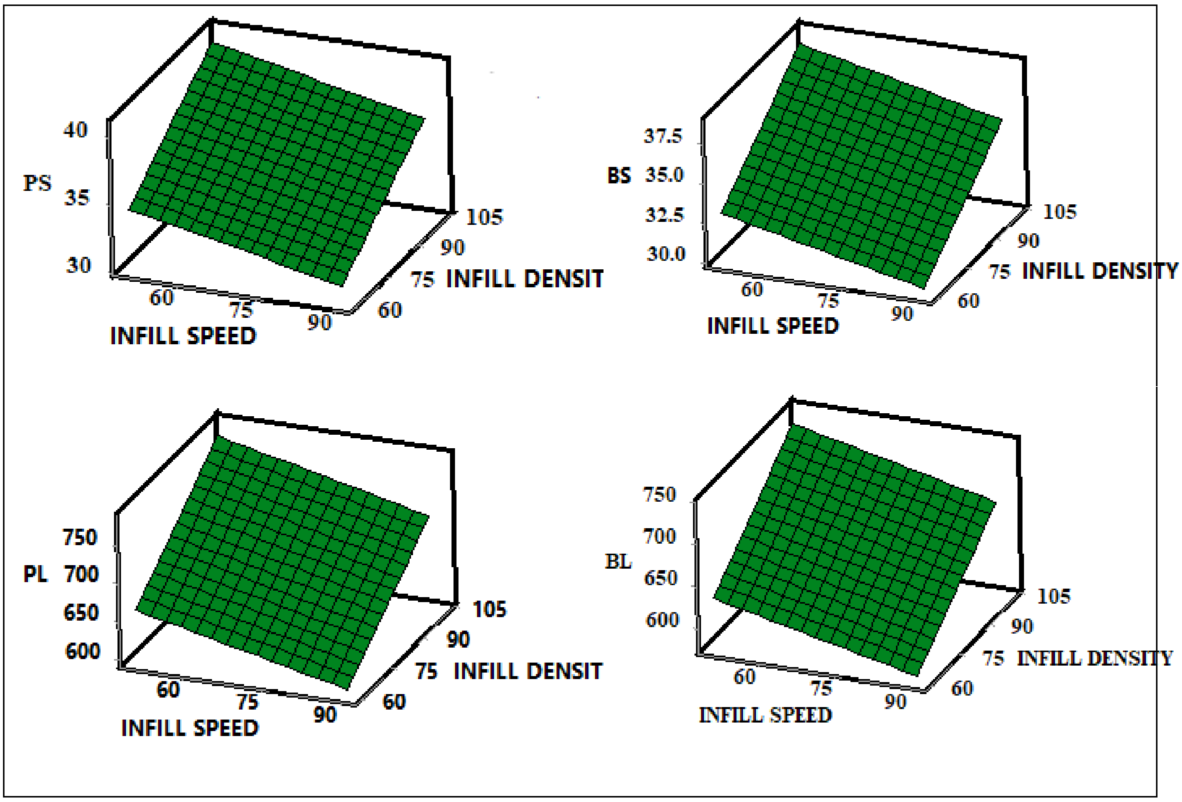

Figure 5.13 Surface plots of tensile properties v/s input parameters

5.2.3 Morphological properties testing

The fractured surfaces of tensile specimens were further subjected to SEM and EDS for morphological properties. The samples have shown the best and worst mechanical strength were analyzed based on microscopic images. The JEOL JSM-6510LV SEM (Japan) was used to take the micrographs of the flexural samples at three different levels of magnification ×150, × 300, and ×500 (as shown in Figure 5.14). SEM images have clearly shown that parts fabricated at the parametric settings shown the best tensile strength have a fibrous structure with good bonding in between them; moreover there is a dimple formation at the fracture surface that supports the more tensile strength in the specimen.

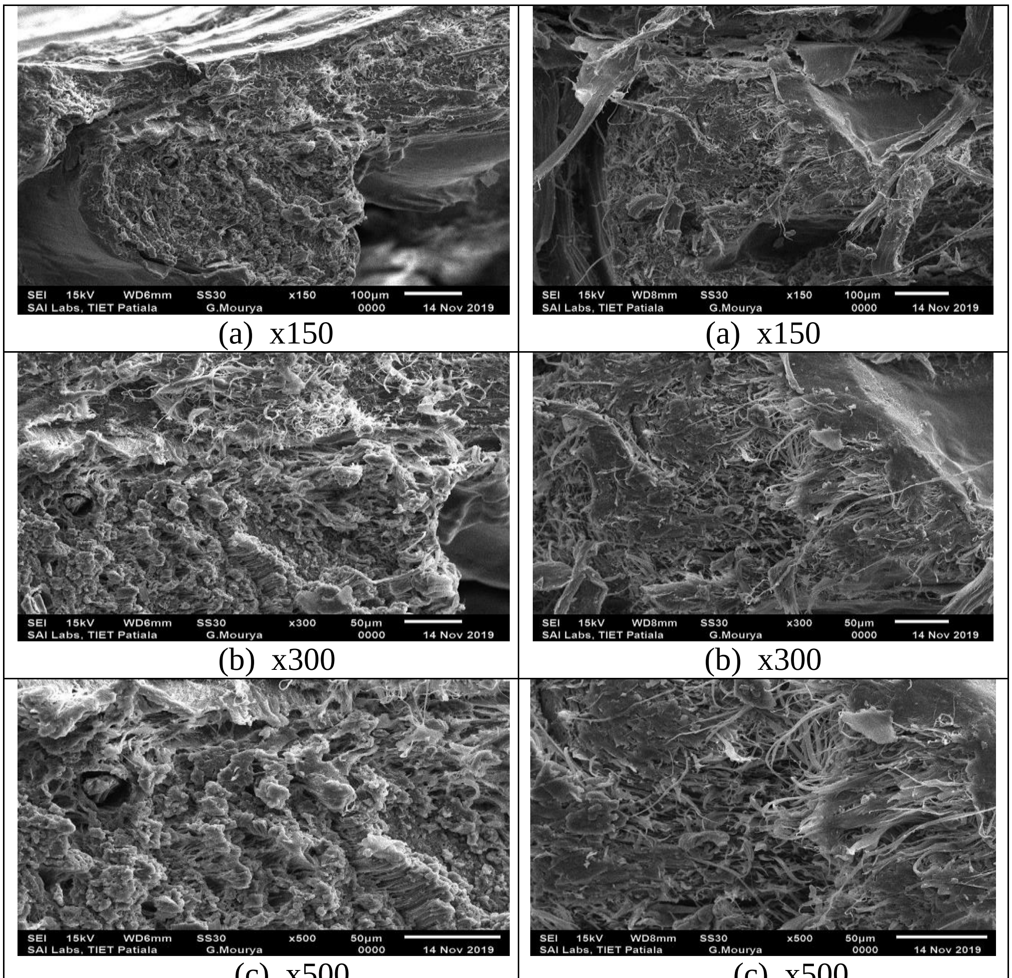

(a) x150	(a) x150
(b) x300	(b) x300
(c) x500	(c) x500
(a) SEM images of the tensile specimen shown worst mechanical strength	(b) SEM images of the tensile specimen shown best mechanical strength

Figure 5.14 SEM images of fractured surfaces of tensile specimens

Further, the SEM images were rendered using a Gwyddion computer-operated software to measure the surface roughness of the specimens. The rendered images and graph of surface roughness shown that the part having maximum tensile strength having low surface roughness.

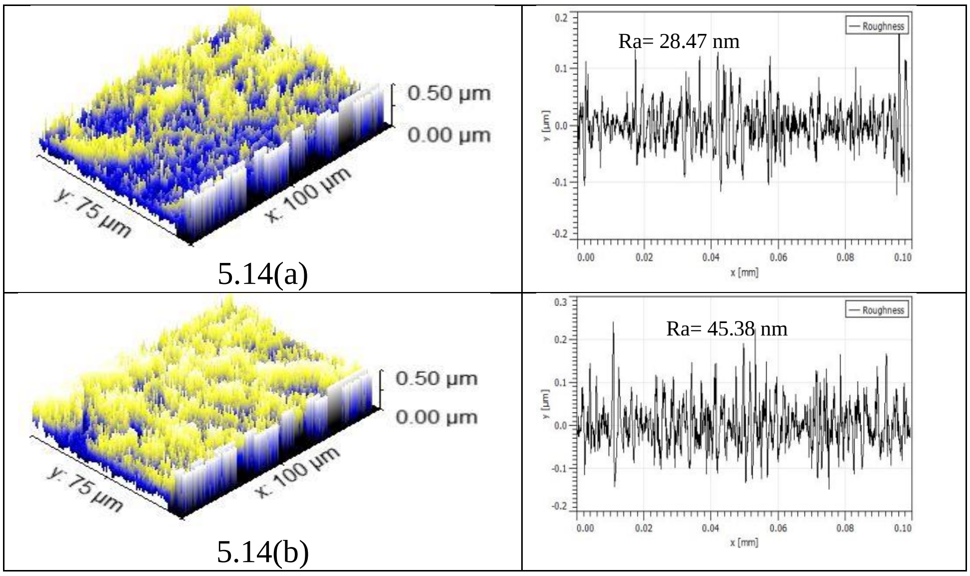

Figure 5.15 3D rendered SEM images of tensile specimens and surface roughness graphs

The EDAX of 3D printed parts fabricated as per different process parameters shown in Figure 5.16. The element analysis for the printed samples having the best mechanical properties (see Figure 5.16(a)) has more carbon, fluorine, oxygen, and titanium as compared to samples fabricated at a low ID level (see Figure 5.16(b)).

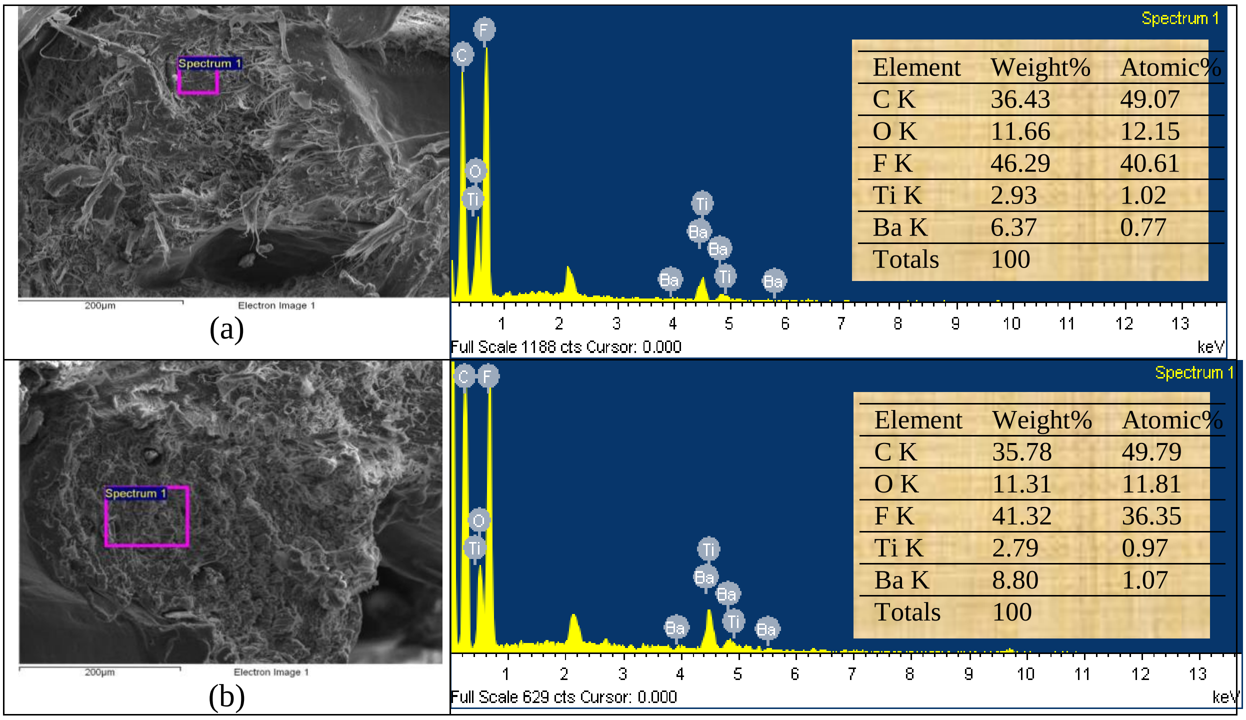

Element	Weight%	Atomic%
C K	36.43	49.07
O K	11.66	12.15
F K	46.29	40.61
Ti K	2.93	1.02
Ba K	6.37	0.77
Totals	100	

Element	Weight%	Atomic%
C K	35.78	49.79
O K	11.31	11.81
F K	41.32	36.35
Ti K	2.79	0.97
Ba K	8.80	1.07
Totals	100	

Figure 5.16 (a) and (b) EDX analysis of sample having worst and best mechanical and thermal properties

5.2.4 Flexural testing of 3D printed specimens

The parts produced according to the design of experiments were further subjected to destructive testing as per the ASTM D790 for flexural testing of plastics for flexural properties on a universal tensile testing machine (Make Shanta Engineering, India). The output values of PL, BL, strength at peak, strength at break, have been noted for flexural testings. Stress-strain curves have been plotted to understand the mechanism of the deformation of the material. The fractured specimens of flexural testing are shown in Figure 5.17. From the elevation, it has been observed that sample 3 bent maximum or we can say maximum bending angle is found in specimen no. 3, during destructive testing. Further, these mechanical properties have been optimized by using ANOVA method, using Minitab software a tool for statistical analysis.

Figure 5.17 Fractured samples after destructive testing

5.2.4.1 Flexural testing

After the completion of the extrusion process, the extruded filament was used for 3D printing of standard flexural specimen. For all the printed specimens flexural test was performed and observed values of PL, BL, flexural strength at peak (PS), and flexural strength at break (BS), flexural modulus (FM) (as shown in Table 5.16) were recorded using UTM interface machine, the flexural modulus and MoT shown in Table 3 were calculated using formula write in equations 1 and 2 respectively.

The Flexural modulus is calculated with the formula given below: -

Flexural modulus = (PLxL3) / (48xIxD) ……. (1)

The MoT is calculated with the formula given below: -

MoT =1/2 x Flexural strength at break x strain at break (Deflection)….. (2)

where

I - Moment of inertia

$I = BH^3/12$

H – Height (thickness) of sample (3.20) in mm

B - Width of sample (12.7) in mm

D - Deflection at the load P in N

L - Support span (40) in mm

Table 5.16 Results obtained from the flexural testing

PL	BL	PS	BS	FM	MoT
53.81	48.44	31.28	28.16	570.44	3.61
82.09	73.87	47.72	42.94	657.52	12.71
93.67	83.35	54.45	48.45	888.45	9.56
69.07	62.74	40.15	36.47	553.21	11.18
100.55	92.81	58.45	53.95	906.03	17.22
48.41	43.59	28.14	25.34	484.66	6.92
78.31	71.46	45.52	41.54	613.57	13.70
51.13	46.00	29.72	26.74	317.72	10.50
56.32	50.72	32.74	29.48	472.10	10.40

The above table has shown that the maximum value of the load at peak (100.55 N), load at break (92.81 N), flexural strength at peak (58.45 MPa), flexural strength at break (53.95 MPa) were noted in experiment no. 5 (IS 70 mm/s, IA 45°, and ID 100 %), however, the minimum flexural strength was found in experiment no. 6. It may be due to stronger bonding between the layers and lack of voids formation at 100% ID when fabricated at an orientation angle of 45°, whereas experiment no. 6 was conducted at lower ID (60%) and IA was 90°. Thus it might have led to lower bonding between the layers due to more gap between the successive layers.

Stress-strain curves obtained from the mechanical testing are shown in Figure 5.18. For these mechanical properties, the signal to noise (SN) ratios at larger the better type case is shown in Table 5.17.

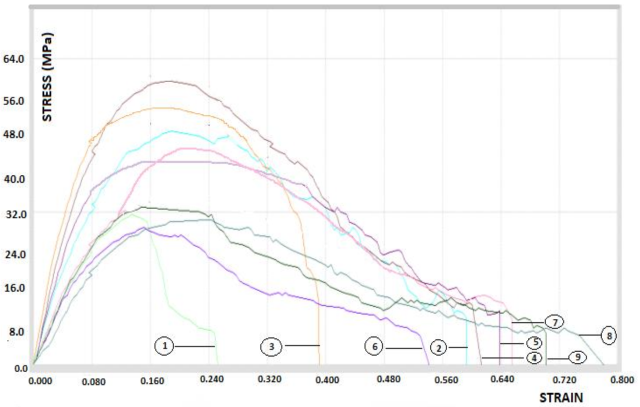

Figure 5.18 Stress-strain curves obtained from flexural testing

Table 5.17 SN values for PS, BS, FM and MT

PS (SN)	BS(SN)	FM(SN)	MoT(SN)
29.905	28.992	55.124	11.143
33.574	32.657	56.358	22.086
34.720	33.705	58.972	19.612
32.073	31.238	54.857	20.970
35.335	34.639	59.142	24.721
28.986	28.076	53.708	16.799
33.164	32.369	55.757	22.731
29.461	28.543	50.040	20.424
30.301	29.390	53.480	20.341

To optimize the FDM process parameters for flexural properties (PS, BS, FM, and MT) ANOVA has been used. ANOVA table created on the basis of SN values of PS shown in Table 5.18. As the probability (P) value of all three selected parameters is less than 0.05, in Table 5.18. Thus, all these parameters were found significant at a 95% confidence level. Moreover, the value of residual error is only 0.20% of the total value supports that the optimization model is significant.

Table 5.18 ANOVA Table based upon the SN values of PS

Factor	DoF	Seq.SS	Adj SS	Adj MS	F	P	%C
IS	2	4.787	4.787	2.393	52.48	0.019	10.61
IA	2	3.415	3.415	1.707	37.43	0.026	7.57
ID	2	36.843	36.843	18.421	403.82	0.002	81.62
Residual Error	2	0.091	0.0912	0.0456			0.20
Total	8	45.137					

The rank table (Table 5.19) shows the rank of process parameters for SN values of strength at the peak that the ID has a most effective role as it was stood 1_{st}, whereas IS and IA ranked 2^{nd} and 3^{rd} respectively. The main effects plot for SN ratios shown in Figure 5.19 represents that the part printed at the first level of IS by keeping the IA 45° and 100% ID shown best mechanical properties.

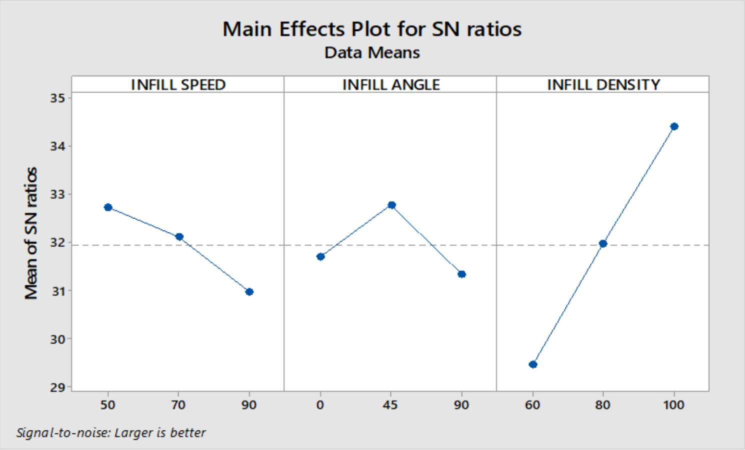

Figure 5.19 SN ratio graph for PS

Table 5.19 Response table of input parameters

Levels	IS	IA	ID
1	32.73	31.71	29.45
2	32.13	32.79	31.98
3	30.98	31.34	34.41
Delta	1.76	1.45	4.96
Rank	2	3	1

For the prediction of optimized values for flexural properties ANOVA statistical tool has been used. The SN values obtained from Minitab software has been further used for the prediction of optimized value using equation 5.8

$\eta_{opt} = R+(R_A–R) +(R_B–R) +(R_C–R)$...........(5.8)

where RA, RB, and RC are the maximum values of IS, IA and ID from Rank Table and R is mean of SN values (obtained from Minitab) for PS.

$R=31.95$, $R_A = 32.73$, $R_B = 32.79$, $R_C = 34.41$

After putting these values in the equation (5.8)

$\eta_{opt} = 36.03$

Now,

$y_{opt}2 = (10)^{\eta opt / 10}$ (for larger the better type case)……….(5.9)

$Y_{opt}^{2} = (10)^{36.03/ 10}$

Y_{opt}=63.31MPa

A total of three repetitive experiments were performed at settings suggested by the ANOVA table and the average PS was found 64.12 MPa which is very close to the calculated value i.e. 63.31 MPa.

5.2.4.2 Contour graphs and regression equations

The contour graphs of PL, BL, PS, and BS are shown in figure 5.20. Contour plots represent the effect of change in two significant input parameters on the output responses. Contour graphs have drawn by taking the IA constant i.e., 45°. ID is taken in the x-direction and IS was taken in the y-direction, whereas in the z-axis it shows the change in values of output response with respect to input parameters.

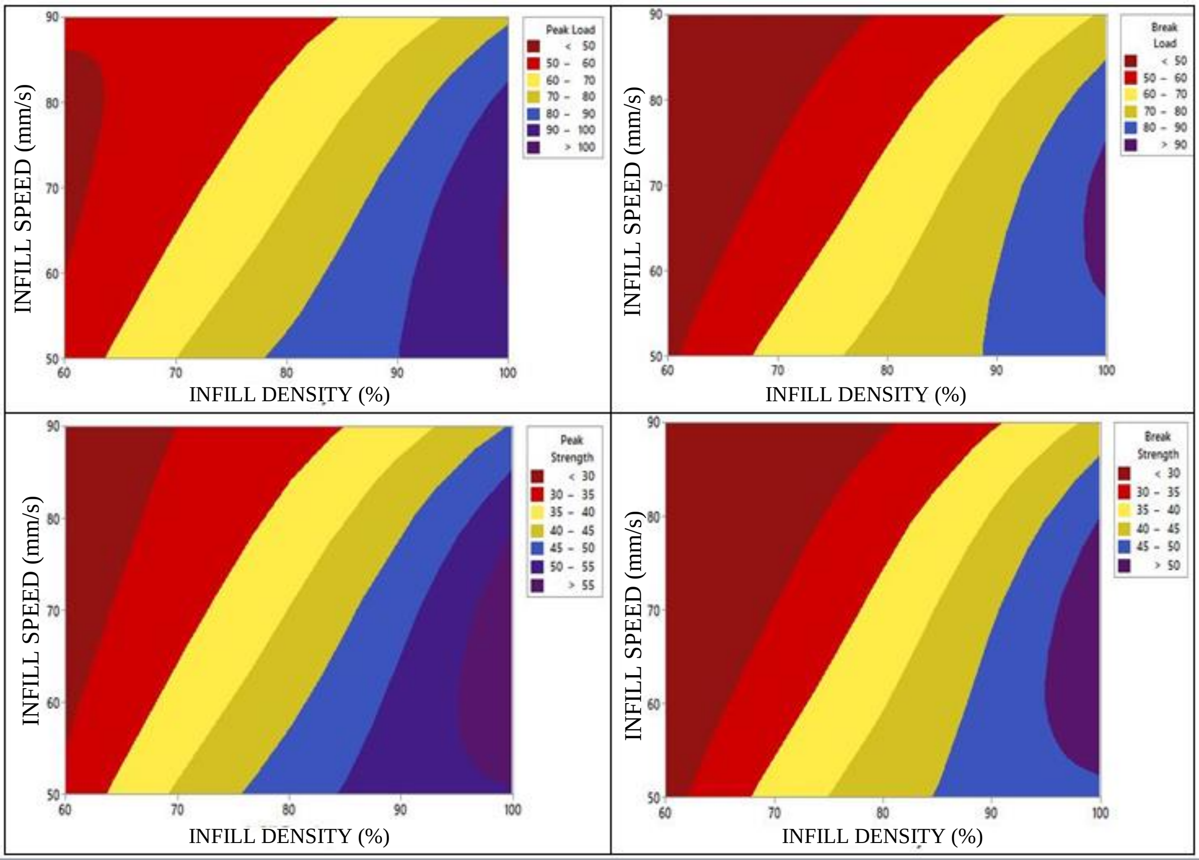

Figure 5.20 Contour graphs of flexural properties

The resulted output values of mechanical testing of each property were further used to fit in the regression model at three levels of interaction, the regression equations of PS, BS, PL and BL are shown in Table 5.20.

Table 5.20 Regression equations of flexural properties

PS= 9.85 - 0.2123 IS - 0.0060 IA + 0.5773 ID	(5.10)
BS=7.74 - 0.1816 IS - 0.0107 IA + 0.5308 ID	(5.11)
PL = 16.9 - 0.365 IS - 0.0103 IA + 0.993 ID	(5.12)
BL = 13.3 - 0.312 IS - 0.0185 IA + 0.913 ID	(5.13)

5.2.5 Pull out testing

Similar to flexural testing, experiments were also performed for pull-out testing that is a relative comparison to check out the pull-out strength of the printed parts. The output values of PL, BL, strength at peak, strength at break, have been noted for pull-out testings. Stress-strain curves have been plotted to understand the mechanism of the deformation of the material. The 3D printed pull-out specimens after testing are shown in Figure 5.21.

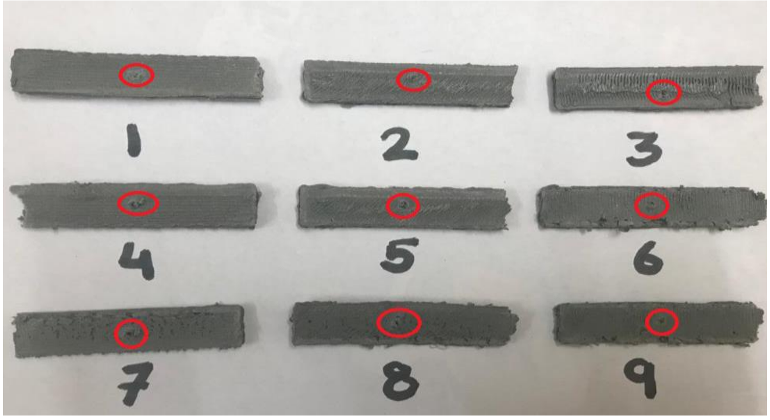

Figure 5.21 3D printed samples of pull out testing

For the pull-out test, a screw was tightened in the specimen and pulling (shear) force was applied to the specimen on UTM. Some properties of the pull-out test like PL, BL, peak elongations, and break elongation were obtained directly from the UTM, whereas some properties like shear strength at peak, shear strength at break, shear modulus, MoT were calculated. The results obtained from the pull-out test are shown in Table 5.21.

Table 5.21 Observations obtained from the pull-out testing

Sample No.	Load at Peak (N)	Load at Break (N)	Peak elongation (mm)	Break elongation (mm)	Shear strength at peak (MPa)	Shear strength at break (MPa)	Shear modulus (MPa)	MoT (MPa)
1	248	223.2	8.4	12.18	11.29	10.16	4.30	19.33
2	337.2	303.48	5.88	9.03	15.35	13.81	8.35	19.49
3	357.8	322.02	8.82	11.76	16.29	14.66	5.91	26.93
4	411.3	391.86	10.29	13.86	18.72	17.84	5.83	38.63
5	400	360	9.87	13.02	18.21	16.39	5.90	33.34
6	236	212.4	7.98	10.08	10.74	9.67	4.31	15.23
7	167.6	150.84	7.77	9.66	7.63	6.87	3.14	10.36
8	142.2	127.98	9.45	11.97	6.47	5.83	2.19	10.89
9	189.2	170.28	7.14	10.08	8.61	7.75	3.86	12.21

It has been observed from Table 5.21 that, sample no. 4 shows maximum shear strength at peak (18.72 MPa) and maximum shear strength at break (17.84 MPa), which was printed by keeping the IS 70 mm/s, at ID 80% and the IA was set at 45^{o}, whereas sample no. 2 shows the maximum shear modulus (8.35 MPa). Figure 5.22 shows the stress versus strain curves obtained from destructive testing performed at UTM.

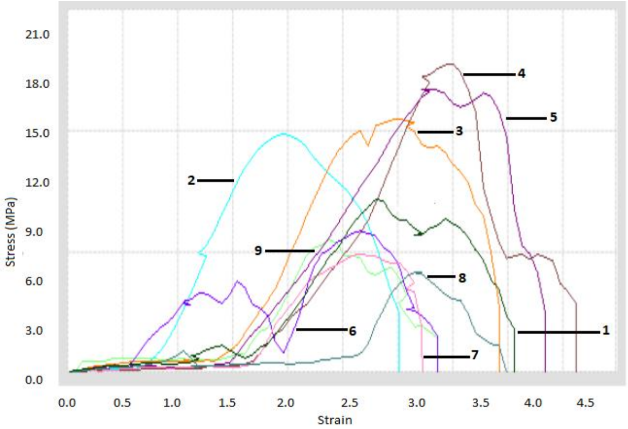

Figure 5.22 Stress-strain curves for pull out properties

Further ANOVA was used, for the further optimization of pull-out properties. SN values for SS at peak, SS at break, SM and MT calculated at larger the best settings are shown in Table 5.22.

Table 5.22 SN values for pull-out properties

SS at Peak (SN)	SS at Break (SN)	SM (SN)	MT (SN)
21.05	20.13	12.66	25.72
23.72	22.80	18.43	25.79
24.24	23.32	15.43	28.60
25.45	25.02	15.79	31.73
25.21	24.29	15.41	30.45
20.62	19.70	12.68	23.65
17.65	16.73	9.93	20.30
16.22	15.31	6.80	20.74
18.70	17.78	11.73	21.73

(SS-Shear Strength, SM- Shear Modulus, MT-MoT, SN- Signal to Noise)

It has been observed from the ANOVA table (shown in Table 5.23) that out of three input parameters, only IS was found significant, however, the IA and ID were found insignificant, as their probability (P) values are more than 0.05. The percentage contribution of residual error is only 2.97 represent the significance of the tool.

Table 5.23 ANOVA table based on SN values of shear strength at peak

Factor	DoF	Seq.SS	Adj SS	Adj MS	F	P	%C
IS	2	69.488	69.488	34.744	25.03	0.038	74.54
IA	2	0.429	0.429	0.215	0.15	0.866	0.46
ID	2	20.535	20.535	10.267	7.40	0.119	22.03
Residual Error	2	2.776	2.776	1.388			2.97
Total	8	93.228					

Table 5.24 shows rank of input process parameters for SN values of shear strength at peak. It was found that IS shown most significant role with ranked 1st followed by ID and IA, which were ranked 2nd and 3rd respectively. The main effects plot for SN ratios shown in Figure 5.23 represents that the part printed by keeping the intermediate level of all three input parameters shown the best mechanical properties.

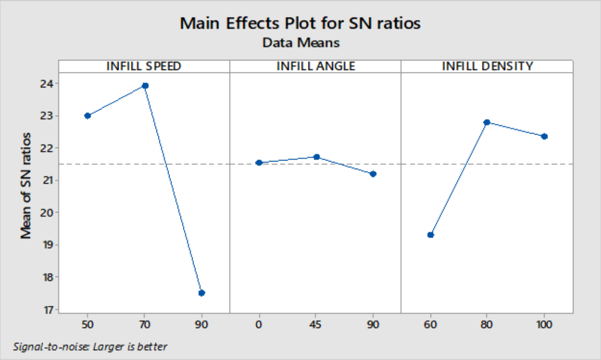

Figure 5.23 SN ratio graph for shear strength at peak

Table 5.24 Response table for input parameters

Levels	IS	IA	ID
1	23.00	21.38	19.30
2	23.76	21.72	22.62
3	17.52	21.19	22.37
Delta	6.23	0.53	3.33
Rank	1	3	2

The SN values obtained from Minitab software has been further used for the prediction of optimized value using equation 1.

$\eta_{opt} = R+(R_x–R) +(R_y–R) +(R_z–R)$ …………(5.14)

where R_x, R_y, and R_z are the maximum values of IS, IA and ID from Rank Table and R_{avg} is mean of SN values (obtained from Minitab) for shear strength at peak.

R_{avg}=21.43, R_x = 23.92, R_y = 21.72, R_z = 22.62

After putting these values in the equation (5.14)

η_{opt}= 25.4

Now

$y_{opt}2 = (10)^{\eta opt/ 10}$ (for larger the better type case)…….(5.15)

$Y_{opt}^{2} = (10)^{25.4/ 10}$

Y_{opt}=18.62MPa

A total of three repetitive experiments were performed at settings suggested by the ANOVA table and the average shear strength at peak was found 18.75MPa which is very close to the calculated value i.e. 18.62 MPa.

5.2.6 Multi-optimization

To obtain the best parametric settings for flexural and pull-out properties, a Taguchi multifactor optimization technique has been used. In this combined optimization process the values of SN ratios of both flexural (strength at peak) and pull-out (shear strength at peak) properties have been used. Table 5.25 shows the SN values of respective properties and combine SN values. Table 5.26 shows the ANOVA table of SN values obtained from multifactor optimization. The main effect plot for combine SN rations is shown in Figure 5.24.

Table 5.25 Combine SN values of input parameters

Sr. No.	IS (mm/s)	IA (°)	ID (%)	SN (Flexural strength)	SN (Pull-out)	SN (Combine)
1	50	0	60	29.905	21.05	27.73
2	50	45	80	33.574	23.72	28.75
3	50	90	100	34.720	24.24	28.97
4	70	0	80	32.073	25.45	29.00
5	70	45	100	35.335	25.21	29.25
6	70	90	60	28.986	20.62	27.51
7	90	0	100	33.164	17.65	26.86
8	90	45	60	29.461	16.22	26.06
9	90	90	80	30.301	18.70	27.04

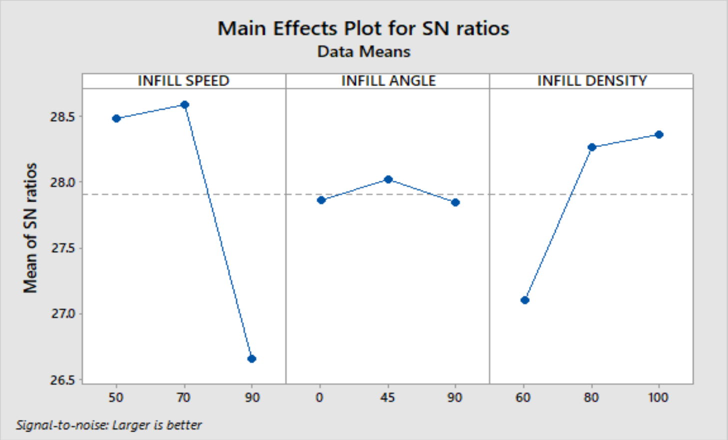

Figure 5.24 Graph for combine SN values

Table 5.26 ANOVA table for combine SN values

Factor	DoF	Seq. SS	Adj SS	Adj MS	F	P	%C
IS	2	7.107	7.107	3.553	39.21	0.025	68.83
IA	2	0.057	0.057	0.028	0.31	0.760	0.55
ID	2	2.979	2.979	1.489	16.44	0.057	28.85
Residual Error	2	0.181	0.181	0.090			1.77
Total	8	10.325					

Table 5.27 shows the rank of the input parameters on the basis of larger the better type for Combine SN ratios.

Table 5.27 Response table for input parameters

Levels	IS	IA	ID
1	28.49	27.86	27.10
2	28.59	28.02	28.27
3	26.65	27.84	28.36
Delta	1.93	0.18	1.27
Rank	1	3	2

The best parametric settings obtained from the multi-optimization for 3D printing is 70 mm/s IS at 45^o IA by keeping the ID 100%. A total of 3 confirmatory experiments were performed at the best parametric settings of FDM suggested by multi-optimization. The output values of flexural and pull-out strength were compared with the optimized values. Table 5.28 shows the results of confirmatory experiments.

Table 5.28 Observations from confirmatory experiments

Sr. No.	Flexural properties (Strength at peak in MPa)	Pull-out testing (shear strength at peak in MPa)
1	62.34	18.74
2	61.15	18.67
3	62.96	18.71

5.2.7 Microscopic analysis

As the optimization of mechanical properties for flexural and pull-out testing of 3D printed parts was completed, the specimen shown best and worst mechanical strength were subjected to microscopic analysis. The JEOL JSM-6510LV SEM (Japan) was used to take the micrographs of the flexural samples at three different levels of magnification ×150, × 300, and ×500 (as shown in Figure 5.25). For SEM analysis the sample should be conductive in nature. Thus to make the polymeric samples conductive, a gold layer has been coated over its surface. Micrographs showed that the sample fabricated as per optimized suggested settings has a solid structure and proper bonding in between the layers. Whereas the sample showed poor mechanical strength is porous and gaps between layers reduced the mechanical strength of the part.

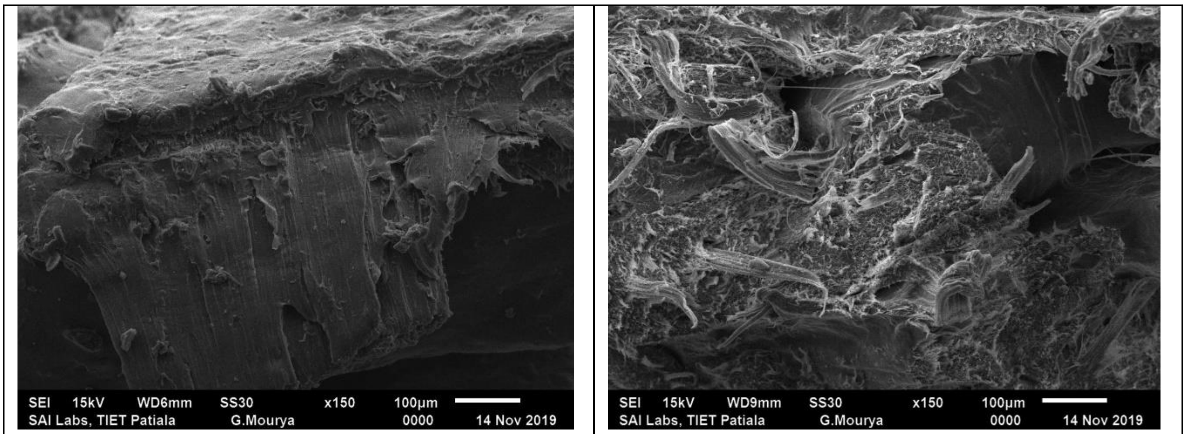

(a) At x150 (b) At x150

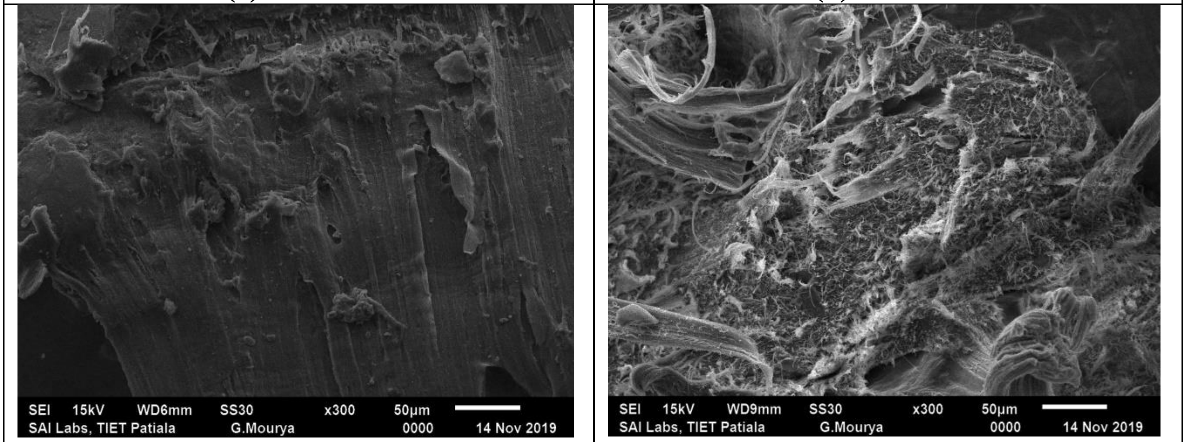

(a) At x300 (b) At x300

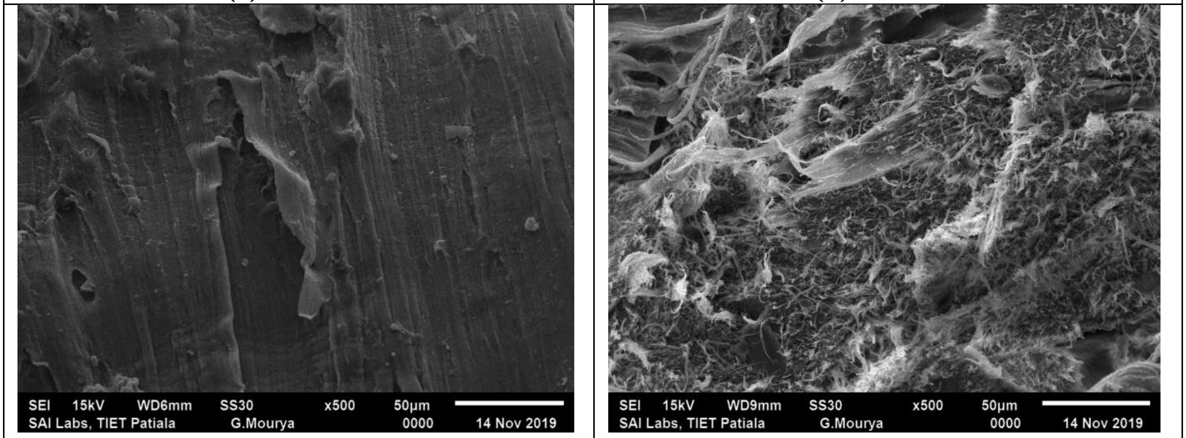

(a) At x500 (b) At x500

Figure 5.25 (a) SEM micrographs of fractured surfaces of samples shown best flexural properties, (b) samples shown worst flexural properties

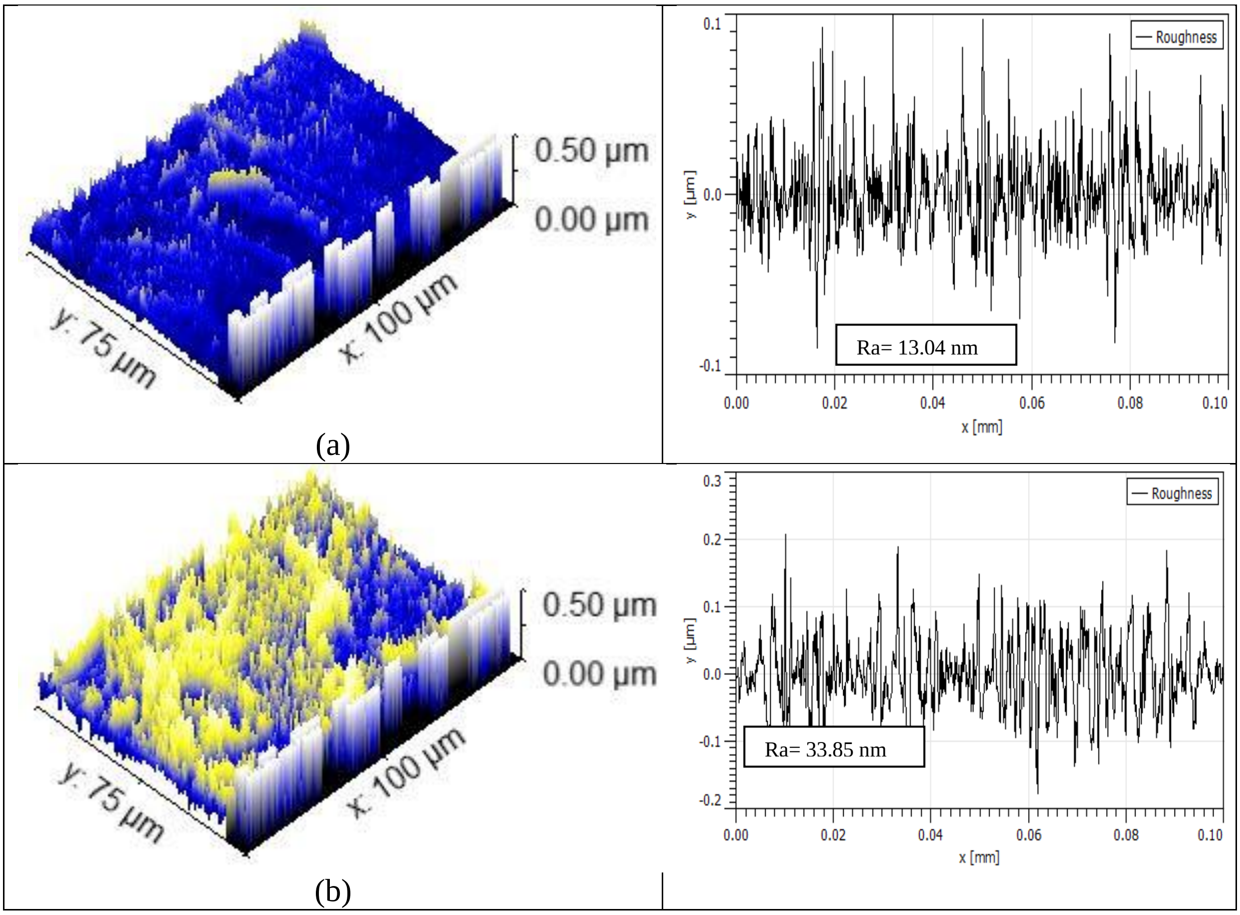

(a)

(b)

Figure 5.26 Rendered SEM images of flexural tested parts shown best (a) and worst (b) mechanical properties respectively

The surface roughness (Ra) of 3D printed parts has been measured by taking the rendered images of SEM of the specimen at x500 magnification. Figure 5.26 shows the rendered images and surface roughness graphs of flexural samples. It has been observed from Figure 5.26 (b) that the parts fabricated as per the settings shown poor mechanical properties having more surface roughness whereas the samples printed as per best settings (Figure 5.26(a)) shown less surface roughness it may be due to better bonding between the layers at higher ID level.

The EDAX of 3D printed parts fabricated as per different process parameters shown in Figure 5.27. The element analysis for the printed samples having the best mechanical properties (see Figure 5.27(a)) shown that it has more carbon, barium, oxygen, and titanium as compared to samples fabricated at a low ID level (see Figure 5.27(b)). The area mapping of the samples, showed the dispersion of elements per unit area (Figure 5.28). Area mapping clearly represents that the parts fabricated as per best settings (as shown in Figure 5.28(a)) having more dispersion of elements per unit area as compared to samples printed at low ID level (Figure 5.28(b)).

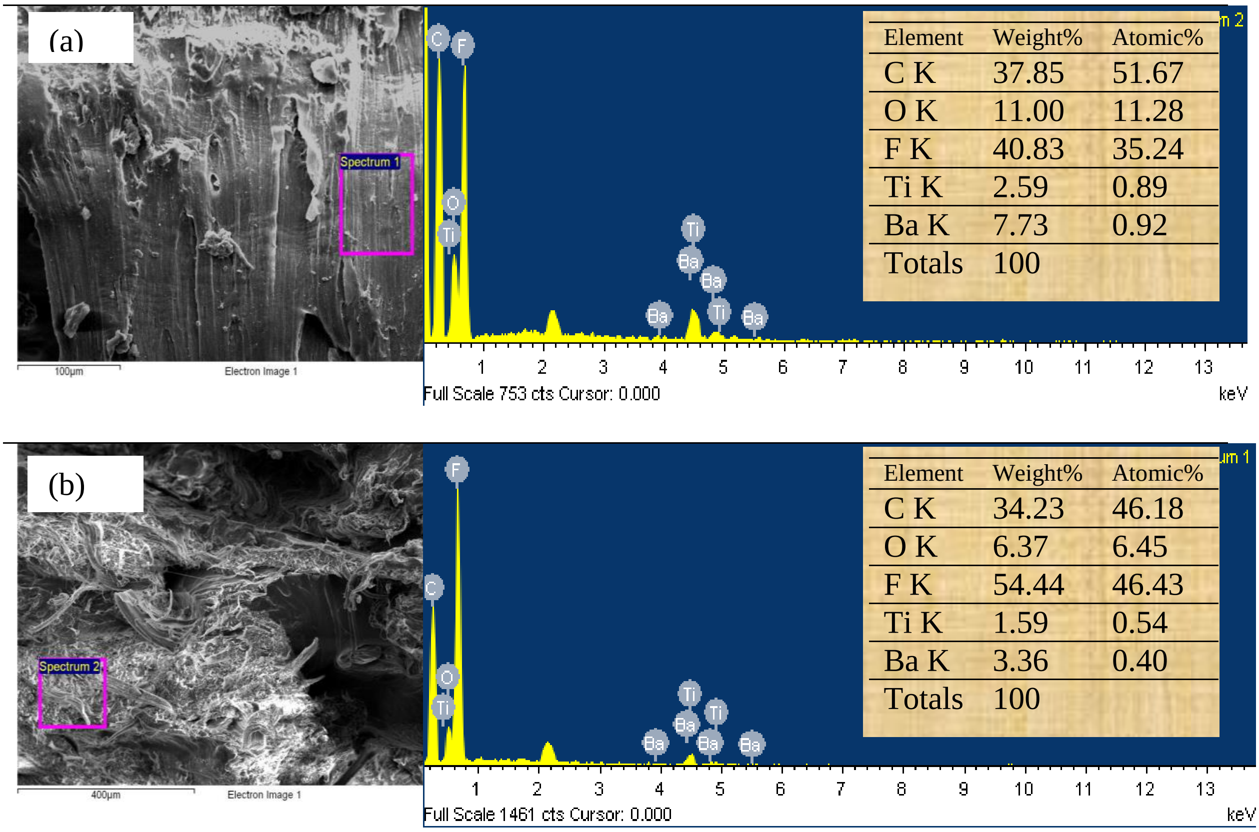

Element	Weight%	Atomic%
C K	37.85	51.67
O K	11.00	11.28
F K	40.83	35.24
Ti K	2.59	0.89
Ba K	7.73	0.92
Totals	100	

Element	Weight%	Atomic%
C K	34.23	46.18
O K	6.37	6.45
F K	54.44	46.43
Ti K	1.59	0.54
Ba K	3.36	0.40
Totals	100	

Figure 5.27 EDAX analysis of 3D printed parts having best (a) and worst (b) mechanical properties

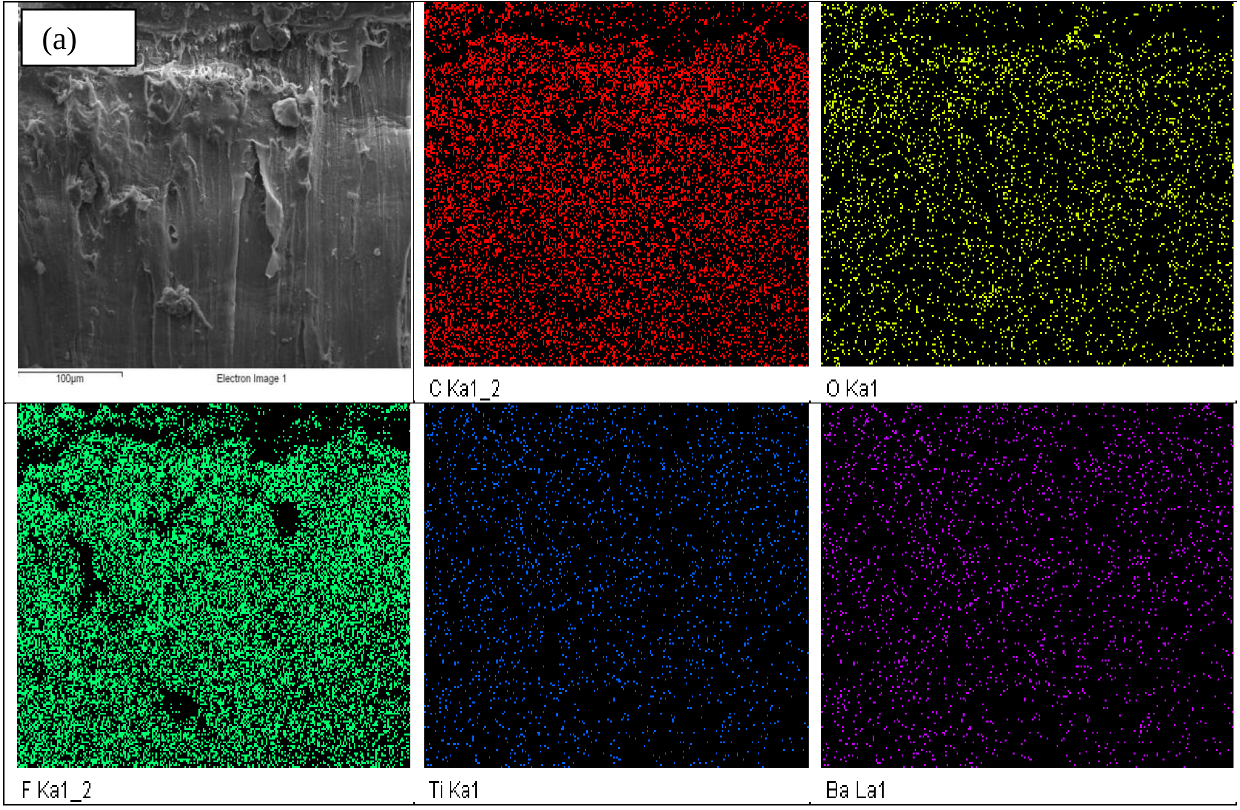

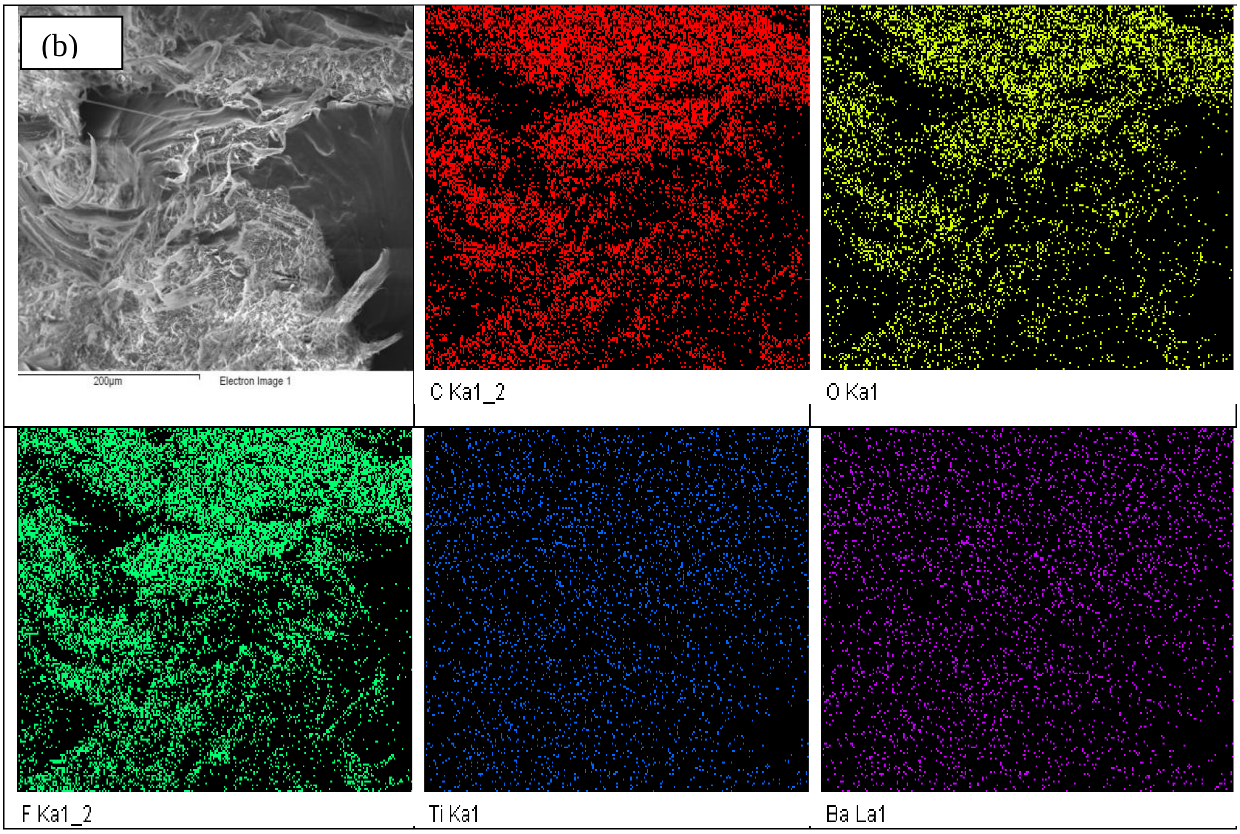

Figure 5.28 Area mapping of 3D printed samples having best (a) and worst (b) mechanical properties

5.2.8 Shore–D hardness

To measure the hardness values of the 3D printed parts a shore D hardness tester was used. It gives resulted values up to three decimal places. Hardness values are shown in Table 5.29. The measured surface hardness values (shore-D) of the 3D printed parts lying in between 63 to 74. The maximum hardness value has been found in experiment no 3. The shore-D hardness value of the confirmatory experiment was 75.2 Shore D i.e., highest values than others.

Table 5.29 Surface hardness values of 3D printed parts

Experiment No.	Shore-D Hardness
1	69.54
2	71.12
3	73.95
4	70.84
5	72.57
6	68.41
7	71.96
8	64.75
9	68.47

5.2.9 Dimensional analysis

After the surface hardness (SH) testing, manufactured specimens were subjected to dimensional analysis. A digital Vernier caliper (make: Mututoyo) having accuracy up to two decimal places was used to measure the thickness (T) in mm of specimens. To minimize the measurement error, each sample was measured three times the average thickness of three measured dimensions of the 3D printed specimens were compared with the standard dimensions of tensile specimens (as shown in Table 5.30). It has been found that the parts manufactured/fabricated at IS of 70 mm/s, and depositing material at an IA 90^o, with 100% ID shown least deviation. Whereas, 3D printing performed as per experiment setting having IS 50 mm/s with 0^o and 60% ID have shown maximum deviation.

Table 5.30 Dimensional deviation observed from dimensional analysis

Exp. No.	IS (mm/s)	IA (^{o})	ID (%)	T1	T2	T3	T avg	T (required)	ΔT
1	50	0	60	2.90	2.95	2.98	2.94	3.2	0.26
2	50	45	80	3.10	3.08	3.12	3.10	3.2	0.10
3	50	90	100	3.14	3.15	3.21	3.17	3.2	0.03
4	70	0	60	3.01	3.05	3.09	3.05	3.2	0.15
5	70	45	80	2.99	3.01	2.97	2.99	3.2	0.21
6	70	90	100	3.12	3.19	3.24	3.18	3.2	0.02
7	90	0	60	3.11	3.04	3.01	3.05	3.2	0.15
8	90	45	80	3.08	3.02	3.06	3.05	3.2	0.15
9	90	90	100	3.01	3.04	2.99	3.01	3.2	0.19

5.2.10 Surface porosity

Figure 5.29 shows the photomicrographs of the surfaces of the filaments with the percentage of Φ on the surface. The red zone shows the porosity in the captured area for the analysis of percentage porosity. It has been observed from the photomicrograph’s that parts fabricated at high density and low IS having less surface porosity as compared to specimen’s 3D printed at high IS and low ID.

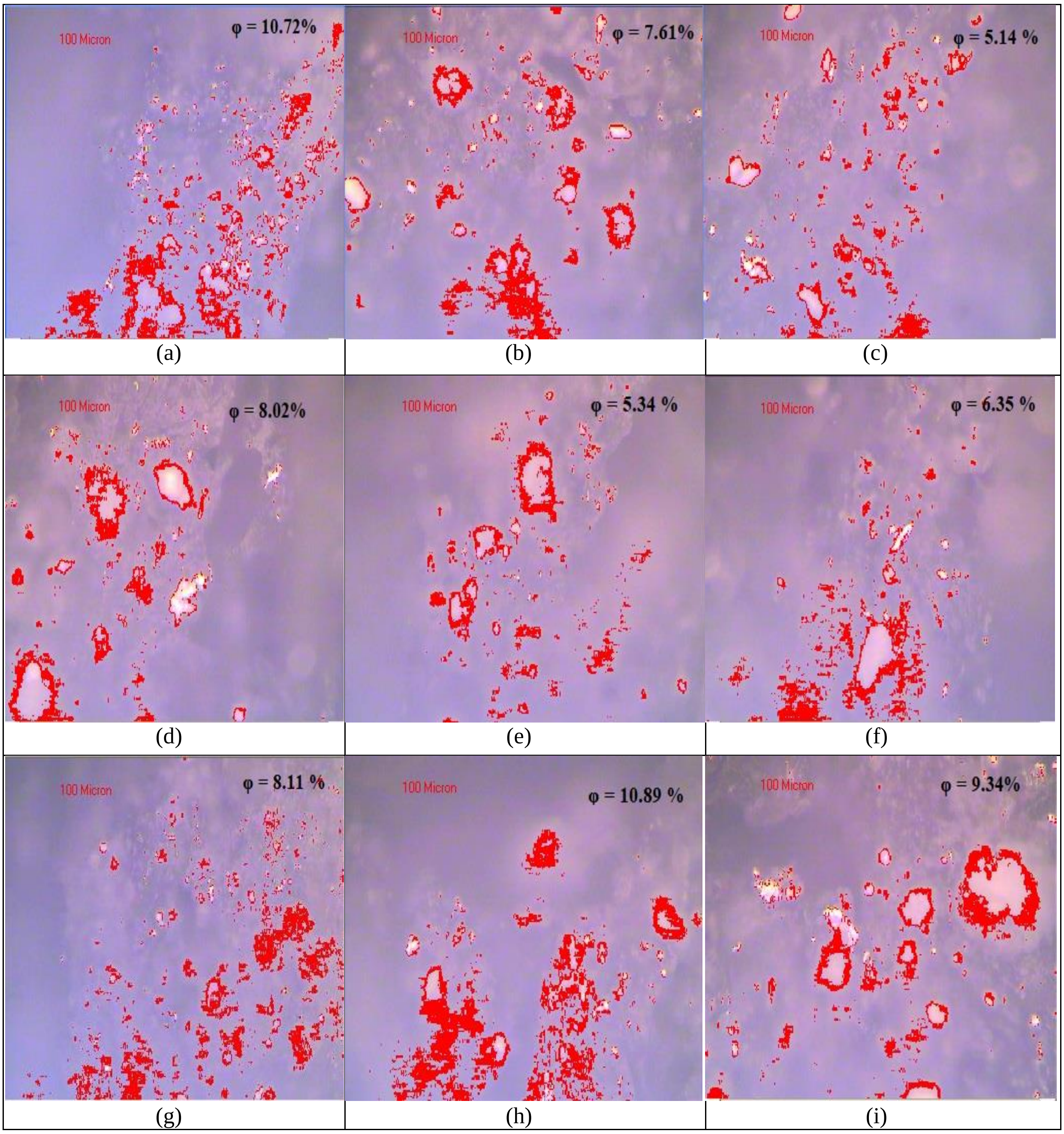

(a) (b) (c)

(d) (e) (f)

(g) (h) (i)

Figure 5.29 Optical photomicrographs with percentage porosity

5.2.11 Results of DMA

DMA is a sensitive method to study the polymer’s viscoelastic behaviour as a function of temperature. An oscillation cycle of frequency was selected to observe the effect of different process parameters on the DMA properties of the material. The testing was performed under an identical thermal environment. Under this cyclic loading, the sample has oscillated at the constant displacement of 10 μm. The force was applied to the samples by using a single cantilever bending method. During the testing, the temperature was increasing from 30°C to

130°C at a rate of 3K/min. Thus, the experimental settings shown best and worst flexural properties were used for 3D printing of DMA sample as shown in Table 5.31.

Table 5.31 FDM process parameters for 3D printing of standard specimens

Sample no.	Sample Type	IS (mm/s)	IA (°)	ID(%)
1	DMA	50	45	100
2	DMA	70	90	60
Process parameters remain constant (i) Nozzle diameter: 0.5 mm (ii) Bed Temperature: 85°C (iii) Nozzle Temperature:250°C (iv) Fan Outpur: 50% (v) Number of parameters: 4 (vi) Fill pattern: rectilinear				

The observed curves of storage modulus and tan δ with respect to temperature for sample 1 and sample 2 are shown in Figure 5.30 (a) and Figure 5.30 (b) respectively.

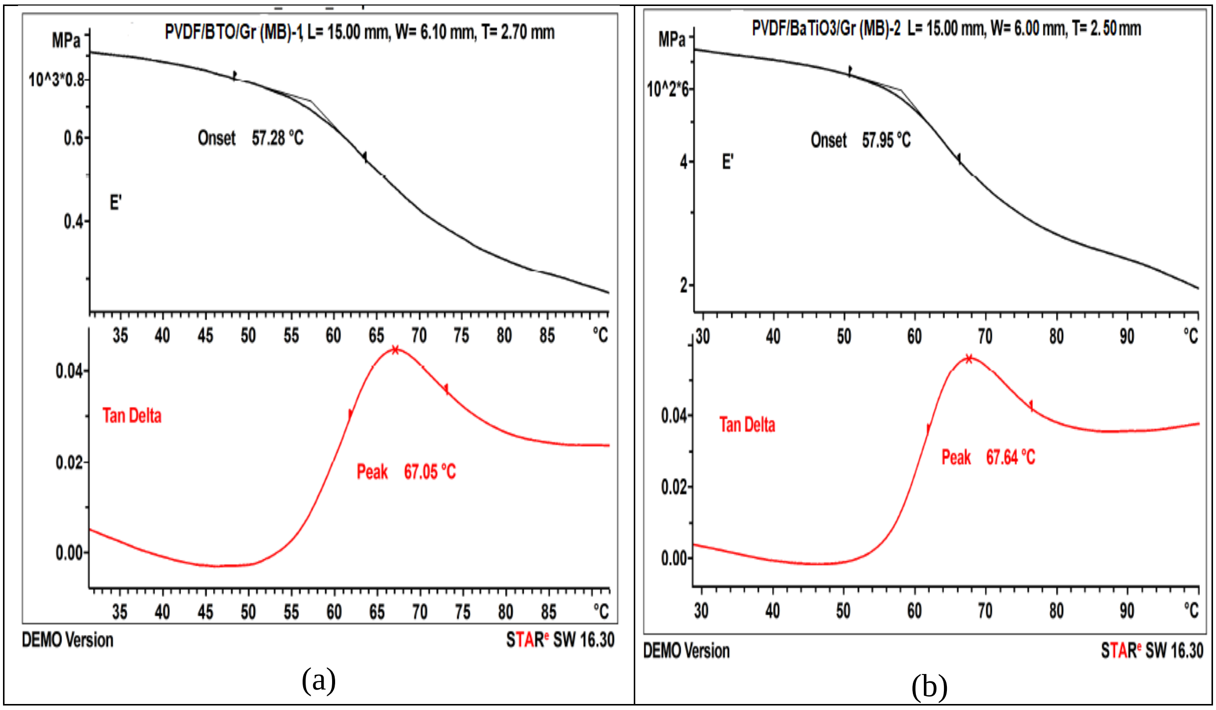

(a)

(b)

Figure 5.30 (a) and (b) DMA curves in term of storage modulus and tan delta as a function of temperature corresponding to MB and CAMB composites

The curves obtained from DMA testing show that with the increase of temperature storage modulus (E') of the material is decreasing. However tan delta is increasing with respect to temperature. It has been observed by comparing both the curves that E' of MB sample 1is more (i.e.$8x10^{\wedge 2}$ MPa) as compared to E' of MB sample 2 ($6x10^{\wedge 2}$ MPa). It means the energy absorbing capacity of MB sample 1 is better than sample 2. The curves of tan δ represent the variation in energy dissipation capacity as a function of temperature. The tan δ curve of sample 2 shows the maximum value of 0.045 at 67°C, whereas in the case of sample 1, the value of tan δ at the same temperature is 0.04 at a similar temperature. Thus it means the ratio of loss modulus to storage modulus is more in sample 2 as compared to specimen 1. Consequently, the sample prepared as per experimental settings shown the best flexural properties also have better stiffness and shape recovery property.

5.2.12 Process Capability Analysis

A total of ten standard tensile specimens and ten standard flexural specimens were 3D printed to report the process capability analysis of 3D printing process parameters. The 3D printed functional prototypes were subjected to a universal testing machine (UTM) for destructive testing. The output results of mechanical testing of both types of specimens in the form of PS, BS, and MoT were noted to perform process capability analysis (see table 5.32). It has been observed from the output results of mechanical testing that very less variations were found by printing the samples under similar processing conditions.

Table 5.32 UTM results for tensile specimens

S.No.	PS (MPa)	BS (MPa)	MoT (MPa)
1	42.95	38.70	3.70
2	43.10	39.02	3.54
3	42.68	37.93	4.27
4	41.98	37.04	4.38
5	42.38	37.82	4.54
6	43.19	38.67	3.79
7	43.40	38.92	3.68
8	42.54	37.84	4.14
9	43.14	40.01	4.72
10	42.25	37.24	3.28

For process capability analysis data are shown in Table 5.32 was processed with the statistical analytical tool. The calculated values of Cp >1 and Cpk>1, for the type of specimens, represented that the 3D printing process was statistically under control. The outcome graphs of process capability analysis in the form of the histogram and normal probability plot for PS, BS, and FT of the tensile specimen are shown in Figure 5.31.the histogram for the observed values of PS shown that values were inside the upper statistical limits (USL) and lower statistical limits (LSL) and the bell-shaped curve outlined that the observed result followed the normal distribution. Further, in the normal probability plot, all the observed values of PS were lying near the normal line, which outlined that process is in control. The calculated results of process capability analysis for PS, BS, and fracture toughness of tensile specimens are shown in Table 5.33.

Table 5.13 Results of process capability analysis for 3D printed tensile specimens

	PS (MPa)	BS (MPa)	MoT (MPa)
Std. Deviation	0.46134	0.96491	0.46783
C_p	1.08	1.04	1.07
C_{pu}	1.11	1.06	1.07
C_{pl}	1.06	1.01	1.07
C_{pk}	1.06	1.01	1.07
CR	0.92	0.96	0.94

Note:

1. *Cp and Cpk measure consistency with average performance. The 'k' stands for 'centralizing factor.' The index takes into consideration the fact that data is maybe not centered.*
2. *For tensile specimen*
   - *(a) For PS the USL and LSL was 44.3 and 41.3 MPa respectively*
   - *(b) For BS the USL and LSL was 41.5 and 35.5 MPa respectively*
   - *(c) For MoT the USL and LSL was 5.5 and 2.5 MPa respectively*

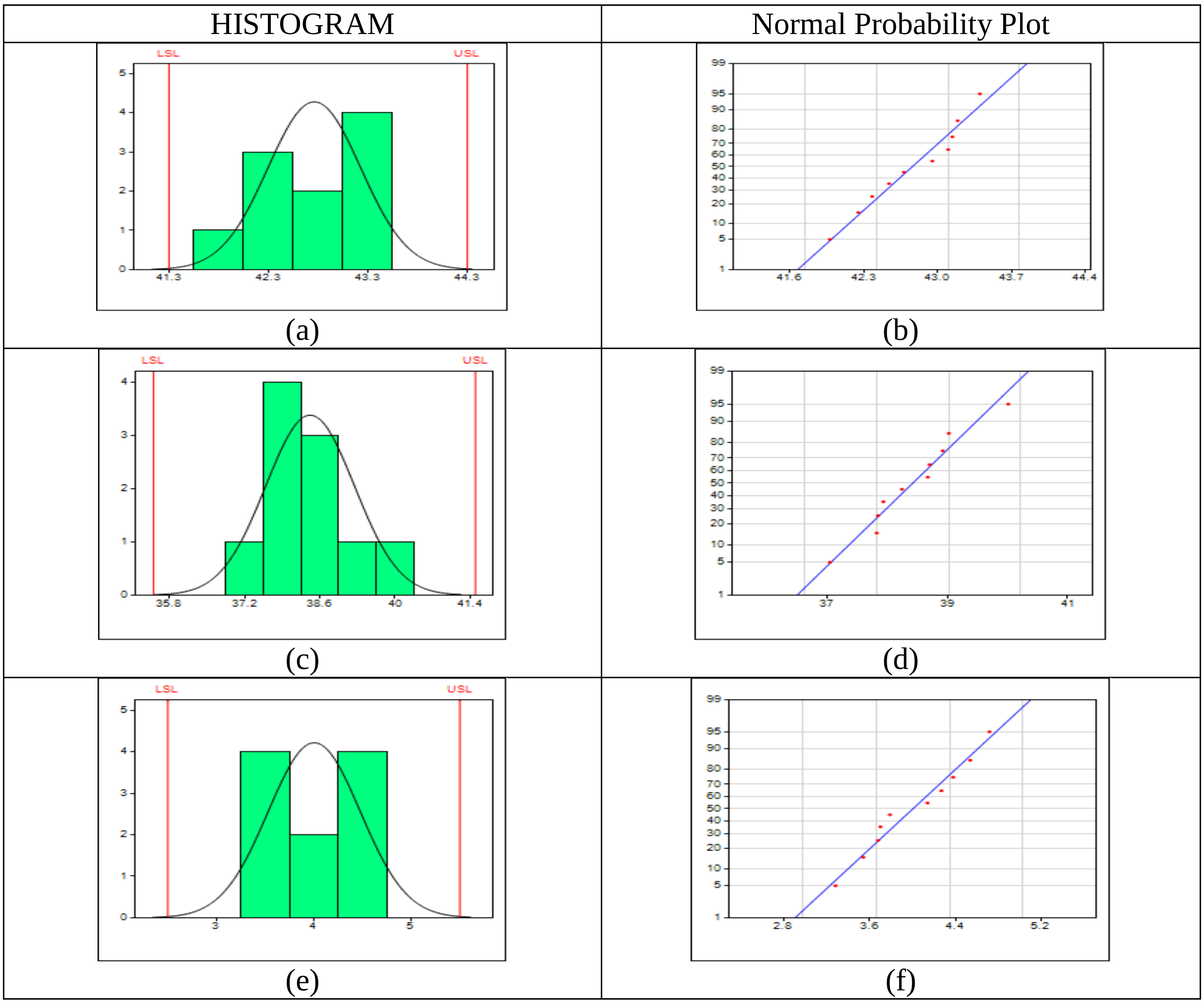

Figure 5.31 Process capability index for PS, BS and FT of tensile specimens

Similar results were also observed for the flexural specimens. Table 5.33 shows the results of flexural testing. Table 5.35 shows the outcome values of process capability analysis. The histogram and normal probability plot for PS, BS and FT of flexural specimens are shown in Figure 5.32.

Table 5.34 UTM results for flexural specimens

S. No	PS (MPa)	BS (MPa)	MoT (MPa)
1	61.97	56.84	12.52
2	62.29	58.26	11.57
3	63.87	58.97	14.25
4	64.08	58.50	13.21
5	63.18	57.96	12.89
6	64.30	60.10	14.65
7	62.80	58.27	13.48
8	63.25	59.34	11.45
9	61.57	57.85	12.78
10	62.49	58.18	14.31

Table 5.35 Results of process capability analysis for 3D printed flexural specimens

	PS (MPa)	BS (MPa)	MoT (MPa)
Std.Deviation	0.88694	1.05913	0.74074
C_p	1.13	1.1	1.24
C_{pu}	1.13	1.12	1.22
C_{pl}	1.12	1.08	1.26
C_{pk}	1.12	1.08	1.22
CR	0.89	0.91	0.81

Note:

1. *Cp and Cpk measure consistency with average performance. The 'k' stands for 'centralizing factor.' The index takes into consideration the fact that data is maybe not centered.*
2. *For flexural specimen*

(d) *For PS the USL and LSL was 66 and 60 MPa respectively*

(e) *For BS the USL and LSL was 62 and 55 MPa respectively*

(f) *For MoT the USL and LSL was 10 and 16 MPa respectively*

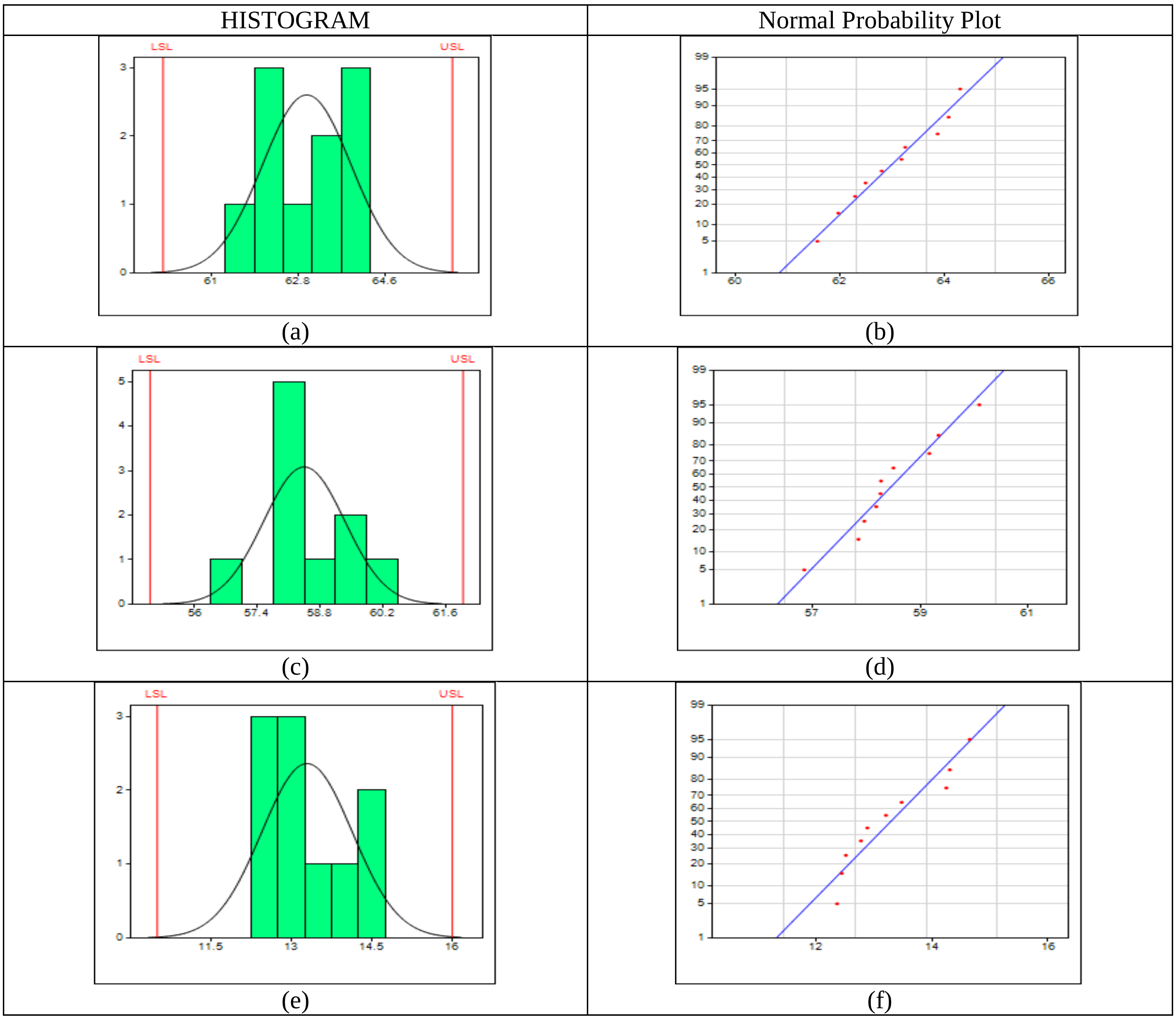

Figure 5.32 Process capability index for PS, BS and FT of flexural specimens

5.3 Results and discussion (Stage 3)

- **Synthesis and development of PVDF/Gr/BTO based composite by CAMB method**

Pilot experimentation was conducted to determine the effect of reinforced particles on the flowability of the base polymer matrix, three proportions of PVDF/Gr/BTO were provisionally selected for the development of composites. In the chemical blending process, initially, thin films of composites at all three proportions were prepared by solvent casting method and followed by the mechanically blending process on TSE for the preparation of feedstock filaments. These feedstock filaments were further used on an open-source 3D printer for the fabrication of standard prototypes and piezoelectric sensors.

5.3.1 MFI of CAMB compositions of PVDF/Gr/BTO

For the chemical blending of materials, the same three proportions of fillers were reinforced in PVDF as used in the MB method. Initially, Gr 2% by weight was added in PVDF, and then BTO was added in three different proportions in 10%, 15%, and 20% by weight of PVDF/Gr. After the chemical mixing of materials, the MFI of all three compositions was checked. Table 5.36 shows the proportion of composition by weight and their respective MFI values.

Table 5.36 MFI at different proportion of materials

Composition/Proportion (wt%)	X [PVDF (98%) +Gr (2%)]	Y [BTO]	MFI (X+Y) (g/10min)
A	90	10	3.98
B	85	15	3.20
C	80	20	2.90

Further the results of MFI were used to determine the n viscosity of the composition prepared by chemical mixing of materials. The following two equations were used to calculate viscosity in relation to density and MFI values

$$\mu = \frac{9.13 \text{ x } 10\text{^}4 \text{ L x } \rho}{1.83 \text{ x MFI}} \quad \text{dynes} - \text{s}$$

or

$$\mu = \frac{9.13 \text{ x } 10\text{^}4 \text{ L x } \rho}{1.83 \text{ x MFI x } 10} \quad \text{Pa} - \text{s}$$

To calculate the density of composition a ratio proportion method was used. Table 5.37 shows the composition along with the density of the composition in g/cm^3 and viscosity of all three compositions.

Table 5.37 Composition of materials along with the density and viscosity

Composition/ Proportion (wt%)	Density (ρ) g/cm^3	MFI g/(10min) CAMB sample	Viscosity (μ) in (Pa-s) of CAMB sample
A	2.187	3.98	5924.31
B	2.392	3.20	8059.03
C	2.597	2.90	9654.85

5.3.2 Tensile testing of feedstock filaments prepared by the mechanically blended method

After successfully synthesis of nanocomposite films of all three proportions of PVDF/Gr/BTO sheets were cleaved into small sizes. These cleaved parts of the sheets were put into the TSE for the development of feedstock filament. The commercial TSE (Make:

Thermo scientific HAAKE, Germany) was used for the extrusion of filament as per the control log of experimentation for available FDM setup, the required diameter of the extruded feedstock filament should be in the range of 1.75±0.05mm, as the nozzle opening of existing FDM supports only this size of filament. After the extrusion process, feedstock filaments were subjected to destructive (tensile) testing on UTM (Make Shanta Engineering, India) by using a load cell of 10 KN, and the accuracy of the load cell is 0.5 N. For tensile testing, the prepared samples were fit in the clamps of the machine. Then the machine was started to put weight on the lower clamp, whereas the upper clamp remains to fix. The applied force is increasing continuously at a very small rate of 5 mm/ min the results of tensile testing in the form of PL, BL, PS, and BS are shown in Table 5.38).

Table 5.38 Results of tensile testing of feedstock filaments

EXP. NO.	PL (N)	BL (N)	PS (MPa)	BS (MPa)
1	75.5	67.95	31.41±1.04	28.26±0.58
2	85.8	77.22	35.69±1.75	32.12±0.60
3	102.9	92.61	42.80±0.86	38.52±1.05
4	83.8	75.42	34.86±0.75	31.37±0.90
5	81.8	73.62	34.03±1.96	30.62±0.48
6	91.6	82.44	38.10±1.25	34.29±0.98
7	56.8	51.12	26.63±0.58	21.26±0.50
8	54.9	49.41	22.84±0.95	20.55±0.74
9	70.6	63.54	29.37±0.80	26.43±0.68

The stress-strain curves obtained from tensile testing of feedstock filaments are shown in Figure 5.33.

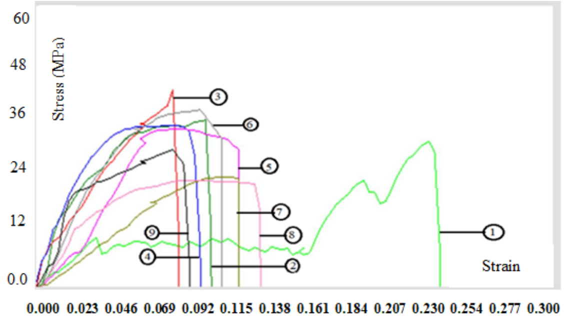

Figure 5.33 Stress versus strain curves for the prepared feedstock filament

Further the results of tensile testing were used to obtain the MoT of the material. It has been calculated from the BS of the material and strain of the developed composites observed in tensile testing. The MoT of extruded filaments is shown in Table 5.39.

Table 5.39 MoT of feedstock filaments

Exp. No.	Strain	BS (MPa)	MoT (MPa)
1	0.234	28.26	3.31
2	0.101	32.12	1.63
3	0.082	38.52	1.59
4	0.095	31.37	1.49
5	0.117	30.62	1.79
6	0.108	34.29	1.85
7	0.117	21.26	1.25
8	0.130	20.55	1.33
9	0.089	26.43	1.17

As observed from Table 5.39, the maximum value of PS (42.80 MPa) and BS (38.52 MPa) were noted in experiment No. 3, however, the minimum tensile strength was found in experiment No.8. Therefore, the processing conditions of experiment No. 8 can be rejected outrightly. Signal to noise values of PL, BL, PS, and BS are shown in Table 5.40). Based upon these observations for 3D printing feedstock filament with maximum tensile strength (experiment No. 3) may be selected for further processing. Further to optimize the processing condition of TSE for tensile strength (PS and BS) ANOVA was performed. For these mechanical properties, the SN ratios at larger the better type case are shown in Table 5.40.

Table 5.40 SN values for PL, BL, PS, and BS

PL (SN)	BL (SN)	PS (SN)	BS (SN)
37.56	36.64	29.94	29.02
38.67	37.75	31.05	30.14
40.25	39.33	32.63	31.71
38.46	37.55	30.85	29.93
38.25	37.34	30.64	29.72
39.24	38.32	31.62	30.70
35.09	34.17	27.47	26.55
34.79	33.88	27.17	26.25
36.98	36.06	29.36	28.44

5.3.3 Optimization for PS

Figure 5.34 shows the SN response for PS. The SN graph represents that extruder temperature shows a remarkable effect when changed from level 1 to level 3. Two parameters of TSE were selected and from the SN graph, it has been found that both parameters put a significant effect on the PS of the specimen. Thus, with the increase in the proportion of BTO in PVDF/Gr, its strength first increases but after that it again starts decreasing. In case of temperature when it was raised from 180 to 200°C, the PS decreases, the rpm of the screws Increases the PS of the specimen at a higher speed more uniform dispersion of fillers may occur in base polymer matrix. However in comparison with SN graph for PS (Figure 5.2) of MB feedstock filaments; composition played a significant role in mechanical blending process. Thus due to different processing routes, the outcome significant parameters are also different.

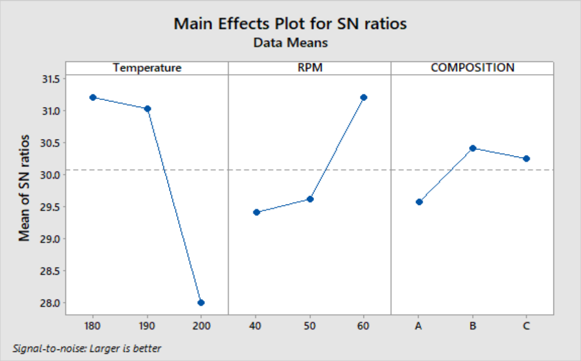

Figure 5.34 SN graph for PS of filaments

The analysis for SN values was carried out at 95% confidence level. The factor having P value less than 0.05 is found significant otherwise the factor may find insignificant. ANOVA of SN ratios for PS shows that two parameters that is extruder temperature and screw speed are found significant at 95% confidence level. However, the composition is found insignificant as its P-value is 0.071 i.e., not less than 0.05. The temperature has a major contribution towards the PS i.e., more than 73%, whereas rpm has an 18% contribution. The total percentage error was only 0.35%, which represents the higher level of accuracy in this model.

Table 5.41 ANOVA for SN ratios (PS of filaments)

Factor	DoF	Seq. SS	Adj SS	Adj MS	F	P	%age Contribution
Temperature	2	19.516	19.516	9.76	216.98	0.005	73.63
rpm	2	4.718	4.718	2.36	63.58	0.015	17.80
Composition	2	2.181	2.181	1.090	13.14	0.071	8.22
Residual Error	2	0.090	0.090	0.045			0.35
Total	8	26.505					

Based upon Table 5.41, the rank table (Table 5.42) shows the ranking of process parameters for SN values of PS. As observed from Table 5.41 and 5.42, the first parameter (temperature) has a most effective role as it stood 1st, whereas rpm and composition of filament ranked 2nd and 3rd respectively. The main effects plot for SN ratios is shown in Figure 5.34, which represents that the filament fabricated at 180°C of extruder temperature and speed of screw 60 rpm and intermediate level of composition will have the best mechanical properties.

Table 5.42 Response table of input parameters for PS of filaments

Levels	Temperature	rpm	Composition
1	31.21	29.42	29.58
2	31.03	29.62	30.42
3	28.00	31.20	30.25
Delta	3.21	1.78	0.84
Rank	1	2	3

The SN values obtained (Table 5.40) has been further used for the prediction of optimized value using equation 5.16

$\eta opt = R+(RA–R) +(RB–R) +(RC–R)$ ……….. (5.16)

$R=30.08, RA = 31.21, RB = 31.20, RC = 30.42$

After putting these values in the equation (5.16)

$\eta opt= 32.67$

Now,

$y_{opt}2 = (10)^{\eta opt / 10}$ (for larger the better type case)……….(5.17)

$Y_{opt}^{2} = (10)^{32.67/ 10}$

$Y_{opt}^{2} = 1849.27$

Yopt=43.00 MPa

Three repetitive confirmatory experiments were conducted at proposed settings and an average value of observed PS is 43.18 MPa, which is very close to the calculated value i.e. 43.00 MPa.

5.3.4 Optimization of BS

Based upon the SN ratios of BS the SN response graph at larger the better conditions are shown in Figure 5.35. Similar to the PS, the results for BS of MB specimens (Figure 5.3) and BS of CAMB specimens (Figure 5.35) shows variation in significant parameters.

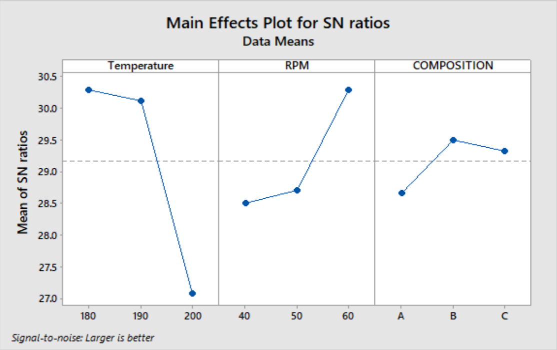

Figure 5.35 SN graph for BS of feedstock filament

Based upon Table 5.40, the ANOVA table for SN values of BS at 95% confidence level is presented in Table 5.43.

Table 5.43 ANOVA Table for SN ratios of BS

Factor	DoF	Seq. SS	Adj SS	Adj MS	F	P	%age Contribution
Temperature	2	20.529	20.529	10.26	216.19	0.005	77.37
rpm	2	5.729	5.729	2.86	63.43	0.016	21.59
Composition	2	0.185	0.185	0.092	13.11	0.071	0.70
Residual Error	2	0.090	0.090	0.045			0.34
Total	8	26.533					

Table 5.44 displays the rank of process parameters based upon the SN ratios of BS. It has been observed that temperature puts a major effect on the BS followed by rpm and composition with rank 2nd and 3rd respectively.

Table 5.44 Response table of input parameters for BS of feedstock filament

Levels	Temperature	rpm	Composition
1	30.29	28.50	28.66
2	30.12	28.70	29.50
2	27.08	30.29	29.33
Delta	3.21	1.78	0.84
Rank	1	2	3

The SN values of BS (Table 9) has been further used for the prediction of optimized value using equation 5.18

$\eta opt = R+(RA–R) +(RB–R) +(RC–R)$ ………… (5.18)

where RA, RB, and RC are the maximum values of temperature, RPM, and composition from Table 5.44 and R is the mean of SN values for PS.

R=29.16, RA = 30.29, RB = 30.29, RC = 29.50

After putting these values in the equation (5.18)

$\eta opt= 31.76$

Now,

$y_{opt}2 = (10)^{\eta opt / 10}$ (for larger the better type case)

$Y_{opt}^2 = (10)^{31.76/ 10}$

$Y_{opt}^2 = 1499.68$

Y_{opt}=38.73 MPa

A total of three repetitive confirmatory experiments were conducted at proposed settings and an average value of observed BS was 38.80 MPa, which is very close to the calculated value i.e. 38.73 MPa.

5.3.5 Dimensional analysis

After mechanical testing of feedstock filaments of PBGC prepared by CAMB process were further subjected to dimensional analysis. To minimize the experimental error, a total of three readings were taken at three different places over the total span length of the filaments. The average diameters (Ø) of the three measured dimensions were compared with the required standard diameter of the filament. Measured dimensions of the filament and their comparison with the standard dimensions are shown in Table 5.45. It has been observed that the filament extruded as per experiment No. 3 has minimum deviation, whereas the filament extruded as per experiment no. 8 has maximum deviation. These observations are in line with the results of mechanical testing.

Table 5.45 Measured dimensions of the feedstock filaments

Experiment No.	Parameter(A) *Temperature (℃)*	Parameter(B) *RPM*	Parameter(C) *Composition wt%*	Ø avg (mm)	Ø (required) (mm)	ΔØ
1	180	40	A	1.69	1.75	0.06
2	180	50	B	1.74	1.75	0.01
3	180	60	C	1.76	1.75	0.01
4	190	40	B	1.69	1.75	0.06
5	190	50	C	1.71	1.75	0.04
6	190	60	A	1.72	1.75	0.03
7	200	40	C	1.89	1.75	0.14
8	200	50	A	1.81	1.75	0.06
9	200	60	B	1.80	1.75	0.05

5.3.6 Surface porosity

After the mechanical and dimensional testing of all fabricated filaments, it has been observed that the filament extruded as per experiment No. 3 (prepared at 180^{o}C processing temperature, 60 rpm, and composition/proportion “B”) has shown the best mechanical properties, and filament extruded as per experiment no. 8 resulted into poor mechanical properties. Further, to ascertain the effect of processing conditions on the surface properties (such as porosity/voids and surface roughness) of the extruded filaments, morphological analysis was performed. Figure 5.36 shows the photomicrographs of the surfaces of the filaments with the percentage of Φ on the surface. The red zone is the porosity in the selected area for the analysis of percentage porosity. It has been observed from the photomicrograph’s filament shown maximum tensile strength has less porosity (Φ=1.53%) on its surface as compared to the other filaments. Whereas the filament having poor mechanical properties is having a maximum percentage of porosity (Φ=5.58%) among the all samples.

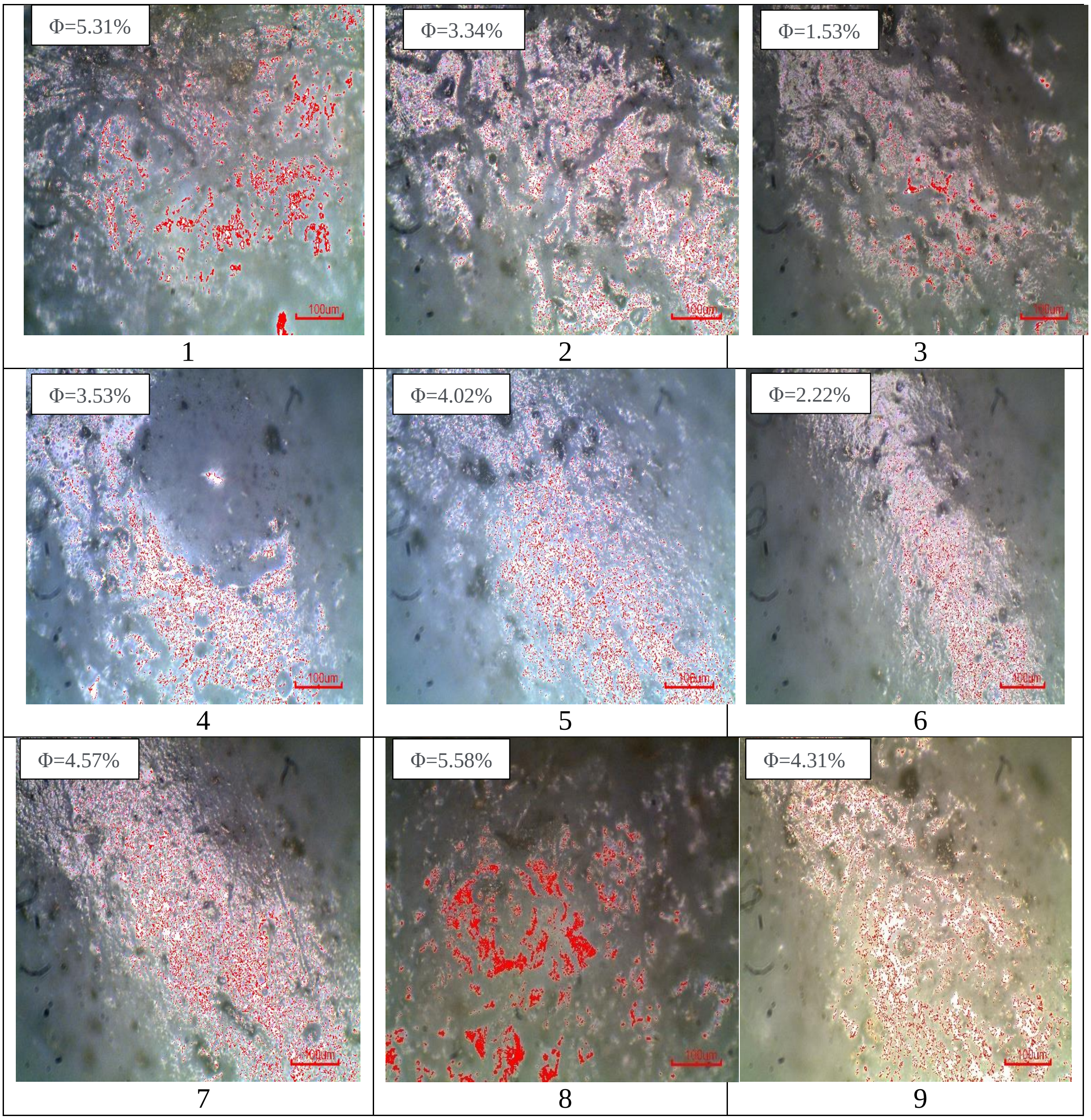

Figure 5.36 Optical photomicrographs with a variation of percentage porosity

5.3.7 Thermal analysis

The PVDF is known for its high thermal resistance; however, to study the effect of reinforced materials on the thermal properties of the polymer matrix, thermal analysis was performed. Thermal properties of the material play a very effective role in the use of the material in a particular application. The results of mechanical testing suggested that the filament extruded at 180°C processing temperature, 60 rpm and composition ‘B’ has maximum tensile strength.

For thermal analysis of the filaments, a DSC (Make: METTLER TOLEDO, Swiss with STARe (SW 14.00) software) was used. In this present study, two samples were prepared for thermal analysis; the first sample was taken from the filament shown the best mechanical strength, and the second sample was taken from the filament with the worst mechanical strength. Thermal analysis was performed in the presence of N_2 gas.

Thermal graphs for two samples are shown in Figure 5.37. Curve 1 is for the filament with maximum tensile strength (prepared at 180°C processing temperature, 60 rpm and composition/ proportion ‘B’), whereas curve 2 is of filament with poor mechanical properties. For thermal analysis, each sample faced two repetitive heating-cooling cycles, by keeping the temperature range from 30°C to 250°C. The samples were heated at the rate of 10K/min. As observed from curve 1, it clearly depicts that, the melting of material starts at 164°C and ends at 177°C. The melting point of composite material is 174°C and the solidification of the material starts at 146°C and ends at 140°C. An almost similar trend has been observed in the 2nd cycle of heating and cooling. Thermal cycles for curve 2 also show almost the same values of the temperature for melting and solidification of the material. Hence, it is ascertained that the addition of Gr and BTO does not affect the liquefaction and solidification of the PVDF matrix even in CAMB. Moreover, the similar trends obtained from both cycles of thermal analysis justify the thermal consistency of the material.

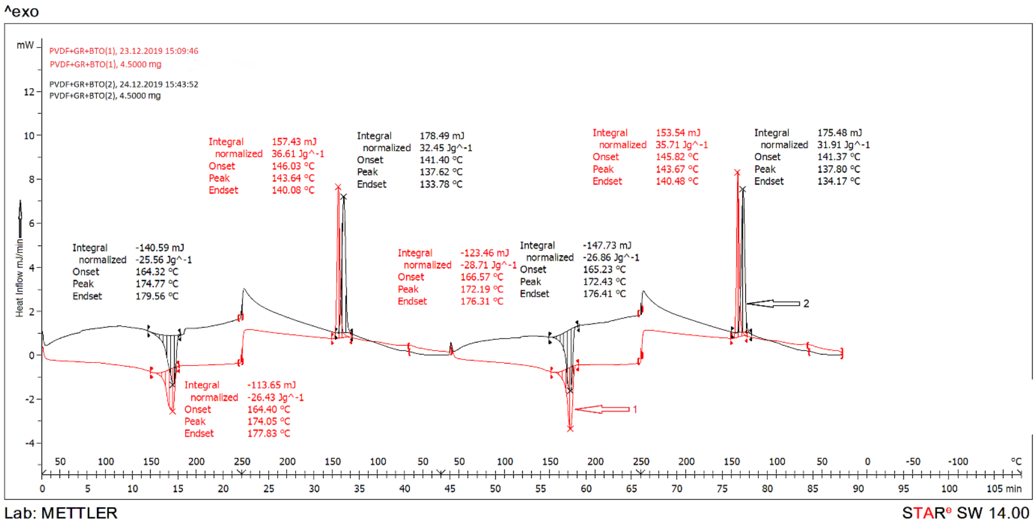

Figure 5.37 DSC graphs of composites developed as per the settings shown best and worst mechanical properties

However, there is a difference in the energy absorption rate of both samples. Curve 1 of the sample having more BTO absorbed 26.43 Jg^{-1} energy, whereas the sample having minimum BTO absorbed less energy i.e., 25.56 Jg^{-1}. However, the 2nd thermal cycles of the samples show that both the samples absorbed more energy than their respective first thermal cycles.

5.3.8 SEM Analysis

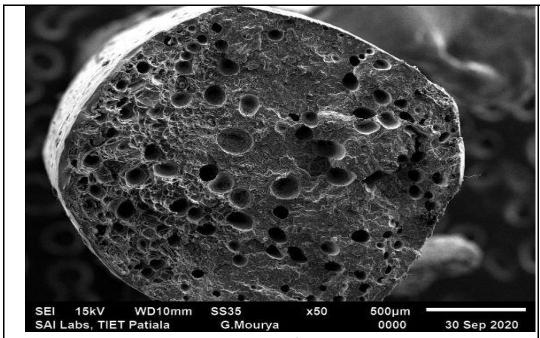 X50	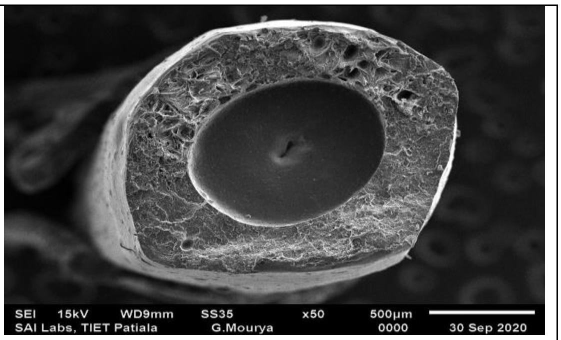 X50
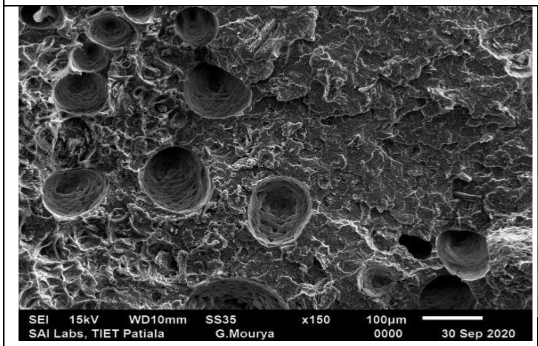 X150	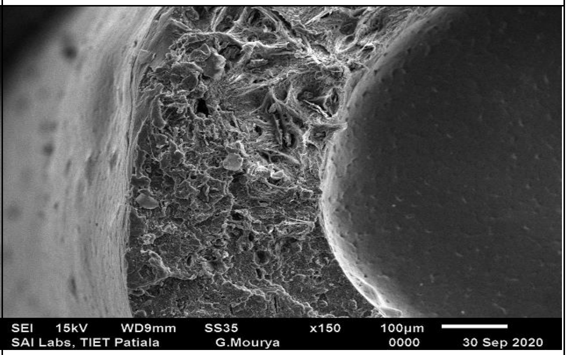 X150
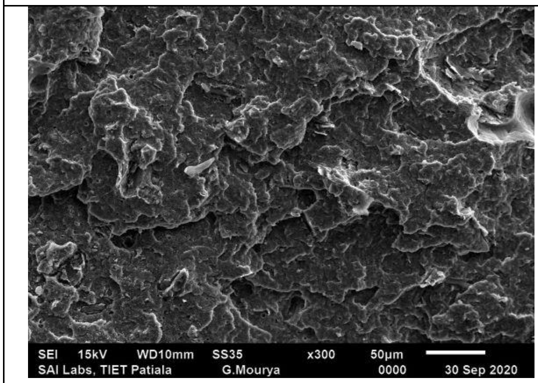 X300	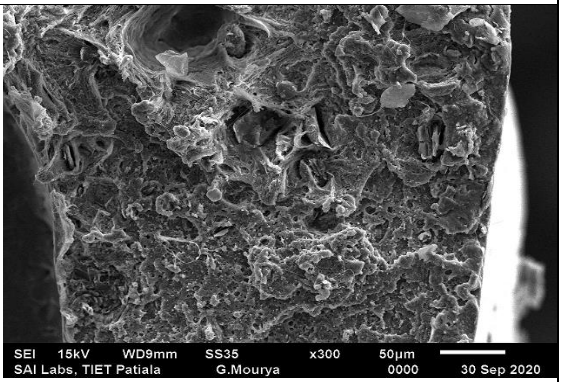 X300
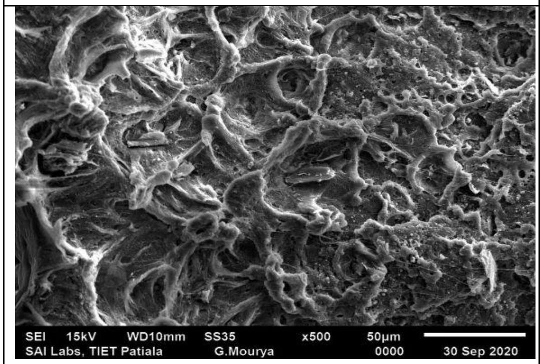 X500	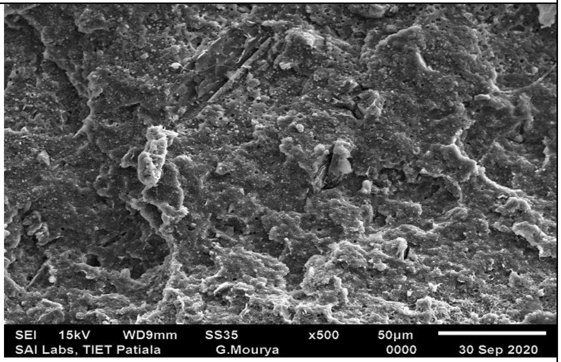 X500
(a) SEM images of CAMB feedstock filament (best mechanical properties)	(b) SEM images of CAMB feedstock filament (worst mechanical properties)

Figure 5.38 SEM images of fractured surfaces of feedstock filaments

Further, the fractured surfaces of feedstock filaments having the best and worst mechanical properties were also subjected to SEM analysis. Morphological analysis of fractured surfaces of feedstock filament was performed by taking microphotographs at various magnification levels of X50, X150, X300, and X500. It has been observed from the microphotographs that dimple formation occurs at both the surfaces, the filament is shown best mechanical properties having uniform dimples throughout its surface, leads to more tensile strength, However, the filament having poor mechanical properties shows only a big dimple in its center whereas the remaining surface is flat thus leads to non-uniform strength over its entire surface.

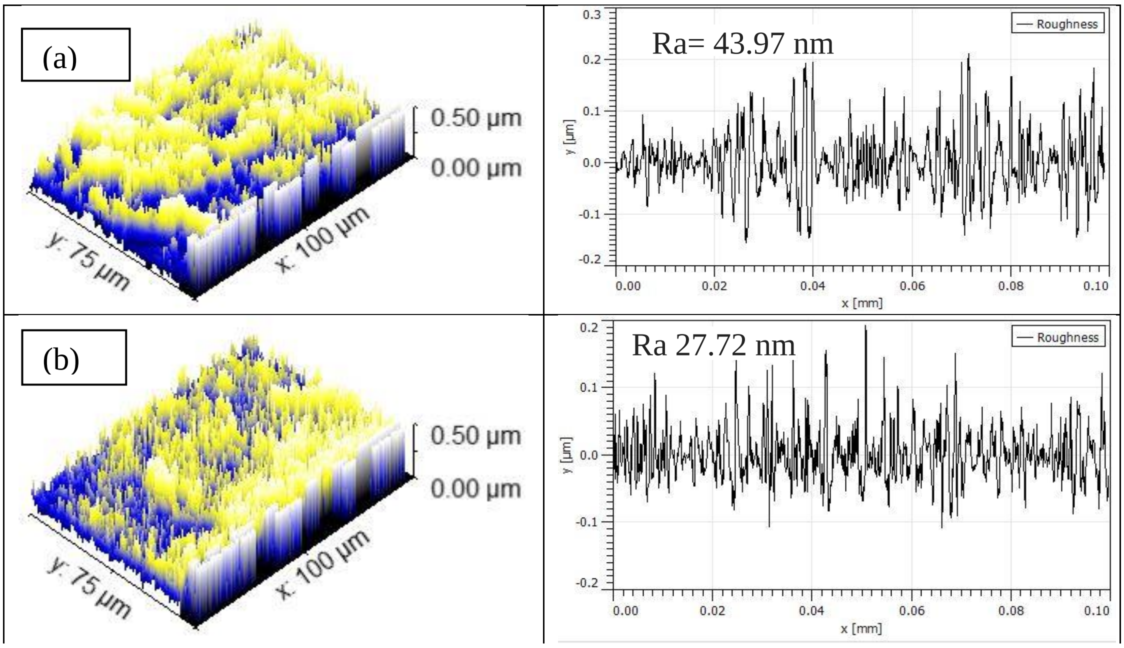

Figure 5.39 (a) and (b) Rendered SEM images of the extruded samples at best and worst parametric settings.

The rendered SEM images taken at X-500 magnification have been used to measure the Ra of the extruded samples (as shown in Figure 5.39). It has been found that the Ra value of sample extruded at settings having poor mechanical properties is less than the Ra value of sample extruded settings having the best mechanical properties. It may be due to more fibrous structure in filament having the best mechanical properties.

Figure 5.40 (a) and (b) shows the EDX analysis of feedstock filament having the worst and best mechanical properties. The element analysis for the filament having poor mechanical strength shown in Figure 5.40 (a) represents that it contains the majority of carbon and fluoride whereas, it contains very less amount of barium, oxygen, and titanium. On the flip side, the element analysis of the filament having the best-required properties (Figure 5.40 (b) shows that it has more amount carbon, barium, titanium, and oxygen as compared to the previous one. Thus, it has been clearly indicated by the EDX analysis that the addition of

BTO and Gr are directly responsible for the enhancement of mechanical and thermal properties of the developed composite.

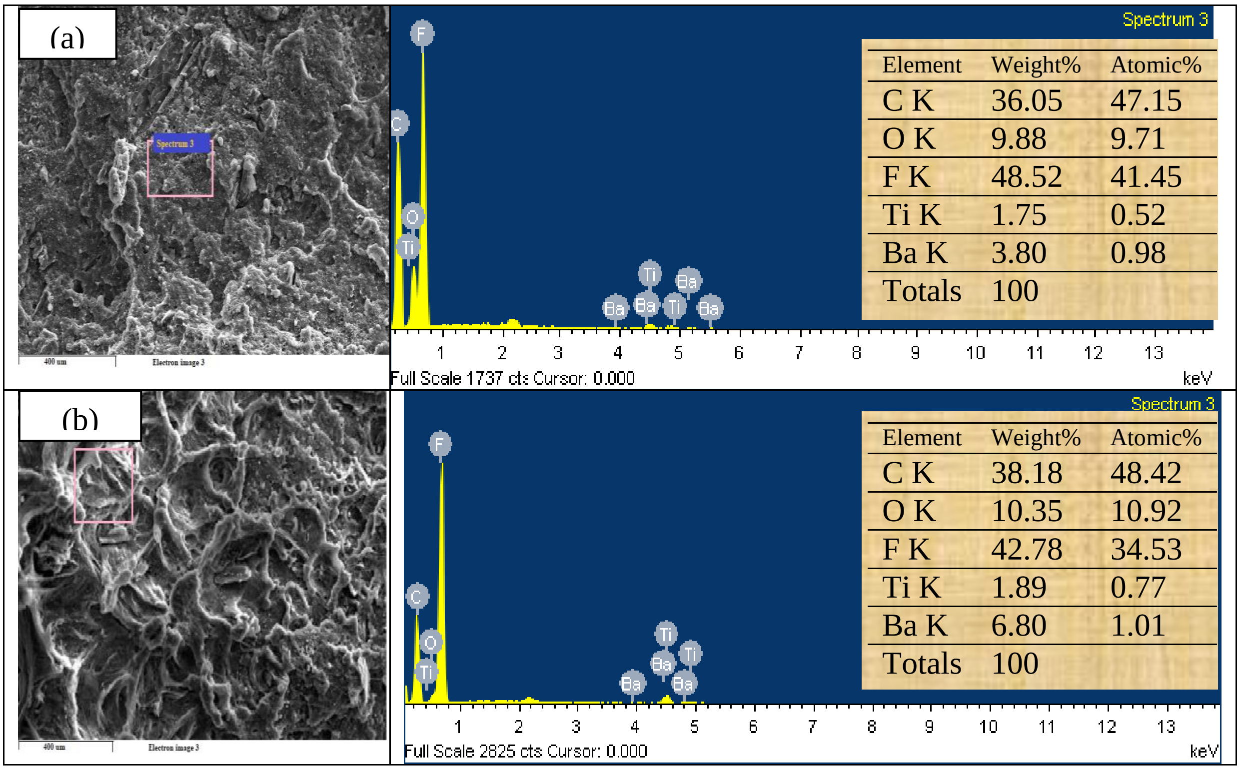

(a)

Element	Weight%	Atomic%
C K	36.05	47.15
O K	9.88	9.71
F K	48.52	41.45
Ti K	1.75	0.52
Ba K	3.80	0.98
Totals	100	

(b)

Element	Weight%	Atomic%
C K	38.18	48.42
O K	10.35	10.92
F K	42.78	34.53
Ti K	1.89	0.77
Ba K	6.80	1.01
Totals	100	

Figure 5.40 (a) and (b) EDX analysis of sample having worst and best mechanical and thermal properties

5.4 Results and discussion (Stage 4)

- **Destructive testing of 3D printed parts for optimization of FDM process parameters**

Feedstock filaments of PBGC prepared by CAMB method having maximum mechanical strength and diameter within 1.75±0.05 mm were further used to run on an open-source 3D printer. A control log of experimentation was prepared as per Taguchi L9 orthogonal array for optimization of FDM process parameters. Standard tensile, flexural, and pull-out specimens were 3D printed as per the design of experiments and further, mechanical testing was performed on the fabricated structures.

5.4.1 Tensile testing

3D printed dumbbell-shaped specimens prepared as per the control log of experimentation were subjected to destructive testing as per ASTM D-638 type IV standard. A total of nine specimens were fabricated as parametric settings (with three repetitions). The tensile testing of specimens was performed on UTM (Make Shanta Engineering, India) by using a load cell of 10 KN and accuracy of load cell is 0.5 N. Results of tensile testing in the form of PL, BL, PS, and BS, are shown in Table 5.46).

The 3D printed parts were further subjected to destructive tensile testing on UTM. Results of tensile testing in the form of PL, BL, PS, and BS, are shown in Table 5.46.

Table 5.46 Output values of tensile strength of 3d printed parts

Exp No.	IS (mm/s)	IA (^{o})	ID (%)	PL (N)	BL (N)	PS (MPa)	BS (MPa)
1	50	0	60	792.0±3.61	730.0±4.58	41.25±0.19	38.02±0.19
2	50	45	80	848.6±4.37	768.4±4.72	44.2±0.23	40.02±0.23
3	50	90	100	1058.7±4.05	950.4±4.88	55.14±0.21	49.5±0.21
4	70	0	60	686.6±3.86	617.5±4.25	35.76±0.20	32.16±0.20
5	70	45	80	919.7±3.48	808.3±2.76	47.9±0.18	42.1±0.18
6	70	90	100	585.6±2.31	541.1±1.58	30.5±0.12	28.18±0.12
7	90	0	60	732.5±1.80	675.8±3.90	38.15±0.09	35.2±0.09
8	90	45	80	427.2±3.29	387.1±3.65	22.25±0.17	20.16±0.17
9	90	90	100	548.9±4.67	500.7±4.90	28.59±0.24	26.08±.024

Table 5.46 has shown the maximum value of PL (1058 N) and BL (950 N) has been found in experiment no. 3, whereas the output values of PS and BS for the same experiment are 55.14 MPa and 49.5 MPa respectively. However, experiment no 8 shows the minimum values of tensile properties such as PL is 427 N and BL 387 N. The output values of tensile testing show that the maximum PS was observed in the part fabricated at the lowest IS (50 mm/s) and having a maximum ID (100%) by depositing the material at 90^o IA. It might be due to proper positioning of material at lower speed and bonding might be also more at 100% ID. However, the part with the worst mechanical properties was built as per experiment no. 8, in which IS was put as maximum and IA was kept 45^o and having an intermediate level of ID. The stress-strain curves obtained from the mechanical testing of 3D printed tensile specimens are shown in Figure 5.41.

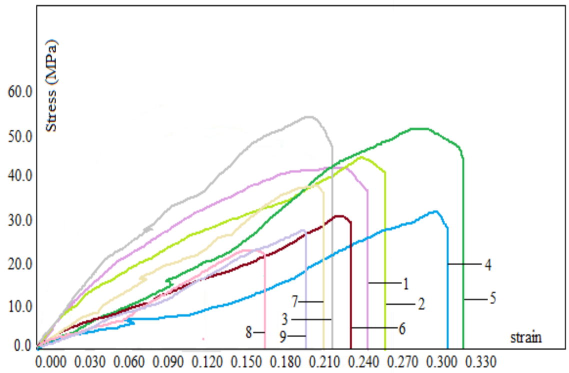

Figure 5.41 Stress-strain curves of tensile tested parts

In stress-strain curves, an area under the curve represents the MoT. The calculated values of MoT are shown in Table 5.47. It has been observed that the maximum value of MoT is 6.82 MPa for experiment no. 5, whereas, experiment no. 8 shows the minimum value of MoT (1.69 MPa).

Table 5.47: MoT of 3D printed parts

Exp. no.	BS (MPa)	Strain	MoT (MPa)
1	38.02	0.249	4.73
2	40.02	0.263	5.26
3	49.5	0.227	5.62
4	32.16	0.312	5.02
5	42.1	0.324	6.82
6	28.18	0.237	3.34
7	35.2	0.212	3.73
8	20.16	0.168	1.69
9	26.08	0.198	2.58

Further, the SN values of the measured tensile properties were calculated using Minitab 17.0 software. For these mechanical properties, the SN at larger the better type case is shown in Table 5.48.

Table 5.48 SN of tensile properties of 3D printed parts

PS (SN)	BS (SN)	FM (SN)	MT (SN)
29.905	28.992	55.124	11.143
33.574	32.657	56.358	22.086
34.720	33.705	58.972	19.612
32.073	31.238	54.857	20.970
35.335	34.639	59.142	24.721
28.986	28.076	53.708	16.799
33.164	32.369	55.757	22.731
29.461	28.543	50.040	20.424
30.301	29.390	53.480	20.341

To optimize the parametric settings of FDM for tensile strength of the printed parts ANOVA tool was used shown in Table 5.49. As the probability (P) value of the first and third parameters (IS and ID) is less than 0.05 (Table 5.49), thus these two parameters are significant at a 95% confidence level. However, for the second parameter (IA) the value of P is not less than 0.05 thus found insignificant. Moreover, the value of residual error is only 1.71% of the total value supports that the optimization model is significant.

Table 5.49 ANOVA for SN ratios (PS)

Factor	DoF	Seq. SS	Adj SS	Adj MS	F	P	%age Contribution
IS	2	25.456	25.456	12.73	31.00	0.031	53.24
IA	2	0.476	0.476	0.24	0.58	0.633	1.00
ID	2	21.064	21.064	10.53	25.65	0.038	44.05
Residual Error	2	0.820	0.820	0.41			1.71
Total	8	47.816					

The main effects plot for SN is shown in Figure 5.42, which represents that the part printed at the first level of IS by keeping the IA 0° and 100% ID having the best mechanical properties. The main graph plot of SN ratios for PS shows that infill speed directly affects the mechanical strength of the part. The increase in infill speed reduced the PS of the 3D printed specimen. However, ID is directly proportional to the tensile strength of the fabricated part. In comparison with the SN graph of 3D printed parts using MB feedstock filaments (Figure 5.11), both charts represent almost similar best levels of IS and ID. However there is difference between the levels of IA.

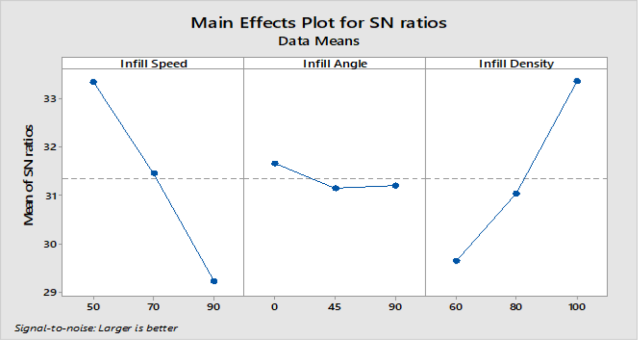

Figure 5.42 SN ratio graph for PS

Based upon Table 5.49, rank table (Table 5.50) shows ranking of process parameters for SN values of PS.

Table 5.50 Response table of input parameters for PS

Levels	IS	IA	ID
1	33.35	31.67	29.65
2	31.45	31.15	31.03
2	29.23	31.21	33.36
Delta	4.12	0.51	3.71
Rank	1	3	2

The SN values obtained (Table 5.51) has been further used for the prediction of optimized value using equation 5.19

$\eta_{opt} = R+(R_A–R) +(R_B–R) +(R_C–R)$ ………… (5.19) where R_A, R_B, and R_C are the maximum values of IS, IA and ID from Table 18 and R is mean of SN values for PS.

$R=31.34$, $R_A = 33.35.21$, $R_B = 31.67$, $R_C = 33.36$

After putting these values in the equation (5.19)

$\eta_{op}t= 35.69$

Now,

$y_{opt}2 = (10)^{\eta opt / 10}$ (for larger the better type case)……….(5.20)

$Y_{opt}^2 = (10)^{35.69/ 10}$

$Y_{opt}^2 = 3706.81$

$Y_{opt} = 60.88$ MPa

Three repetitive confirmatory experiments were conducted at proposed optimized settings and an average value of PS was 62.78 MPa, which is very close to the calculated value i.e. 60.88 MPa. Contour plats represent the effect of change in two significant input parameters on the output responses. Contour graphs have drawn by taking the IA constant i.e., 45°. IS is taken in the Y direction and ID was taken in the x-direction, whereas in the z-axis it shows the change in values of output response with respect to input parameters. The contour graphs of PL, BL, PS, and BS are shown in Figure 5.43.

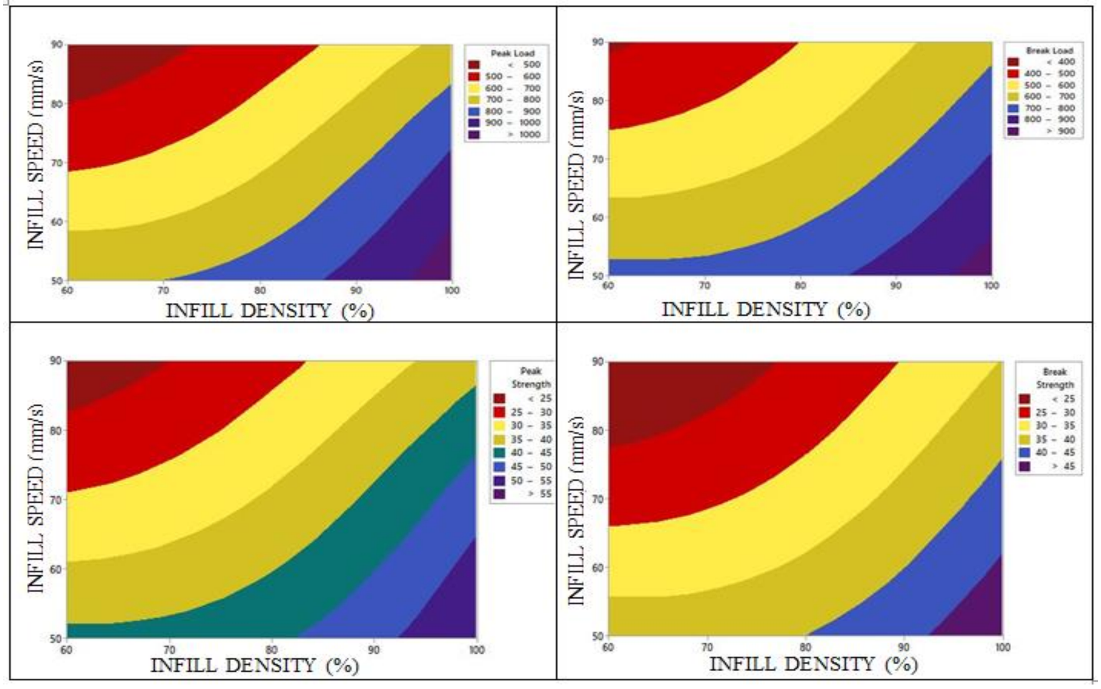

Figure 5.43 Contour graphs of tensile properties

The resulted output values of mechanical testing of each property were further used to fit in the regression model at three levels of interaction, the regression equations of PS, BS, PL, and BL are shown in Table 5.51.

Table 5.51 Regression equations of mechanical properties

PS = 36.99 - 0.4300 IS - 0.0034 IA + 0.3933 ID	(5.21)
BS = 34.80- 0.3842 IS - 0.0060 IA + 0.3370 ID	(5.22)
PL = 710.2 - 8.2560 IS - 0.0660 IA + 7.5500 ID	(5.23)
BL = 668.2 - 7.3760 IS - 0.1150 IA + 6.4700 ID	(5.24)

5.4.2 Morphological properties testing

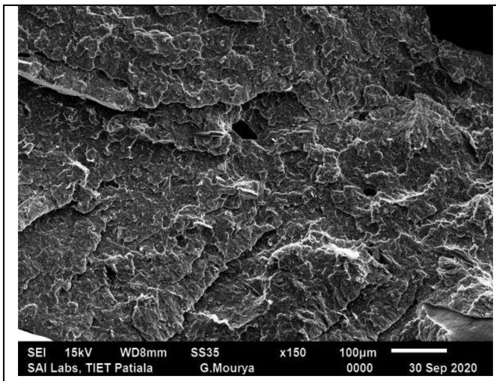 (a) x150	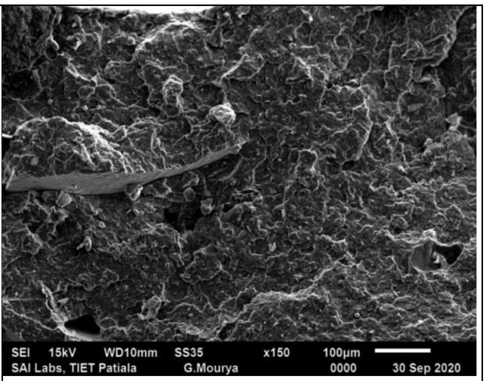 (a) x150
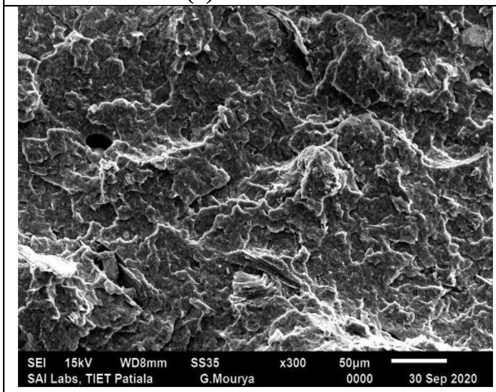 (b) x300	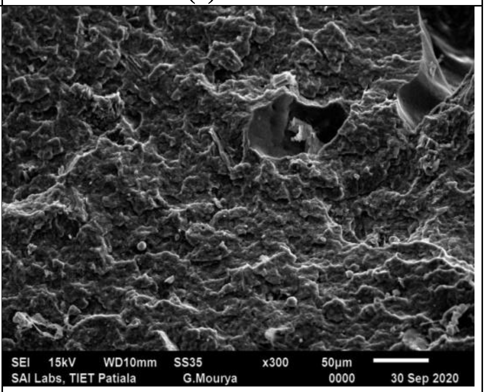 (b) x300
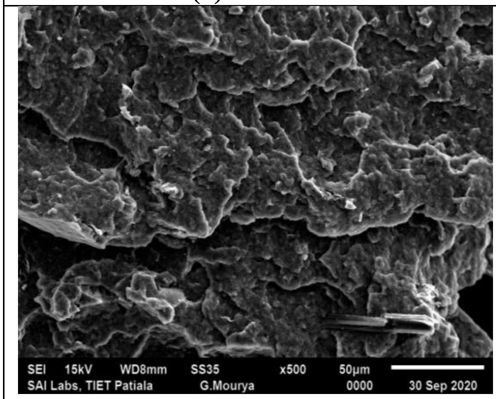 (c) x500	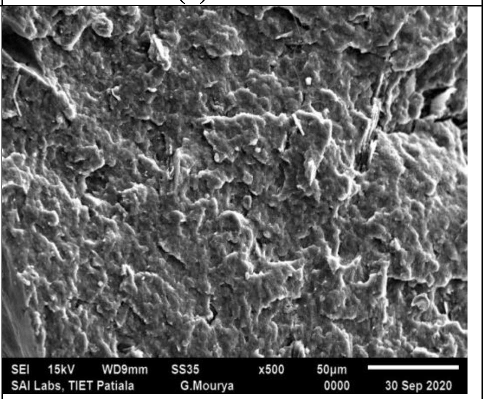 (c) x500
(a) SEM images of the tensile specimen shown best mechanical strength	(b) SEM images of the tensile specimen shown worst mechanical strength

Figure 5.44 SEM images of fractured surfaces of tensile specimens

After destructive testing, fractured surfaces of 3D printed tensile specimens were further to SEM analysis for morphological properties. The samples that have shown best and worst tensile properties were analyzed based on microscopic images. The JEOL JSM-6510LV SEM (Japan) was used to take the micrographs of the flexural samples at three different levels of magnification ×150, × 300, and ×500 (as shown in Figure 5.44). SEM images have clearly shown that parts fabricated at the parametric settings shown the best tensile strength have a fibrous structure with good bonding in between them; moreover there is a dimple formation at the fracture surface that supports the more tensile strength in the specimen.

Further, the SEM images taken at X-500 magnification were rendered using a Gwyddion computer-operated software to measure the R_a of the specimens. The rendered images and graph of R_a shown that the part having maximum tensile strength having low R_a.

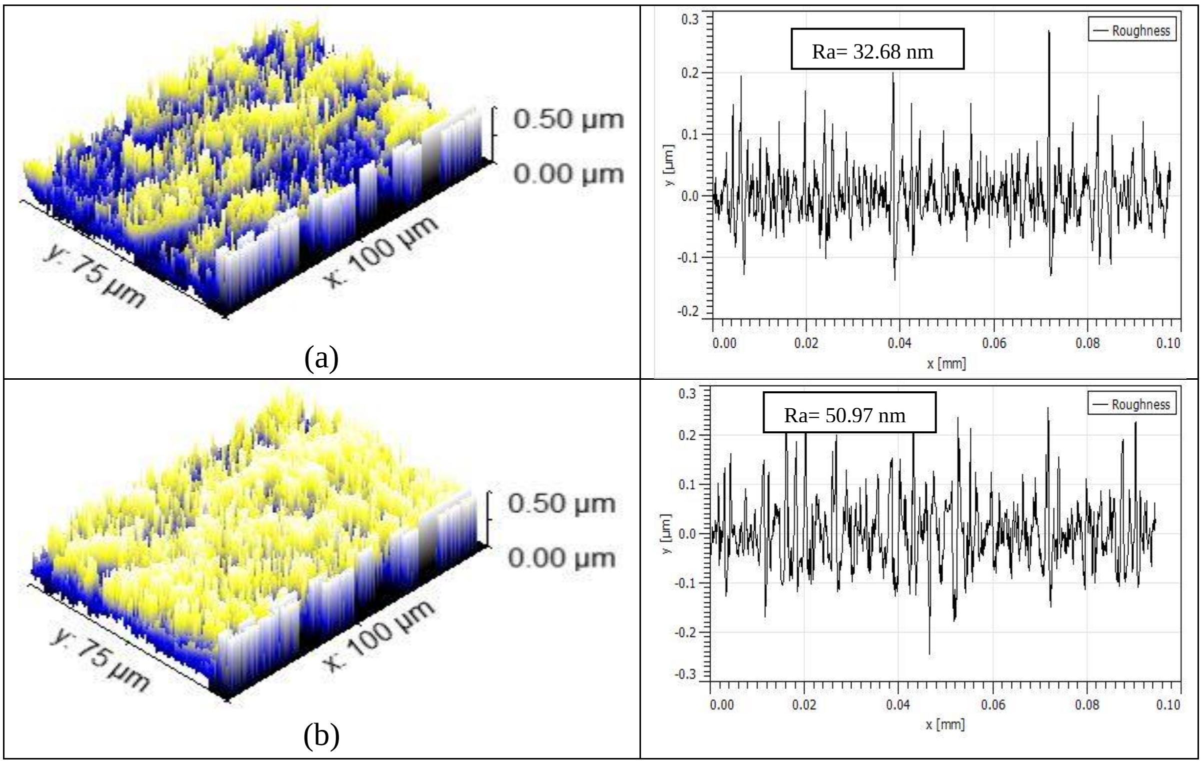

(a)

(b)

Figure 5.45 Rendered SEM images of fractured surfaces and roughness graphs

5.4.3 Flexural Testing

3D printed flexural specimens were also subjected to destructive testing as per ASTM D-790 standard. For flexural testing of standard prototypes, UTM interfaces a computer-controlled machine was used. For all the printed specimens flexural test was performed and observed values of PL, BL, flexural PS, and flexural BS (as shown in Table 5.52) was recorded, further to calculate the flexural modulus and MoT same equations as used for MB specimens were used.

Table 5.52 Flexural testing output

S.No.	PL	BL	PS	BS	FM	MoT
1	88±0.65	78±0.83	51±0.81	45±0.82	1294±9	2.58±0.04
2	100±0.84	86±0.47	58±0.82	49±0.65	1530±13	2.45±0.03
3	105±1.7	95±0.86	61±0.67	55±0.86	2308±37	2.20±0.03
4	109±1.2	100±0.97	63±0.76	58±0.77	1538±17	4.40±0.05
5	123±1.2	107±0.19	71±0.47	62±1.25	1677±17	4.13±0.08
6	99±0.90	88±0.96	57±0.47	51±0.46	1446±13	2.90±0.02
7	97±1.23	86±0.83	56±1.16	50±0.73	2125±27	1.70±0.02
8	83±0.91	73±0.75	48±0.81	42±0.52	1731±18	1.52±0.01
9	90±0.74	83±0.73	52±0.47	48±0.47	1229±10	3.01±0.03

Based upon Table 5.52, maximum value of PL (123.11 N), BL (107.58 N), PS (71.00 MPa), BS (62.04 MPa) were noted in experiment no. 5 (IS 70 mm/s, IA 45^{o} and ID 100 %). This may be due to more strong bonding between the layers and lack of voids formation at 100 % ID when fabricated at IA of 45^{o}, however, the minimum flexural strength was found in experiment no. 8.That was printed at higher IS, i.e. 90 mm/s, lower ID (60 %) and IA was 45^{o}. Thus it might have led to lower bonding between the layers due to more gap between the successive layers.

Stress-strain curves obtained from the mechanical testing are shown in Figure 5.46. For these mechanical properties, the SN ratios at larger the better type case is shown in Table 5.53.

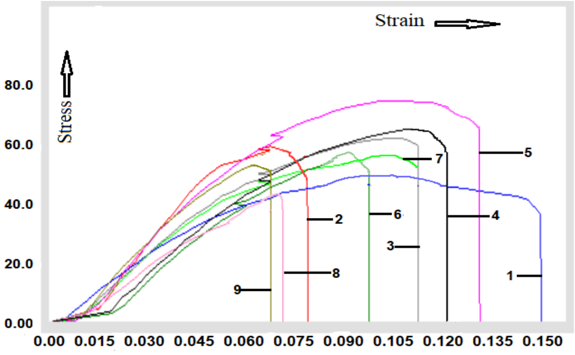

Figure 5.46 Stress-strain curves obtained from flexural testing

To optimize the FDM process parameters for flexural properties (PS, BS, FM, and MT) ANOVA has been used (Table 5.54 As the probability (P) value of all three selected parameters is less than 0.05, in Table 5.54, thus all these parameters are significant at 95 %

confidence level. Moreover, the value of residual error is only 0.13 % of the total value which supports that optimization model is significant.

Table 5.53 SN values for PS, BS, FM and MT

PS (SN)	BS(SN)	FM(SN)	MT(SN)
34.15	33.11	62.24	8.23
35.27	33.91	63.69	7.78
35.65	34.83	67.27	6.85
35.97	35.25	63.74	12.87
37.03	35.85	64.49	12.32
35.12	34.15	63.21	9.25
34.94	33.94	66.55	4.61
33.63	32.50	64.77	3.64
34.32	33.62	61.79	9.57

Table 5.54 ANOVA table based upon the SN values of PS

Factor	DoF	Seq. SS	Adj SS	Adj MS	F	P	%C
IS	2	4.598	4.598	2.299	431.77	0.002	54.04
IA	2	0.161	0.161	0.080	15.15	0.062	1.89
ID	2	3.738	3.738	1.869	351.02	0.003	43.94
Residual Error	2	0.011	0.011	0.005			0.13
Total	8	8.508					

Based upon Table 5.54, Table 5.55 shows rank of process parameters for the main effects plot for SN ratios is shown in Figure 5.47.

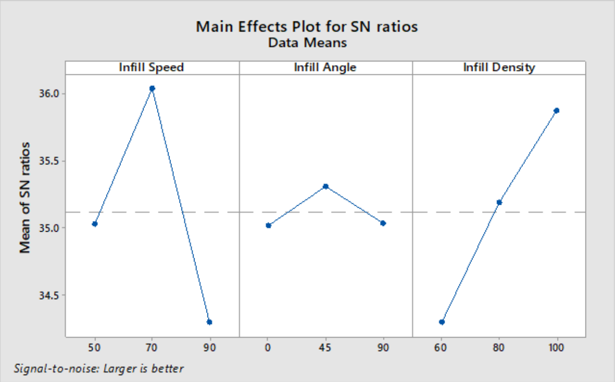

Figure 5.47 SN ratio graph for PS

Table 5.55 Ranking of input parameters for PS

Levels	IS	IA	ID
1	35.03	35.02	34.30
2	36.04	35.31	35.19
3	34.29	35.03	35.87
Delta	1.74	0.29	1.57
Rank	1	3	2

For prediction of optimized values for flexural properties ANOVA statistical tool has been used. The SN values obtained from Minitab software has been further used for the prediction of optimized value using equation 5.25

$\eta_{opt} = R+(R_{A2}–R) +(R_{B2}–R) +(R_{C3}–R)$ ……….. (5.25)

where R_{A2}, R_{B2}, and R_{C3} are the maximum values of IS, IA and ID from Rank Table and R is mean of SN values (obtained from Minitab) for PS.

$R=35.12$, $R_{A1} = 36.04$, $R_{B2} = 35.31$, $R_{C3} = 35.87$

After putting these values in the equation 5.25

$\eta_{opt} = 36.98$

Now,

$y_{opt}2 = (10)^{\eta opt / 10 (}$for larger the better type case) ……… (5.26)

$Y_{opt}^{2} = (10)^{36.98/ 10}$

$Y_{opt}=70.63$ MPa

A total of three repetitive experiments performed at settings suggested by ANOVA table and the average PS was found 71.00 MPa which is very close to the calculated value i.e., 70.63 MPa.

The contour graphs of PL, BL, PS, and BS are shown in figure 5.48.

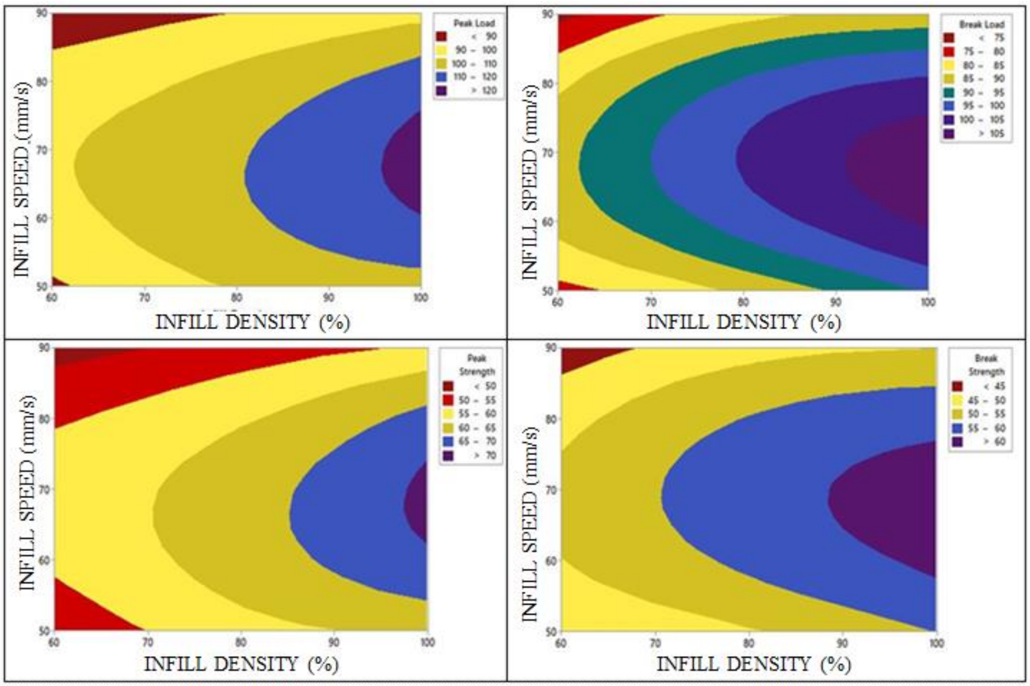

Figure 5.48 Contour graphs of flexural properties

Contour plots represent the effect of change in two significant input parameters on the output responses. Contour graphs have drawn by taking the IA constant i.e., 45°. ID is taken in the x direction and IS was taken in y direction, whereas in z axis it shows the change in values of output response with respect to input parameters.

The resulted output values of mechanical testing of each property were further used to fit in regression model at three level of interaction, the regression equations of PS, BS, PL and BL are shown in the Table 5.56.

Table 5.56 Regression equations of flexural properties

PS = 44.5 - 0.116 IS - 0.0002 IA + 0.262 ID	(5.27)
BS = 37.7 - 0.083 IS + 0.0043 IA + 0.238 ID	(5.28)
PL = 77.2 - 0.200 IS - 0.0003 IA + 0.455 ID	(5.29)
BL = 65.4 - 0.144 IS + 0.0076 IA + 0.413 ID	(5.30)

5.4.4 Pull out Testing

Similar to flexural testing, experiments were also performed for pull out testing that is a relative comparison to check out the pull-out strength of the printed parts. For establishment of pull out properties of 3D printed samples, an eye bolt screw was used. It was screwed inside the 3D printed specimen with 3 cycles of thread. The dimensions of the screw threads are shown in the Table 5.57.

Table 5.57 Thread profile of a screw

S. No.	Terminology	value
1.	Outer Diameter	2.2 mm
2.	Inner Diameter	1.6 mm
3.	Pitch	1.06 mm
4.	Thread angle	75^o

The pull-out test was performed on the UTM (Make: Shanta Engineering, Pune, India) of 5000 N capacity. For pull-out test, screw was tightened in the specimen and pulling (shear) force was applied to the specimen on UTM. The results obtained from the pull-out test are shown in Table 5.58. It has been observed from the Table 5.58 that, the sample no. 7 shows maximum shear PS (22.63 MPa) and maximum shear BS (20.36 MPa), which was printed by keeping the IS 90 mm/s, at ID 100 % and the IA was set at 0^o, whereas sample no. 1 shows the maximum shear modulus (8.07 MPa). Figure 5.49 shows the stress versus strain curves obtained from destructive testing performed at UTM.

Table 5.58 Observations obtained from the pull-out testing

Sample No.	PL (N)	BL (N)	Peak elongation (mm)	Break elongation (mm)	Shear strength at peak (MPa)	Shear strength at break (MPa)	Shear modulus (MPa)	MoT (MPa)
1	242	218.43	4.37	4.94	11.02	9.94	8.07	7.67
2	205	189.58	8.55	8.55	9.33	8.63	3.49	11.53
3	248.4	230	15.10	15.24	11.31	10.47	2.40	24.93
4	283	268	9.31	16.03	12.88	12.20	4.43	30.55
5	323.4	291.06	9.12	9.12	14.72	13.25	5.16	18.88
6	199.8	179.82	7.22	10.45	9.09	8.18	4.03	13.36
7	497.1	447.39	10.83	11.78	22.63	20.36	6.69	37.48
8	245.4	220.86	8.36	8.55	11.17	10.05	4.28	13.43
9	229.2	206.28	7.6	7.98	10.43	9.39	4.39	11.71

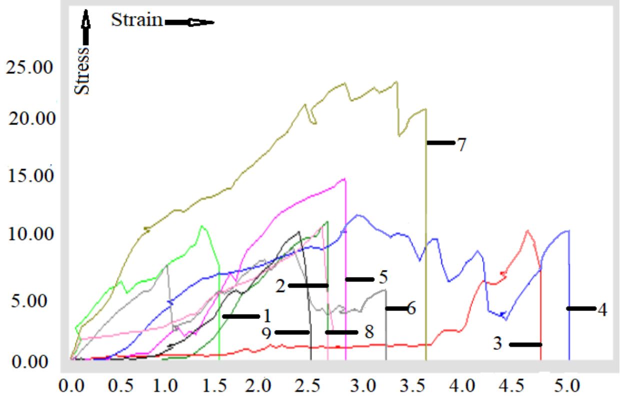

Figure 5.49 Stress strain curves for pull out properties

Further ANOVA was used, for the optimization of pull-out properties. SN values for SS at peak, SS at break, SM and MT calculated at larger the best settings (Table 5.59).

Table 5.59: SN values for pull-out properties

SS at Peak (SN)	SS at Break (SN)	SM (SN)	MT (SN)
20.84	19.95	18.14	17.70
19.40	18.720	10.86	21.24
21.07	20.40	7.60	27.93
22.19	21.73	12.93	29.70
23.36	22.44	14.25	25.52
19.17	18.25	12.11	22.52
27.10	26.18	16.51	31.48
20.96	20.04	12.63	22.56
20.37	19.45	12.85	21.37

It has been observed from Table 5.60 that P value for all three input parameters is less than 0.05 so all have found significant at 95 % confidence level. The percentage contribution of residual error is only 0.8% represents the significance of tool.

Table 5.60 ANOVA Table based on SN values of SS at peak

Factor	DoF	Seq.SS	Adj SS	Adj MS	F	P	%C
IS	2	8.429	8.429	4.215	22.51	0.043	17.87
IA	2	15.743	15.743	7.871	42.04	0.023	33.38
IID	2	22.617	22.617	11.309	60.40	0.016	47.95
Residual Error	2	0.374	0.374	0.187			0.8
Total	8	47.164					

The Table 5.61 shows rank of input process parameters for SN values of SS at peak. The main effects plot for SN ratios is shown in Figure 5.50.

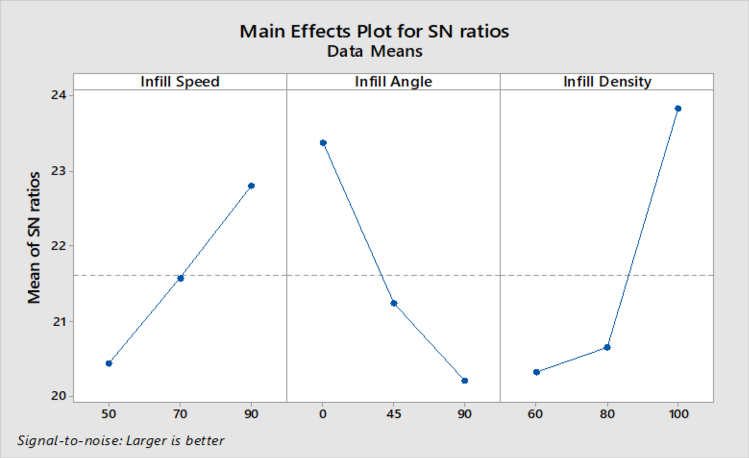

Figure 5.50 SN ratio graph for shear strength at peak

Table 5.61 Rank table for input parameters for SS at peak

Levels	IS	IA	ID
1	20.44	23.38	20.33
2	21.58	21.24	20.65
3	22.81	20.20	23.84
Delta	2.37	3.18	3.52
Rank	3	2	1

The SN values obtained from Minitab software has been further used for the prediction of optimized value using equation 5.31

$\eta_{opt} = R+(R_{x3}-R) +(R_{y1}-R) +(R_{z3}-R)$ ………… (5.31) where R_{x3}, R_{y1}, and R_{z3} are the maximum values of IS, IA and ID from Rank Table and R_{avg} is mean of SN values (obtained from Minitab) for SS at peak.

R_{avg}=21.61, R_{x3} = 22.81, R_{y1} = 23.38, R_{z3} = 23.84

After putting these values in the equation 5.31

η_{opt}= 26.81

Now

$y_{opt}2 = (10)^{\eta opt/ 10}$ (for larger the better type case)………..(5.32)

$Y_{opt}^2 = (10)^{26.81/ 10}$

Y_{opt}=21.90 MPa

A total of three repetitive experiments performed at settings suggested by ANOVA table and the average SS at peak was found 22.63 MPa which is very close to the calculated value i.e. 21.90 MPa.

5.4.5 Multi-optimization

To obtain best parametric settings for flexural and pull-out properties, a Taguchi multifactor optimization technique has been used. In this combine optimization process the values of SN ratios of both flexural (PS) and pull-out (SS at peak) properties have used. Table 5.62 shows the SN values of respective properties and combine SN values. The Table 5.63 shows the ANOVA table of SN values obtained from multifactor optimization. The main effect plot for combine SN rations is shown in Figure 5.51.

Table 5.62 Combine SN values of input parameters

S.no	IS	IA	ID	SN (FS)	SN (Pull-out)	SN (Combine)
1	50	0	60	34.15	20.84	28.01
2	50	45	80	35.27	19.40	27.61
3	50	90	100	35.65	21.07	28.18
4	70	0	80	35.97	22.19	28.53
5	70	45	100	37.03	23.36	28.92
6	70	90	60	35.12	19.17	27.53
7	90	0	100	34.94	27.10	29.62
8	90	45	60	33.63	20.96	28.01
9	90	90	80	34.32	20.37	28.95

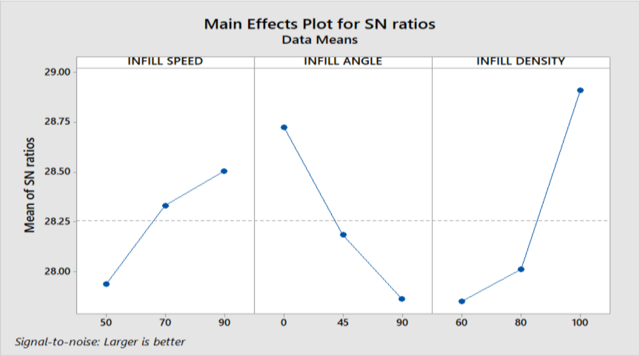

Figure 5.51 Graph for combine SN values

Table 5.63 ANOVA table for combine SN values

Factor	DoF	Seq. SS	Adj SS	Adj MS	F	P	%C
IS	2	0.506	0.506	0.253	378.83	0.003	14.08
IA	2	1.131	1.131	0.565	847.12	0.001	31.47
IS	2	1.955	1.955	0.977	1464.03	0.001	54.39
Residual Error	2	0.001	0.001	0.000			0.06
Total	8	3.594					

Table 5.64 shows the rank of the input parameters on the basis of larger the better type for Combine SN ratios.

Table 5.64 Response table for input parameters

Levels	IS	IA	ID
1	27.94	28.72	27.85
2	28.33	28.19	28.01
3	28.51	27.86	28.91
Delta	0.57	0.86	1.06
Rank	3	2	1

The best parametric settings obtained from the multi-optimization for 3D printing is 90 mm/s IS at 0^{o} infill angle by keeping the ID 100%. A total of 3 confirmatory experiments were performed at the best parametric settings of FDM suggested by multi-optimization. The output values of flexural and pull-out strength were compared with the optimized values. The Table 5.65 shows the results of confirmatory experiments.

Table 5.65 Observations obtained from confirmatory experiments

S.no.	Flexural properties (PS in MPa)	Pull-out testing (SS at peak in MPa)
1	67.41	21.68
2	66.82	22.10
3	67.10	21.84

5.4.6 Microscopic analysis

After the successfully completion of optimization of mechanical properties for flexural and pullout strength of the 3D printed parts, the specimen with best and worst flexural strength were subjected to SEM analysis.

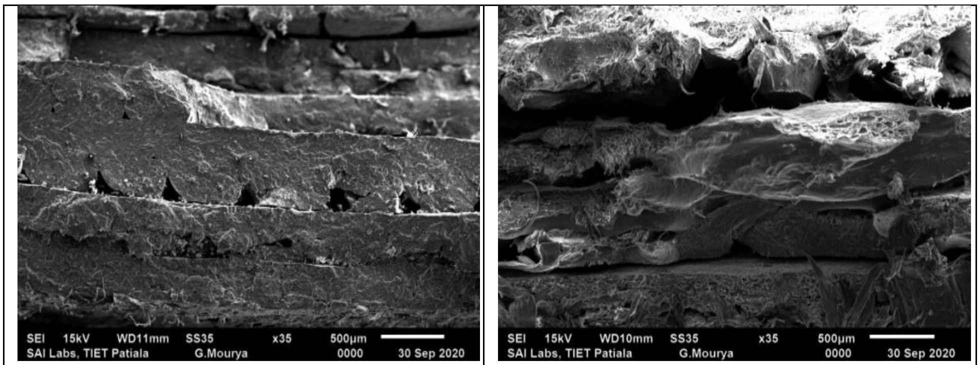

(a) At x35 (b) At x35

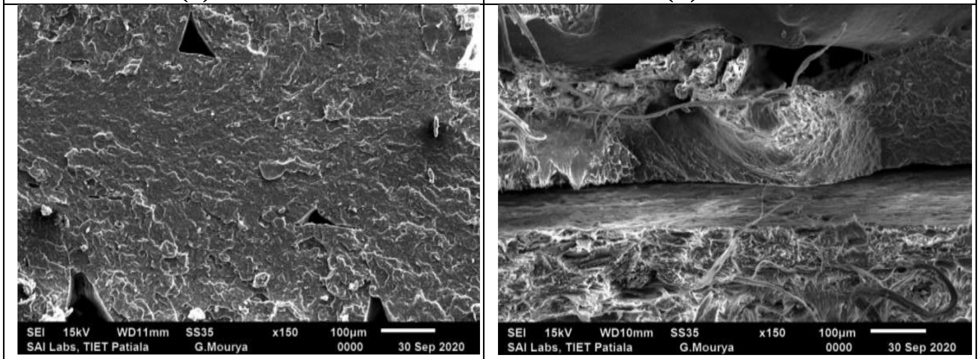

(a) At x150 (b) At x150

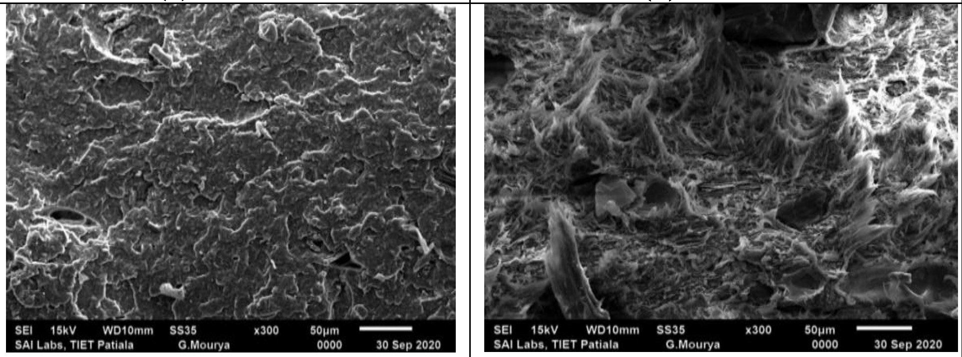

(a) At x300 (b) At x300

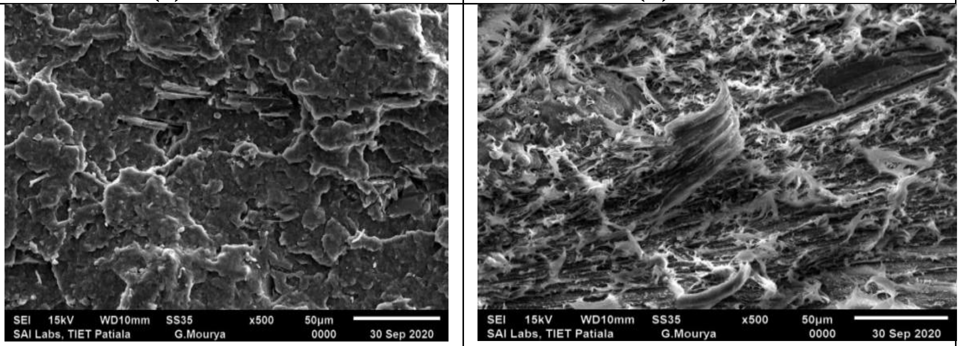

(a) At x500 (b) At x500

Figure 5.52 Fracture surfaces of samples with best flexural properties (a), fracture surfaces of samples with worst flexural properties

The micrographs were taken at magnification levels ×35, ×150, ×300 and ×500 (Figure 5.52). For SEM analysis the sample should be conductive in nature. Thus to make the polymeric samples conductive, a gold layer has been coated over its surface. Micrographs clearly shown that the sample fabricated as per optimized suggested settings have solid structure with proper bonding in between the layers. Whereas the sample shown poor mechanical strength is porous and gaps between layers reduced the mechanical strength of the part.

The R_a of 3D printed parts has been measured by taking the rendered images of SEM of the specimen at x500 magnification (Figure 5.53). It has been observed from the Figure 5.53 (b) that the parts fabricated as per the settings shown poor mechanical properties is having more R_a whereas the samples printed as per best settings 5.53(a) shown less R_a. This may be due to better bonding between the layers at higher ID level.

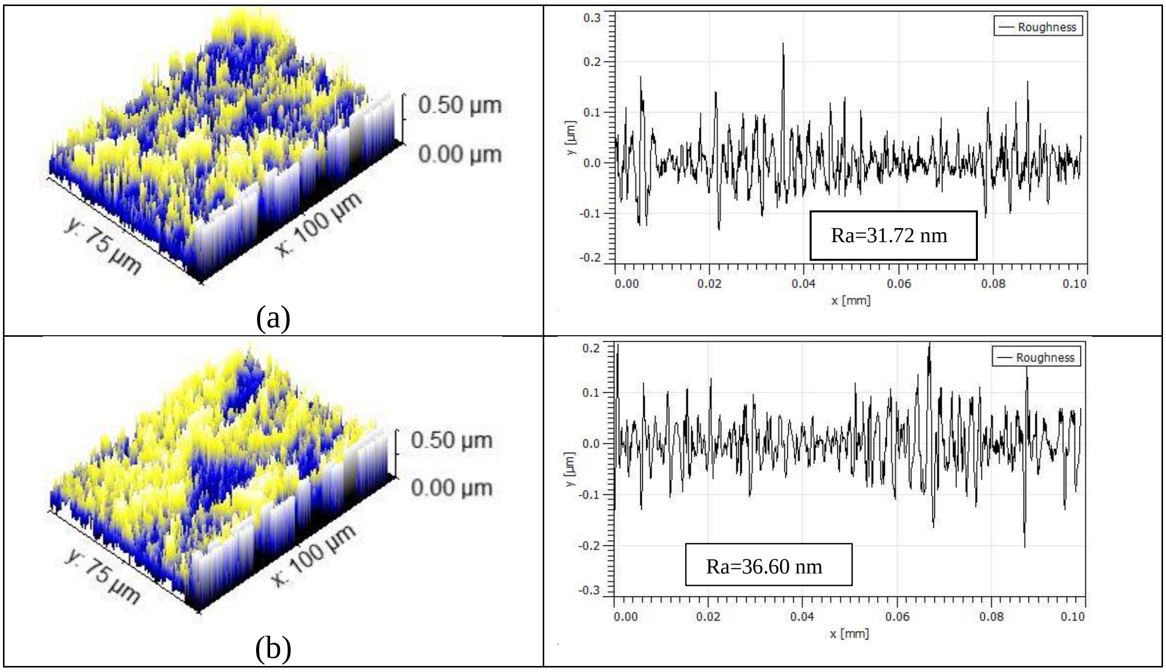

(a)

(b)

Figure 5.53 Rendered SEM images of flexural tested parts with best mechanical properties (a) and worst mechanical properties (b)

In addition to SEM analysis for material characterization, the samples were also subjected to EDAX for elemental level analysis. To ensure whether both tested sample having same composition EDAX was performed at both specimens shown best and worst mechanical properties. The element analysis for the printed samples having best and worst mechanical properties is shown in Figure 5.54 (a) and (b). It has been clearly observed from the Figure 5.54 that both the specimens having same elements with almost equal quantity. Thus it supports that the variation in mechanical properties is only due to printing parameters of FDM. The area mapping of the samples shows the dispersion of elements per unit area (Figure 5.55).

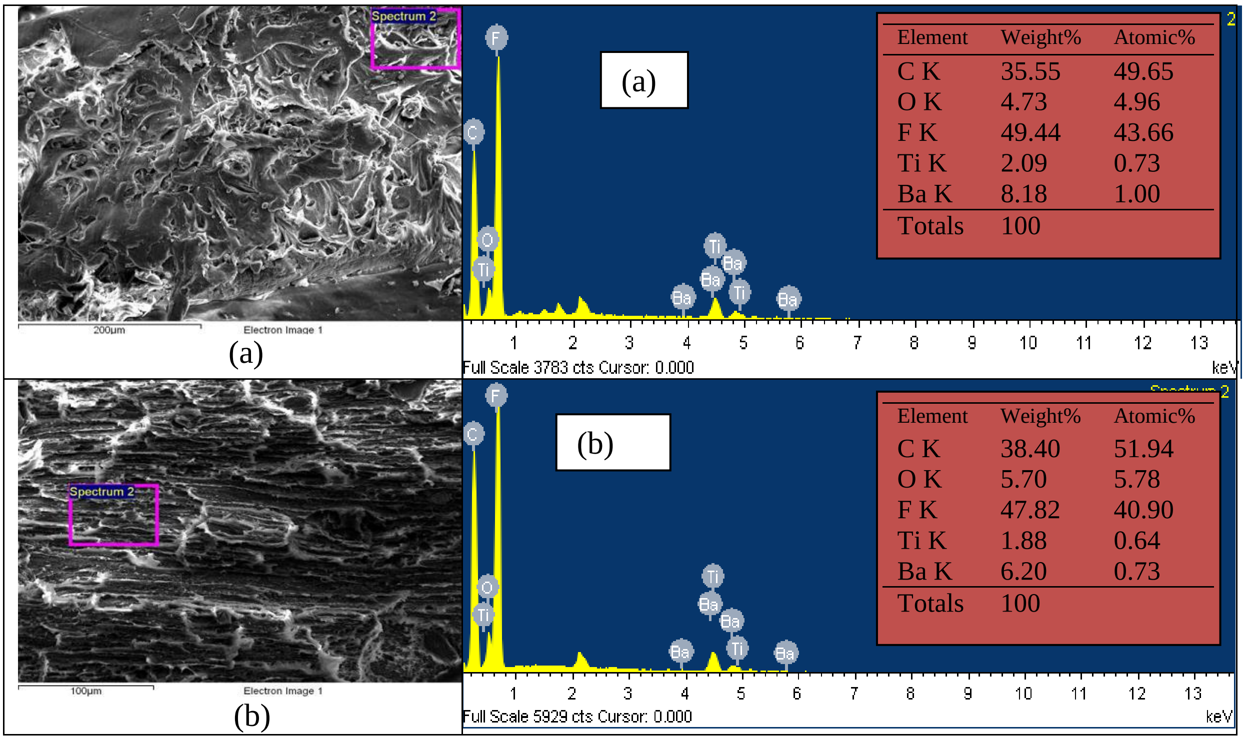
(a)

Element	Weight%	Atomic%
C K	35.55	49.65
O K	4.73	4.96
F K	49.44	43.66
Ti K	2.09	0.73
Ba K	8.18	1.00
Totals	100	

(b)

Element	Weight%	Atomic%
C K	38.40	51.94
O K	5.70	5.78
F K	47.82	40.90
Ti K	1.88	0.64
Ba K	6.20	0.73
Totals	100	

Figure 5.54 (a) and (b) EDAX analysis of 3D printed parts having best (a) and worst (b) mechanical properties

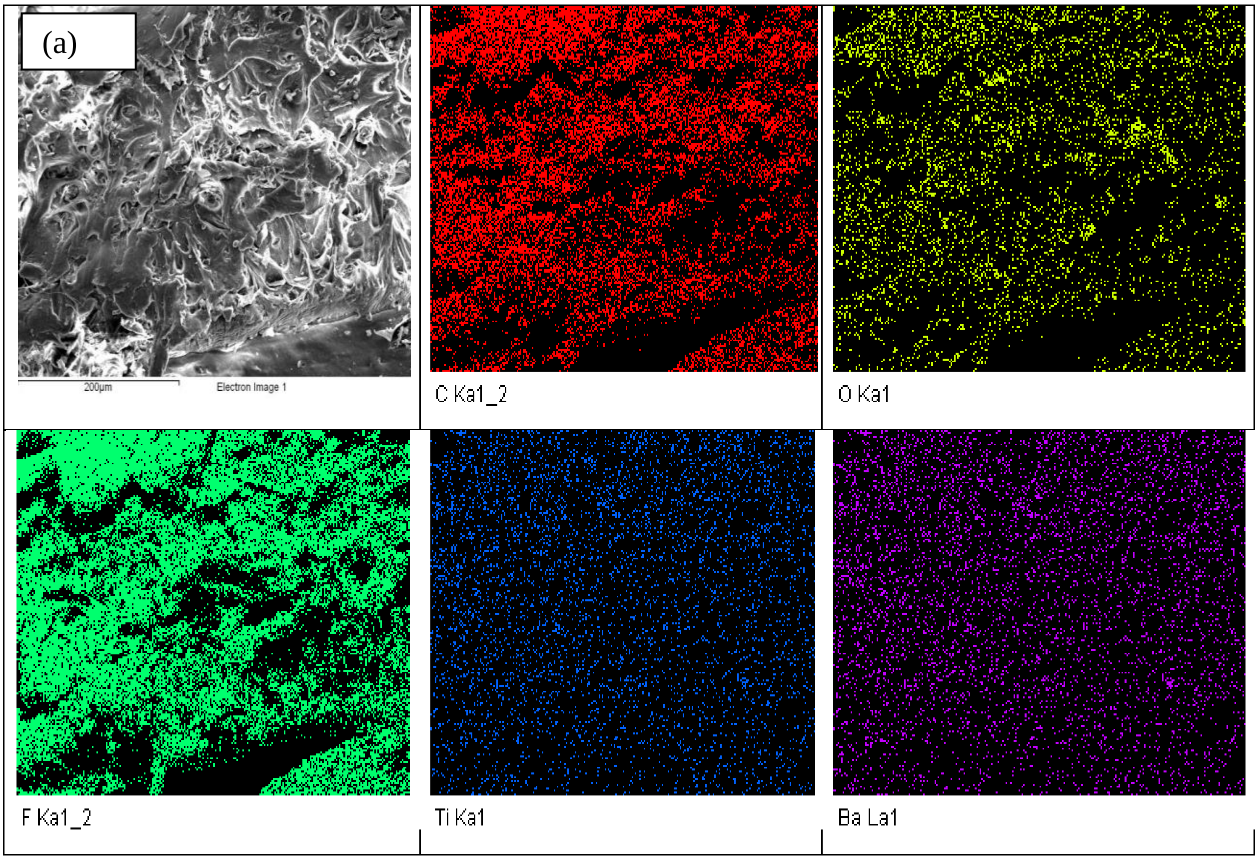

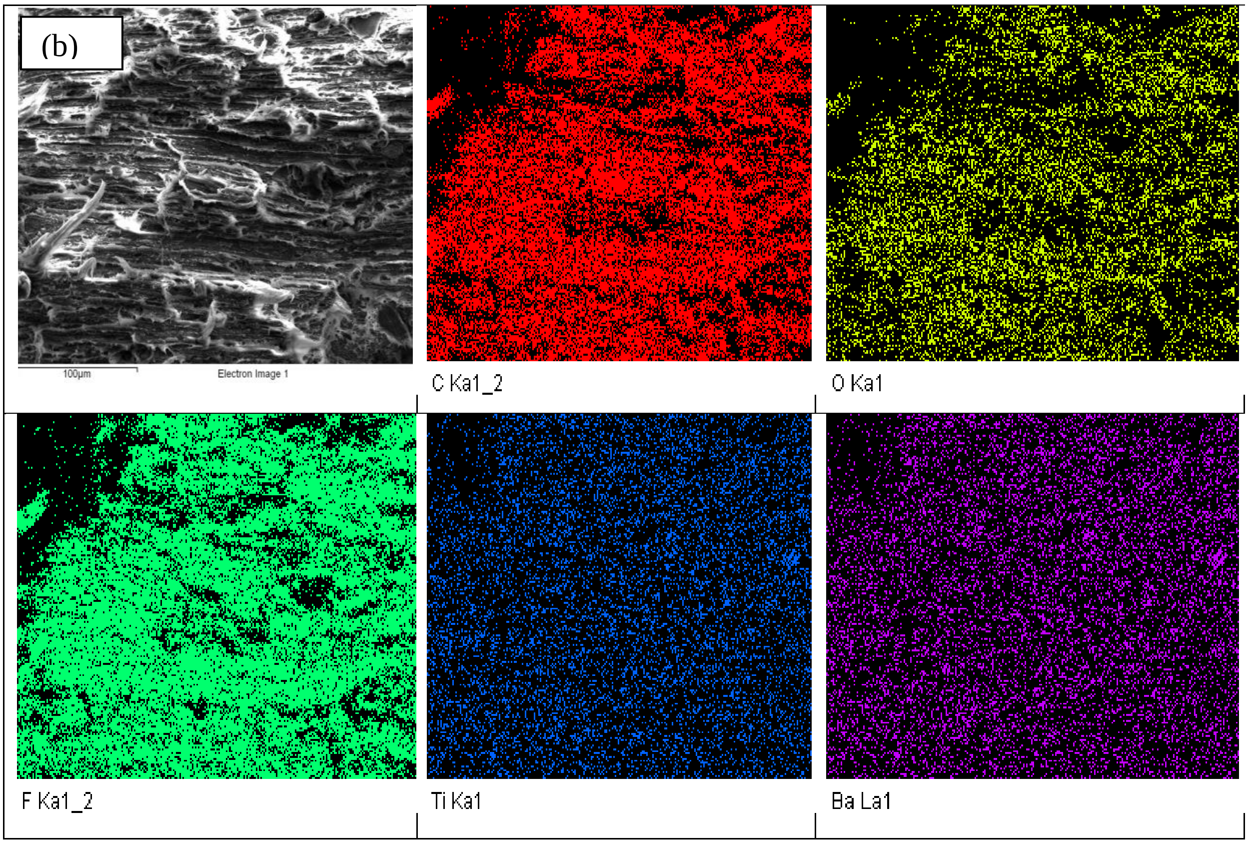

Figure 5.55 Area mapping of 3D printed samples having best (a) and worst (b) mechanical properties

5.4.7 Shore-D hardness (SH)

SH was measured with shore-D hardness tester. The hardness of fabricated parts were lying in between 65 to 77 shore-D. Table 5.66 shows the outcome values of hardness of fabricated parts. The maximum hardness value has been found in the experiment no 3. The shore-D hardness value of the confirmatory experiment was 77.50 Shore D i.e. highest values than others.

Table 5.66 SH (shore-D) values of fabricated parts

Exp. No.	IS (mm/s)	IA (^{o})	ID (%)	Shore-D Hardness
1	50	0	60	73.25
2	50	45	80	74.48
3	50	90	100	76.89
4	70	0	60	71.57
5	70	45	80	72.57
6	70	90	100	69.84
7	90	0	60	72.04
8	90	45	80	65.07
9	90	90	100	66.34

5.4.8 Dimensional analysis

After the SH testing, manufactured specimens were subjected to dimensional analysis. A digital Vernier calliper (make:Mututoyo) having accuracy up to two decimal places was used to measure the thickness of specimens. To minimize the measurement error, each sample was measured three times the average thickness of three measured dimensions of the 3D printed specimens were compared with the standard dimensions of tensile specimens (as shown in Table 5.67). It has been found that the parts manufactured/fabricated at IS of 70 mm/s, and depositing material at an IA 90^o, with 100% ID shown least deviation. Whereas, 3D printing performed as per experiment setting having IS 90 mm/s with 90^o and 100% ID shown maximum deviation.

Table 5.67 Dimensional deviation observed from dimensional analysis

Exp. No.	IS (mm/s)	IA (^{o})	ID (%)	T1	T2	T3	T avg	T (required)	ΔT
1	50	0	60	2.91	2.99	3.04	2.98	3.2	0.22
2	50	45	80	2.98	3.05	3.12	3.05	3.2	0.15
3	50	90	100	3.10	3.12	3.20	3.14	3.2	0.06
4	70	0	60	3.10	3.15	3.19	3.14	3.2	0.05
5	70	45	80	3.05	3.01	2.97	3.01	3.2	0.19
6	70	90	100	3.19	3.0	3.26	3.15	3.2	0.05
7	90	0	60	3.21	3.05	3.04	3.10	3.2	0.10
8	90	45	80	2.99	2.85	3.10	2.98	3.2	0.22
9	90	90	100	2.80	3.10	2.83	2.91	3.2	0.29

5.4.9 Surface porosity

As all types of specimens were prepared according to same DOE, thus only tensile specimens were used to analysis the surface porosity. Figure 5.56 shows the photomicrographs of the surfaces of the filaments with the percentage of Φ on the surface. It has been observed from the photomicrograph's parts fabricated at high density and low infill speed having less surface porosity as compared to specimen's 3D printed at high infill speed and low ID.

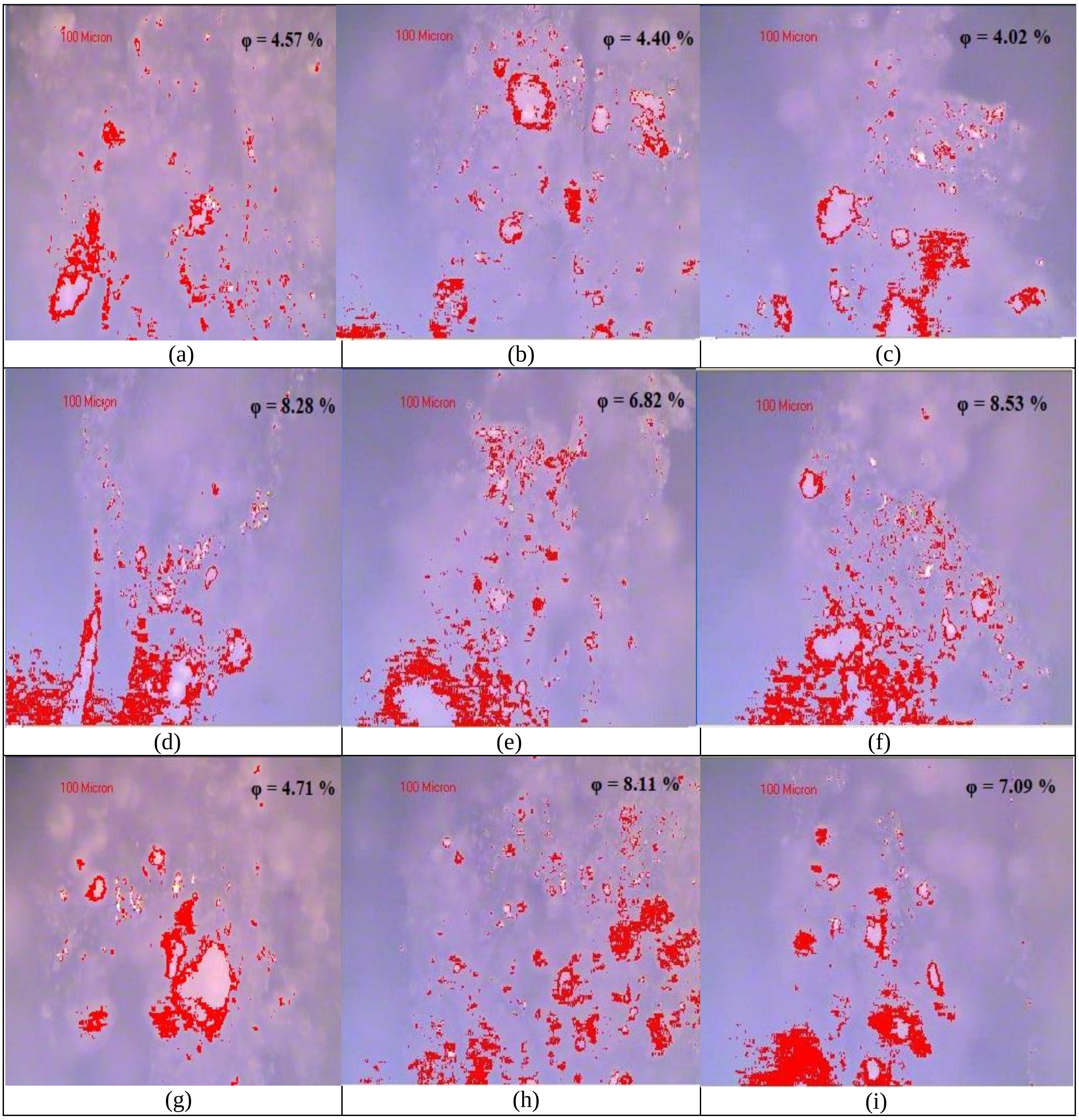

(a) (b) (c)

(d) (e) (f)

(g) (h) (i)

Figure 5.56 Optical photographs shown the surface porosity of 3D printed specimens

5.4.10 Dynamic mechanical analysis (DMA)

For 3D printing of DMA standard samples experimental settings shown best and worst flexural properties were used. Similar controllable process parameters [IS, IA and ID] of FDM setup were used for 3D printing of parts using CAMB composites as shown in Table 5.68.

Table 5.68 FDM process parameters for 3D printing of standard specimens

Smaple no.	Sample Type	IS (mm/s)	IA (°)	ID (%)
1	DMA	70	45	100
2	DMA	90	45	60

Process parameters remain constant during the 3D printing are as:
(i) Nozzle diameter: 0.5 mm (ii) Bed Temperature: 85°C (iii) Nozzle Temperature:250°C
(iv) Fan Outpur: 50% (v) Number of parameters: 4 (vi) Fill pattern: rectilinear

The observed curves of storage modulus and tan δ with respect to temperature for sample 1 and sample 2 are shown in Figure 5.57 (a) and Figure 5.57 (b) respectively.

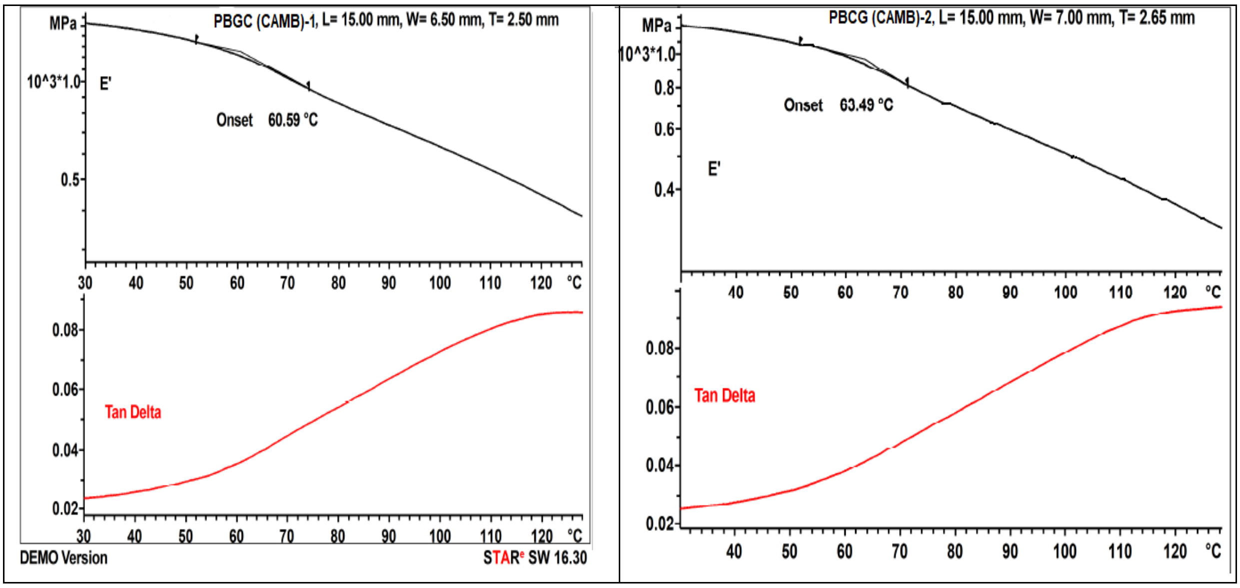

Figure 5.57 (a) and (b) DMA curves in term of storage modulus and tan delta as a function of temperature corresponding to MB and CAMB composites

The curves obtained from DMA testing shows that with the increase of temperature storage modulus (E') of the material is decreasing. However tan delta is increasing with respect to temperature. It has been observed by comparing both the curves that E' of MB sample 1 is more (i.e.,1.5x10$^{\wedge 3}$ MPa approx.) as compared to E' of MB sample 2 (1.210$^{\wedge 3}$ MPa). It means the energy absorbing capacity of MB sample 1 is better than the sample 2. The curves of tan δ represent the variation in energy dissipation capacity as a function of temperature. The tan δ curve of sample 2 shows the maximum value of 0.08 at 130°C, whereas in case of sample 1, the value of tan δ at same temperature is 0.09 at similar temperature. Thus it means the ratio of loss modulus to storage modulus is more in sample 2 as compared to specimen 1. Consequently, the sample prepared as per experimental settings shown best flexural properties also have better stiffness and shape recovery property.

5.4.11 Process Capability Analysis

Similar to the MB process, In CAMB process same total of ten standard tensile specimens and ten standard flexural specimens were 3D printed to report the process capability analysis of 3D printing process parameters. The 3D printed functional prototypes were subjected to

UTM for destructive testing. The output results of mechanical testing of both type of specimens in the form of PS, BS and FT were noted to perform process capability analysis (see Table 5.69). It has been observed from the output results of mechanical testing that very less variations were found by printing the samples under similar processing conditions.

Table 5.69 UTM results for tensile samples

S. No.	PS (MPa)	BS (MPa)	FT (MPa)
1	61.05	54.45	6.18
2	60.82	55.87	6.93
3	59.85	53.98	5.80
4	61.58	55.72	6.88
5	62.01	55.24	6.37
6	60.74	53.65	5.90
7	59.98	53.05	5.57
8	61.89	54.42	6.37
9	61.74	54.07	5.81
10	60.71	53.79	6.02

Table 5.70 UTM results of flexural samples

S. No	PS (MPa)	BS (MPa)	FT (MPa)
1	71.2	62.1	4.13
2	72	61.9	4.18
3	70.5	63.18	4.20
4	69.98	61.52	4.09
5	68.95	60.85	3.90
6	69	61	4.06
7	71.2	62.41	4.15
8	72.5	63.05	3.95
9	71.28	62.9	4.18
10	70.48	61.45	4.09

For process capability analysis data shown in Table 5.69 and 5.70 was processed with statistical analytical tool. The calculated values of Cp >1 and Cpk>1, for type of specimens, represented that the 3D printing process was statistically under control. The outcome graphs of process capability analysis in the form of histogram and normal probability plot for PS, BS, and FT of tensile specimen are shown in Figure 5.58. The calculated results of process capability analysis for PS, BS and FT of tensile specimen are shown in Table 5.71.

Table 5.71 Results of process capability analysis for 3D printed tensile specimens

	PS (MPa)	BS (MPa)	FT (MPa)
Std. Deviation	0.70175	0.91617	0.44184
C_p	1.04	1.06	1.06
C_{pu}	1.03	1.08	1.07
C_{pl}	1.06	1.03	1.04
C_{pk}	1.03	1.03	1.04
CR	0.96	0.95	0.95

Note:
Cp and Cpk, measures consistency with average performance. The 'k' stands for 'centralizing factor.' The index takes into consideration the fact that data is maybe not centered.

For tensile specimen

- *(g) For PS the USL and LSL was 63.2 and 58.8 MPa respectively*
- *(h) For BS the USL and LSL was 57.4 and 51.6 MPa respectively*
- *(i) For FT the USL and LSL was 7.6 and 4.8 MPa respectively*

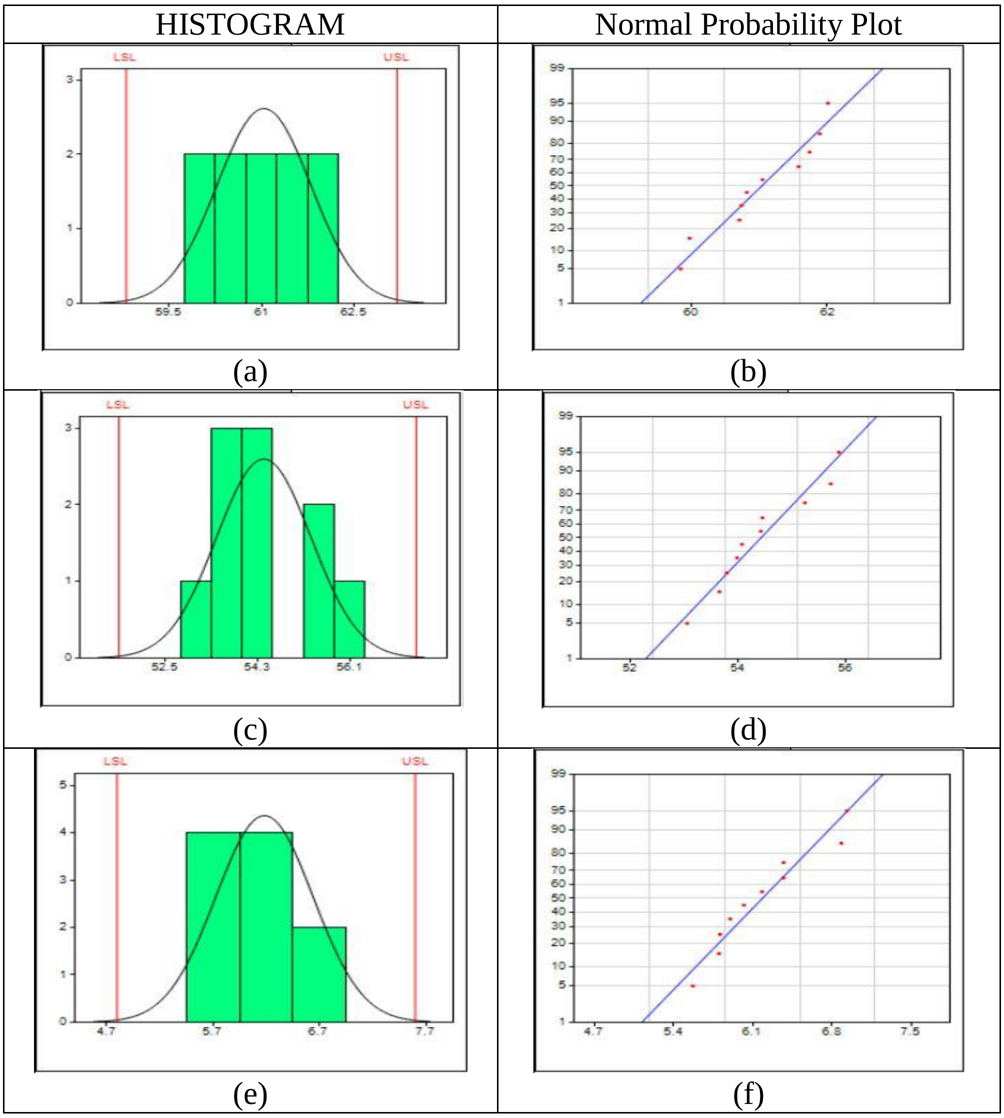

Figure 5.58 Process capability index for PS, BS and FT of tensile specimens

Similar results were also observed for the flexural specimens. The Table 5.72 shows the outcome values of process capability analysis. The histogram and normal probability plot for PS, BS and FT of flexural specimens are shown in Figure 5.59.

Table 5.72 Results of process capability analysis for 3D printed flexural specimens

	PS (MPa)	BS (MPa)	FT (MPa)
Std. Deviation	1.27680	0.756985	0.09746
C_p	1.07	1.06	1.11
C_{pu}	1	1.04	1.05
C_{pl}	1.15	1.07	1.17
C_{pk}	1	1.04	1.05
CR	0.93	0.95	0.9

Note: Cp and Cpk measures consistency with average performance. The 'k' stands for 'centralizing factor.' The index takes into consideration the fact that data is maybe not centered.

For flexural specimen

(j) For PS the USL and LSL was 74.6 and 66.4 MPa respectively

(k) For BS the USL and LSL was 64.4 and 59.6 MPa respectively

(l) For FT the USL and LSL was 4.4 and 3.75 MPa respectively

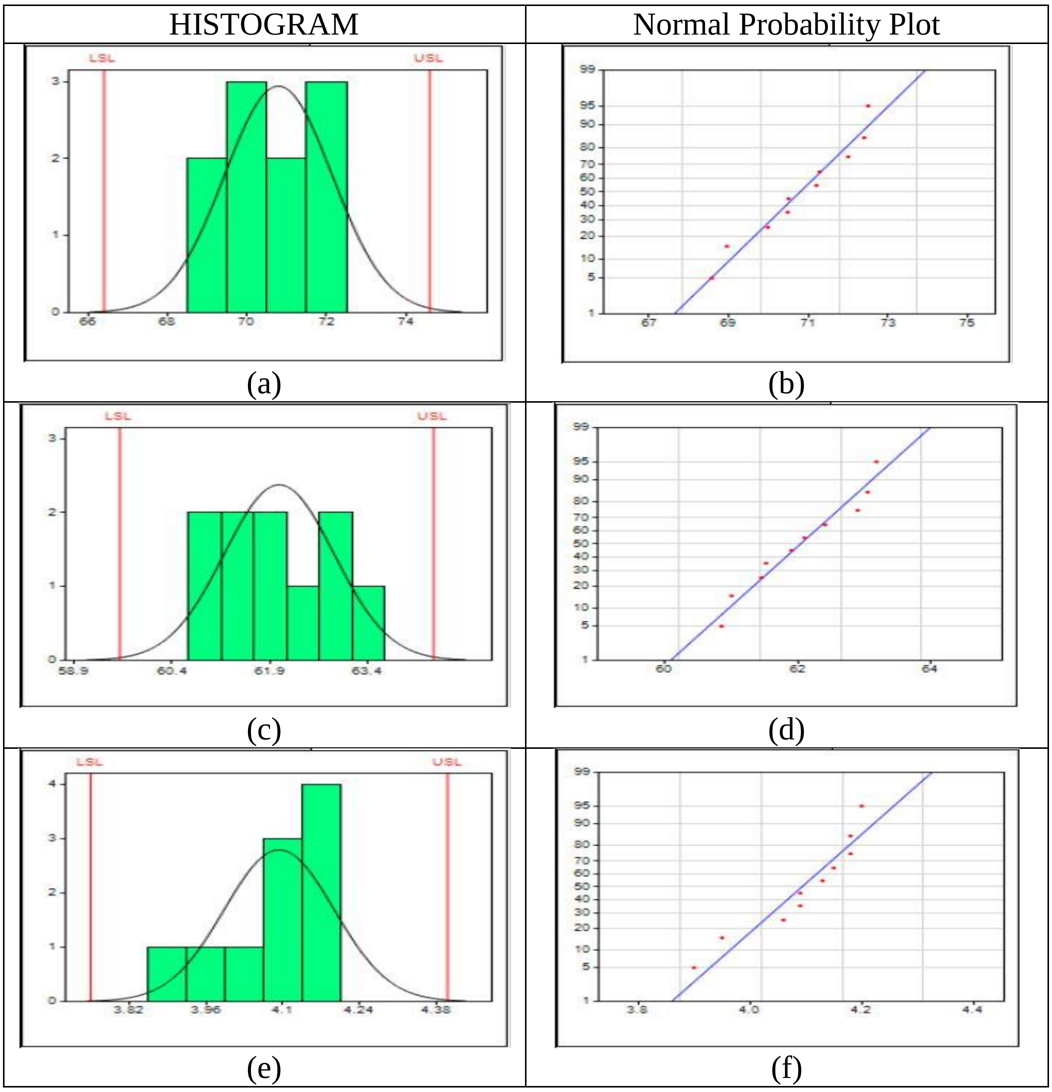

(a) (b)

(c) (d)

(e) (f)

Figure 5.59 Process capability index for PS, BS and FT of flexural specimens

5.5 Results and discussion (Stage 5)

5.5.1 X-ray diffraction analysis for MB 3D printed specimen

As PVDF is a semi crystalline material with no more than 50-60 % crystal content. PVDF mainly exists in three crystalline phases such as α, β and ɣ-phases. In this research work, for crystal structure characterization of 3D printed specimens of BTO/Gr/PVDF, X-ray diffraction analysis was performed. The specimen for XRD testing was 3D printed at the optimized settings of FDM. Further for poling, the sample was subjected to high voltage supply at elevated temperature. The 3D printed specimen before poling and after poling was analyzed through XRD (Figure 5.60). The observed spectrums have been matched with standard directory cards (for PVDF and BTO the ICDD/JCPDS:00-038-1638 and ICDD/JCPDS: 01-079-2264 were used respectively). In the non-poled part the peaks at 18.4° (020), 20.1° (110) represents the monoclinic α- phase, a peak at an angle of 26.8° (022) and a small peak at 35.9° (200) corresponding to ɣ- phase and orthorhombic β- phase respectively. Whereas the peaks at 22.2° (100), 31.6° (110), 38.9° (111) and 45.3° (200) corresponds to BTO nano-powder. However, after poling the peak of 20.1° is slightly shifted at 20.8° (100) and a broad peak is observed at 35.9° (200) corresponds to the more β-phase content. That clearly shows the effect of electrical poling on the 3D printed part. Whereas similar peaks have been observed for BTO in both specimens represents the homogenous dispersion of BTO nanoparticle in PVDF matrix. The results of XRD analysis were found to be in correlation with the previously published research works [147,168-169].

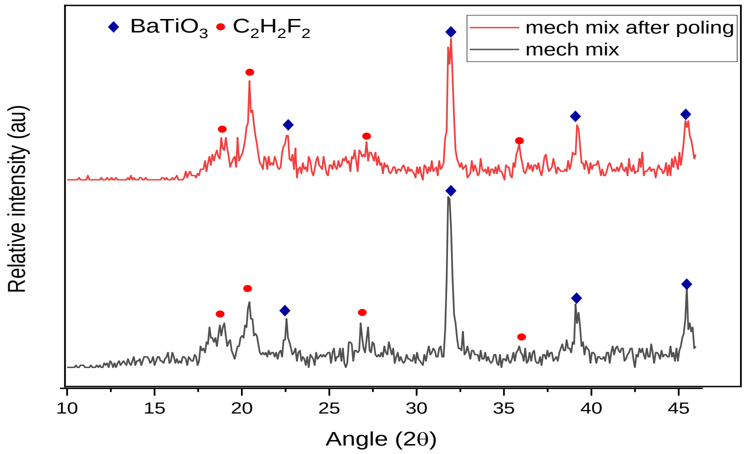

Figure 5.60 XRD spectra of 3D printed specimens

5.5.2 FTIR for MBD 3D printed specimen

In FTIR analysis, absorption bands were used to determine the degree of crystallinity of α, β and ɣ-phases. Generally, PVDF exists in α-phase until it goes through some extra processing conditions like electrical poling, mechanical stretching, thermal poling or by doping some other material in it. The β-phase of PVDF is showing its eligibility for energy harvesting applications. Figure 5.61 shows the FTIR spectra of 3D printed discs of MBCof PBG, before and after thermal poling. The effect of poling is clearly observed in the FTIR analysis. The FTIR analysis indicate the absorption peaks for α-phase are formed at wavenumber of 614,761,795, 1149, and 1382 cm^{-1}, β-phase is formed at wavenumber of 836,1278 cm^{-1} and ɣ-phase formed at wavenumber of 1236 cm^{-1}. In non-poled sample more α-phase content appears. However, very small peaks are formed at 836 cm^{-1} and 1278 cm^{-1} corresponding to β-phase content. On the flipside, the big peaks formed at 836 cm^{-1} and 1276 cm^{-1} clearly represents that electroactive β-phase increases with electrical poling process. FTIR results were found to be in line with the previously published literatures [52-54]. It has been ascertained from XRD and FTIR analysis, that electrical poling plays a very prominent for transformation of α-phase into electroactive β-phase in PVDF based composites.

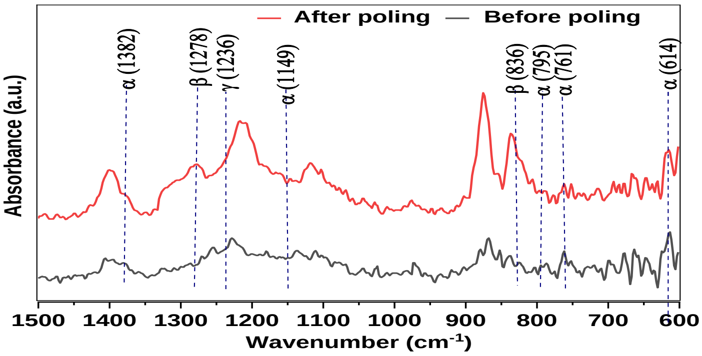

Figure 5.61 FTIR absorption bands of 3D printed specimens

5.5.3 Piezoelectric constant Measurement for MBD 3D printed specimen

After thermal poling, the 3D printed discs of MBD composites of PVDF/Gr/BTO were used to measure the piezoelectric coefficient by two probe method A d_{33} meter (Model YE2730A D33 make: Marine India) has been used with high degree of resolution i.e. 0.1 pC/N. In this study 3D printed cylindrical disc having diameter of 10 mm and thickness is 0.4 mm was used for testing. The piezoelectric constant (d_{33}) value of cylindrical disc is 20 pc/N, which is close to the solvent casted film of PVDF+ BTO. Figure 5.62 shows D_{33} meter used to measure piezoelectric constant and silver coated 3D printed disc under the probes.

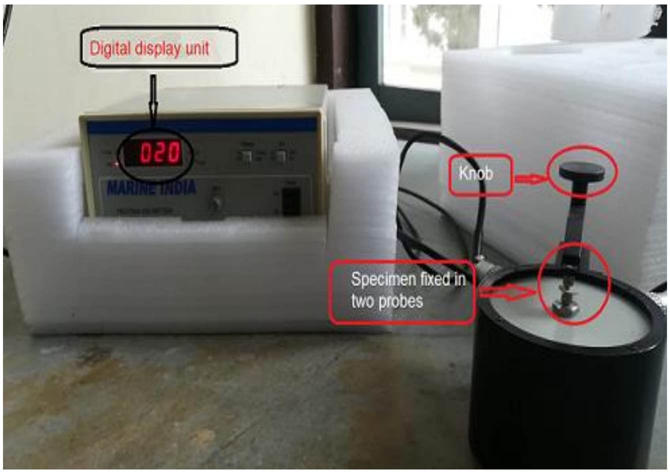

Figure 5.62 D_{33} meter used to measure piezoelectric coefficient

5.5.4 XRD analysis of CAMBD 3D printed specimen

The specimen for XRD testing was 3D printed at the optimized settings of FDM. Further for poling, the sample was subjected to high voltage supply at elevated temperature. The 3D printed specimen before poling and after poling was analyzed through XRD (Figure 5.63). The observed spectrums have been matched with standard directory cards (for PVDF and BTO the ICDD/JCPDS:00-038-1638 and ICDD/JCPDS: 01-079-2264 were used respectively). In the non-poled part the peaks at 18.4° (020), 20.1° (110) represents the monoclinic α- phase, a peak at an angle of 26.8° (022) and a small peak at 35.9° (200) corresponding to ɣ- phase and orthorhombic β- phase respectively. Whereas the peaks at 22.2° (100), 31.6° (110), 38.9° (111) and 45.3° (200) corresponds to BTO nano-powder. However, after poling the peak of 20.1° is slightly shifted at 20.8° (100) and a broad peak is observed at 35.9° (200) corresponds to the more β-phase content. That clearly shows the effect of electrical poling on the 3D printed part. Whereas similar peaks have been observed for BTO in both specimens represents the homogenous dispersion of BTO nanoparticle in PVDF matrix. The results of XRD analysis were found to be in correlation with the previously published research works [147, 168-169].

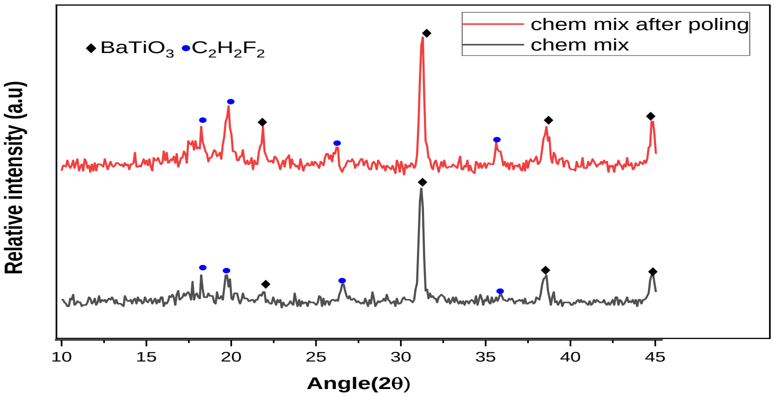

Figure 5.63 XRD spectra of 3D printed specimens

5.5.5 FTIR analysis of CAMBD 3D printed specimen

In FTIR analysis, absorption bands were used to determine the degree of crystallinity of α, β and ɣ-phases. Generally, PVDF exists in α-phase until it goes through some extra processing conditions like electrical poling, mechanical stretching, thermal poling or by doping some other material in it. The β-phase of PVDF is showing its eligibility for energy harvesting applications. Figure 5.64 shows the FTIR spectra of 3D printed films before and after thermal poling. The effect of poling is clearly observed in the FTIR analysis. The FTIR analysis indicate the absorption peaks for α-phase are formed at wavenumber of 614,761,795, 1149, and 1382 cm^{-1}, β-phase is formed at wavenumber of 836,1278 cm^{-1} and ɣ-phase formed at wavenumber of 1236 cm^{-1}. In non-poled sample more α-phase content appears. However, very small peaks are formed at 836 cm^{-1} and 1278 cm^{-1} corresponding to β-phase content. On the flipside, the big peaks formed at 836 cm^{-1} and 1276 cm^{-1} clearly represents that electroactive β-phase increases with electrical poling process. FTIR results were found to be in line with the previously published literatures [147,168-169]. It has been ascertained from XRD and FTIR analysis, that electrical poling plays a very prominent for transformation of α-phase into electroactive β-phase in PVDF based composites.

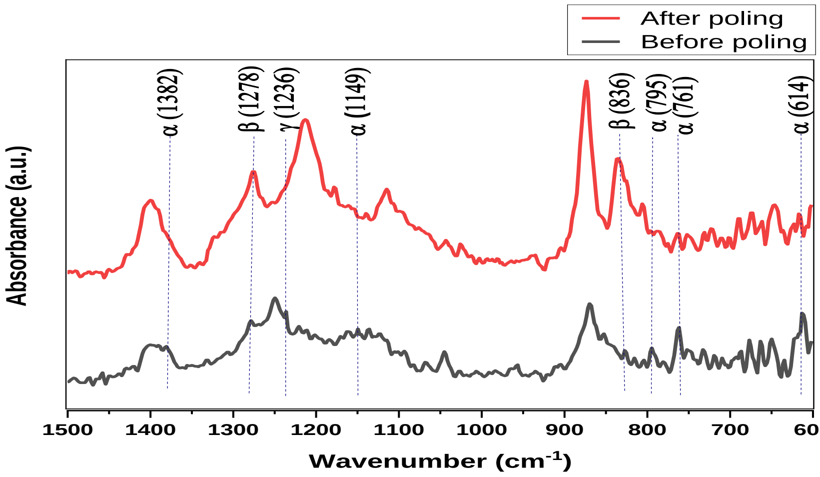

Figure 5.64 FTIR absorption bands of 3D printed specimens

5.5.6 Measurement of Piezoelectric coefficient of CAMBD 3D printed specimen

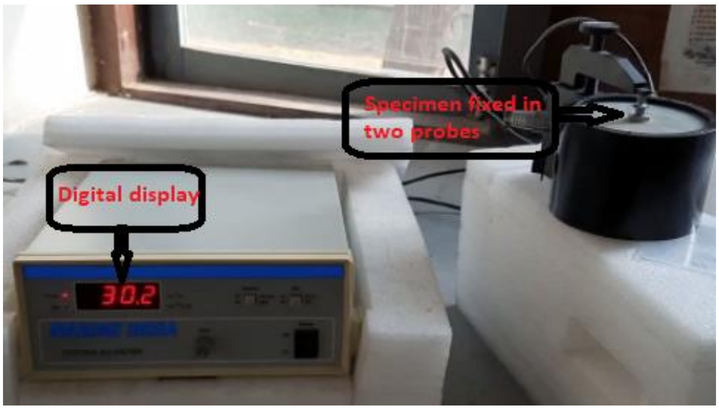

Figure 5.65 Setup used to measure the piezoelectric coefficient (d_{33})

The piezoelectric coefficient of the PVDF/Gr/ BTO based 3D printed film was measured using a two probe method. A disc having 10 mm diameter and 0.4 mm thickness was 3D printed. The printed disc was coated with silver paint from both sides to make it conductive. Further the disc was subjected to high voltage electric filed with temperature for 3 hours of poling process, After electrical poling, the disc has been placed in between the probes of d_{33} meter and tighten the knob properly. Figure 5.65 shows the d_{33} meter that is used to measure piezoelectric coefficient, and silver-coated 3-D printed disc. The meter is then switched on, that displays the digital value of d_{33} in pC/N. The piezoelectric constant (d_{33}) value of 3D printed disc is 30.2 pC/N.

5.5.7 Comparison among the properties of feedstock filaments prepared from MB and CAMB composites of PVDF/Gr/BTO

After the fabrication and characterizations of feed stock filaments and 3D printed parts of MBD and CAMBD composites of PVDF/Gr/BTO on the basis of mechanical, dimensional, thermal, morphological and piezoelectric properties, a comparative study was performed to determine the effect of blending process, on various properties of feedstock filaments, and 3D printed parts of composites processed on similar parameters of TSE and FDM. In this part of the study, initially the various properties of feedstock filaments prepared form MB and CAMB composites were compared. Further the properties of 3D printed parts prepared from MB and CAMB composites-based feedstock filaments have compared.

5.5.7.1 Rheological properties

Viscosity of PVDF/Gr/BTO composites prepared by MB and CAMB method was calculated from their density and MFI values. Initially shear stress and shear rate was calculated. Further the viscosity (μ), has been calculated from shear stress (τ) divided by the shear rate (γ). the comparison of viscosity of MBD and CAMBD composites is shown in Figure 5.66. The viscosity graph clearly represents the effect of blending process on the rheological properties of the developed composites. It has been observed that MB composites of PBG having more viscosity than CAMB composites at same proportion of material.

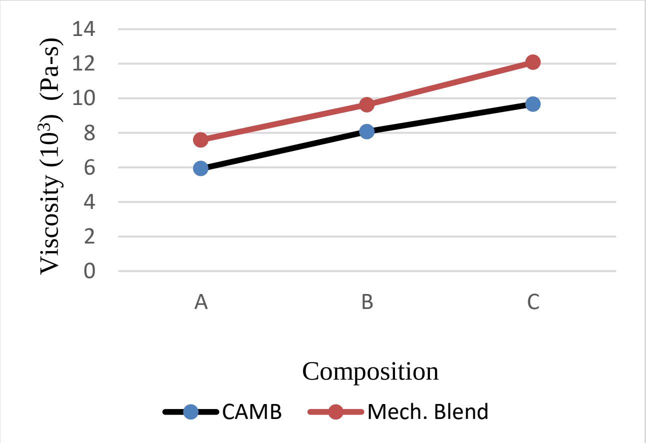

Figure 5.66 Comparison of viscosity of MB and CAMB composites

5.5.7.2 Tensile properties of feedstock filaments

A comparison was made between the tensile properties of extruded filaments of MB and CAMB composites. The values of PS of the filaments of MB composites and PS of the filaments of CAMB are shown in bar graph (Figure 5.67). In both cases the extrusion of filaments was performed at similar experimental condition. It should be noted that the methods of preparation of composites were different. Thus, it has been revealed from the bar graph that the filaments of chemically mixed composites having higher PS as compared to filaments of mechanically blended composites. Moreover, the best parametric settings of the TSE are also different in both cases. As in case of chemically mixed composites, the optimised settings to fabricate the filament shown maximum tensile strength were: 180°C of extruder temperature, 60 rpm screw speed and 15% of BTO. However, for mechanically mixed composites, the optimised settings are 200°C processing temperature; 50 rpm screw speed and 20% BTO. The results of mechanical testing shown that feedstock filaments prepared by CAMB containing only 15 % BTO shown better mechanical properties, than MB composites containing 20% BTO. Thus, it has been observed that blending process plays very prominent role on mechanical properties of developed composite.

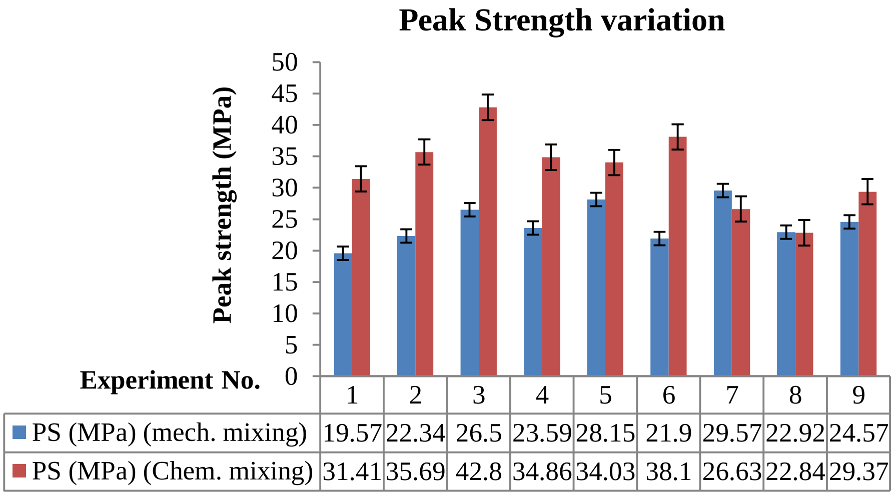

Experiment No.	1	2	3	4	5	6	7	8	9
🟦 PS (MPa) (mech. mixing)	19.57	22.34	26.5	23.59	28.15	21.9	29.57	22.92	24.57
🟥 PS (MPa) (Chem. mixing)	31.41	35.69	42.8	34.86	34.03	38.1	26.63	22.84	29.37

Figure 5.67 Comparison of PS for filaments (mechanically extruded and CAMB composites)

Similar to PS a comparison was also made between the BS of filaments prepared via chemically/mechanically mixed composites as shown in Figure 5.68.

The results of mechanical testing shown that feedstock filaments prepared by CAMB containing only 15 % BTO shown better mechanical properties, than MB composites containing 20% BTO. Thus, it has been observed that blending process plays very prominent role on mechanical properties of developed composite.

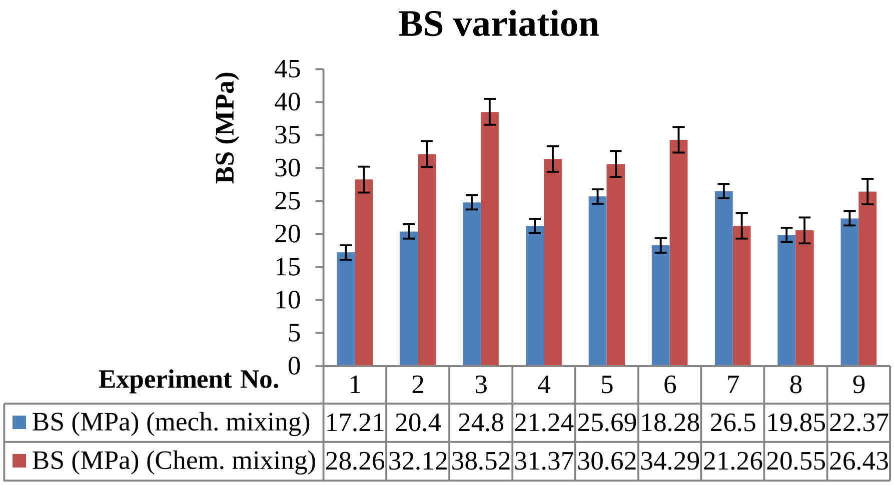

Experiment No.	1	2	3	4	5	6	7	8	9
🟦 BS (MPa) (mech. mixing)	17.21	20.4	24.8	21.24	25.69	18.28	26.5	19.85	22.37
🟥 BS (MPa) (Chem. mixing)	28.26	32.12	38.52	31.37	30.62	34.29	21.26	20.55	26.43

Figure 5.68 Comparison of BS for filaments of mechanically blended and CAMB composites

5.5.7.3 Dimensional properties

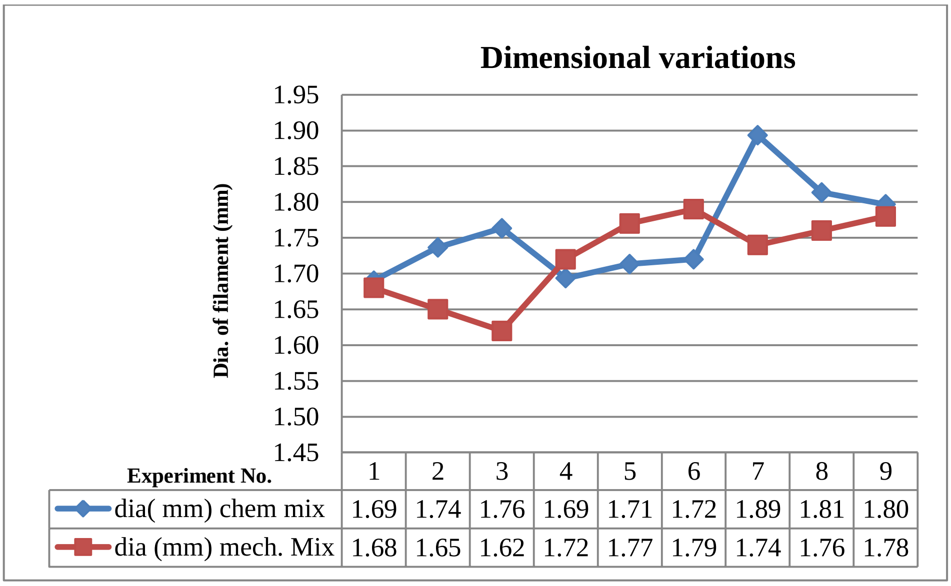

Experiment No.	1	2	3	4	5	6	7	8	9
◆ dia(mm) chem mix	1.69	1.74	1.76	1.69	1.71	1.72	1.89	1.81	1.80
■ dia (mm) mech. Mix	1.68	1.65	1.62	1.72	1.77	1.79	1.74	1.76	1.78

Figure 5.69 Dimensional measurements of filaments (CAMBD/MBD composite)

The existing FDM setup supports only the filament having diameter within the range of 1.75±0.05mm. Thus, it was necessary to perform the dimensional analysis of the extruded filaments. After successfully comparison of tensile properties, dimensional properties of feedstock filaments prepared by MB and CAMB were also compared. To minimize the experimental error, total of three readings were taken at three different places over the total span length of both types of filaments. The average diameter (Ø) of three measured dimensions is taken as final for all the filaments. To make a comparison in between the measured dimensions of filaments of CAMBD/MBD of PBGC line graph has been used (Figure 5.69).

5.5.7.4 Thermal Properties

PVDF is mainly known for its good thermal resistance properties. However, some processing conditions or doping may change its thermal properties. Thus, to evaluate the effect processing conditions (MB or CAMB) used for reinforcing materials on the thermal properties of PVDF, DSC analyses were performed. After the mechanical testing of the filaments of PVDF/BTO/Gr composites prepared via MB and CAMB were subjected to the DSC platform for thermal analysis. Two samples, one from MB composite and the other from CAMB composite-based feedstock filaments were taken. Each sample was gone through two repeating cycles of heating and cooling within the temperature range of 30℃ to 250℃. The obtained thermal curves of both the samples are shown in Figure 5.70.

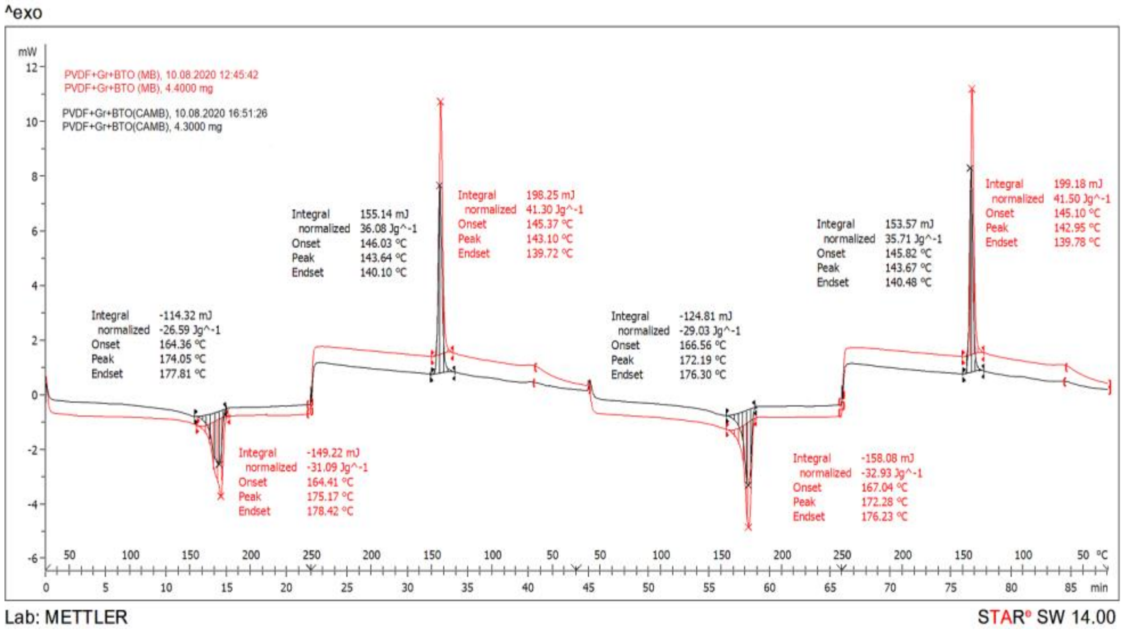

Figure 5.70 Thermal behaviour curves of MB and CAMB composites obtained from DSC

The red curve of MB composites depicts that the melting range of material is164℃ to 178℃, whereas the melting point of composite material, is 175℃. A similar pattern has been shown in the 2nd consecutive cycle of heating and cooling. On the other hand, the black curve of

CAMB based composite also shows similar results on melting and solidification of materials. Thus, it implies that the processing condition does not show much effect on the liquidation and solidification of developed composites. However, the energy absorption rate is found different in both of the samples. MB composites absorbed more energy (31.09 J/g) as compared to CAMB composites, which absorbs only 26.59 J/g of energy. In the 2nd consecutive cycle, both samples absorbed more energy as compared to their first respective thermal cycles. Thus, the results of thermal analyses show that the mechanically blended material has better heat-absorbing capacity than the CAMB composites. However, for reusability both samples showed equivalent results.

5.5.7.5 SEM analysis of prepared feed stock filaments

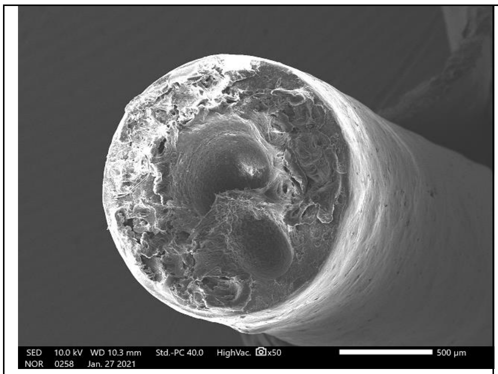 X50	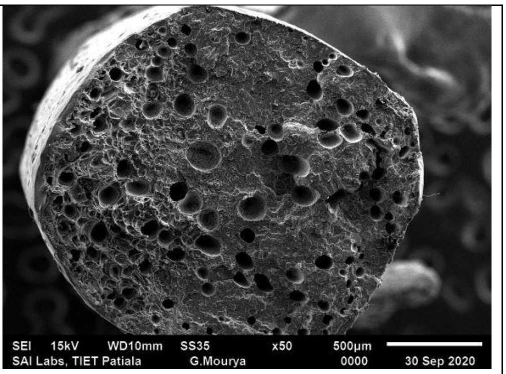 X50
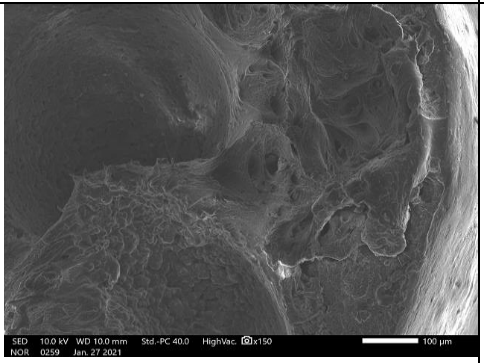 X150	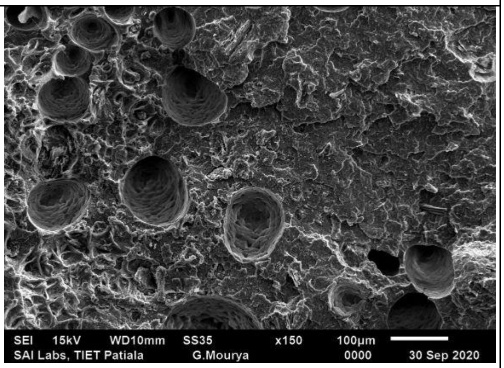 X150
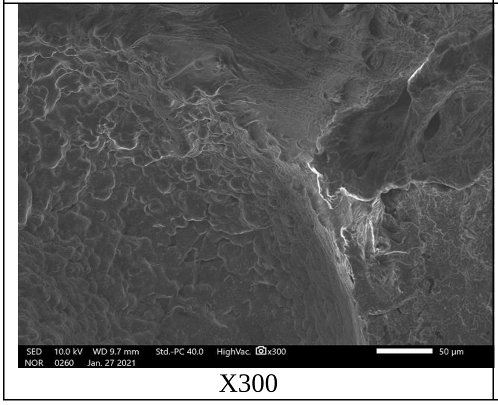 X300	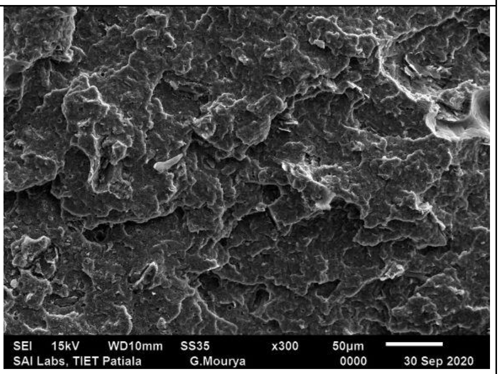 X300

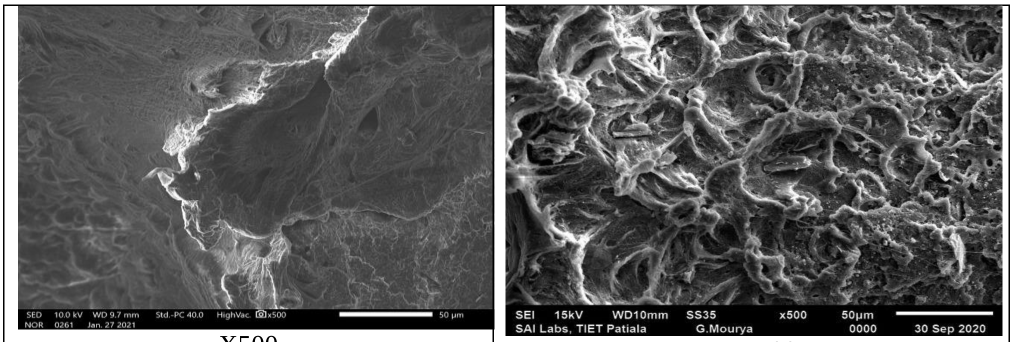

X500	X500
(a)SEM images of MB feedstock filament	(b) SEM images of CAMB feedstoc filament

Figure 5.71 Microphotographs of correctional view of feedstock filaments of MBD (a) and CAMBD (b) composites at X50, X150, X300 and X500

After successful comparison mechanical, dimensional and thermal properties, the morphological properties of feedstock filaments of MBD and CAMBD composites having maximum mechanical properties were compared. Morphological analysis of fractured surfaces of feedstock filament was performed by taking microphotographs at various magnification levels of X50, X150, X300, and X500 (see Figure 5.71). At X50 of CAMBD composite shows dimples formation throughout the surface, whereas only two dimples are seen in MBD composites and the remaining surface is almost plan.

This uniform dimple formation may show the high tensile strength of filament developed by the chemical assisted blending process. Moreover, at higher magnification, the material structure seems homogenous in CAMBD composites. Porosity testing revealed that both types of feedstock filament shown good surface properties. However, from comparison point of view, CAMBD composites have less surface porosity.

5.5.8 Comparison among the properties of 3D printed parts prepared form MBD and CAMBD composite based feedstock filament

5.5.8.1 Tensile Testing of 3D printed parts

The feed stock filaments fabricated by MB and CAMB were used to run at FDM for 3D printing of standard tensile, flexural and pull-out specimens. To obtain the mechanical properties, prepared samples were subjected to destructive testing. A universal testing machine with a load cell of 10 KN was used to perform the tensile and flexural testing. The output results of tensile, flexural and pull-out testing in the form of PS, BS and MoT are shown in Figure 5.72 and Figure 5.73 respectively.

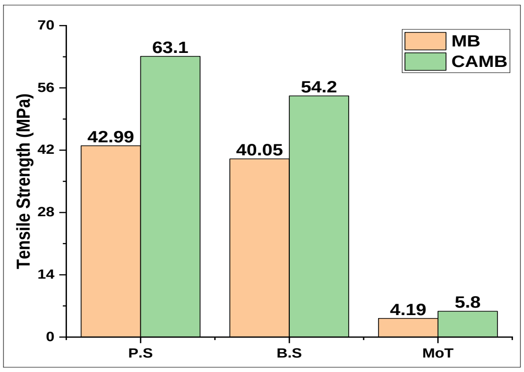

Figure 5.72 Comparison of tensile properties of the 3D printed parts prepared from MBD and CAMBD composites

The results of tensile strength show that the specimens prepared by using a CAMBD composite having more PS i.e., 63.1 MPa as compared to specimens fabricated by using MBD composites whose PS was found 42.99 MPa. Similarly, the bar graph also shows that other tensile properties such as BS and MoT were also found better in parts fabricated by using CAMBD composite materials.

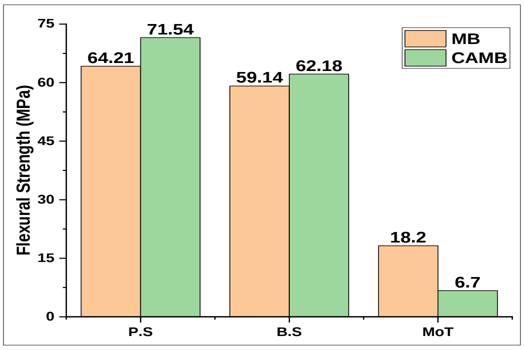

Figure 5.73 Comparison of flexural properties of the 3D printed parts prepared from MBD and CAMBD composites

Figure 5.73 shows the flexural properties of 3D printed parts. It has been observed that the flexural strength of the CAMB based 3D printed specimen is found more i.e., 71.54 MPa. Whereas the PS of the MB-based 3D printed part is 64.21 MPa. Consequently, the results of tensile and flexural properties suggested that the chemically blended composites-based specimens shown comparatively better results even containing less amount of BTO (15%) as compared to MB composites having 20% BTO.

After tensile and flexural properties, pull out properties of 3D printed parts of MBD and CAMBD composites have been also compared as shown in Figure 5.74. It has been observed that SS at peak of 3D printed parts prepared from CAMBD composites is 120.5% more than the parts of MB composites. However, MoT of MBD specimens is better than parts fabricated from CAMBD composites.

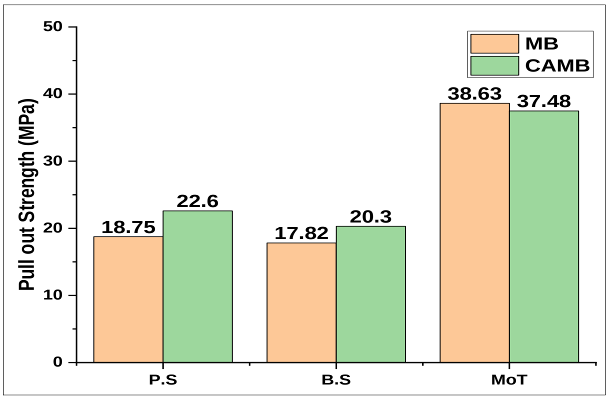

Figure 5.74 Comparison of pull-out properties of the 3D printed parts prepared from MBD and CAMBD composites

5.5.8.2 DMA of 3D printed functional prototypes

DMA is a sensitive method to study the polymer's viscoelastic behaviour as a function of temperature. A similar oscillation cycle of frequency was selected for a meaningful comparison between the MBD and CAMBD specimen under identical thermal environments. A controlled force of 1N is dynamically applied at the frequency of 10 Hz. Under this cyclic loading, the sample oscillated at a constant displacement of 10 μm. The force was applied to the samples by using a single cantilever bending method. During the testing, the temperature was increasing from 30oC to 130OC at a rate of 3K/min. The observed curves of storage modulus and tan δ as a function of temperature for MB and CAMB based specimens are shown in Figure 5.75 (a) and Figure 5.75 (b) respectively.

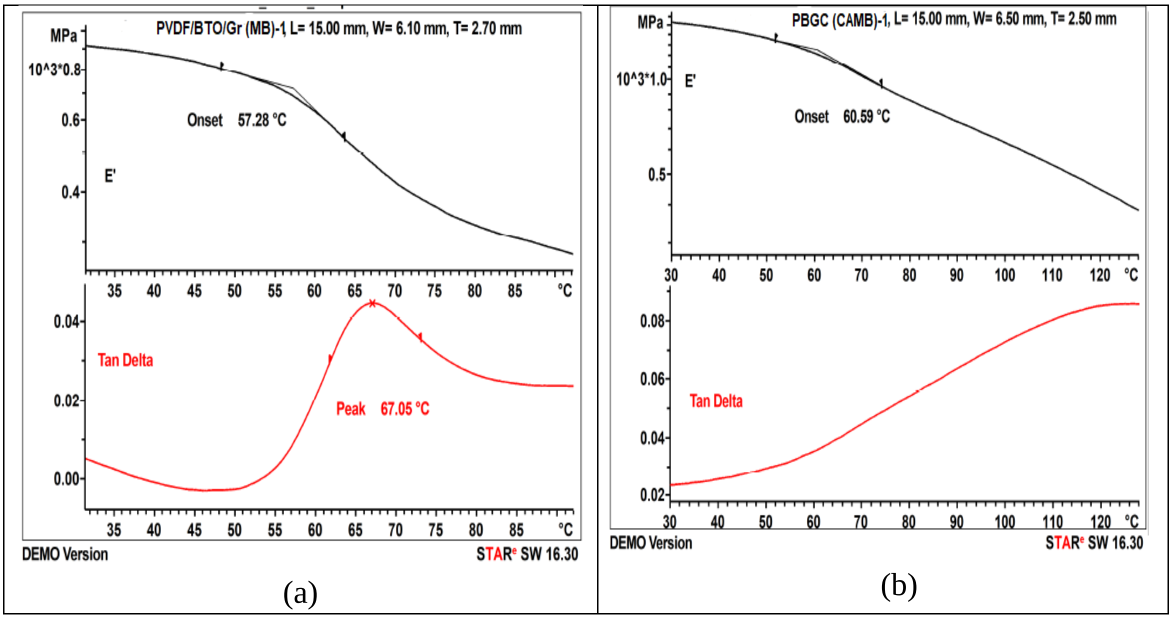

(a) (b)

Figure 5.75 (a) and (b) DMA curves in term of storage modulus and tan delta as a function of temperature corresponding to MBD and CAMBD composites

It has been observed from both the curves that the storage modulus (E') of the material is decreasing with the increase in temperature. However, if we compare both the curves, then the E' of CAMB specimen is more (i.e.$10x10^{\wedge 2}$ MPa) as compared to E' of MBD specimen ($8x10^{\wedge 2}$ MPa). It means the energy absorbing capacity of the CAMBD part is better than the part prepared from MBD composites. The curves of tan δ represent the variation in energy dissipation capacity as a function of temperature. The tan δ curve of MBD composite shows the maximum value of 0.05 at 67°C, whereas in the case of CAMB, the value of tan δ at the same temperature is 0.04. Thus, it means the ratio of loss modulus to storage modulus is more in MB specimen as compared to CAMBD specimen. Consequently, the CAMBD composites have better stiffness and shape recovery property than the MBD composites

5.5.8.3 SEM analysis of 3D printed functional prototypes

The morphology and fractured behaviour of tensile and flexural specimens were further analysed by SEM images. Figure 5.76 shows the microphotographs of fractured surfaces of tensile and flexural specimens prepared from MBD and CAMBD composites.

3D printed parts of MB composites	3D printed parts of CAMB composites
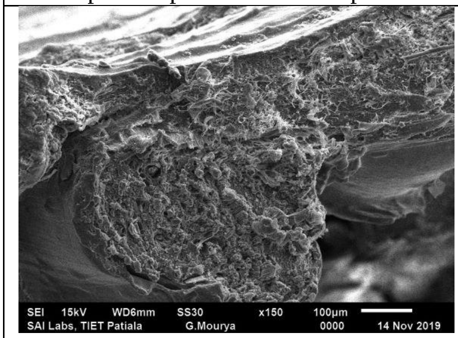 (a)Tensile(MB) X150	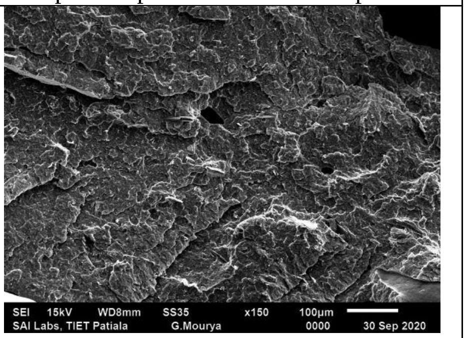 (b)Tensile(CAMB) X150
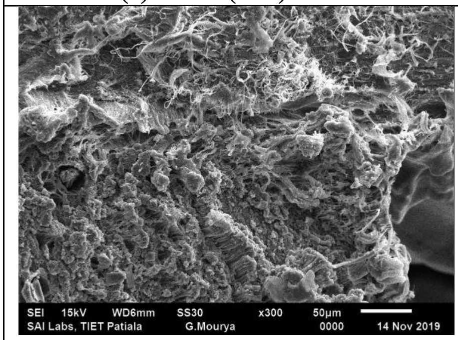 (c)Tensile(MB) X300	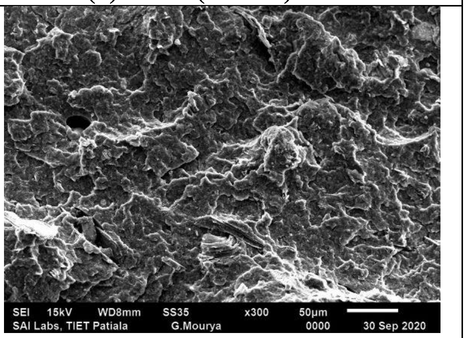 (d)Tensile(CAMB) X300
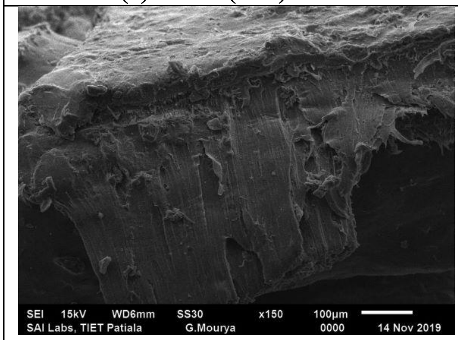 (e)Flexural (MB) X150	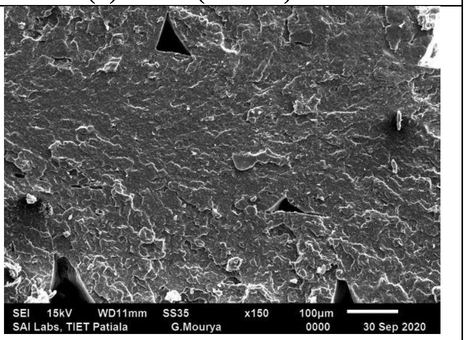 (f)Flexural (CAMB) X150

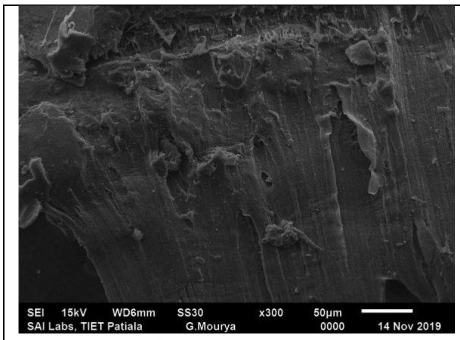

(g)Flexural (MB) X300 (h)flexural (CAMB) X300

Figure 5.76 SEM images of tensile specimens (a)-(d), flexural specimens (e)-(h), prepared by MBD and CAMBD composites respectively.

It has been observed from Figure 5.76 (b) that more elongated pores are observed in Figure 5.76 (a), which indicates that the ductility of (b) is more than (a). It has been also observed that a proper flow of material seems in CAMBD composites as compared to MBD composites. This may be due to the uniform mixing of materials in the CAMB process. The fractured surfaces of the MBD flexural specimen seem to be more brittle as compared to the flexural specimen prepared by the CAMBD process.

The surface roughness of 3D printed parts of mechanically and chemically blended composites have been ascertained from the rendered images of SEM at X300 for each specimen. Figure 5.77 shows the 3D rendered images of fractured surfaces along with the R_a graph of tensile and flexural specimens

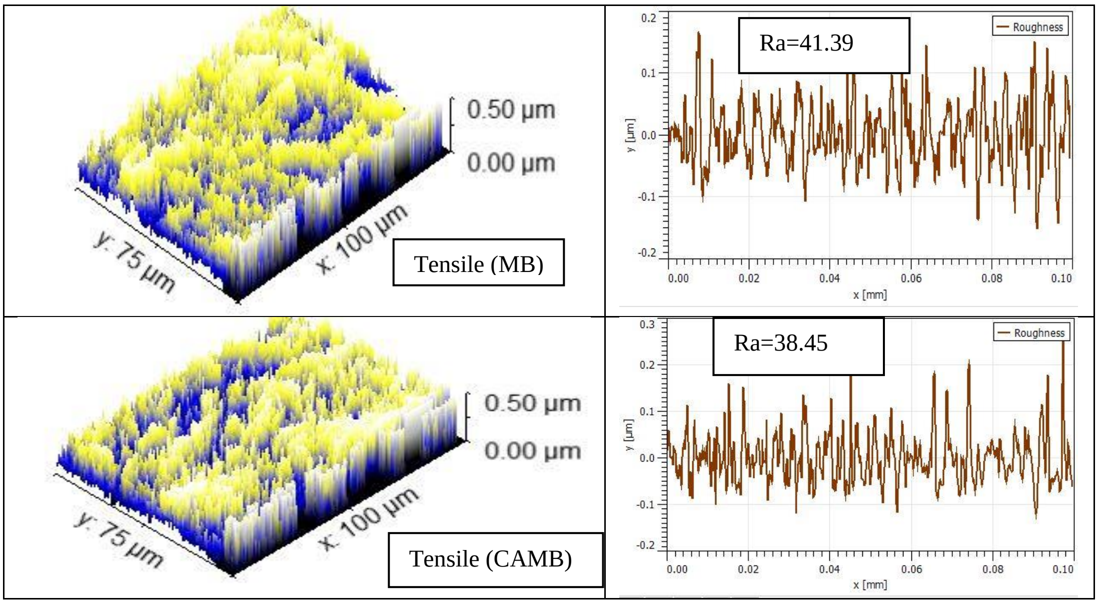

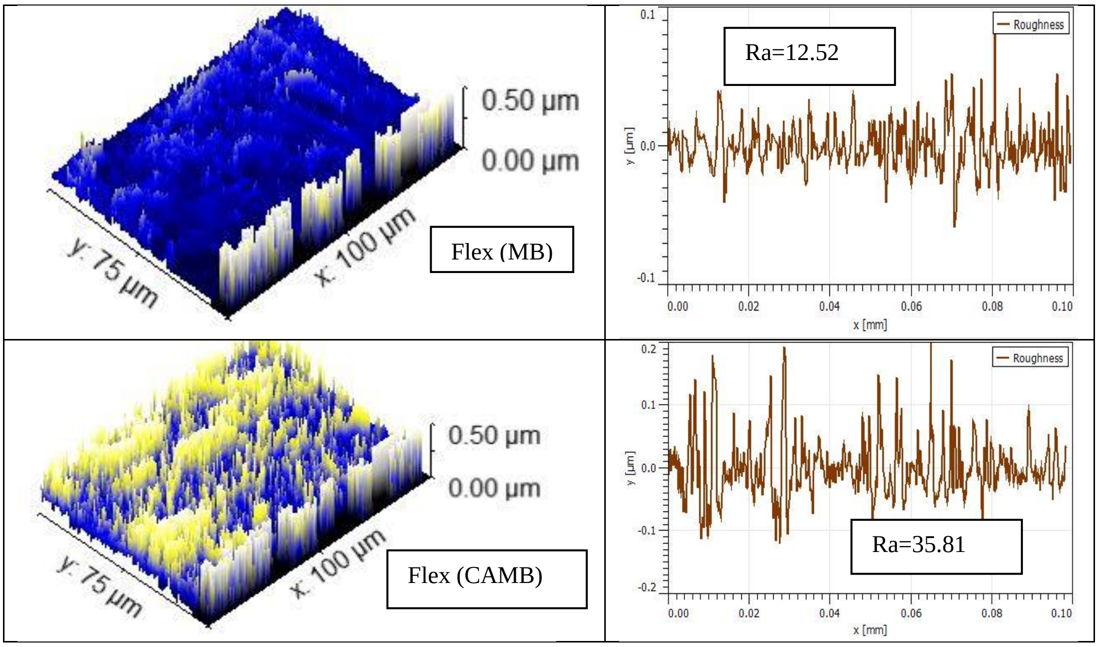

Figure 5.77 3D rendered images of fractured surfaces along with R_a graph of tensile and flexural specimens

It has been observed that the R_a of tensile prototypes prepared from chemically blended composites is comparatively less than parts prepared by using mechanically blended composites. However, for flexural specimens, the R_a of MBD composites has less as compare to CAMBD composites-based specimens.

Figure 5.78, shows the surface porosity values of the best mechanical blended specimen and CAMBD specimen are to be shown. The MB based specimen has porosity (5.14 %) compared to CAMBD composites having porosity (4.02 %). Porosity results show that chemical associated mechanical blended specimen may have comparatively better surface properties as compared to specimen prepared from MBD composites.

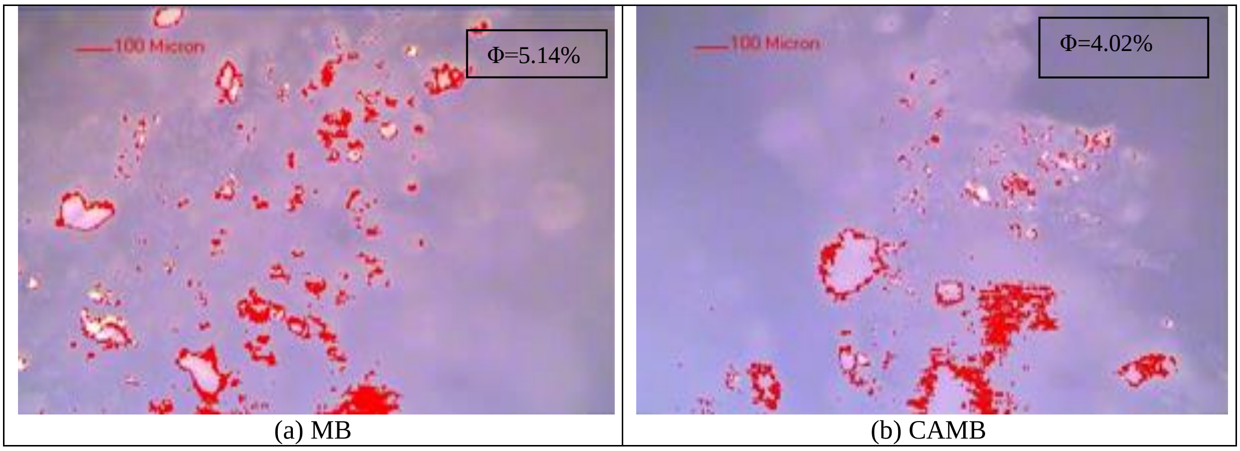

(a) MB

(b) CAMB

Figure 5.78 Surface porosity of 3D printed specimens prepared from (a) MBD and (b) CAMBD composite

5.5.8.4 XRD Analysis

For XRD analysis thin cylindrical discs were 3D printed at the optimized settings of FDM by using MB and CAMB composites. Further for polling, the discs were subjected to a high voltage supply at elevated temperatures.3D printed discs of MBD and CAMBD composites, before polling and after polling were analysed through XRD (see Figure 5.79). The observed spectrums have been matched with standard directory cards such as for PVDF and BTO the ICDD/JCPDS:00-038-1638 and ICDD/JCPDS: 01-079-2264 were used respectively. In the non-poled parts of both MBD and CAMBD composites, peaks at 18.4° (020), 20.1° (110) represents the monoclinic α- phase, a peak at an angle of 26.8° (022) and a small peak at 35.9° (200) corresponding to ɣ- phase and orthorhombic β- phase respectively. Whereas the peaks at 22.2° (100), 31.6° (110), 38.9° (111), and 45.3° (200) corresponds to BTO nano-powder. However, after polling sharp peaks are observed at 20.8° (I00) and a broad peak is observed at 35.9° (200) corresponds to the more β-phase content. As electric poling transforms the β-phase in both MBD and CAMBD composite-based discs, however, the intensity of peak corresponding to β-phase was found more in discs prepared from CAMBD composites containing only 15% BTO as compared to 20% BTO in MB composites. Thus, it has been observed that chemical mixing plays very dominating role in the formation of β-phase in the prepared composite. The results of XRD analysis were found to be in correlation with the previously published research works.

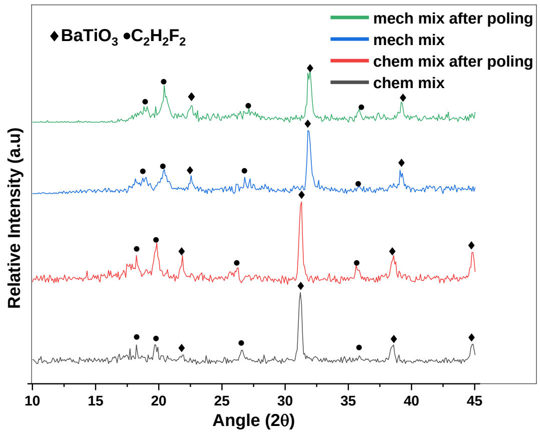

Figure 5.79 XRD spectra of 3D printed specimens

5.5.8.5 FTIR analysis

Figure 5.80 shows the FTIR spectra of 3D printed discs of MBD and CAMBD composites, before and after thermal poling. The effect of polling is observed in the FTIR analysis. The FTIR analysis indicates the absorption peaks for α-phase are formed at a wavenumber of

614,761,795, 1149, and 1382 cm^{-1}, β-phase is formed at a wavenumber of 836, 1278 cm^{-1} and γ-phase formed at a wavenumber of 1236 cm^{-1}. In a non-poled sample, more α-phase content appears in both types of discs.

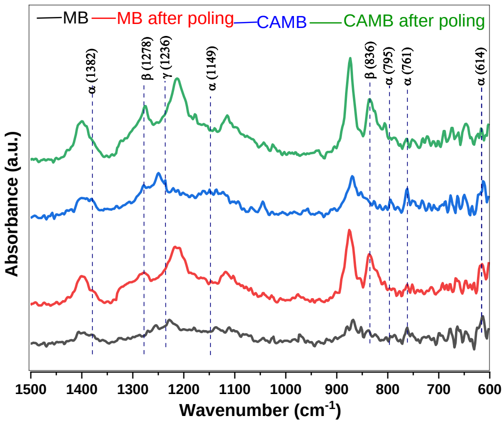

Figure 5.80 FTIR absorption bands of 3D printed specimens

After poling small peaks are formed at 836 cm^{-1} and 1278 cm^{-1} corresponding to β-phase content in discs of MBD composites. On the flip side, the big peaks were generated at 836 cm^{-1} and 1276 cm^{-1} in the discs prepared from CAMBD composites after the electrical poling process. FTIR results were found to be in line with the previously published literature [168-169]. It has been ascertained from XRD and FTIR analysis, that transformation of β-phase is more in CAMBD composites as compared to MBD composites under the identical poling conditions.

5.5.8.6 Dielectric properties

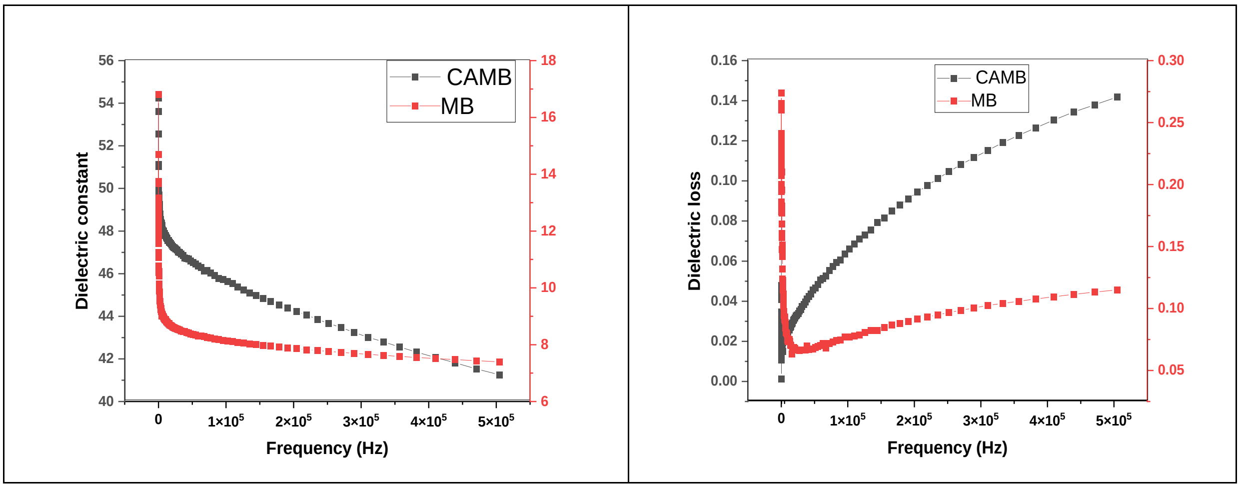

Figure 5.81 Variation of Dielectric constant (a) and dielectric loss (b) of MBD and CAMBD composites with respect to the frequency at room temperature.

Figure 5.81 shows the Dielectric constant and dielectric loss of composites prepared by mechanical and chemical blending of the materials. The variation of dielectric constant and dielectric loss with respect to the frequency at room temperature for both MBD and CAMBD composites has been studied. Chemically blended composites have a high dielectric constant at a low-frequency range, after that it starts decreasing linearly. The graph of dielectric loss depicts that more dielectric loss occurs in MBD composites as compared to CAMBD composites. It has been observed that the dielectric constant of the composites decreases with the increase in frequency. Thus, results obtained from dielectric testing shown that composites prepared by CAMB having more charge carrying capacity even with less proportion of barium titanate. It implies that processing conditions have more effect than composition of the material

5.5.8.7 Piezoelectric coefficient (d_{33})

Further the piezoelectric properties of the thin cylinders discs prepared from MB and CAMB process were compared. The d_{33} of a specimen prepared from MBD composites was 20 pC/N. whereas the d_{33} value of the part prepared from CAMBD composites was 30.2 pC/N. Therefore, CAMB process provides better properties from piezoelectric point of view.

CHAPTER 6
CONCLUSIONS

Following are the stage wise conclusions in this study:

6.1 Conclusions (Stage 1)

In this stage of research work, PVDF, BTO, and Gr-based composite have been developed by MB process for the fabrication of feedstock filament for 4-D printing applications. Following outcomes have been found based on experimental results.

(a) From the MFI testing, it has been found that the composite material flows continuously only when BTO is added from 10% to 20% by weight in the PVDF matrix, whereas the proportion of Gr was kept fixed at 2% by weight. The viscosity of composites calculated at different proportions shown that, with the increase in the proportion of BTO from 10% to 20%, the viscosity was increased from 7.58 x10^^{3} Pa-s to 12.07 x 10^^{3} Pa-s.

(b) The results of mechanical testing suggested that the feedstock filament having composition PVDF (78%) + Gr (2%) + BTO (20%) and extruded at temperature 200°C at 40 rpm has shown maximum mechanical strength and feedstock filament fabricated at low extrusion temperature and having composition PVDF (88%) + Gr (2%) + BTO (10%) shown comparatively poor mechanical properties.

(c) The results of ANOVA outlines that composition has maximum contribution (90% and 82%), followed by extruder temperature (16% and 8%) toward the BS and PS, respectively, whereas screw speed was found insignificant.

(d) The feedstock filament having composition PVDF (78%) + Gr (2%) + BTO (20%) and extruded at temperature 200°C at 50 rpm has shown optimized mechanical strength. The optimized values of PL, BL, PS, BS, and modulus of toughness are 71.81 N, 65.81 N, 29.92 MPa, 27.42 MPa, and 1.71 MPa respectively.

(e) It was observed from dimensional analysis that feedstock filaments extruded at six out of nine experimental settings have a diameter within the permissible limit of 175 ± 0.05 mm.

(f) Surface porosity results are in lined with results of mechanical properties. The filament having maximum strength shown very less surface porosity (4.93 %) as compared to 7.4 % porosity on the surface of feedstock filament having minimum mechanical strength.

(g) The graphs obtained from DSC analysis illustrated that the developed composite has shown the same consistency over two thermal cycles. The addition of Gr and BTO does not affect the processing conditions of the PVDF matrix. There was no change observed in the melting point of the developed composite as compared to virgin PVDF. The developed wire at the aforementioned parametric settings can be easily used without any change in hardware. Moreover, the energy absorption capacity has been increased in developed composite during the heating cycle.

(h) Further the results of surface characterization based upon the surface roughness and fractured surface microphotographs obtained from the SEM, EDAX, and area mapping, proven the correlation between mechanical and morphological properties of the prepared filaments.

6.2 Conclusions (Stage 2)

In this stage of research work, the filament shown best mechanical properties at stage 1 was used to run on an FDM setup. Functional prototypes as per ASTM standards were fabricated using DOE to optimize the process parameters of FDM. Following conclusions have observed for this stage:

(a) An EAP polymer-based feedstock filament comprising of PVDF (78% by weight), BTO (20% by weight), and Gr (2% by weight) was successfully prepared via a mechanical blending process through TSE. Fabricated feedstock filament was used for 3D printing of functionally graded prototypes. The 3D printed parts were subjected to destructive testing, for tensile, flexural, and pull-out properties.

(b) It has been ascertained from the mechanical testing that standard specimens 3D printed at infill speed of 50 mm/s and infill angle of 45° with 100% infill density provides better tensile and flexural strength. Also, the regression equations for extrapolating various mechanical properties have been developed. The observed values of mechanical properties were found near the predicted values at a 95% confidence level.

(c) The observed value of PS, BS, and modulus of toughness of tensile specimen printed at optimized experimental settings was 42.98 MPa, 39.15 MPa, and 4.32 MPa respectively. The optimized value of PS, BS, flexural modulus, and modulus of toughness of flexural specimen was 64.12 MPa, 59.07MPa, 1018.17 MPa, and 18.05 MPa, respectively.

(d) The results of pull-out testing outlined that part fabricated at infill speed 70 mm/s and infill angle 45° at 80% infill density provide maximum value of PS 18.75 MPa. From multi optimization for flexural and pull-out properties ascertained that the part fabricated at IS 70mm/s, IA 45^o and ID 100% shows better flexural and pull-out strength. However, experimental settings with infill speed 90mm/s, infill angle 90^o, and infill density 60% shown the worst mechanical properties as compared to all.

(e) Microscopic images illustrated that parts fabricated at high infill density with low infill speed shown less porosity/void formation which contributed to better mechanical performance as compared to parts fabricated at low-density level.

(f) The 3D printed specimens were further used to measure the surface hardness with a shore-D durometer. It was found that shore-D values were in line with tensile and flexural properties.

(g) It was revealed from the dimensional analysis that infill speed 50 mm/s, infill angle 45° and infill density 100% were optimized settings for 3D printing of parts, whereas parts fabricated at high infill speed shown more dimensional deviation.

(h) Further the fractured surfaces of the tensile and flexural specimen were examined by SEM, EDS, and area mapping analysis. Results of the morphological analysis were in correlation with mechanical properties. Area mapping analysis illustrated that more homogenous dispersion of elements was found in specimens having better mechanical strength.

(i) For surface roughness analysis, 3D rendered SEM images were used with the help of Gwyddion (an image processing) software. The observed values of surface roughness of specimen shown maximum tensile and flexural strength were 28.47 nm and 13.04 nm, respectively.

(j) Results of the dynamic mechanical analysis revealed that the part shown better flexural properties also having more storage modulus and absorbs more energy under the repeated cyclic force. Thus it may suit better for piezoelectric applications.

(k) From process capability indices the observed values of C_p and C_{pk} were found greater than 1 for both tensile and flexural properties. Therefore FDM printing of PVDF+Gr+BTO based composite at optimized parametric settings was a statistically controlled process.

6.3 Conclusions (Stage 3)

In this stage, the EAP-based matrix of PVDF was reinforced with BTO and Gr to prepare PBGC for the fabrication of a feedstock filament by CAMB process for FDM (for possible 4D applications). Followings outcomes have been drawn from the study performed at stage 3.

(a) The results of rheological testing shown that MFI of the composites decreased by loading of more filler proportion in the base polymer matrix. Further, the viscosity was also measured and found to increase as opposed to MFI.

(b) Results of mechanical testing shown that feedstock filament having composition PVDF 78%+2%Gr+20%BTO, extruded at 180°C at 60 rpm has shown maximum mechanical strength and feedstock filament fabricated at 200°C and 50 rpm having PVDF 88%+2%Gr+10%BTO shown comparatively poor mechanical performance.

(c) Results of ANOVA shown that extruder temperature has maximum contribution (74% and 77%), followed by screw speed (18% and 22%) toward the PS and BS, respectively, whereas composition has been found insignificant. Thus the optimized experimental settings of TSE for better mechanical properties are 180°C extruder temperature, screw speed 60 rpm with composition having 83% PVDF+2%Gr+15% BTO.

(d) The observed values of PL, BL, PS, BS, and modulus of toughness of specimens prepared at optimized settings are 103.2 N, 92.95 N, 43.00 MPa, 38.73 MPa, and 1.70 MPa respectively.

(e) Results of dimensional analysis and surface porosity analysis shown that filaments of CAMB composites shown better mechanical strength also have the least dimensional deviation (0.01) and low surface porosity (1.53%), whereas filament is shown poor mechanical performance having a more porous surface. Conclusively, the results of dimensional analysis and surface porosity are in correlation with the mechanical properties of the prepared filaments.

(f) DSC analysis performed on filaments having the best and poor mechanical properties illustrated the thermal consistency of the developed composite over two thermal cycles. It was observed that the energy absorbing capacity of composite has been increased in 2^{nd} consecutive cycle.

(g) SEM microphotographs of fractured surfaces illustrated that filament shown best mechanical strength having uniform dimples formation throughout its surfaces. These dimples may be formed due to the more ductility of the composite. Morphological results are in line with the mechanical performance shown by the CAMBD composites.

6.4 Conclusions (Stage 4)

In this stage of research work feedstock filament prepared by CAMB was used to run on an open-source FDM printer. Based on the experimental results, the following outcomes have drawn:

(a) An EAP polymer-based composite comprising PVDF (83% by weight), BTO (15% by weight), and Gr (2% by weight) was successfully prepared via a chemical mixing process. Prepared films of composites were chopped and used on the TSEfor the fabrication of feedstock filament. Fabricated feedstock filament was used for 3D printing of functionally graded prototypes. Standard tensile and flexural specimens were successfully prepared on the existing low-cost FDM setup (without changing any hardware/software). The 3D printed parts were subjected to destructive testing for tensile, flexural, and pull-out properties.

(b) Results of tensile testing outlined that experimental setting with infill speed 50mm/s, infill angle 0°, and infill density 100% was best to provide maximum value of PS (63.1 MPa), BS (54.2 MPa), and fracture toughness (5.8 MPa). However, specimen prepared with infill speed 90 mm/s, infill angle 45°, and infill density 80% shown poor tensile properties.

(c) Flexural testing results shown that maximum value of PS (71.54 MPa), BS (62.18 MPa) and MoT (6.7 MPa) was found in specimen fabricated by keeping infill speed 70 mm/s, infill angle 45°, and infill density 100% as process parameters of FDM. However, an experiment conducted with an infill speed of 90 mm/s, infill angle of 45°, and infill density of 60% shown the worst mechanical properties.

(d) Multi optimization of flexural and pull-out properties ascertained that the part fabricated at IS 90 mm/s, IA 0^o and ID 100% shows better flexural and pull-out strength. However, experimental settings with infill speed 50 mm/s, infill angle 90^o, and infill density 60% shown the worst mechanical properties as compared to all. From pull-out testing, the maximum value of PS, BS, and modulus of toughness was 22.63 MPa, 20.36 MPa, and 37.48 MPa, respectively.

(e) Dimensional analysis performed on 3D printed specimens illustrated that minimum dimensional deviation was found in the parts printed at 100% infill density, whereas parts printed at high infill speed and low infill density shown more deviation.

(f) Surface hardness of 3D printed parts, measured by shore-D durometer revealed that maximum shore D value (72,87) was found in the part fabricated at 100% infill density, infill speed 50 mm/s with infill angle 90^o. The photomicrographs captured with a metallurgical microscope concluded that results of surface porosity are in lined with the mechanical strength of the 3D printed parts.

(g) SEM images of fractured surfaces of tensile and flexural specimens, shown that a proper layer to layer joining was found in CAMB composites, even more number of uniformly distributed dimples was observed in part shown better mechanical properties. Further, results of mechanical strength were supported by EDAX and area mapping analysis.

(h) 3D rendered SEM images were used for predicting the surface roughness of 3D printed parts. Surface roughness of the specimen shown best tensile and flexural strength was 32.68nm and 31.72 nm, respectively.

(i) Results of DMA analysis shown that the specimen fabricated with infill speed 70 mm/s, infill angle 45, and infill density 100% having more storage modulus $1.5x10^{\wedge 3}$ MPa. The energy absorbing capacity of the composite decreased with the increase in temperature. However, the part shown poor flexural strength dissipates more energy under low force cyclic loading conditions.

(j) Results of process capability indices, shown that the value of C_p and C_{pk} was found greater than 1, therefore, 3D printing of CAMB composite at optimized parametric settings of FDM was found as a statistically controlled process.

6.5 Conclusions (Stage 5)

(a) Thin cylindrical discs were successfully 3D printed using optimized settings of FDM for MB and CAMB composites. These cylindrical discs were electrically poled at the very high electric voltage for proper alignment of PVDF dipoles.

(b) The 3D printed discs before and after poling was characterized and compared by using XRD and FTIR. XRD spectra showed the identical peaks of BTO in both cases, which represent the homogeneous dispersion of BTO powder in the PVDF matrix. Moreover, it has been also ascertained that more β-phase content was obtained in the electrically poled specimen as compare to the non- poled part. The FTIR analysis demonstrated that under the high voltage electrical field, the dipoles of PVDF are aligned properly, thus α and ɣ phases have transformed into β phase.

(c) Then 3D printed discs were used to identify the variation in dielectric constant and dielectric loss as a function of frequency in both the composites prepared by the MB and CAMB process. It was found that for both the composites value of the dielectric constant decreased with the increase of frequency, whereas dielectric loss was increased as opposed to the dielectric constant. The results of the dielectric analysis revealed that CAMBD composite-based disc having more dielectric constant as compared to disc prepared from MBD composite.

(d) Piezoelectric coefficient of 3D printed discs was measured by using d_{33} meter. d_{33} value of discs prepared from MBD and CAMBD composites has been found 20 pC/N and 30.2 pC/N respectively. Thus the developed composites may be easily used as sensors for 4D applications.

- **Comparative analysis: To study the effect of MB and CAMB process on the properties of feedstock filaments and 3D printed parts**

Effects of blending techniques have been compared based on different properties of feedstock filaments and 3D printed parts. Following conclusions have drawn from this comparative study:

(a) Mechanical testing performed on feedstock filaments prepared from MBD and CAMBD composites shown that filaments prepared from CAMBD composites having 45% more tensile strength even with less amount of BTO (15% by weight) than MBD composites having 20% (by weight) of BTO.

(b)Result of SEM analysis has shown the uniform dimple formation at the fractured surface of CAMBD composite-based filament whereas only two dimples were observed in MB-based composites. Uniform dimple formation may represent the high ductility and tensile strength of CAMBD composites. Moreover, porosity testing has shown that filaments prepared from CAMB have 69% less surface porosity.

(c) DSC analysis shown that MBD composites absorbed more heat (31.09 J/g) during the heating cycle as compared to heat absorbed by CAMBD composite (26.59 J/g). As regards thermal stability, both MBD and CAMBD composites showed similar trends in 2nd consecutive cycle of heating and cooling.

(d) The results of tensile and flexural testing performed on the 3D printed functional prototypes shown that parts prepared from CAMBD composites having 47%, 11%, and 21% more tensile, flexural, and pull-out strength respectively, as compared to parts prepared from MB composites.

(e) SEM analysis performed on fractured surfaces of 3D printed tensile and flexural specimens depicts the proper adhesion of material and shows strong bonding in between the layers in 3D printed parts prepared from CAMBD composites.

(f) DMA results shown that parts prepared from CAMBD composites having a high value of storage modulus. Thus, chemically blended composites dissipated low energy under low force cyclic loading, whereas MBD composites dissipated more energy under cyclic loading conditions.

(g) The 3D printed discs before and after poling were characterized and compared by using XRD and FTIR analysis. XRD analysis ascertained that more β-phase content was obtained in the electrically poled specimen of CAMBD composite as compared to an electrically poled sample of MB composite. The FTIR analysis demonstrated that the intensity of β phase peaks was observed more in CAMBD composites having 15% BTO, as compared to MBD composites having 20% BTO, after an identical poling process. It implies that the mode of mixing played a better role in β phase formation as compared to the composition of developed PVDF-based composites.

(h) The dielectric properties of both the samples were measured at room temperature. The dielectric constant value of CAMBD composite was 3 times more than the dielectric constant of MB composite at the same frequency level. However, the dielectric constant of both samples was decreased with the increase of frequency.

(i) Piezoelectric coefficient of the 3D printed disc was measured by using d_{33} meter. d_{33} value of discs prepared from MBD and CAMBD composites has been found 20 pC/N and 30.2 pC/N respectively. Thus, the developed composites may be suitable for pressure sensors, touch-sensitive buttons, or other user interface control, actuators for bio-mimetic-based 4D applications.

The overall conclusion of this study represents that the CAMB process provides better mechanical, morphological, dielectric, and piezoelectric properties in developed composites even having less proportion of filler material (BTO) in the base polymer matrix (PVDF). This may be due to the homogeneous dispersion of doping particles in the PVDF matrix during the chemical mixing process. This study represents that as compared to the composition of the material, the mode of mixing played the more dominant role to improve the various above-mentioned properties of developed composites.

CHAPTER 7

FUTURE SCOPE

- In this research work, functional prototypes of PBGC have been 3D printed. Further, studies may be conducted for recyclability analysis and life cycle assessment of developed composite.
- In this study, MB and CAMB of virgin PVDF have been studied. Further, study may be performed on MB and CAMB of primarily recycled polymer matrix.
- In this study, the effect of filler particles on the various properties of polymer matrix has been discussed at constant particle size; Further, this study may be extended by varying the size of filler particles in a polymer matrix.
- As PVDF exists in five different phases, in this research work, the only transformation of β-phase to α-phase has been discussed. Further, a research study may be performed to study other phases of PVDF.
- In this study, the effect of single-particle size (SPS), double particle size (DPS), and triple particle size (TPS) has not been discussed. Therefore, in the future, this study may extend by studying the contribution of SPS, DPS, and TPS on developed composites.
- In this present study, only technical properties have been discussed, further, this research work may be extended by studying the techno-economic analysis of developed composites
- In this research work, the Taguchi L9 method was used for the optimization of the process parameters. In the future, some other optimization techniques may be used.

REFERENCES

1. Flowers J. RP in Technology. The Technology Teacher. 2002; 62(3), 7-11.
2. Jiménez M, Romero L, Domínguez IA, Espinosa MD, Domínguez M. AM technologies: an overview about 3D printing methods and future prospects. Complexity. 2019 Feb;2019.
3. Kruth JP. Material incress manufacturing by RP techniques. CIRP annals. 1991 Jan 1;40(2):603-14.
4. Davim JP, editor. Additive and Subtractive Manufacturing: Emergent Technologies. De Gruyter; 2019 Dec 16.
5. Khoo ZX, Teoh JE, Liu Y, Chua CK, Yang S, An J, Leong KF, Yeong WY. 3D printing of smart materials: A review on recent progresses in 4D printing. Virtual and Physical Prototyping. 2015 Jul 3;10(3):103-22.
6. Pandey PM, Reddy NV, Dhande SG. Slicing procedures in layered manufacturing: a review. Rapid prototyping journal. 2003 Dec 1; 9(5):274-88.
7. Wong KV, Hernandez A. A review of AM. ISRN Mech Eng 2012: 1–10.
8. Touri M, Kabirian F, Saadati M, Ramakrishna S, Mozafari M. AM of biomaterials−the evolution of rapid prototyping. Advanced Engineering Materials. 2019 Feb;21(2):1800511.
9. Noorani R. Rapid prototyping: principles and applications. John Wiley & Sons; 2006.
10. Cooper KP. Building components by laser-additive processing. Jom. 2001 Sep 1;53(9):29.
11. Kumar N, Jain PK, Tandon P, Pandey PM. The effect of process parameters on tensile behavior of 3D printed flexible parts of ethylene vinyl acetate (EVA). Journal of Manufacturing Processes. 2018 Oct 1;35:317-26.
12. Ghomi ER, Khosravi F, Neisiany RE, Singh S, Ramakrishna S. Future of AM in Healthcare. Current Opinion in Biomedical Engineering. 2020 Oct 25:100255.
13. Zhang Y, Bernard A, Harik R, Karunakaran KP. Build orientation optimization for multi-part production in AM. Journal of Intelligent Manufacturing. 2017 Aug 28; (6):1393-407.
14. Sharma R, Singh R, Batish A. Investigations for BTO and Graphene Reinforced PVDF Matrix for 4D Applications, Elsevier, 2020..

15. Adediran A, Oyedele A. Operational aspects and regulatory gaps in AM. AM Handbook: Product Development for the Defense Industry. 2017 May 19;129:9781315119106-8.
16. Kumar P, Ahuja IP, Singh R. Application of fusion deposition modelling for rapid investment casting–a review. International Journal of Materials Engineering Innovation. 2012 Jan 1;3(3-4):204-27.
17. Negi S, Dhiman S, Sharma RK. Basics, applications and future of AM technologies: A review. Journal of Manufacturing Technology Research. 2013;5(1/2):75.
18. Ghorpade A, Karunakaran KP, Tiwari MK. Selection of optimal part orientation in fused deposition modelling using swarm intelligence. Proceedings of the Institution of Mechanical Engineers, Part B: Journal of Engineering Manufacture. 2007 Jul 1;221(7):1209-19.
19. Sharma R, Singh R, Batish A. On multi response optimization and process capability analysis for surface properties of 3D printed functional prototypes of PVC reinforced with PP and HAp. Materials Today: Proceedings. 2020 Jan 1;28:1115-22.
20. Jiang J, Xu X, Stringer J. Support structures for AM: a review. Journal of Manufacturing and Materials Processing. 2018 Dec;2(4):64.
21. Farina I, Sharma R, Singh R, Batish A, Singh N, Fraternali F, Colangelo F. Mechanical characterization of FDM filaments with PVDF matrix reinforced with Graphene and Barium Titanate. In IOP Conference Series: Materials Science and Engineering 2020 Nov 1 (Vol. 999, No. 1, p. 012010). IOP Publishing.
22. Pandey PM, Reddy NV, Dhande SG. Part deposition orientation studies in layered manufacturing. Journal of materials processing technology. 2007 Apr 30;185 (1-3):125-31.
23. Lizardo BF, Vieira LM, Carlos Campos Rubio J, Panzera TH, Davim JP. An assessment of thermosetting infiltrate in powder-based composites made by AM. Journal of Composite Materials. 2019 Mar;53(7):873-82.
24. Bajpai PK, Singh I, Madaan J. Tribological behavior of natural fiber reinforced PLA composites. Wear. 2013 Jan 15;297(1-2):829-40.
25. Sharma R, Singh R, Batish A, Ranjan N. Investigations on Chemical Assisted Mechanically Blended 3D Printed Functional Prototypes of PVDF-BTO-Gr Composite. Reference Module in Materials Science and Materials Engineering, Elsevier, 2021, https://doi.org/10.1016/B978-0-12-820352-1.00144-9.

26. Zolfagharian A, Kouzani AZ, Khoo SY, Moghadam AA, Gibson I, Kaynak A. Evolution of 3D printed soft actuators. Sensors and Actuators A: Physical. 2016 Oct 15;250:258-72.
27. Farina I, Fabbrocino F, Colangelo F, Feo L, Fraternali F. Surface roughness effects on the reinforcement of cement mortars through 3D printed metallic fibers. Composites Part B: Engineering. 2016 Aug 15;99:305-11.
28. Sharma R, Singh R, Batish A. On effect of chemical-assisted mechanical blending of BTOand graphene in PVDF for 3D printing applications. Journal of Thermoplastic Composite Materials. 2020 Aug 4:0892705720945377.
29. Bernard A, Taillandier G, Karunakaran KP. Evolutions of rapid product development with rapid manufacturing: concepts and applications. International Journal of Rapid Manufacturing. 2009 Jan 1;1(1):3-18.
30. Farina I, Singh N, Colangelo F, Luciano R, Bonazzi G, Fraternali F. High-performance nylon-6 sustainable filaments for AM. Materials. 2019 Jan;12(23):3955..
31. Bajpai PK, Singh I, Madaan J. Development and characterization of PLA-based green composites: A review. Journal of Thermoplastic Composite Materials. 2014 Jan;27(1):52-81..
32. Li YC, Zhang YS, Akpek A, Shin SR, Khademhosseini A. 4D bioprinting: the next-generation technology for bio fabrication enabled by stimuli-responsive materials. Bio fabrication. 2016 Dec 1;9(1):012001.
33. Tibbits S. Self-assembly lab: experiments in programming matter. Taylor & Francis; 2016 Nov 10.
34. Mironov V, Reis N, Derby B. Bioprinting: a beginning. Tissue engineering. 2006 Apr 1;12(4):631-4.
35. Ueberschlag P. PVDF piezoelectric polymer. Sensor review. 2001 Jun 1, 21(2), 118-126.
36. González-Henríquez CM, Sarabia-Vallejos MA, Rodriguez-Hernandez J. Polymers for AM and 4D-printing: Materials, methodologies, and biomedical applications. Progress in Polymer Science. 2019 Jul 1;94:57-116.
37. Bauer S, Bauer F. Piezoelectric polymers and their applications. In Piezoelectricity 2008 (pp. 157-177). Springer, Berlin, Heidelberg.
38. Li Y, Feng Z, Hao L, Huang L, Xin C, Wang Y, Bilotti E, Essa K, Zhang H, Li Z, Yan F. A Review on Functionally Graded Materials and Structures via AM: From

Multi-Scale Design to Versatile Functional Properties. Advanced Materials Technologies. 2020 Jun;5(6):1900981.

39. Yang J. An introduction to the theory of piezoelectricity. New York: Springer; 2005 Jan.
40. Karim AN, Begum S, Hashmi MS. Performance and Failure during Energy Testing of Zinc Oxide Varistor Processed from Different Powder Size Fraction and Passivation Thickness. International Journal of Mechanical and Materials Engineering. 2010;5(2):175-81.
41. Park S, Kim Y, Jung H, Park JY, Lee N, Seo Y. Energy harvesting efficiency of piezoelectric polymer film with graphene and metal electrodes. Scientific reports. 2017 Dec 11;7(1):1-8.
42. Smith M, Kar-Narayan S. Piezoelectric Polymers: theory, challenges and opportunities. International Materials Reviews. 2021 Apr 30:1-24.
43. Sharma R, Singh R, Batish A. On mechanical and surface properties of electro-active polymer matrix-based 3D printed functionally graded prototypes. Journal of Thermoplastic Composite Materials. 2020 Feb 20:0892705720907677.
44. Singh AK, Kumar S, Singh VP. Effect of the addition of conductive powder in dielectric on the surface properties of superalloy Super Co 605 by EDM process. The International Journal of Advanced Manufacturing Technology. 2015 Mar 1;77(1-4):99-106.
45. Kontodina T, Tzetzis D, Davim JP, Kyratsis P. 5 AM for patient-specific medical use. Additive and Subtractive Manufacturing: Emergent Technologies. 2020 Jan 20;4:199.
46. Chorsi MT, Curry EJ, Chorsi HT, Das R, Baroody J, Purohit PK, Ilies H, Nguyen TD. Piezoelectric biomaterials for sensors and actuators. Advanced Materials. 2019 Jan;31(1):1802084.
47. Singh AK, Kumar S, Singh VP. Optimization of parameters using conductive powder in dielectric for EDM of super Co 605 with multiple quality characteristics. Materials and Manufacturing Processes. 2014 Mar 4;29(3):267-73.
48. Bajpai PK, Singh I, Madaan J. Comparative studies of mechanical and morphological properties of polylactic acid and polypropylene based natural fiber composites. Journal of Reinforced Plastics and Composites. 2012 Dec;31(24):1712-24.
49. Zhang JX, Xiang B, He Q, Seidel J, Zeches RJ, Yu P, Yang SY, Wang CH, Chu YH, Martin LW, Minor AM. Large field-induced strains in a lead-free piezoelectric material. Nature nanotechnology. 2011 Feb;6(2):98-102.

50. Singh R, Sharma R, Davim JP. Mechanical properties of bio compatible functional prototypes for joining applications in clinical dentistry. International Journal of Production Research. 2018 Dec 17;56(24):7330-40.
51. Miranda R, Babilio E, Singh N, Santos F, Fraternali F. Mechanics of smart origami sunscreens with energy harvesting ability. Mechanics Research Communications. 2020 Apr 1;105:103503.
52. Mishra S, Unnikrishnan L, Nayak SK, Mohanty S. Advances in piezoelectric polymer composites for energy harvesting applications: a systematic review. Macromolecular Materials and Engineering. 2019 Jan;304(1):1800463.
53. Kumar S, Singh KK, Ramkumar J. Comparative study of the influence of graphene nanoplatelets filler on the mechanical and tribological behavior of glass fabric-reinforced epoxy composites. Polymer Composites. 2020 Dec;41(12):5403-17.
54. Rahman MA, Chung GS. Synthesis of PVDF-graphene nanocomposites and their properties. Journal of Alloys and Compounds. 2013 Dec 25;581:724-30.
55. Wang K, Hussain A, Jo W, Rödel J. Temperature-Dependent Properties of (Bi 1/2 Na 1/2) TiO 3–(Bi 1/2 K 1/2) TiO 3–SrTiO 3 Lead-Free Piezoceramics. Journal of the American Ceramic Society. 2012 Jul;95(7):2241-7.
56. Su J, Zhang J. Recent development on modification of synthesized BTO ($BaTiO_3$) and polymer/$BaTiO_3$ dielectric composites. Journal of Materials Science: Materials in Electronics. 2019 Feb;30(3):1957-75.
57. Rahman M, Haider J, Akter T, Hashmi MS. 1.02 Techniques for Assessing the Properties of Advanced Ceramic Materials. Comprehensive Materials Processing. 2014 Apr 7:3.
58. Fraternali F, Amendola A. Novel Actuators and Sensors with Tensegrity Architecture. InKey Engineering Materials 2019 (Vol. 826, pp. 105-110). Trans Tech Publications Ltd.
59. Biggs J, Danielmeier K, Hitzbleck J, Krause J, Kridl T, Nowak S, Orselli E, Quan X, Schapeler D, Sutherland W, Wagner J. EAPs: developments of and perspectives for dielectric elastomers. Angewandte Chemie International Edition. 2013 Sep 2;52(36):9409-21.
60. Wang ZL. Functional and smart materials. Wiley Encyclopedia of Electrical and Electronics Engineering. 2001 Aug 21.

61. Kochervinskii VV. Piezoelectricity in crystallizing ferroelectric polymers: Poly (vinylidene fluoride) and its copolymers (A review). Crystallography Reports. 2003 Jul;48(4):649-75.
62. Cauda V, Stassi S, Bejtka K, Canavese G. Nanoconfinement: an effective way to enhance PVDF piezoelectric properties. ACS applied materials & interfaces. 2013 Jul 10;5(13):6430-7.
63. Breitenbach J. Melt extrusion: from process to drug delivery technology. European journal of pharmaceutics and biopharmaceutics. 2002 Sep 1;54(2):107-17.
64. Hashmi MS. Aspects of tube and pipe manufacturing processes: meter to nanometer diameter. Journal of Materials Processing Technology. 2006 Oct 20;179(1-3):5-10.
65. Singh R, Singh S, Fraternali F. Development of in-house composite wire based feed stock filaments of fused deposition modelling for wear-resistant materials and structures. Composites Part B: Engineering. 2016 Aug 1;98:244-9.
66. Kashiwagi T, Harris Jr RH, Zhang X, Briber RM, Cipriano BH, Raghavan SR, Awad WH, Shields JR. Flame retardant mechanism of polyamide 6–clay nanocomposites. Polymer. 2004 Feb 1;45(3):881-91.
67. Kelly AL, Brown EC, Coates PD. The effect of screw geometry on melt temperature profile in single screw extrusion. Polymer Engineering & Science. 2006 Dec;46(12):1706-14.
68. Zhang M, Bai X, Zhang Z. Extrusion process improves the functionality of soluble dietary fiber in oat bran. Journal of Cereal Science. 2011 Jul 1;54(1):98-103.
69. Zheng H, Yan G, Lee Y, Alcaraz C, Marquez S, de Mejia EG. Effect of the extrusion process on allergen reduction and the texture change of soybean protein isolate-corn and soybean flour-corn mixtures. Innovative Food Science & Emerging Technologies. 2020 Aug 1;64:102421.
70. Tripathi P, Katiyar PK, Ramkumar J, Balani K. Synergistic role of carbon nanotube and yttria stabilised zirconia reinforcement on wear and corrosion resistance of Cr-based nano-composite coatings. Surface and Coatings Technology. 2020 Mar 15;385:125381.
71. Begum S, Fawzia S, Hashmi MS. PMCwith natural and synthetic fibres. Advances in Materials and Processing Technologies. 2020 Jul 2;6(3):547-64.
72. Raquez JM, Narayan R, Dubois P. Recent advances in reactive extrusion processing of biodegradable polymer-based compositions. Macromolecular Materials and Engineering. 2008 Jun 16;293(6):447-70.

73. Kumar S. Simultaneous improvement of micro-hardness and surface finish in die steels by powder-mixed EDM process. In ASME International Mechanical Engineering Congress and Exposition 2014 Nov 14 (Vol. 46445, p. V02BT02A021). American Society of Mechanical Engineers..
74. Vynckier AK, Dierickx L, Voorspoels J, Gonnissen Y, Remon JP, Vervaet C. Hot-melt co-extrusion: requirements, challenges and opportunities for pharmaceutical applications. Journal of pharmacy and pharmacology. 2014 Feb;66(2):167-79.
75. Aleksovski A, Van Bockstal PJ, Roškar R, Sovány T, Regdon Jr G, De Beer T, Vervaet C. Comparison of metoprolol tartrate multiple-unit lipid matrix systems produced by different technologies. European Journal of Pharmaceutical Sciences. 2016 Jun 10;88:233-45.
76. Gonzalez-Gutierrez J, Cano S, Schuschnigg S, Kukla C, Sapkota J, Holzer C. AM of metallic and ceramic components by the material extrusion of highly-filled polymers: A review and future perspectives. Materials. 2018 May;11(5):840.
77. Mori K, Maeno T, Fukui Y. Spline forming of ultra-high strength gear drum using resistance heating of side wall of cup. CIRP annals. 2011 Jan 1;60(1):299-302.
78. Roy D, Cambre JN, Sumerlin BS. Future perspectives and recent advances in stimuli-responsive materials. Progress in Polymer Science. 2010 Jan 1;35(1-2):278-301.
79. Hadimani RL, Bayramol DV, Sion N, Shah T, Qian L, Shi S, Siores E. Continuous production of piezoelectric PVDF fibre for e-textile applications. Smart Materials and structures. 2013 Jun 6;22(7):075017.
80. Patel I, Siores E, Shah T. Utilisation of smart polymers and ceramic based piezoelectric materials for scavenging wasted energy. Sensors and Actuators A: Physical. 2010 May 1;159(2):213-8.
81. Grinberg D, Siddique S, Le MQ, Liang R, Capsal JF, Cottinet PJ. 4D Printing based piezoelectric composite for medical applications. Journal of Polymer Science Part B: Polymer Physics. 2019 Jan 15;57(2):109-15.
82. Ramadan KS, Sameoto D, Evoy S. A review of piezoelectric polymers as functional materials for electromechanical transducers. Smart Materials and Structures. 2014 Jan 17;23(3):033001.
83. Ribeiro C, Sencadas V, Correia DM, Lanceros-Méndez S. Piezoelectric polymers as biomaterials for tissue engineering applications. Colloids and Surfaces B: Biointerfaces. 2015 Dec 1;136:46-55.

84. Guo HF, Li ZS, Dong SW, Chen WJ, Deng L, Wang YF, Ying DJ. Piezoelectric PU/PVDF electrospun scaffolds for wound healing applications. Colloids and Surfaces B: Biointerfaces. 2012 Aug 1;96:29-36.
85. Zeng Y, Jiang L, Sun Y, Yang Y, Quan Y, Wei S, Lu G, Li R, Rong J, Chen Y, Zhou Q. 3D-Printing Piezoelectric Composite with Honeycomb Structure for Ultrasonic Devices. Micromachines. 2020 Aug;11(8):713.
86. Mallik N, Ray MC. Effective coefficients of piezoelectric fiber-reinforced composites. AIAA journal. 2003 Apr;41(4):704-10.
87. Takagi K, Li JF, Yokoyama S, Watanabe R. Fabrication and evaluation of PZT/Pt piezoelectric composites and functionally graded actuators. Journal of the European Ceramic Society. 2003 Sep 1;23(10):1577-83.
88. Safari A, Allahverdi M, Akdogan EK. Solid freeform fabrication of piezoelectric sensors and actuators. Frontiers of Ferroelectricity. 2006:177-98.
89. Qiu J, Tani J, Yamada N, Takahashi H. Fabrication of piezoelectric fibers with metal core. InSmart Structures and Materials 2003: Active Materials: Behavior and Mechanics 2003 Aug 13 (Vol. 5053, pp. 475-483). International Society for Optics and Photonics.
90. Darestani MT, Coster HG, Chilcott TC, Fleming S, Nagarajan V, An H. Piezoelectric membranes for separation processes: Fabrication and piezoelectric properties. Journal of membrane science. 2013 May 1;434:184-92.
91. Xu S, Poirier G, Yao N. Fabrication and piezoelectric property of PMN-PT nanofibers. Nano Energy. 2012 Jul 1;1(4):602-7.
92. Yildirim YA, Toprak A, Tigli O. Piezoelectric membrane actuators for micro pump applications using PVDF-TrFE. Journal of Microelectromechanical Systems. 2017 Dec 1;27(1):86-94.
93. Sharma T, Je SS, Gill B, Zhang JX. Patterning piezoelectric thin film PVDF–TrFE based pressure sensor for catheter application. Sensors and Actuators A: physical. 2012 Apr 1;177:87-92.
94. Xu J, Dapino MJ, Gallego-Perez D, Hansford D. Microphone based on PVDF micro-pillars and patterned electrodes. Sensors and Actuators A: Physical. 2009 Jun 25;153(1):24-32.
95. Haddadi SA, Ghaderi S, Amini M, Ramazani SA. Mechanical and piezoelectric characterizations of electrospun PVDF-nanosilica fibrous scaffolds for biomedical applications. Materials Today: Proceedings. 2018 Jan 1;5(7):15710-6.

96. Chen X, Han X, Shen QD. PVDF-based ferroelectric polymers in modern flexible electronics. Advanced Electronic Materials. 2017 May;3(5):1600460.
97. Wang YR, Zheng JM, Ren GY, Zhang PH, Xu C. A flexible piezoelectric force sensor based on PVDF fabrics. Smart Materials and Structures. 2011 Mar 15;20(4):045009.
98. Gaytan SM, Cadena MA, Karim H, Delfin D, Lin Y, Espalin D, Macdonald E, Wicker RB. Fabrication of BTOby binder jetting AM technology. Ceramics International. 2015 Jun 1;41(5):6610-9.
99. Karaki T, Yan K, Adachi M. BTO piezoelectric ceramics manufactured by two-step sintering. Japanese Journal of Applied Physics. 2007 Oct 22;46(10S):7035.
100. Eswaraiah V, Sankaranarayanan V, Ramaprabhu S. Functionalized graphene–PVDF foam composites for EMI shielding. Macromolecular Materials and Engineering. 2011 Oct 12;296(10):894-8.
101. Uchino K. The development of piezoelectric materials and the new perspective. InAdvanced Piezoelectric Materials 2017 Jan 1 (pp. 1-92). Woodhead Publishing.
102. Kim K, Zhu W, Qu X, Aaronson C, McCall WR, Chen S, Sirbuly DJ. 3D optical printing of piezoelectric nanoparticle–polymer composite materials. ACS nano. 2014 Oct 28;8(10):9799-806.
103. Frederik PM, Hubert DH. Cryo electron microscopy of liposomes. Methods in enzymology. 2005 Jan 1;391:431-48.
104. Nath C, Rahman M, Neo KS. A study on the effect of tool nose radius in ultrasonic elliptical vibration cutting of tungsten carbide. Journal of Materials Processing Technology. 2009 Aug 19;209(17):5830-6.
105. Singh R, Bedi P, Fraternali F, Ahuja IP. Effect of single particle size, double particle size and triple particle size Al2O3 in Nylon-6 matrix on mechanical properties of feed stock filament for FDM. Composites Part B: Engineering. 2016 Dec 1;106:20-7.
106. Singh S, Singh R. Effect of process parameters on micro hardness of Al–Al2O3 composite prepared using an alternative reinforced pattern in fused deposition modelling assisted investment casting. Robotics and Computer-Integrated Manufacturing. 2016 Feb 1;37:162-9.
107. Singh R, Sandhu GS, Penna R, Farina I. Investigations for thermal and electrical conductivity of ABS-graphene blended prototypes. Materials. 2017 Aug;10(8):881.

108. Bedi P, Singh R, Ahuja IP. Effect of SiC/Al2O3 particle size reinforcement in recycled LDPE matrix on mechanical properties of FDM feed stock filament. Virtual and physical prototyping. 2018 Oct 2;13(4):246-54.
109. Daniel WW, Cross CL. Biostatistics: a foundation for analysis in the health sciences. Wiley; 2018 Nov 13.
110. Kumar R, Singh R, Ahuja IP, Penna R, Feo L. Weldability of thermoplastic materials for friction stir welding-A state of art review and future applications. Composites Part B: Engineering. 2018 Mar 15;137:1-5.
111. Maridass B, Gupta BR. Performance optimization of a counter rotating TSE for recycling natural rubber vulcanizates using response surface methodology. Polymer Testing. 2004 Jun 1;23(4):377-85.
112. Ranjan N, Singh R, Ahuja IP, Singh J. Fabrication of PLA-HAp-CS Based Biocompatible and Biodegradable Feedstock Filament Using Twin Screw. AM of Emerging Materials. 2018 Aug 1:325.
113. Régibeau N, Hurlet J, Tilkin RG, Lombart F, Heinrichs B, Grandfils C. Synthesis of medical grade PLLA, PDLLA, and PLGA by a reactive extrusion polymerization. Materials Today Communications. 2020 Sep 1;24:101208.
114. Sharma R, Singh R, Batish A. Study on BTO and graphene reinforced PVDF matrix for 4D applications. Journal of Thermoplastic Composite Materials. 2019 Jul 22:0892705719865004.
115. Li N, Li Y, Liu S. R Pof continuous carbon fiber reinforced polylactic acid composites by 3D printing. Journal of Materials Processing Technology. 2016 Dec 1;238:218-25.
116. Upcraft S, Fletcher R. The RP technologies. Assembly Automation. 2003 Dec 1.
117. Modeen T, Pasquire C, Soar R. Ubiquitous customization–utilizing rapid manufacturing in the production of design and architecture. Management. 2005;1:341-51.
118. Marcinova V. The foregin in totalitarian theatre: the reception of American drama in Slovakia during 1948-1949 (Doctoral dissertation, Universidad de Jaén).
119. Romero PE, Barrios JM. Improvement of Surface Roughness and Hydrophobicity in PETG Parts Manufactured via FDM(FDM): An Application in 3D Printed Self–Cleaning Parts. Materials. 2019 Jan;12(15):2499.
120. Torres J, Cotelo J, Karl J, Gordon AP. Mechanical property optimization of FDM PLA in shear with multiple objectives. Jom. 2015 May;67(5):1183-93.

121. Singh R, Singh R, Dureja JS, Farina I, Fabbrocino F. Investigations for dimensional accuracy of Al alloy/Al-MMC developed by combining stir casting and ABS replica based investment casting. Composites Part B: Engineering. 2017 Apr 15;115:203-8.
122. Dul S, Fambri L, Pegoretti A. Fused deposition modelling with ABS–graphene nanocomposites. Composites Part A: Applied Science and Manufacturing. 2016 Jun 1;85:181-91.
123. Berretta S, Davies R, Shyng YT, Wang Y, Ghita O. Fused Deposition Modelling of high temperature polymers: Exploring CNT PEEK composites. Polymer Testing. 2017 Oct 1;63:251-62.
124. Feng KC, Pinkas-Sarafova A, Ricotta V, Cuiffo M, Zhang L, Guo Y, Chang CC, Halada GP, Simon M, Rafailovich M. The influence of roughness on stem cell differentiation using 3D printed polylactic acid scaffolds. Soft matter. 2018;14(48):9838-46.
125. Jamróz W, Kurek M, Łyszczarz E, Szafraniec J, Knapik-Kowalczuk J, Syrek K, Paluch M, Jachowicz R. 3D printed orodispersible films with Aripiprazole. International journal of pharmaceutics. 2017 Nov 30;533(2):413-20.
126. Kariz M, Kuzman MK, Sernek M. Adhesive bonding of 3D-printed ABS parts and wood. Journal of adhesion science and Technology. 2017 Aug 3;31(15):1683-90.
127. Kaur M, Yun TG, Han SM, Thomas EL, Kim WS. 3D printed stretching-dominated micro-trusses. Materials & Design. 2017 Nov 15;134:272-80.
128. León-Cabezas MA, Martínez-García A, Varela-Gandía FJ. Innovative functionalized monofilaments for 3D printing using FDM for the toy industry. Procedia Manufacturing. 2017 Jan 1;13:738-45.
129. Mohamed AW, Hadi AA, Fattouh AM, Jambi KM. LSHADE with semi-parameter adaptation hybrid with CMA-ES for solving CEC 2017 benchmark problems. In2017 IEEE Congress on evolutionary computation (CEC) 2017 Jun 5 (pp. 145-152). IEEE.
130. Hao W, Liu Y, Zhou H, Chen H, Fang D. Preparation and characterization of 3D printed continuous carbon fiber reinforced thermosetting composites. Polymer Testing. 2018 Feb 1;65:29-34.
131. Silva FD, Borovikov I, Kolen J, Aghdaie N, Zaman K. Exploring gameplay with AI agents. In Proceedings of the AAAI Conference on Artificial Intelligence and Interactive Digital Entertainment 2018 Sep 25 (Vol. 14, No. 1).

132. Singh R, Ranjan N. Experimental investigations for preparation of biocompatible feedstock filament of FDM(FDM) using twin screw extrusion process. Journal of Thermoplastic Composite Materials. 2018 Nov;31(11):1455-69.
133. Wei X, Liu Y, Zhao D, Ge SS. 3D printing of piezoelectric BTOwith high density from milled powders. Journal of the European Ceramic Society. 2020 Dec 1;40(15):5423-30.
134. Roach DJ, Hamel CM, Dunn CK, Johnson MV, Kuang X, Qi HJ. The m4 3D printer: A multi-material multi-method AM platform for future 3D printed structures. AM. 2019 Oct 1;29:100819.
135. Pei E, Shen J, Watling J. Direct 3D printing of polymers onto textiles: experimental studies and applications. RP Journal. 2015 Aug 17.
136. Tibbits S. 4D printing: multi-material shape change. Architectural Design. 2014 Jan;84(1):116-21.
137. Zhou Y, Huang WM, Kang SF, Wu XL, Lu HB, Fu J, Cui H. From 3D to 4D printing: approaches and typical applications. Journal of Mechanical Science and Technology. 2015 Oct;29(10):4281-8.
138. Leist SK, Zhou J. Current status of 4D printing technology and the potential of light-reactive smart materials as 4D printable materials. Virtual and Physical Prototyping. 2016 Oct 1;11(4):249-62.
139. Tibbits S, McKnelly C, Olguin C, Dikovsky D, Hirsch S. 4D printing and universal transformation. 2012.
140. Tibbits MM, Haran M, Liechty JC. Parallel multivariate slice sampling. Statistics and Computing. 2011 Jul 1;21(3):415-30.
141. Torres H, Rodríguez Ripoll M, Prakash B. Tribological behaviour of self-lubricating materials at high temperatures. International Materials Reviews. 2018 Jul 4;63(5):309-40.
142. Gladman AS, Matsumoto EA, Nuzzo RG, Mahadevan L, Lewis JA. Biomimetic 4D printing. Nature materials. 2016 Apr;15(4):413-8.
143. Kamila S. Introduction, classification and applications of smart materials: an overview. American Journal of Applied Sciences. 2013 Aug 1;10(8):876.
144. Kim H, Wilburn BR, Castro E, Garcia Rosales CA, Chavez LA, Tseng TL, Lin Y. Multifunctional SENSING using 3D printed CNTs/BTO/PVDF nanocomposites. Journal of Composite Materials. 2019 May;53(10):1319-28.

145. Dadbakhsh S, Speirs M, Kruth JP, Schrooten J, Luyten J, Van Humbeeck J. Effect of SLM parameters on transformation temperatures of shape memory nickel titanium parts. Advanced Engineering Materials. 2014 Sep;16(9):1140-6.
146. Rossiter J, Walters P, Stoimenov B. Printing 3D dielectric elastomer actuators for soft robotics. InEAP actuators and devices (EAPAD) 2009 2009 Apr 6 (Vol. 7287, p. 72870H). International Society for Optics and Photonics.
147. Bodkhe S, Turcot G, Gosselin FP, Therriault D. One-step solvent evaporation-assisted 3D printing of piezoelectric PVDF nanocomposite structures. ACS applied materials & interfaces. 2017 Jun 21;9(24):20833-42.
148. Raviv. D (2014). Explainer: what is 4D printing?http://theconversation.com/explainer-what-is-4d-printing-35696
149. Srivastava V, Chester SA, Ames NM, Anand L. A thermo-mechanically-coupled large-deformation theory for amorphous polymers in a temperature range which spans their glass transition. International Journal of Plasticity. 2010 Aug 1;26(8):1138-82.
150. Hager MD, Bode S, Weber C, Schubert US. Shape memory polymers: Past, present and future developments. Progress in Polymer Science. 2015 Oct 1;49:3-3.
151. Lendlein A. Progress in actively moving polymers. Journal of Materials Chemistry. 2010;20(17):3332-4.
152. Ge Q, Qi HJ, Dunn ML. Active materials by four-dimension printing. Applied Physics Letters. 2013 Sep 23;103(13):131901.
153. Mao Y, Yu K, Isakov MS, Wu J, Dunn ML, Qi HJ. Sequential self-folding structures by 3D printed digital shape memory polymers. Scientific reports. 2015 Sep 8;5(1):1-2.
154. Ge Q, Dunn CK, Qi HJ, Dunn ML. Active origami by 4D printing. Smart materials and structures. 2014 Aug 11;23(9):094007.
155. Kravchenko A, Shevchenko A, Ovchinnikov V, Priimagi A, Kaivola M. Optical Interference Lithography Using Azobenzene-Functionalized Polymers for Micro-and Nanopatterning of Silicon. Advanced materials. 2011 Sep 22;23(36):4174-7.
156. Martins P, Lopes AC, Lanceros-Mendez S. Electroactive phases of poly (vinylidene fluoride): Determination, processing and applications. Progress in polymer science. 2014 Apr 1;39(4):683-706.
157. Sencadas V, Gregorio Jr R, Lanceros-Méndez S. α to β phase transformation and microestructural changes of PVDF films induced by uniaxial stretch. Journal of Macromolecular Science®. 2009 May 21;48(3):514-25.

158. hoon Kim T, Arias AC. Characterization and applications of piezoelectric polymers. Electric al Engineering and Computer Sciences University of California at Berkeley. 2015 Dec 18.

159. Lau K, Liu Y, Chen H, Withers RL. Effect of annealing temperature on the morphology and piezoresponse characterisation of poly (vinylidene fluoride-trifluoroethylene) films via scanning probe microscopy. Advances in Condensed Matter Physics. 2013 Sep;2013.

160. Satapathy S, Gupta PK, Pawar S, Varma KB. Crystallization of Beta-phase Poly (vinylidene fluoride) films using dimethyl sulfoxide (DMSO) solvent and at suitable annealing condition. arXiv preprint arXiv:0808.0419. 2008 Aug 4.

161. Veith M, Mathur S, Lecerf N, Huch V, Decker T, Beck HP, Eiser W, Haberkorn R. Sol-gel synthesis of nano-scaled BTO, BaZrO3 and BaTi0. 5Zr0. 5O3 oxides via single-source alkoxide precursors and semi-alkoxide routes. Journal of sol-gel science and technology. 2000 Feb;17(2):145-58.

162. Xu Y. Ferroelectric materials and their applications. Elsevier; 2013 Oct 22.

163. Neto AC, Guinea F, Peres NM, Novoselov KS, Geim AK. The electronic properties of graphene. Reviews of modern physics. 2009 Jan 14;81(1):109.

164. Zhang LL, Zhou R, Zhao XS. Graphene-based materials as supercapacitor electrodes. Journal of Materials Chemistry. 2010;20(29):5983-92.

165. Singh R, Kumar R, Ranjan N, Penna R, Fraternali F. On the recyclability of polyamide for sustainable composite structures in civil engineering. Composite Structures. 2018 Jan 15;184:704-13.

166. Singh D, Singh R, Boparai KS. Development and surface improvement of FDM pattern-based investment casting of biomedical implants: A state of art review. Journal of Manufacturing Processes. 2018 Jan 1;31:80-95.

167. Ranjan N, Singh R, Ahuja IP. Investigations for In-house prepared Biocompatible Feed Stock Filament of Fused Deposition Modelling: A Process Capability study. Journal of Mechanical Engineering. 2018;48(1):18-23.

168. Kim H, Fernando T, Li M, Lin Y, Tseng TL. Fabrication and characterization of 3D printed BTO/PVDF nanocomposites. Journal of Composite Materials. 2018 Jan;52(2):197-206.

169. Cai X, Lei T, Sun D, Lin L. A critical analysis of the α, β and γ phases in poly (vinylidene fluoride) using FTIR. RSC advances. 2017;7(25):15382-9.